EXPERIMENTAL EVALUATION OF NITINOL FOR ENERGY DISSIPATING DEVICES

by

Kent K. Sasaki

ABSTRACT

This report presents the results of experimental testing of the nickel-titanium alloy nitinol for use in energy dissipating devices. Nitinol possesses the unique property of superelasticiy - the ability of a material to be deformed past the proportional limit and up to a limiting strain and not incur permanent set. Though there is no permanent set, hysteresis and therefore energy dissipation does occur.

The overall purpose of this report was to determine if nitinol could be used as an energy dissipating device which would not develop permanent set. The following material tests were conducted to gain an understanding of nitinol deformation behavior:

1) torsion tests on rectangular nitinol bars
2) bending tests on rectangular nitinol bars
3) bending tests on X - shaped nitinol bars
4) tensile tests on nitinol wire
5) tensile tests on nitinol springs
6) earthquake simulation testing of a model 3 story structure base isolated with nitinol springs

The results of the material tests revealed that for nitinol to be used effectively as an energy dissipating material without incurring permanent set the deformation type and device shape should be such that uniform strains are developed over the cross-section and length of the nitinol device. For the torsion and bending tests, non-uniform strains were developed and signficant amounts energy dissipation were accompanied by permanent set. Efficient devices which could produce uniform strains are uniaxial tension members or thin-walled circular tubes loaded in pure torsion.

ACKNOWLEDGMENTS

The research reported herein was supported by the National Science Foundation under Grant No. ECE-8414036 and was conducted at the University of California, Berkeley Earthquake Simulator Laboratory in Richmond, California and at the University of California, Berkeley Civil Engineering Laboratory in Berkeley, California. Professor James Kelly was the principal investigator for this project.

The authors would like to thank the National Science Foundation for their support, and Dr. D. Hogdson of Shape Memory Applications, Inc. for supplying the material and giving valuable advice. The assistance and advice during the course of testing and report preparation of Dr. R. Krumme, Dr. A. Whittaker and graduate student I. Aiken was greatly appreciated.

The staff of the Earthquake Engineering Research Center, especially Messrs. D. Clyde, W. Neighbor, and I. Van Asten provided invaluable assistance and advice over the course of the experimental work. The staff of the Civil Engineering Laboratory, especially Messrs. R. Stephans and L. Baker also provided invaluable assistance and advice over the course of the experimental work.

Table of Contents

List of Tables

Table

List of Figures

1.0 INTRODUCTION

It is generally accepted in structural design that buildings subjected to severe earthquake ground motions must dissipate energy to survive without collapse. In most buildings, a significant portion of energy is dissipated by the inelastic action of structural members and connections. If significant inelastic action is sustained over several cycles, degradation of these elements may occur leading to the collapse of the building.

One strategy to prevent such a failure is to install energy dissipating devices into the structure. These devices, not the structural components, dissipate the earthquake input energy.

In the past, these devices have been called structural fuses since they protect a structural system in much the same manner that electrical fuses protect an electrical system. Instead of electrical energy, structural fuses protect a building from energy inputs due to earthquake ground motion. When a severe earthquake occurs, the inelastic action is concentrated in the energy dissipating devices thereby protecting the main structural system. If these dissipating devices are based on conventional materials such as mild steel (as are eccentric bracing [1] and Added Damping And Stiffness (ADAS) elements [2]) they, just like electrical fuses, must be replaced. Finding a reusable structural fuse or energy dissipating device is the basis for this research on nitinol.

Nitinol is a nickel - titanium shape memory alloy. The term "shape memory alloy" in general refers to metals which are able to be deformed, and on heating regain their original shape. Most shape memory alloys also possess superelasticity.

Superelasticity describes the ability of a material to be deformed past its proportional limit and on unloading return to its original location under zero load, i.e. no permanent set is induced. Unlike the general shape memory phenomenon, no external temperature change is required for superelasticity to occur. Although

as the ideal superelastic stress - strain curve in Figure 1.1 shows, hysteresis and therefore energy dissipation occurs.

The superelastic behavior of nitinol was studied in this research. Specifically, we looked at the capability of superelastic nitinol to dissipate energy without developing permanent set. In this way, it was hoped we could use nitinol in a device to produce a reusable structural fuse.

The feasibility of using nitinol as a reusable structural fuse was determined by conducting a series of material tests. These material tests consisted of tests in torsion, bending, and tension. Nitinol in the form of plates, wire and springs were tested. The testing concluded with an earthquake simulation test of a 3 story model structure base isolated with nitinol springs.

2.0 NITINOL

2.1 Shape Memory Alloys

The shape memory alloy is a relatively new engineering material. It was only 25 years ago that Buehler and Wiley of the U.S. Naval Ordinance Laboratory developed a unique material that possessed "memory". This memory material was able to be deformed and then remember its shape when subjected to certain conditions, hence the name "shape memory".

Nitinol is such a shape memory alloy. Nitinol describes an alloy with nearly equiatomic compositions of nickel and titanium. It is the shape memory alloy that Buehler and Wiley first developed - since that time, however, many other shape memory alloys have been discovered. To date, only the NiTi based and Cu-based alloys have been found to be commercially viable for engineering applications.

The behavior of nitinol is controlled by many parameters. A full discussion of these parameters is found in papers by Perkins and Duerig [3, 4]. For this study, the main interest is the property of superelasticity since it allows nitinol to dissipate energy without damage or permanent set.

2.2 Superelasticity

For the purpose of this report, superelasticity is defined to be the ability of a metallic alloy under constant temperature to be strained past its proportional limit and on unloading return to its original shape. This interesting behavior occurs because superelastic materials deform by stress-induced phase transformations and not by plastic slip as is usual for materials like steel or aluminum.

The stress-strain curve in Figure 2.1 illustrates this stress-induced phase transformation. Initially, the nitinol is in the austenite phase which is characterized by a face centered cubic crystalline structure. The initial slope of the stress-

strain curve, k_1, reflects the stiffness of this austenite phase. As the stress is increased to the critical loading stress, σ_l, the crystal structure changes to that of the martensite phase (characterized by a body centered tetragonal structure) and the material begins to yield. The new reduced stiffness is k_2. The reduction in stiffness is due to the change in crystalline structure from austenite to martensite and not plastic slip. The loading plateau extends from the critical loading strain, ϵ_l, to the elastic limit strain, ϵ_{el}. Strains above ϵ_{el} induce plastic slip and therefore permanent strain, ϵ_p, in the material. Values of the elastic limit strain, ϵ_{el}, for nitinol are usually from 5% to 10%. These values are very large when compared to typical materials such as steel where ϵ_{el} ranges from 0.2% to 0.5%. On unloading, nitinol transforms from martensite back to austenite. If the strain levels are kept below ϵ_{el} then the permanent strain, ϵ_p, is zero and the material returns to its original shape.

For full superelasticity to occur the temperature must be above the transformation temperature A_f (austenite finish) and below M_d (the temperature at which martensite can no longer be stress-induced): this defines the superelastic temperature range (Figure 2.2). At temperatures below the transformation temperature A_f, the stress induced martensite remains stable and does not revert to austenite, therefore a large permanent strain, ϵ_p, results. At temperatures above M_d, austenite cannot be stress induced to martensite. The superelastic temperature range can be as large as 60° F (30° C). For example, a typical value of A_f is 40° F, thus for a temperature range of 60° F, M_d would be approximately 100° F. Superelasticity would therefore occur from 40° F to 100° F.

2.3 Advantages of Nitinol

Besides superelasticity, nitinol has other desirable engineering properties. Nitinol has excellent corrosion resistance [5, 8]. It is more corrosion resistant than most structural materials including brasses and cupronickels. Nitinol has a long

fatigue life [5]. Although this is currently a subject of debate, experiments by the Lawrence Berkeley Laboratory showed that under certain conditions the shape memory effect could be repeated over many millions of cycles [6, 7]. With respect to other shape memory alloys, nitinol is stronger and stiffer [5]. It can also operate without memory loss under higher temperatures than other shape memory alloys [5].

2.4 Disadvantages of Nitinol

Nitinol has several disadvantages that currently limit its commercial implementation. Nitinol is expensive. Its current cost in bulk form is on the order of five hundred dollars a pound. This high cost is due to several factors. One factor is that titanium is a main raw material in nitinol. Nitinol must also be closely monitored during processing and production. As was mentioned before in section 2.2, the transformation temperatures are extremely sensitive to the proportions of nickel and titanium. A 0.3 percent variation in the titanium content could be responsible for a change of 50° F to 100° F in the transition temperatures [8]. This necessitates close inspection during production which in turn increases the cost.

For a single composition of nitinol, temperature can greatly affect its mechanical properties (σ_l, σ_u, ϵ_l, ϵ_{el}, k_1, k_2). This factor should be considered where nitinol is used in environments subject to large temperature fluctuations. Currently, the superelastic behavior of nitinol can only be attained over a temperature range of 60° F. For many civil engineering structures this temperature range may be inadequate and therefore a temperature controlled environment maybe required to ensure the superelastic behavior of nitinol. As mentioned in section 2.3, nitinol's fatigue characteristics are a subject of debate. A recent report by Ritchie [9] found that the crack growth rates are relatively fast and the fatigue threshold values low compared to other metallic alloys of similar strength. Machining nitinol is also more difficult than other metals. To deal with this problem, some

supply and development firms have developed their own machining procedures.

3.0 MATERIAL TESTING

3.1 Purpose of Tests

During the early stages of the study, extensive literature was found on the single crystalline behavior of nitinol, but only limited literature was found on the polycrystalline behavior of nitinol. Therefore, the purpose of the material tests was to gain an understanding for the behavior of nitinol in polycrystalline form. Would the polycrystalline nitinol behave in a similar to the nitinol previously tested in single crystal form [7]? It was hoped it would since the initial interest was the stress-strain behavior of nitinol in single crystal form (Figure 1.1).

3.2 Specimen Size and Shapes

The size and shape of the test specimens were limited by cost and commercial availability. Most current commercial applications use nitinol in relatively small form. Nitinol wire 0.5 to 1.0 mm in diameter, and nitinol springs 2 to 5 lb/in in stiffness are common. Large forms typical of civil engineering applications are not readily available since past applications have been targeted to mechanical or electrical engineering applications. The specimens received were: four 1 1/8" x 1/4" x 8" bars, 5 feet of 2 mm diameter wire, and four 2.7 lb/in springs, and two 1.8 lb/in springs. The bars, springs and wire were supplied by Shape Memory Applications of Cupertino, California.

3.3 Test Plan

A test plan was developed based on the size and shape of the specimens and the deformation type that might be used in an actual energy dissipating devices. The nitinol bars were first tested in torsion, and then bending. The wire and springs were to be tested in tension. Finally, the nitinol springs were installed in a small base isolated model and subjected to a series of simulated ground motions. The response of the nitinol base isolated structures were compared to the same structure base isolated with linear elastic springs

4.0 TORSION TESTS

4.1 Purpose of Torsion Tests

The intent of the torsion tests was to determine nitinol's energy dissipative capacity in torsion. Research by Kelly and Tsztoo has shown that torsional devices can be used effectively in dissipating energy [10].

4.2 Torsion Test Setup

Torsion tests were conducted on a 1 1/8" x 1/4" x 8" nitinol bar. This shape was chosen because it could easily fit into the existing torsion tester and it could be used for the bending tests to follow.

The torsion tests were conducted in the Civil Engineering Materials Test Laboratory of the University of California, at Berkeley. The testing apparatus can be seen in Figures 4.11 and 4.12. It is a Tinius-Olsen machine primarily used for testing concrete samples, therefore the range of test speeds were rather slow - 1 to 80 degree rotation per minute.

The operation of the machine is simple. The right half of the machine is mounted on rollers and can be moved back to accommodate the sample. One end of the test coupon is clamped into the rotational drum on the left. The right half of the machine is then rolled forward until the drum engages the free end of the coupon. The clamps are then tightened, resulting in a torsionally fixed-ended bar. In operation, the right drum rotates while the left drum remains stationary.

This torsion tester can only be displacement controlled, i.e. the only control is the speed at which the right drum rotates. A built-in force transducer measures the torque developed in the specimen. The torque readings are given on the dial readout of the tester. Rotation had to be measured by an LVDT (Linear Variable Differential Transformer) since the tester was not equipped with a electronic measurement device. Because of the LVDT setup, rotations were limited to plus or

minus 90 degrees. Data was acquired via one of the portable University of California, at Berkelely data acquisition systems controlled by an IBM PC.

4.3 Torsion Test Parameters

To observe strain-rate effects, two rotational speeds were chosen: 8 deg/min. and 80 deg/min. To observe strain-level effects two maximum rotation levels were chosen: 60 degrees and 90 degrees. Four full cycles were run during the 80 deg/min tests and two full cycles were run during the 8 deg/min tests. One full cycle describes the bar being rotated to its positive maximum rotation, then being rotated in the opposite direction to its negative maximum rotation and back to its original location at zero rotation.

4.4 Torsion Test Results

The results from the torsion tests are seen graphically in Figures 4.4.1 to 4.9 and in tabular format in Tables 4.4.1 to 4.4.4.

The torque-rotation curves of Figure 4.1 to 4.4 seem to be similar whether the specimen is rotated in the positive (clockwise) direction or the negative (counterclockwise) direction. The results in Tables 4.4.1 and 4.4.2 support this. The unprimed values in Tables 4.4.1 to 4.4.4 were measured from the curve when the rotations were positive, similarly, the primed values were measured from the curve when the rotations were negative. In Table 4.4.1 for the nitinol coupons, both the initial stiffness, k_1, and plateau stiffness, k_2, are similar (within 5%) for positive or negative rotations. The yield torque in the positive direction, T_y, and the yield torque in the negative direction, T_y', are also very similar (within 1%). The maximum torques are different because the maximum rotations in the positive and negative directions were sometimes different since the tester could only be controlled manually.

One can also see from Figures 4.1 to 4.4 that the reduction in stiffness on yielding is not as dramatic as one would expect for an elastic-perfectly plastic system. This is in part due to the rectangular shape of the torsion test specimen. Rectangular sections do not yield simultaneously over their cross-sectional area when subjected to torsion about the longitudinal axis. Some outer fibers maybe yielding, but the inner fibers are still elastic, therefore the overall stiffness will not follow the classic elastic-perfectly plastic shape of a specimen in tension. Another reason maybe that the tensile stress-strain curve of the bar material does not approach that of an elastic-plastic material.

Figures 4.3 and 4.4 reveal that for these rotational levels a permanent set resulted. The shear strain levels must have been such that some of the stress-induced martensite deformed by plastic slip, which resulted in permanent set.

As was expected, an increase in strain rate increased the stiffness of the nitinol. This can be seen in Figures 4.5 and 4.6. The solid line indicates the tests that were performed at a speed of 80 deg/min. The broken line indicates the tests that were performed at a speed of 8 deg/min. For both Figures 4.5 and 4.6, the initial stiffness of the fast tests was greater than the slow tests.

The hysteresis loops for the nitinol specimen were smaller than were expected. One can compare the hysteresis loops of nitinol with a non-superelastic material like aluminum. Figures 4.8 and 4.9 compare nitinol hysteresis with aluminum hysteresis. The area enclosed by the aluminum hysteresis curve is much larger than that for the nitinol specimens. Note that the levels of rotation for the nitinol specimens are much higher than maximum rotation of the aluminum specimen. In order to obtain the same amount of energy dissipated as by the aluminum specimen, much more nitinol material would be required.

Compared to conventional materials such as aluminum, the permanent set of nitinol is small. The ratios in Table 4.4.4 illustrate this. The rotational ductility,

μ_θ, and the permanent set ratio, γ_θ, are defined as follows:

$$\mu_\theta = \frac{\theta_{max}}{\theta_y}$$

$$\gamma_\theta = \frac{\theta_p}{\theta_{max} - \theta_y}$$

where: θ_y = the rotation at the proportional limit

θ_{max} = the maximum rotation of that test

θ_p = the rotation at zero torque after test

The rotational ductility, μ_θ, is a common engineering quantity which measures deformation past the elastic limit. It was not, however, adequate to characterize the unique behavior of superelastic materials like nitinol. In an attempt to better characterize the behavior of nitinol, the permanent set ratio, γ_θ, was defined. The permanent set ratio indicates the percentage of the deformation beyond yield that is permanent. For conventional metals strained past their proportional limit, γ_θ = 100%, i.e. the permanent set = the deformation beyond the proportional limit. This is not the case for superelastic materials such as nitinol. Table 4.4.4 shows that for rotational ductilities up to 4, the permanent set ratio is less than 10%. These low values of γ_θ are our main interest because nitinol can be deformed past its proportional limit without incurring significant permanent set.

Having low values of γ_θ is desirable since permanent set is small, but in order to function as an energy dissipating device the hysteretic damping provided by the nitinol must be significant. To measure the amount of hysteretic damping the

equivalent viscous damping ratio, ξ_{eff} is used, where:

$$\xi_{eff} = \frac{w_D}{4 \pi w_S}$$

Where w_D is the area enclosed by the torque-rotation curve and w_S is the area between a horizontal axis at torque = 0 and a line drawn from point of maximum rotation. These quantities are illustrated in Figure 4.10. In order to obtain the effect of both positive and negative rotations, the values of w_D and w_S include areas from both the first and third quadrants.

The quantity ξ_{eff} is used extensively to equate hysteretic damping to viscous damping. This has its faults since hysteretic damping is displacement dependent while viscous damping is essentially velocity dependent. For this section, ξ_{eff} shall be used as a quantitative measure of hysteretic damping. Table 4.4.4 reveals that ξ_{eff} for nitinol is much smaller than the ξ_{eff} for aluminum, i.e. plastic deformation in aluminum dissipates more energy per unit deformation in the plastic range than the phase shifted deformation of nitinol in the elastic range.

5.0 BENDING TESTS

5.1 Purpose of Bending Tests

The intent of the bending tests was to determine nitinol's energy dissipative capacity in flexure. Research has already been conducted on steel bending devices. Kelly, Skinner and Beucke have tested a steel cantilever energy dissipating device based on flexural deformation [11]. Recently, Bertero and Whittaker conducted extensive testing on steel X - shaped energy dissipating devices (Added Damping And Stiffness (ADAS) elements) [2]. Both systems performed well, but inelastic action in these steel devices resulted in permanent set. It was hoped that nitinol could be substituted for steel in these devices resulting in energy dissipation without significant permanent set.

5.2 Bending Test Setup

Bending tests were conducted on two 1 1/8" x 1/4" x 8" nitinol bars. The 1st fixture system (Figure 5.1) went through three subsequent design iterations. "Fixture system" refers to both the test fixture configuration and the shape of test specimens. Fixture system 2 used larger clamping bolts and roughened clamp surfaces. Fixture system 3 was identical to system 2, except rounded clamp corners were used. Fixture system 4 (Figures 5.2 to 5.5) was identical to system 3, except X-shaped bars were used.

Fixture system 2 was developed because the ends of the test specimens slipped in the clamps of fixture system 1. The slip was caused by tensile forces developed in the specimens due to the shortening of the test span. Significant shortening occurred because the end displacements were large (0.7") compared to the length of the test span (2.0"). To stop the slip larger bolts were used to increase the normal force and the bar surfaces in contact with the clamps were roughened with a mill file to increase the friction coeficient. These alterations were enough to prevent further bar slip in the clamps.

Fixture system 1 and 2 both used 90° corners at the clamp ends (Figure 5.1). During testing it was found that these 90° corners caused stress concentrations large enough to fracture the nitinol bars. To relieve the stress concentrations, the clamps were rounded at the top and bottom. This is fixture system 3. This alteration helped, but did not prevent bar fracture which occurred at an end displacement $\delta = 0.7"$. The final design , fixture system 4, was to shape the test specimens into a X or hour-glass shape (Figure 5.6). This shape would distribute the yielding over the length of the specimen instead of concentrating yielding at the fixed ends.

The overall test setup is seen in Figures 5.7 and 5.8. A Material Testing System (MTS) cyclic tester was used to load the specimen. For the level of test displacements expected (0.1" to 1.0"), the MTS was able to cycle to a rate of 5Hz. The MTS could either be displacement or force controlled. To prevent excessive displacement and possible bar fracture, displacement control was chosen. The data was acquired via a portable University of California at Berkeley data acquisition system controlled by an IBM PC.

5.3 Bending Test Parameters

The strain rate and strain level were the two main test parameters. Tests were conducted at speeds of 0.01Hz and 0.1Hz. Test speeds were kept low to observe the deformation of the specimen in the test fixture. End displacements, δ, were varied from 0.1" to 0.9" in increments of 0.1". Tests were run for one full cycle since the primary interest was the shape of the hysteresis curve.

5.4 Bending Test Results

Overall, none of the bending tests produced large hysteresis loops similiar in shape to Figure 1.1. The reduction of stiffness on yielding was not as dramatic as hoped and the hysteresis loops were thinner than expected with a substantial amount of permanent set occurring. Values of the permanent set ratio, γ_θ, defined

in section 4.4 were as high as 40%.

Figures 5.9 to 5.11 and 5.12 to 5.14 show the load-displacement and load-strain curves for specimens tested in the fixture system 2. Figure 5.9 shows that the yield point for the negative displacements is not as well defined as the yield point in the positive displacements. The suppression of the yield point for the negative displacements is thought to be due to tension stiffening effects caused by the test fixture. This stiffening effect is not seen in the load-strain curves of Figures 5.12 to 5.14. Fracture of the upper bar near the clamp end occurrred at $\delta =$ 0.7".

Before the next series of test, the fixture clamps were rounded (fixture system 3) to prevent stress concentrations and early bar fracture. The bars were also taken back to the supplier who heat-treated them to produce a stress-strain curve in tension as shown in Figure 5.15. The results of these tests for the rounded clamps and newly heat-treated bars is seen in Figures 5.16 to 5.19 and Figures 5.20 to 5.24. The results shown in Figures 5.16 to 5.19 were conducted at 0.01Hz. Those of Figures 5.20 to 5.24 were conducted at 0.1Hz. Figure 5.24 shows the load-strain curve for $\delta = 0.5$". This was the largest displacement for the system 3 tests. Even at this displacement, the hysteretic area was still small and permanent set was significant.

The final alteration (fixture system 4) was to grind down the bars into a X or hourglass shape in hopes of obtaining greater hysteretic damping and smaller permanent set. Fixture system 4 did not seem to accomplish this as the force-displacement curves of Figures 5.25 to 5.30 and Figures 5.31 to 5.37 show. The yield point is difficult to identify and the permanent set ratios are larger than any of the other test.

With the results of the bending tests being unsatisfactory, the testing continued in a more basic form: tension testing of nitinol wire and springs.

6.0 TENSION TESTS

6.1 Purpose of Tension Tests

The intent of the tension tests was to determine the energy dissipative capacity of nitinol wire. Nitinol wire could be used in diagonal tension cross-bracing in buildings. Nitinol cross-bracing could serve the dual purpose of adding stiffness and damping to a structure. Nitinol cross-bracing would have an advantage over steel cross-bracing since no permanent set would be accumulated during loading excursions beyond the proportional limit of the cross-braces. The accumulation of permanent set has been the main problem of steel cross-bracing since after each cycle of inelastic action the length of the steel bracing increases, therefore larger structure displacements are required to activate the bracing in the subsequent cycles. Large structure displacements may cause extensive damage to columns, beams and joints and eventually lead to failure of the structural system.

6.2 Tension Test Setup

Tension Tests were conducted on 2 mm nitinol wire in the Civil Engineering Materials Test Laboratory of the University of California at Berkeley. The test fixture is seen in Figures 6.1 and 6.2. The tensile load is measured by an internal load cell. The extension of the wire is measured by the extensiometer attached to the wire between the clamp ends. The tension tester can only be manually force-controlled. Data was collected via a portable University of California at Berkeley data aquisition system.

6.3 Tension Test Parameters

Tension tests were were conducted at two loading rates: 2 lbs/sec (low) and 200 lbs/sec (high) (rates measured while loading along the initial stiffeness). The tests were conducted at 3 temperatures: 40° F, 65° F and 150° F. Room temperature was 65° F. An ice water bath was used to cool the wire specimens down to 40° F and a 150 watt light bulb was placed next to the test fixture to raise the

test temperature to 150° F.

6.4 Tension Test Results

Tension test results can be seen in Figure 6.3. Figure 6.3a shows that extensive permanent set occurred at room temperture during slow loading. This was not expected, and as was latter found out, the nitinol wire supplied was non-superelastic at room temperature. Figure 6.3b shows that some recovery of permanent set does occur at fast loading rates. Also, the plateau stiffness increases with subsequent cycles during fast loading rates. A comparison of Figures 6.3a and 6.3c shows that high temperatures can increase the yield load by a factor of 2. This increase could be due to inducing an austenite crystal structure which occurs at elevated temperatures. Cooling the specimen to 40° F did not significantly change the yield load, but the fast loading rate caused partial recovery to occur and an increase in plateau stiffness (Figure 6.3d).

7.0 SPRING TESTS

7.1 Purpose of Spring Tests

The intent of the spring tests was to determine the energy dissipative capacity and the superelastic behavior of nitinol springs. The springs tested were then used in earthquake simulation testing of a model 3 story building.

7.2 Spring Test Setup

The nitinol spring tests were conducted at the Earthquake Engineering Research Center, Richmond, California. A MTS cyclic tension-compression tester was used to test the springs in tension. The tensile load was measured by a 500 pound load cell and the displacement was measured by a LVDT. The test was controlled and the data was acquired by a digital system, ATS (Automatic Testing System).

7.3 Spring Test Parameters

Two nitinol springs were tested: a 0.5" long (measured from centerline of outside spring coil to centerline of outside spring coil), 2.7 lbs/in spring and a 1.0" long, 1.8 lbs/in spring. Tension tests were conducted at 0.1 Hz and 1.0 Hz. Spring displacements varied from 2.0" to 3.0" for the short (0.5") springs and from 4.0" to 6.0" for the long (1.0") springs. Each test was run for 10 cycles.

7.4 Spring Test Results

Test results can be seen in Figures 7.1 to 7.8 and Table 7.4.1. Negligible permanent set occurred in all tests. This maybe due to the circular cross-section of the spring which caused a more uniform distribution of stress over the cross-section (as compared to the rectangular coupon cross-section used in the previous torsion (Chapter 4.0) and bending (Chapter 5.0) tests) and a more uniform distribution of stress over the length of the member (as compared to the bending tests). The reduction of stiffness after reaching the yield load is low ($\alpha_k = 3$) and maybe

7.0 SPRING TESTS

7.1 Purpose of Spring Tests

The intent of the spring tests was to determine the energy dissipative capacity and the superelastic behavior of nitinol springs. The springs tested were then used in earthquake simulation testing of a model 3 story building.

7.2 Spring Test Setup

The nitinol spring tests were conducted at the Earthquake Engineering Research Center, Richmond, California. A MTS cyclic tension-compression tester was used to test the springs in tension. The tensile load was measured by a 500 pound load cell and the displacement was measured by a LVDT. The test was controlled and the data was acquired by a digital system, ATS (Automatic Testing System).

7.3 Spring Test Parameters

Two nitinol springs were tested: a 0.5" long (measured from centerline of outside spring coil to centerline of outside spring coil), 2.7 lbs/in spring and a 1.0" long, 1.8 lbs/in spring. Tension tests were conducted at 0.1 Hz and 1.0 Hz. Spring displacements varied from 2.0" to 3.0" for the short (0.5") springs and from 4.0" to 6.0" for the long (1.0") springs. Each test was run for 10 cycles.

7.4 Spring Test Results

Test results can be seen in Figures 7.1 to 7.8 and Table 7.4.1. Negligible permanent set occurred in all tests. This maybe due to the circular cross-section of the spring which caused a more uniform distribution of stress over the cross-section (as compared to the rectangular coupon cross-section used in the previous torsion (Chapter 4.0) and bending (Chapter 5.0) tests) and a more uniform distribution of stress over the length of the member (as compared to the bending tests). The reduction of stiffness after reaching the yield load is low ($\alpha_k = 3$) and maybe

due to the non-uniform distribution of stress over the cross-section, i.e. not all portions of the cross-section yield at the same time. The effective viscous damping, ξ_{eff} (calculated similarly as in Section 4.4), ranged from 2.5% to 3.3% for the short springs and 2.4% to 2.7% for the long springs. The initial stiffness, k_1, increased by approximately 10% when the test speed was increased from 0.1 Hz to 1.0 Hz. It is difficult to determine whether the plateau stiffness k_2 increased with the increased test speed since the determination of k_2 was quite approximate.

8.0 EARTHQUAKE SIMULATION TESTING

Nitinol springs were placed in a 3 story base isolated model structure (Figures 8.2 to 8.14) and subjected to a series of system identification tests and simulated earthquake ground motions. The results of the nitinol base isolated model tests were compared with those of the same model structure base isolated with linear elastic springs. All tests were conducted in the Earthquake Simulation Laboratory of the University of California at Berkeley.

8.1 Base Isolated Model

The base isolated model was developed to study the response and behavior of actual base isolated structures. Assuming some simplifications, base isolated structures can be theoretically modelled as shown in Figure 8.17. The superstructure sits atop frictionless rollers which provide infinite vertical stiffness and zero horizontal stiffness. The horizontal springs model the lateral stiffness of the isolation system. This theoretical model was then replicated in the laboratory resulting in the base isolated model seen in Figures 8.2 to 8.14. To model the behavior of the rollers, the experimental supersturcture is mounted on an air bearing which provides a nearly frictionless sliding surface. The horizontal springs are attached from the base of the structure to the shake table which replicates the theoretical model identically (Figures 8.10 to 8.14).

8.2 The Superstructure

The superstructure is a steel-welded 3 story moment-resisting frame. Each story is 10 inches high, therefore the length scale factor is approximately 1/14 (assuming a prototype story height = 12 ft). The stiffness was instead chosen such that the natural frequencies of the superstructure could be excited by the shaking table (which can operate from 0 to 20Hz). The dimensions of the superstructure can be seen in Figure 8.18. The mass and weights of the superstructure are listed in Table 8.2.1. Based on these dimensions and weights, an eigenvalue

analysis was performed to evaluate the mode shapes and frequencies of the superstructure in a fixed base condition. From that analysis, the natural frequencies of the fixed-base superstructure for the 1st, 2nd and 3rd modes were found to be 3.24 Hz, 9.34 Hz, and 13.8 Hz respectively.

8.3 Base Isolation Springs

Four types of base-isolation springs were used in these tests. They are shown in Figure 8.1. The two springs in the upper left are the long nitinol springs followed (in a clockwise direction) by the four short nitinol springs, the four #142 linear elastic, and the two #135 linear elastic. The properties of each spring are seen in Table 8.3.1. The two types of nitinol springs were the same as those tested in Chapter 7. The two types of linear elastic springs were chosen such that when placed in the base isolated model, the linear elastic spring base isolated systems had similar fundamental natural frequencies to that of the nitinol base isolated systems. With these springs, five different test configurations were developed. System 1 used four #142 linear elastic springs and system 2 used four of the short nitinol springs. System 4 consisted of two #135 linear elastic springs and system 5 consisted of the two long nitinol springs. System 4 and 5 used two springs because only two long nitinol springs were available. System 3, which comprised of four linear elastic springs in parallel with four short nitinol springs, was not tested.

8.4 Model Instrumentation

The instrumentation of the base isolated model can be seen in Figure 8.19. The displacements at each level of the superstructure were measured by DCDTs (Linear Variable Direct Current Differential Transformers) mounted to a reference frame. As seen in Figure 8.19, the reference frame is fixed to the shake table base and not the shake table. Therefore, the displacements measured by the DCDTs are with respect to the shake table base. The displacement of the shake table is

measured by a DCDT also mounted to the base. Figure 8.20 shows the different displacement quantities of a base isolated system. As instrumented, the reference frame DCDTs measure the total displacements, v_t. The shake table DCDT measures the shake table displacement, v_g. Accelerometers were placed on each level of the superstructure as well as the shake table. The data channels associated with each piece of instrumentation are listed in Table 8.4.1.

8.5 Earthquake Simulation Test Laboratory

The testing of the base isolated model was conducted in the Earthquake Simulation Laboratory (ESL) of the University of California at Berkeley. The shake table has a usable area of 52" x 54" for mounting model structures. It is driven by one hydraulic actuator (Figure 8.15 and 8.16). The shake table was controlled and the data was collected via the ESL electronic control and data acquistion system.

8.6 Dynamic Test Program

8.6a Free Vibration Tests

A series of free vibration tests were conducted to identify the characteristics of the four base isolated systems. These tests consisted of pullback tests and impulse tests. The small size of the model allowed these tests to be performed by hand. For the pullback tests, one level of the base isolated structure was pulled back while the rest of the structure was held stationary. The pulled back level was then released and the base isolated structure was allowed to vibrate freely. The impulse tests consisted of hitting the frame at one level with a hand, then allowing the base isolated model to vibrate freely. The pullback and impulse tests were conducted on each system at each of the four levels. Data acquistion began just before the structure was released or impacted. Data acquistion ended when the structure was no longer seen moving.

The pullback tests and impulse tests were also conducted on the superstructure in a fixed-base condition.

8.6b Ground Motion Tests

The ground motion tests consisted of a random noise test, a square wave test and 3 simulated earthquakes. The types of earthquakes varied from those with predominantly low frequency content, to those with predominantly high frequency content. The earthquake used are listed below:

(1) Imperial Valley Earthquake (El Centro, EC) of May 18, 1940 - S00E component.

(2) Mexico City Earthquake (Mexico City Station, SCT) of September 19, 1985 - S60E component.

(3) Michoacan Earthquake (Zacatula Station, Zac) of September 19, 1985 - S00E

The El Centro earthquake was chosen for its broad frequency range, while the SCT earthquake was chosen for its low frequency range. The Zacatoula earthquake was chosen for its high frequency content. All earthquakes were time scaled by 1/2.

8.7 Dynamic Test Results

8.7a Free Vibration Test Results

From the free-vibration tests the natural frequencies of the base isolated systems and the fixed-base structure were found. Table 8.7.1 list these results. Typical acceleration time histories for levels 3 and 4 (Channel 36 and Channel 37) and a FFT (Fast Fourier Transform) of the level 4 acceleration time history are seen in Figures 8.21 to 8.24. The name of the test appears in the upper left corner. Two numbers follow the test name. The 1st number denotes the test system.

The 2nd number indicates the level of the structure excited. The frequencies were found from FFT plots. The mode shapes for System 1 (Figure 8.25) were found by plotting the amplitudes of a FFT plot for each structural level (degree of freedom). The other base isolated systems had nearly identical mode shapes.

The equivalent viscous damping ratio, ξ, for the fundamental frequency was found from the 1st level pullback tests. The logarithmic decrement approach was used with the following equation:

$$\xi = \frac{v_n - v_{n+m}}{2 \pi m v_{n+m}}$$

The test results are seen in Table 8.7.1.

The damping ratios for the fixed-base structure and linear elastic spring base isolated structures ranged from 1.5% to 1.7%. The damping ratios for the nitinol base isolated structures were dependent on the level of deformation in the springs, and ranged from 11% to 15%.

To obtain the damping ratio for higher modes, FFTs were bandpass filtered to obtain modal displacement time histories. The procedure used is outlined by Whittaker [1]. Having found the modal displacement time histories, a the conventional logarithmic decrement approach was used to obtain the damping ratio. The value of damping ratio was very sensitive to the type of filter used, therefore no reliable values of higher mode damping were found.

8.6b Ground Motion Test Results

The table displacement, table acceleration, FFT of the table acceleration, and acceleration response spectrum are shown for each ground motion (Figures 8.26 to 8.40). The maximum acceleration at each level for ground motion is plotted in Figures 8.41 to 8.48. System 1 (four elastic springs) is compared to System 2 (four nitinol springs) and System 4 (two elastic springs) is compared System 5

(two nitinol springs).

For every ground motion, the nitinol springs (both long and short) produced accelerations that were significantly less than those of the linear elastic spring systems. The reductions ranged from 20% to 75%. System 4 acceleration values for Figure 8.56 are high because the base of the superstructure impacted one end of the air bearing.

The reductions in displacement were also significant ranging from 5% to 70%. The maximum level displacements are plotted in Figures 8.49 to 8.56.

The maximum interstory drift which describes the relative amount of movement between two levels is plotted in Figures 8.57 to 8.64. The interstory drift for story 1 is calculated by subtracting the maximum positive displacement for level 1 from the maximum positive displacement for level 2 and dividing by the story height (10"). For most of the ground motions, the nitinol system interstory drifts for the 1st and 2nd story were substantially lower (70%) than the elastic system interstory drifts. However, the reductions in the 3rd story interstory drifts were not as substantial, and in some cases the nitinol system interstory drift was higher than that of the elastic system.

9.0 IMPLICATIONS OF TEST RESULTS

On the basis of the material tests conducted, conclusions were drawn in several areas.

In order for nitinol to be effective in dissipating energy while maintaining low values of permanent set, a deformation type and device shape must be chosen such that uniform strains are produced over the device cross section and over the device length. The uniform strains optimize the use of nitinol in the device. All fibers are enlisted to dissipate energy. If the device is designed correctly, the strains in the nitinol should remain below the elastic limit strain - thereby ensuring no permanent set.

Nitinol devices which do not produce uniform strains do not seem to be efficient in dissipating energy and maintaining low values of permanent set. The results of the torsion tests and the bending test attest to this. In both the torsion and bending tests, the strain distribution is not uniform. The extreme fibers of the rectangular torsion and bending members yield, but the inner fibers remain in the linear elastic range. This linear elastic core does not dissipate energy. In fact, to dissipate a significant amount of energy, the extreme fibers must be strained past the elastic limit strain, ϵ_{el}. Once this occurs, permanent strain will be induced into those fibers and produce a permanent set in the device. This was illustrated in the torque-rotation curves of Chapter 4 and force-displacement curves of Chapter 5. These non-uniform strains produced by device shape and deformation type are most probably the reason why polycrystalline and single crystalline stress-strain curves were very different.

Uniform strains are also important in ensuring that a substantial reduction in device stiffness occurs when the nitinol first reaches the proportional limit. The reduction of stiffness in the devices and the resulting softening of the structure is crucial because it may shift the period of the structure into a region of lower

seismic energy thereby reducing the response and damage of the structure.

The torsion, bending and spring tests had stiffness reductions at the proportional limit of 1.5 to 5 . Most of the wire tension tests had stiffness reductions of 10 to 20.

Temperature significantly affects the behavior of nitinol. This was observed from the results of the wire tensile tests. All properties of the stress-strain curve can be significantly affected (such as a 30% difference in yield stress) by temperature differentials of 100° F. To guarantee a certain range of behavior, the nitinol devices may need to be placed in a temperature controlled environment (one which maintains say a 40° F temperature range). For the new "smart" buildings, this temperature range should be easily attained.

The base isolation results show how nitinol can improve the performance of a linear elastic base isolation system by increasing the system's effective damping. Nitinol devices might also be used in conjunction with rubber base isolators to increase the system damping and help center the building after a severe earthquake.

Since uniform strains are important in producing a nitinol device which dissipates energy without incurring permanent set, devices such as uniaxial members in tension or thin-walled circular tubes in torsion seem to be the most promising device configurations. Since thin-walled circular tubes aren't readily available, a dissipating device based on uniaxial tension seems the most feasible option. At the final writing of this report, tests are planned for a 3 story model structure fitted with nitinol wire cross bracing. The tests should begin sometime in the summer of 1989.

REFERENCES

[1] A. S. Whittaker, C. M. Uang, and V. V. Bertero, "Earthquake Simulation Tests and Associated Studies of a 0.3-Scale Model of a Six-Story Eccentrically Braced Steel Structure," *UCB/EERC-87/02*, Earthquake Engineering Research Center, University of California, Berkeley, July 1987.

[2] A. Whittaker, V. V. Bertero, J. Alonso, and C. Thompson, "Earthquake Simulator Testing of Steel Plate Added Damping and Stiffness Elements," *UCB/EERC-89/02*, Earthquake Engineering Research Center, University of California, Berkeley, January 1989.

[3] T. W. Duerig and K. N. Melton, *Designing with the Shape Memory Effect*, Raychem Corporation, Menlo Park, California 94025.

[4] T. W. Duerig and R. Zadao, *An Engineer's Perspective of Psuedoelasticity*, Raychem Corporation, Menlo Park, California 94025.

[5] J. Perkins, "Ti-Ni and Ti-Ni-X Shape Memory Alloys," *Metals Forum*, Vol. 4, No.3, 1981.

[6] R. Banks, *Nitinol Heat Engines*, paper presented in reference [7]

[7] J. Perkins, "Shape Memory Effects in Alloys," *International Symposium on Shape*

Memory Effects and Applications, Plenum Press, New York, New York, 1975.

[8] C. M. Jackson, H. J. Wagner, and R. J. Wasilewski, "55 Nitinol - The Alloy with a Memory: Its Physical, Metallurgical Properties and Applications," *SP-5110*, NASA, Washington, D.C., 1972.

[9] R. H. Dauskardt, T. W. Duerig, and R. O. Ritchie, "Effects of Insitu Phase Transformation on Fatigue-Crack Propagation in Titanium-Nickle Alloys," *LBL-25491*, Lawrence Berkeley Laboratory, Berkeley, California.

[10] J. M. Kelly and D. F. Tsztoo, "The Development of Energy-Absorbing Devices for Aseismic Base Isolation Systems," *UCB/EERC-78/01*, Earthquake Engineering Research Center, University of California, Berkeley, January 1978.

[11] J. M. Kelly, M. S. Skinner, and K. E. Buecke, "Experimental Testing of an Energy-Absorbing Base Isolation System," *UCB/EERC-80/35*, Earthquake Engineering Research Center, University of California, Berkeley, October 1980.

TABLES

Test				Stiffness (kip-in/deg)				α_k	
Name	Type	Speed (deg/min)	θ_{max} (deg)	k_1	k_2	k_1'	k_2'	α_k	α_k'
Ttest2	NiTi	80	60	35	10	35	10	3.5	3.5
Ttest3	NiTi	8	60	33	8.4	33	8.0	3.9	4.1
Ttest4	NiTi	80	90	29	7.3	28	8.0	3.9	4.0
Ttest5	NiTi	8	90	29	7.0	29	7.0	4.1	4.1
Ttestal	Al	10	38	120	12.5	*	*	9.6	*

TABLE 4.1 TORSION TEST RESULTS: *Stiffness, k*

where:

unprimed values measured from positive rotation region
primed values measured from negative rotation region
asterisk unable to obtain value

$$\alpha_k = \frac{k_1}{k_2}$$

Test				Torque (kip-in)			
Name	Type	Speed (deg/min)	θ_{max} (deg)	T_y	T_{max}	T_y'	T_{max}'
Ttest2	NiTi	80	60	850	1150	850	1200
Ttest3	NiTi	8	60	850	1100	850	1150
Ttest4	NiTi	80	90	940	1420	950	1350
Ttest5	NiTi	8	90	880	1300	880	1280
Ttestal	Al	10	38	2200	2400	*	*

TABLE 4.2 TORSION TEST RESULTS: *Torque, T*

Test			Rotation (deg)					
Name	Type	Speed (deg/min)	θ_{max}	θ_y	θ_p	θ'_{max}	θ'_y	θ'_p
Ttest2	NiTi	80	60	24	2.5	62	22	0.0
Ttest3	NiTi	8	60	25	2.5	61	22	0.0
Ttest4	NiTi	80	90	22	4.0	92	30	10
Ttest5	NiTi	8	92	24	5.0	90	28	6.0
Ttestal	Al	10	38	19	19	*	*	*

TABLE 4.3 TORSION TEST RESULTS: *Rotations*, θ

Test				Ratios				
Name	Type	Speed (deg/min)	θ_{max} (deg)	μ_θ	μ'_θ	γ_θ (%)	γ'_θ (%)	ξ_{eff} (%)
Ttest2	NiTi	80	60	2.6	2.8	6.7	0.0	2.7
Ttest3	NiTi	8	60	2.4	7.0	2.8	0.0	3.1
Ttest4	NiTi	80	90	4.1	3.1	5.9	16	4.6
Ttest5	NiTi	8	92	3.3	3.2	7.4	7.0	4.7
Ttestal	Al	10	38	1.9	*	100	*	16

TABLE 4.4 TORSION TEST RESULTS: *Ratios*

where:

$$\mu_\theta = \frac{\theta_{max}}{\theta_y}$$

$$\gamma_\theta = \frac{\theta_p}{\theta_{max} - \theta_y}$$

$$\xi_{eff} = \frac{w_D}{4\,\pi\,w_S}$$

Test Parameters				Test Results				
Name	Spring Length (in.)	Speed (Hz)	δ_{max} (in.)	k_1 (lbs/in)	k_2 (lbs/in)	α_k (k_1/k_2)	F_y (lbs)	ξ_{eff}
spr1	0.5	0.1	2.0	2.6	1.0	2.6	2.8	2.5%
spr2	0.5	1.0	2.0	2.8	0.9	3.1	2.8	*
spr3	0.5	0.1	3.0	2.6	0.9	2.8	2.6	3.3%
spr4	0.5	1.0	3.0	2.8	0.8	2.9	2.9	*
spr7	1.0	0.1	4.0	1.8	0.6	2.8	2.9	2.4%
spr8	1.0	1.0	4.0	1.5	0.5	3.0	*	*
spr9	1.0	0.1	6.0	1.8	0.6	2.6	2.6	2.7%
spr10	1.0	1.0	6.0	1.5	0.5	3.0	*	*

* Unable to obtain from test.

TABLE 7.4.1 SPRING TEST RESULTS

Type	Level	Mass (g)	Weight (lb)	Size (in)
Floor Plates (Steel)	4	2520	5.54	10 x 8 x 1/4
	3	2540	5.59	" " "
	2	2500	5.50	" " "
Lead Weight	4	1920	4.22	9 1/2 x 6 1/2 x 1/8
	3	1810	3.98	8 9/16 x 6 1/2 x 1/8
	2	1830	4.03	" " "
Mounting Plate (Aluminum)		3120	6.86	10 x 9 7/8 x 1/2
Columns (Steel)		120	0.12	1/8 x 2/8 *
Bearing Plates (Aluminum)	Top	1650	3.62	7 x 7 x 3/4
	Side	623	1.37	7 x 3/4 x 3/4
	Bott	1650	3.62	7 x 7 x 3/4
Cross Bar (Aluminum)		359	0.79	16 1/8 x 1 x 1/2
Accelerometer Mounts & DCDT Mounts (Aluminum)		6.3	0.014	1 x 1 x 3/8

* Weak directions runs N-S.

TABLE 8.2.1 SUPERSTRUCTURE WEIGHTS AND DIMENSIONS

System [1]	Type[2]	Diameter[3] (in)	Length[4] (in)	Initial Stiffness (lb/in)	Plateau Stiffness (lb/in)
1	(4) Steel - #142	15/16	8 1/2	2.1	*
2	(4) Nitinol - Short	5/16	10/16	2.7	0.9
4	(2) Steel - #135	13/16	8 1/2	1.7	*
5	(2) Nitinol - Long	5/16	1	1.8	0.6

1 System 3 was not tested.
2 Number of springs used in each system listed in parentheses. Standard designation of steel springs listed after dash.
3 Diameter measured from outside to outside of coil diameter.
4 Length measured from outside to outside of end coils.
* Steel springs remained linear elastic - no plateau stiffness.

TABLE 8.3.1 PROPERTIES OF BASE ISOLATION SPRINGS

Channel*	Instrument	Variable
32	DCDT	horiz. table displ.
33	Accelerometer	horiz. table accel.
34	Accelerometer	level 1 horiz. accel.
35	Accelerometer	level 2 horiz. accel.
36	Accelerometer	level 3 horiz. accel.
37	Accelerometer	level 4 horiz. accel.
38	DCDT	level 1 horiz. displ.
39	DCDT	level 2 horiz. displ.
40	DCDT	level 3 horiz. displ.
41	DCDT	level 4 horiz. displ.

* Channels 1 to 31 not used.

DCDT = Linear Variable Direct Current Differential Transformer

TABLE 8.4.1 MODEL & TABLE INSTRUMENTATION

System[1]	Natural Frequencies (Hz)				ξ [2]
	1	2	3	4	
1	1.3	4.8	9.9	13.8	1.7%
2	1.4	4.8	9.8	13.6	15%
4	0.8	4.7	9.7	13.6	1.6%
5	0.8	4.7	9.7	13.7	11%
Fixed	3.2	9.3	13.6	*	1.5%

1 System 3 not tested.

2 1st mode damping ratio.

* Fixed system has only 3 degrees of freedom.

TABLE 8.7.1 NATURAL FREQUENCIES AND 1ST MODE DAMPING RATIO

FIGURES

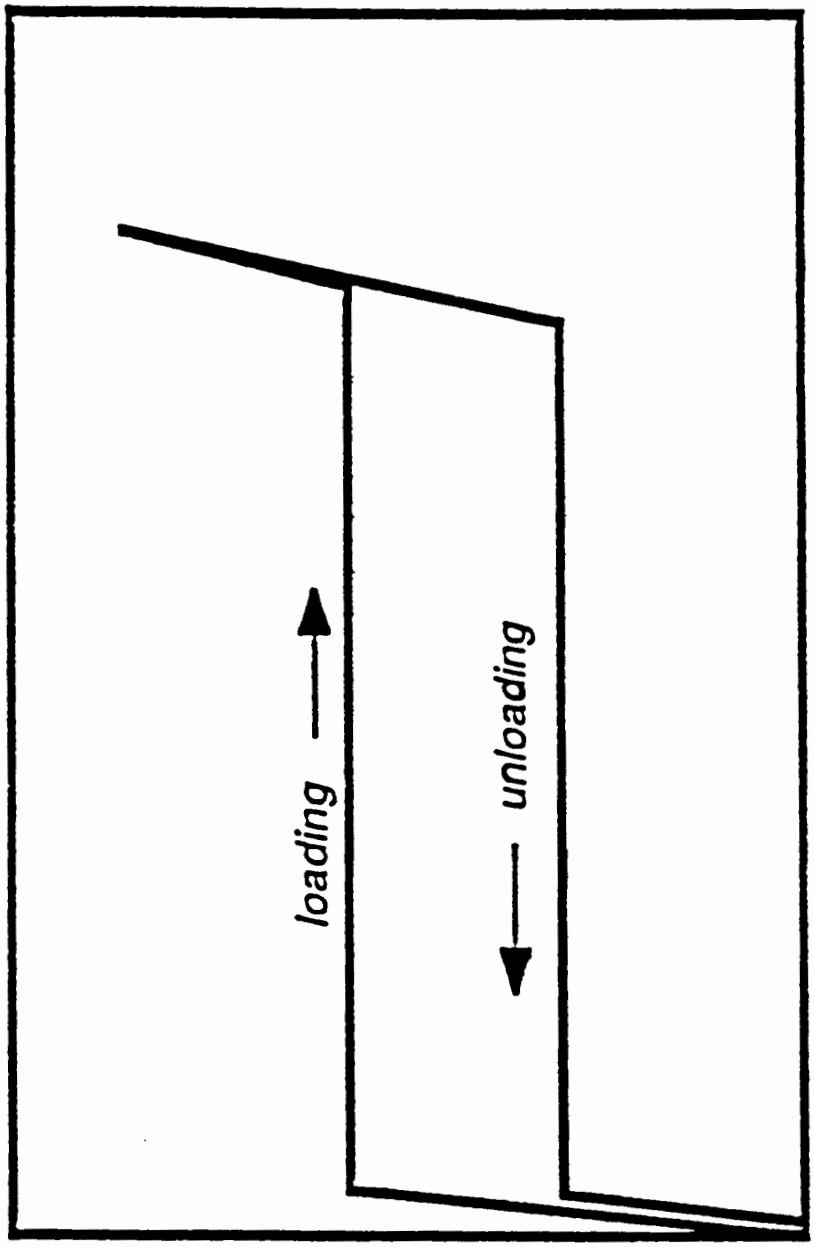

FIGURE 1.1 SUPERELASTIC STRESS - STRAIN CURVE

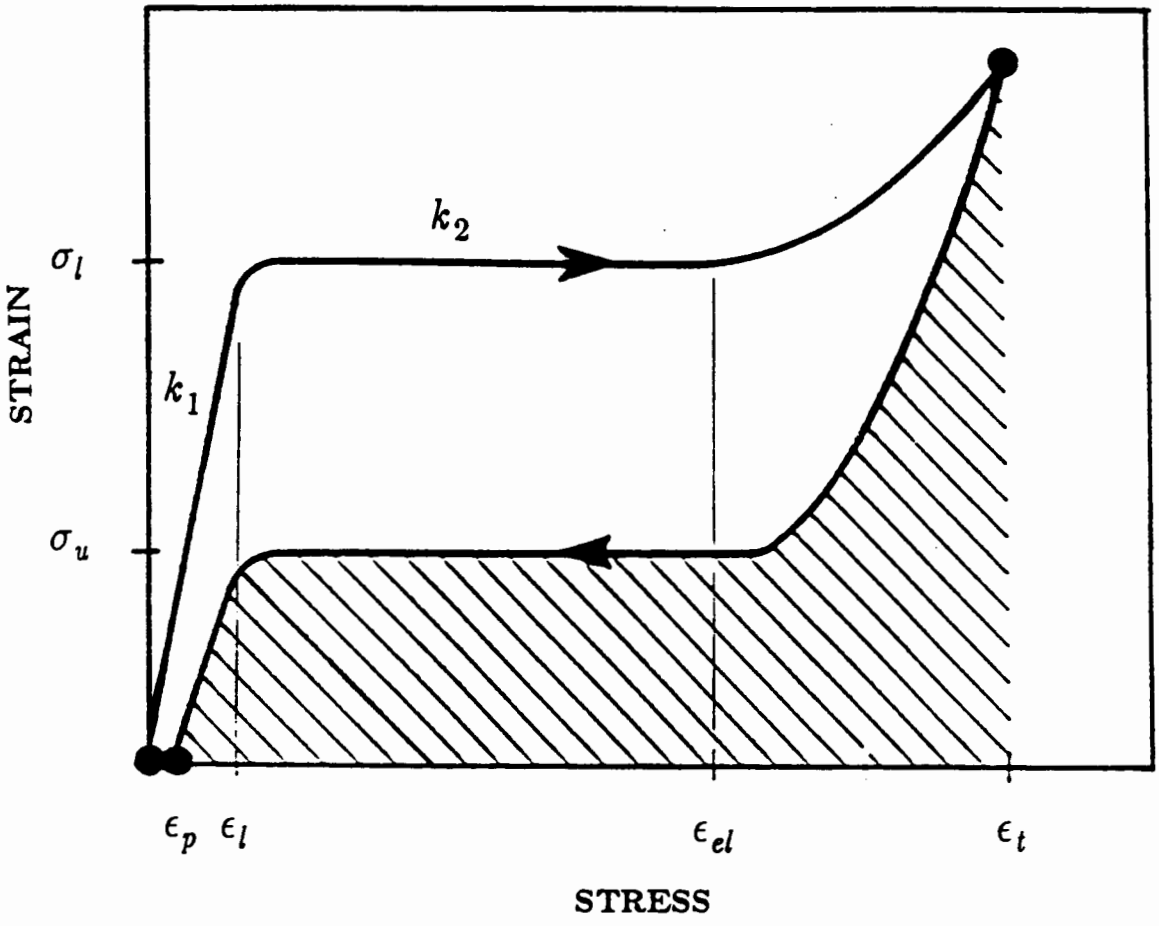

where:

ϵ_p = permanent strain
ϵ_l = critical loading strain
ϵ_{el} = elastic limit strain
ϵ_t = total strain
σ_l = critical loading stress
σ_u = critical unloading stress
k_1 = initial stiffness
k_2 = reduced stiffness

FIGURE 2.1 SUPERELASTICITY

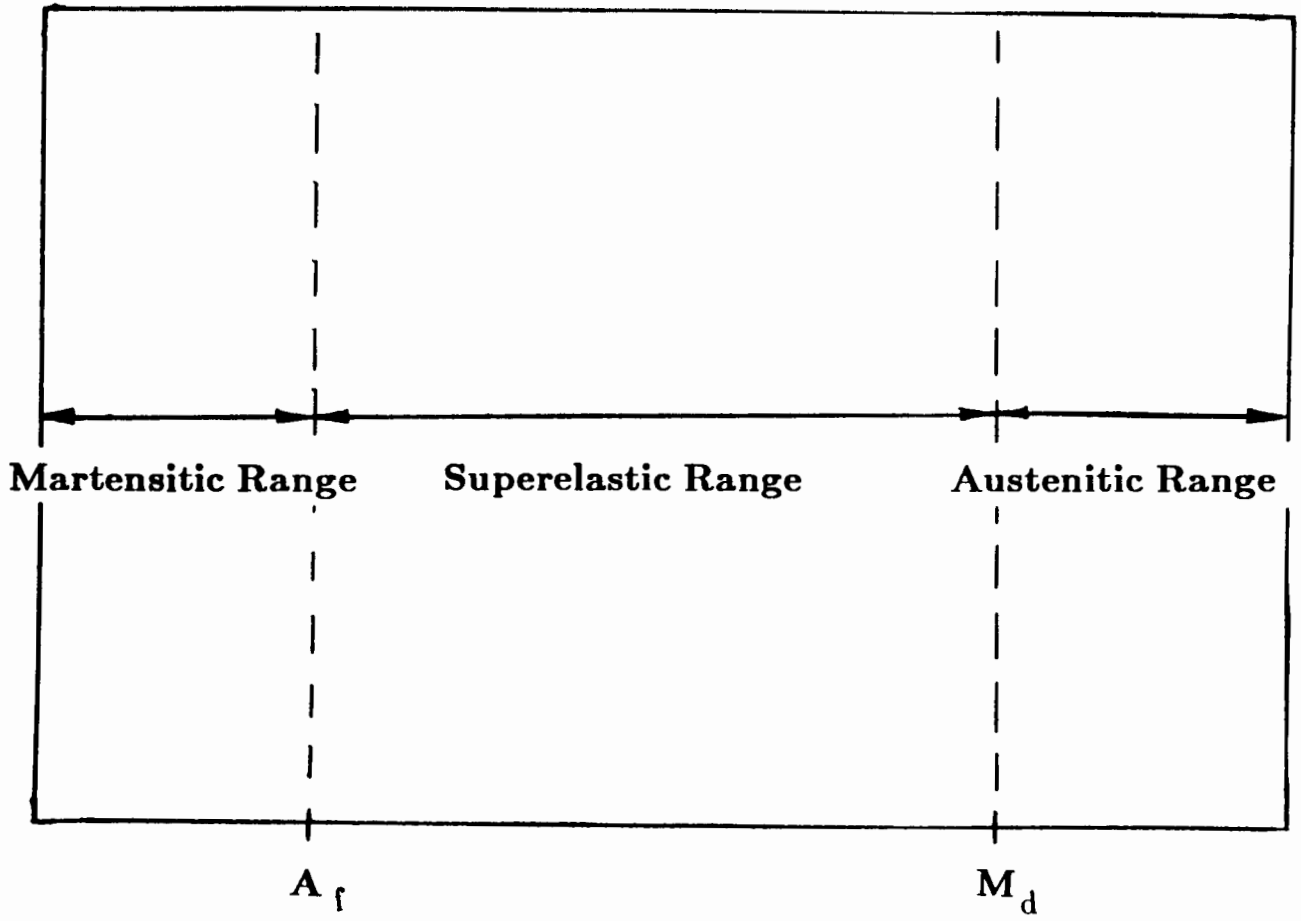

FIGURE 2.2 SUPERELASTIC TEMPERATURE RANGE

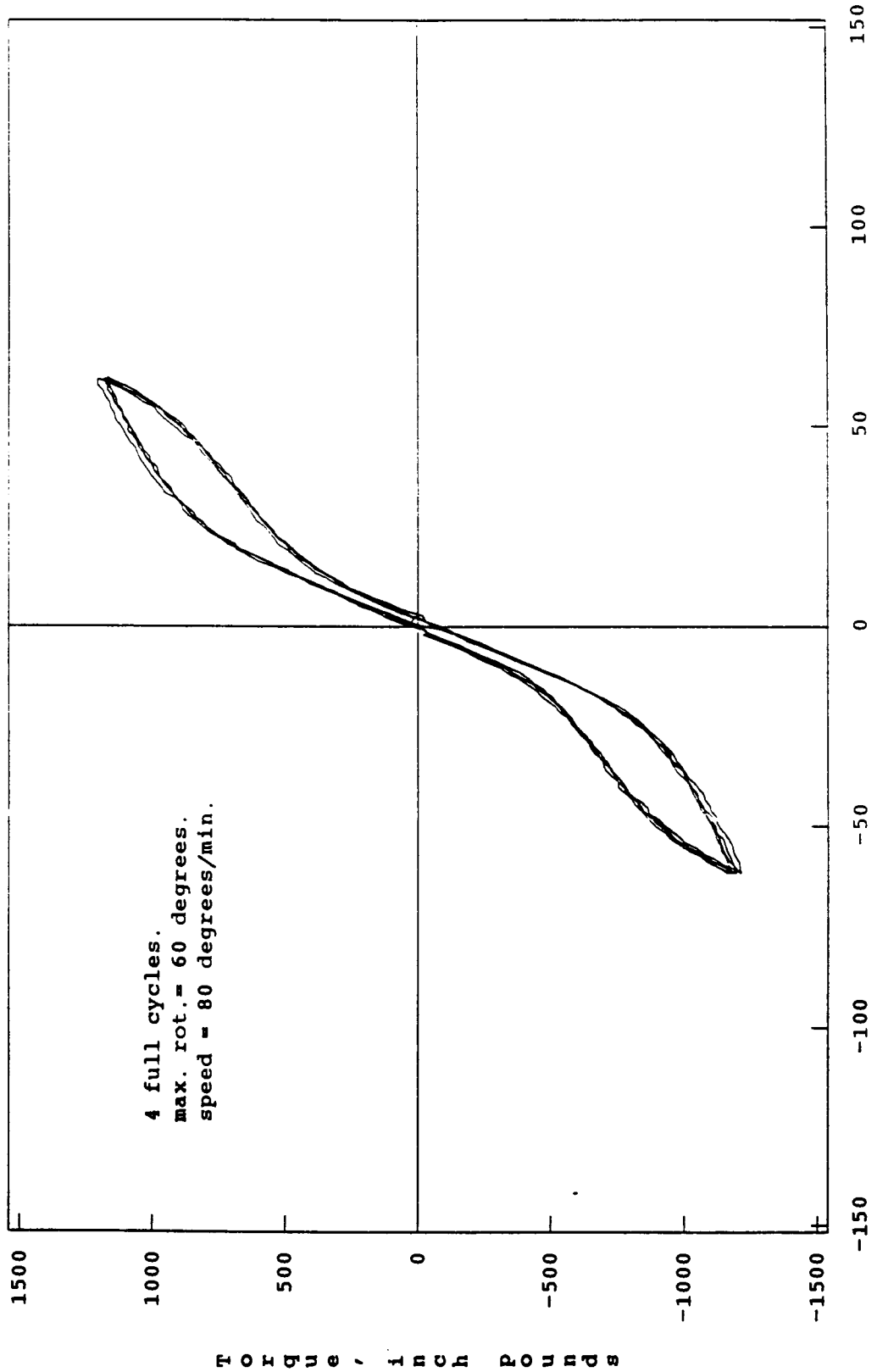

Figure 4.1 Torque-Rotation Hysteresis Loops for TTEST2

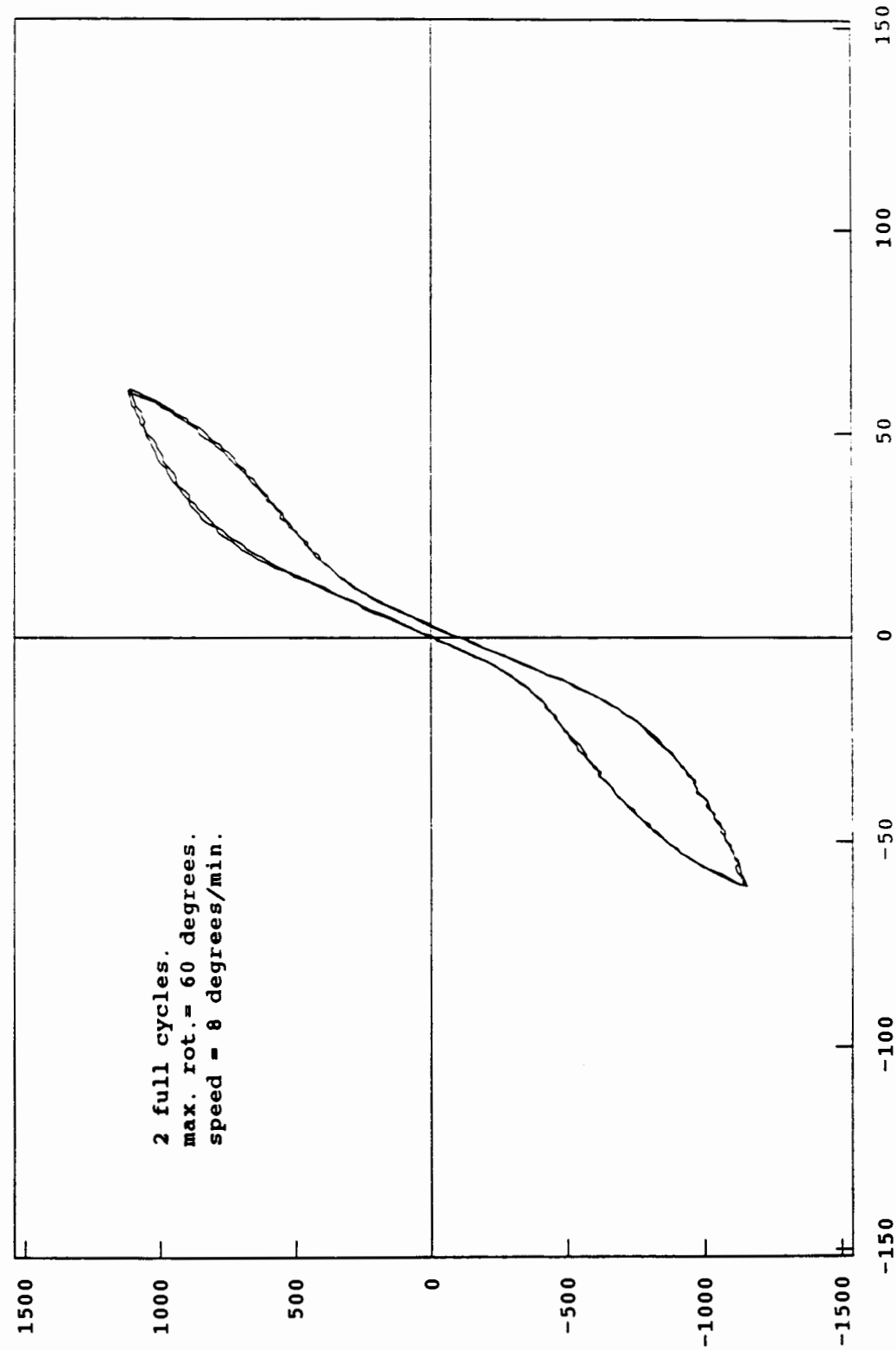

Figure 4.2 Torque-Rotation Hysteresis Loops for TEST3

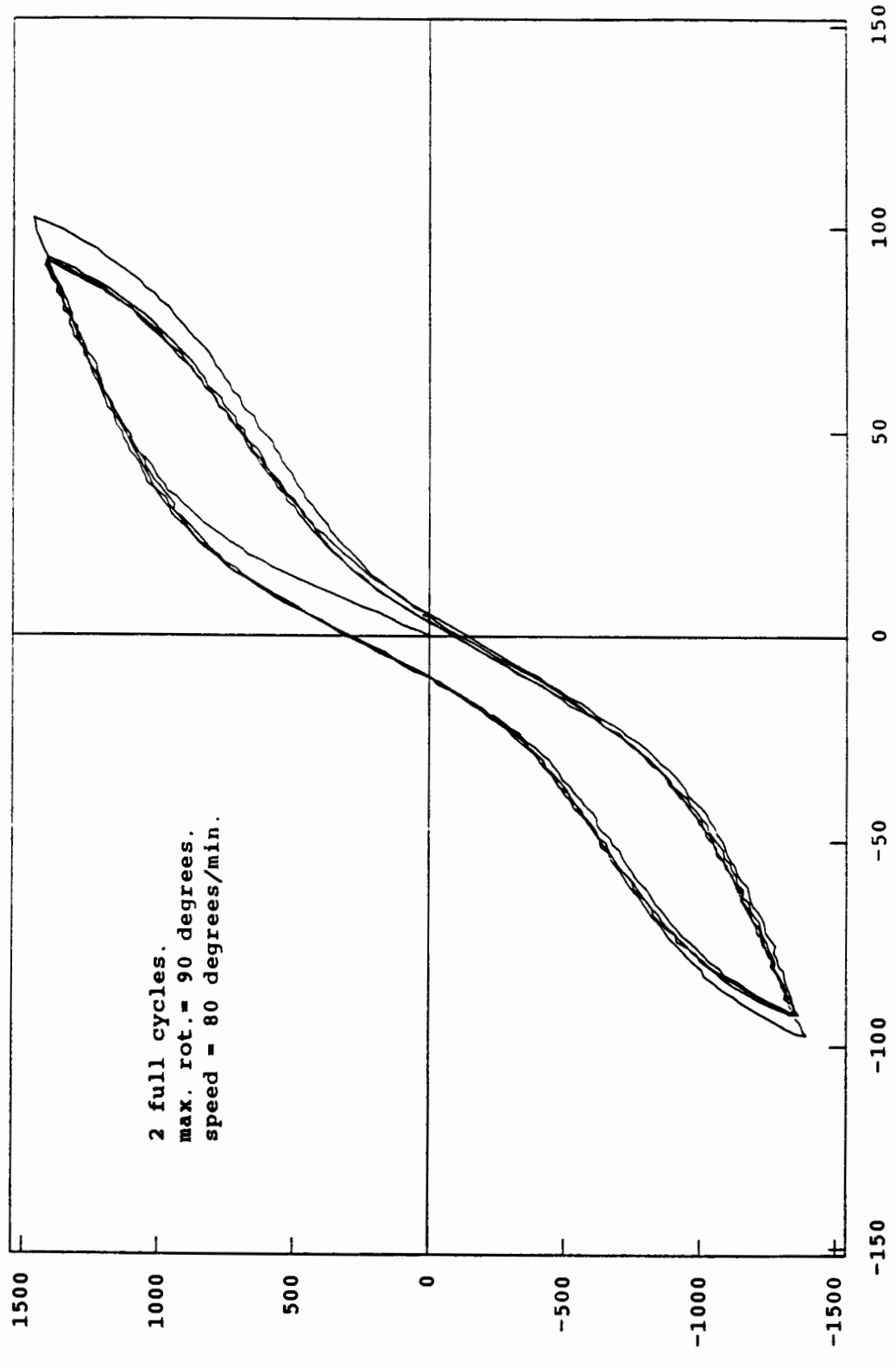

Figure 4.3 Torque-Rotation Hysteresis Loops for TTEST4

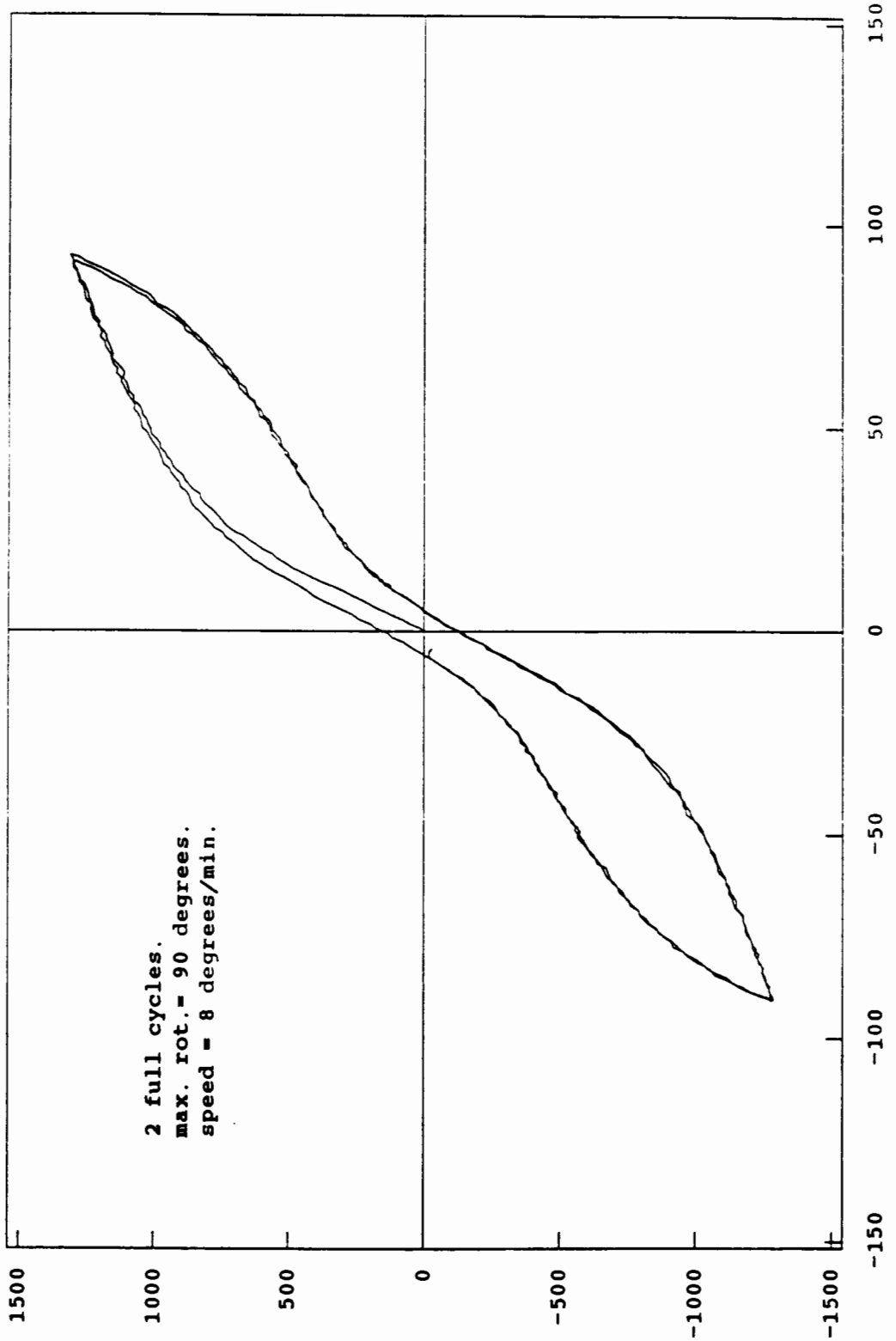

Figure 4.4 Torque-Rotation Hysteresis Loops for TEST5

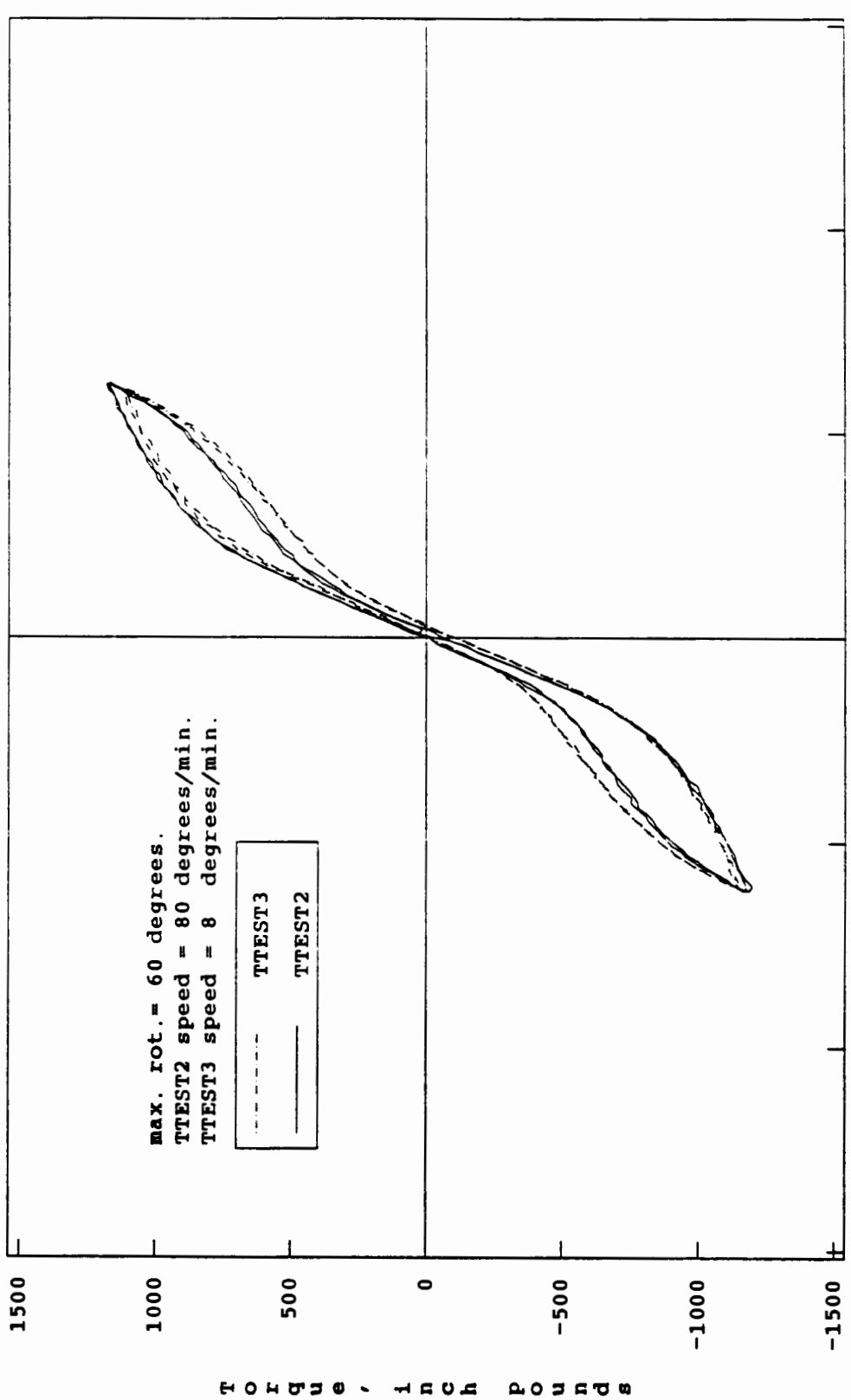

Figure 4.5 Torque-Rotation Hysteresis Loops

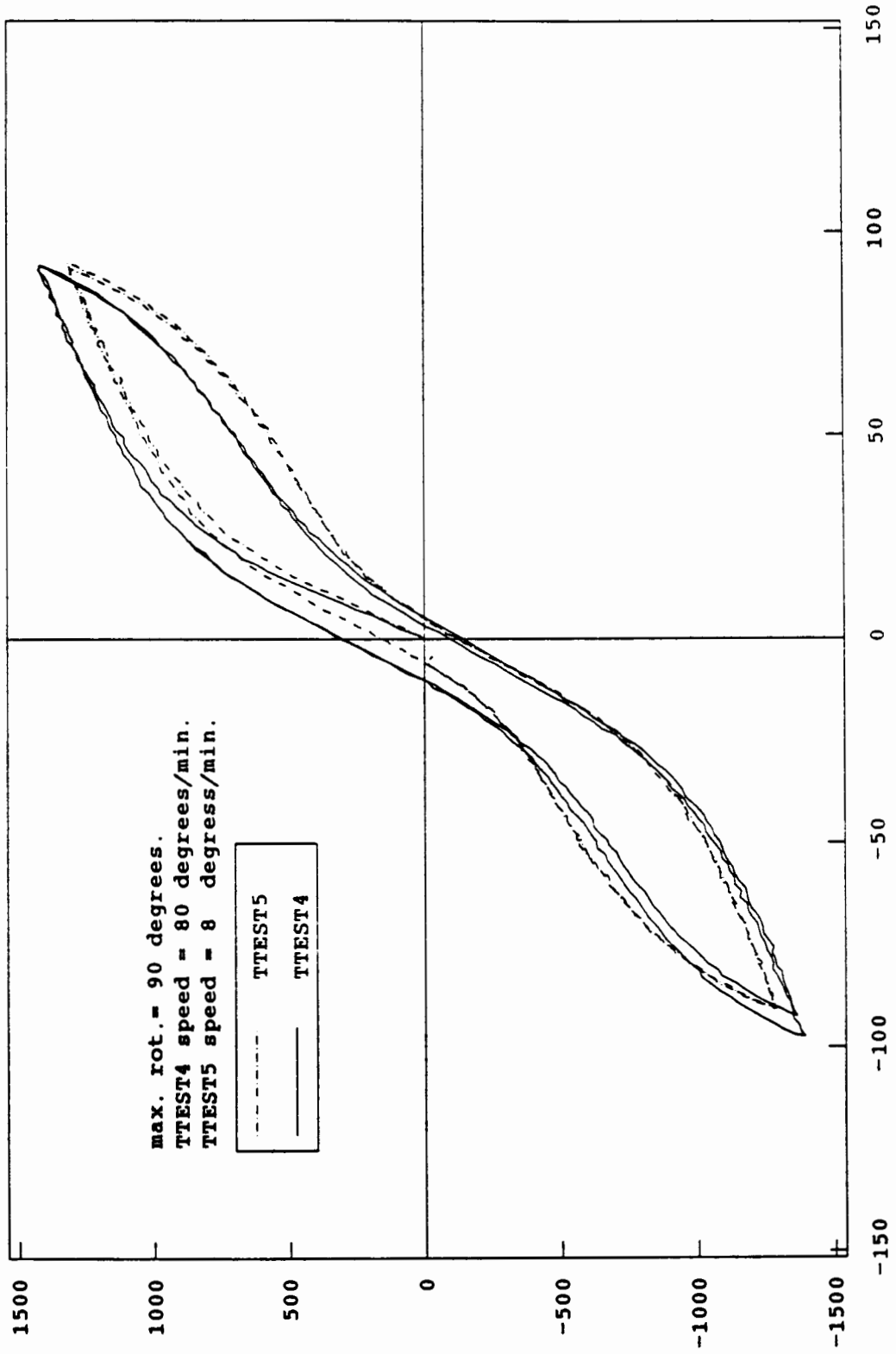

Figure 4.6 Torque-Rotation Hysteresis Loops

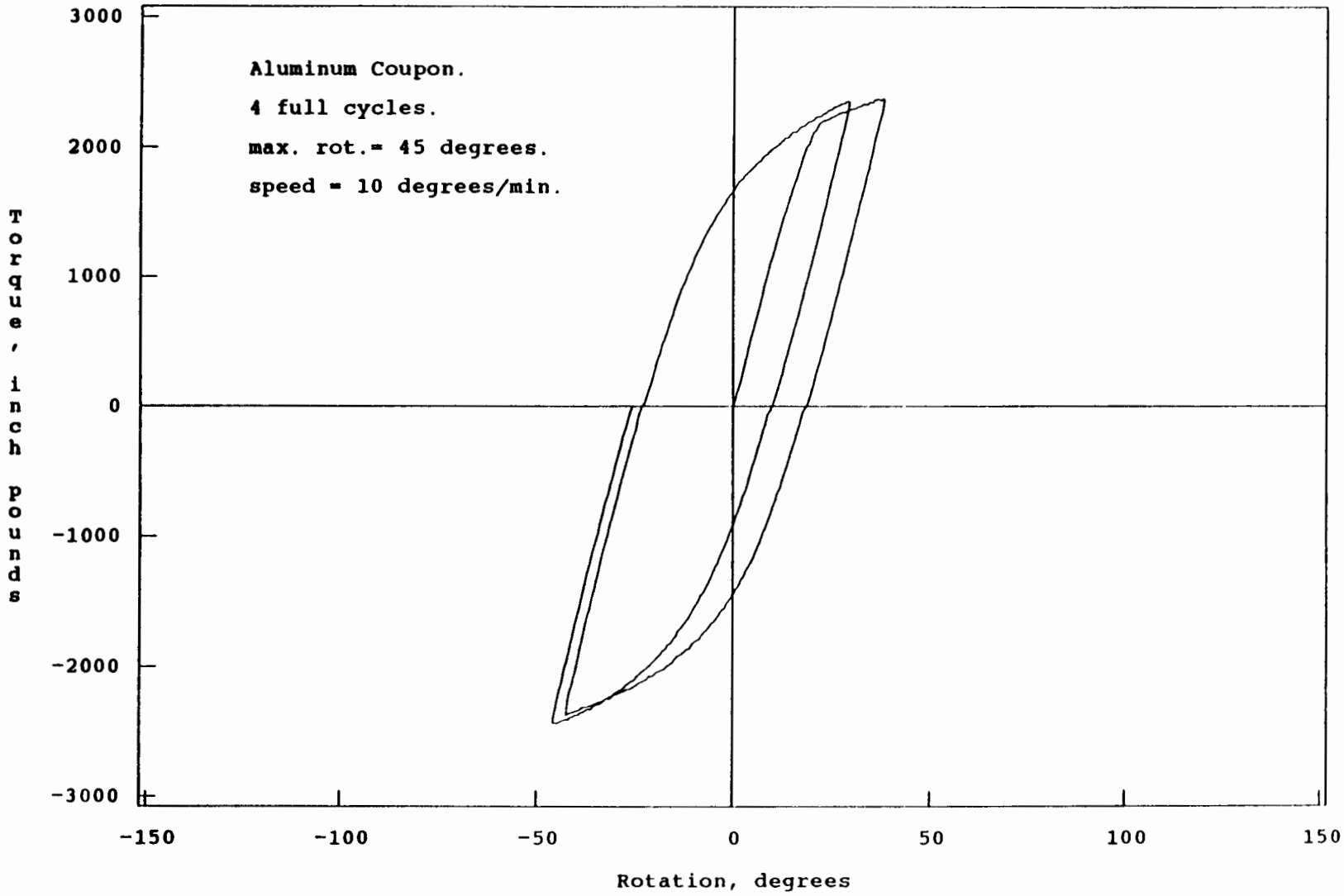

Figure 4.7 Torque-Rotation Hysteresis Loops for TTESTAL

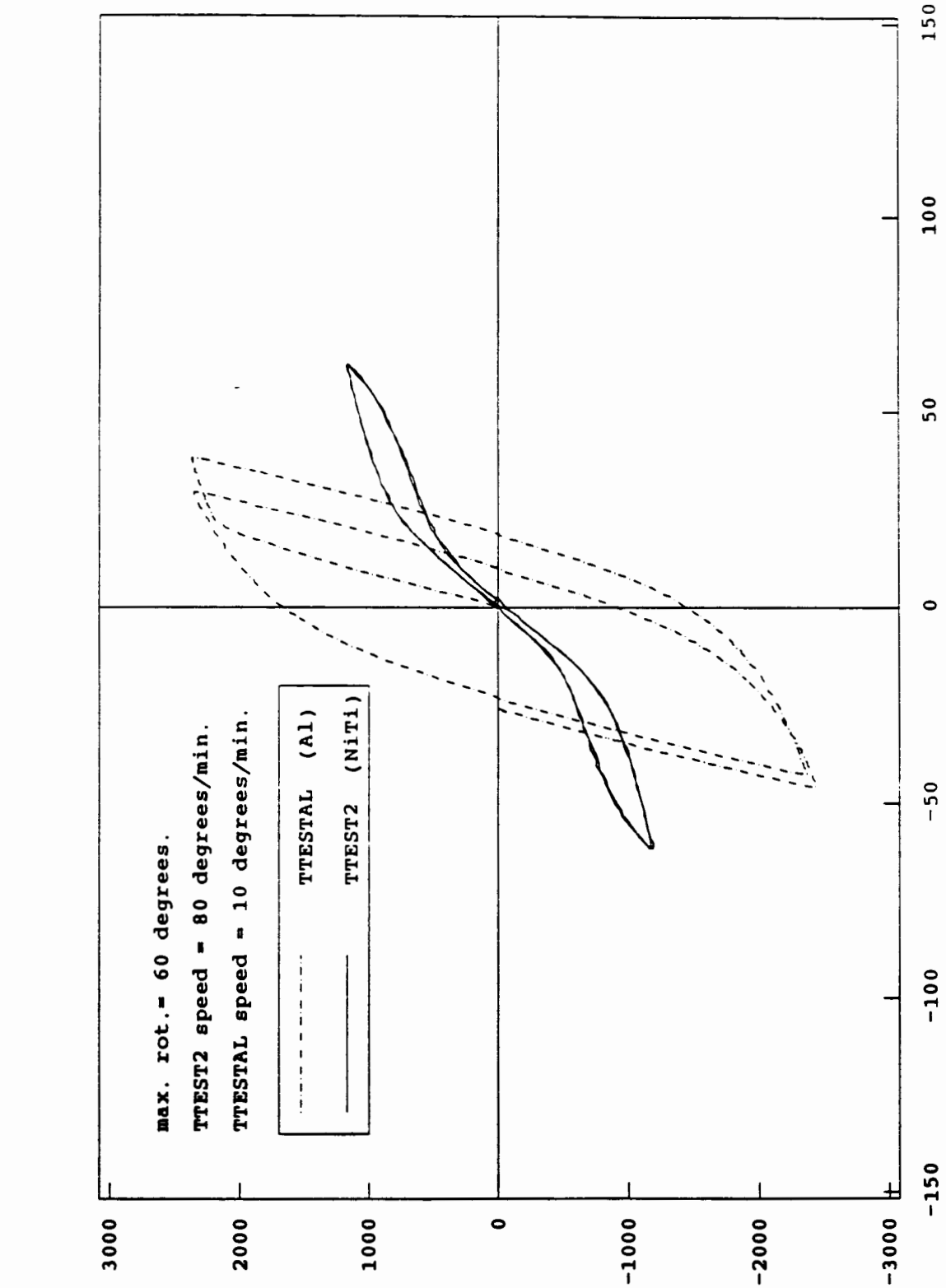

Figure 4.8 Torque-Rotation Hysteresis Loops

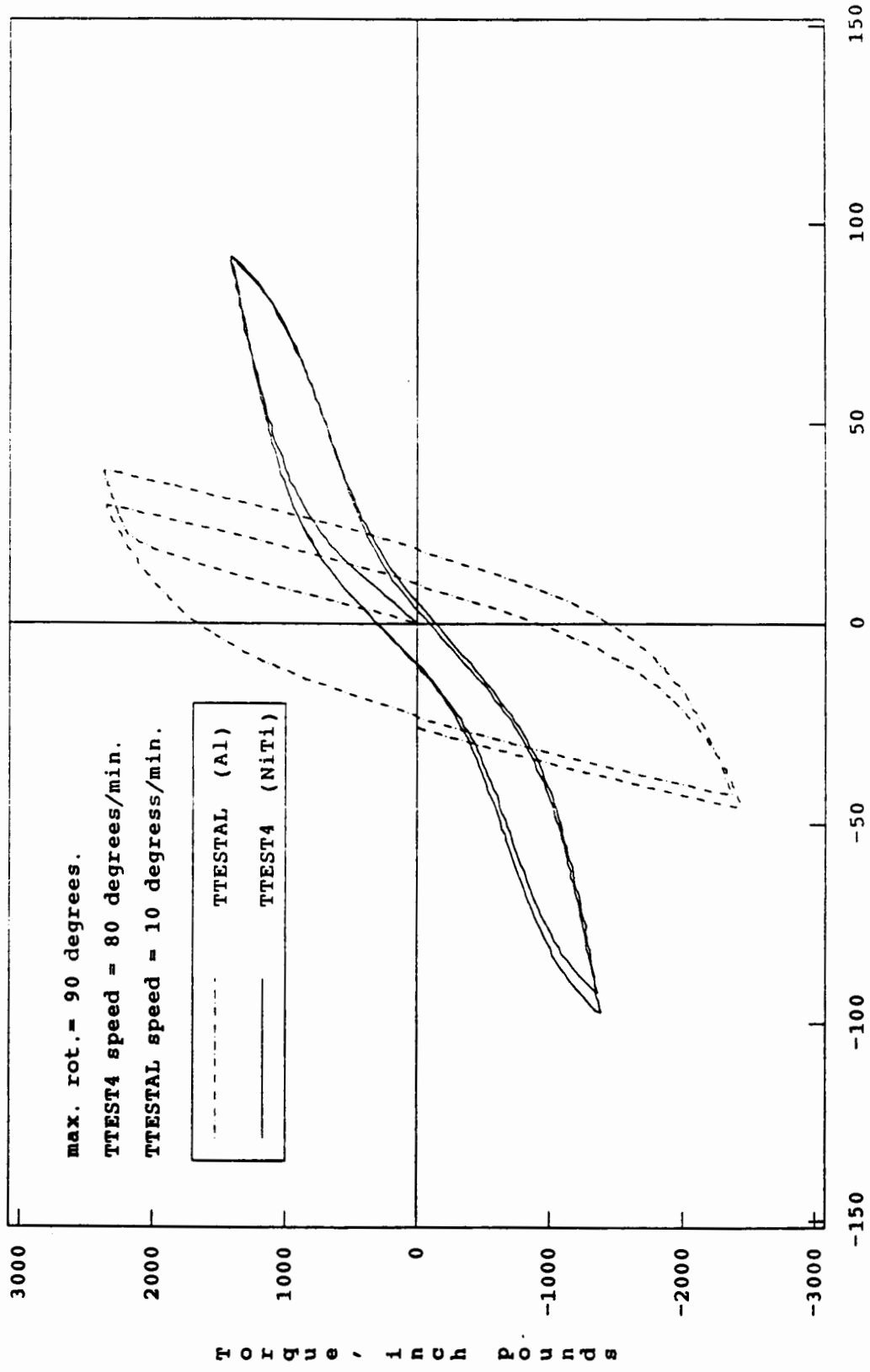

Figure 4.9 Torque-Rotation Hysteresis Loops

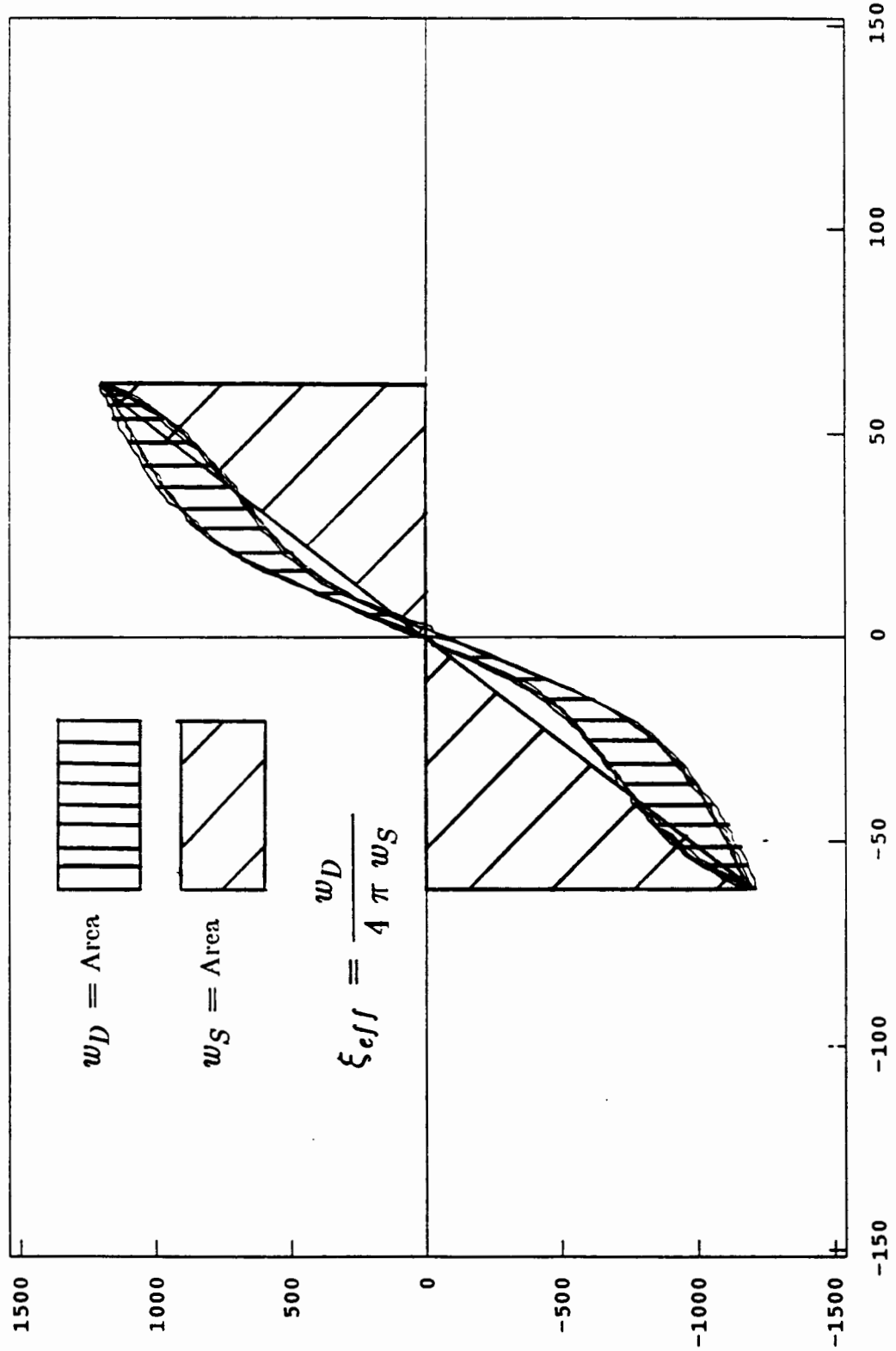

FIGURE 4.10 CALCULATION OF THE EFFECTIVE DAMPING RATIO, ξ_{eff}

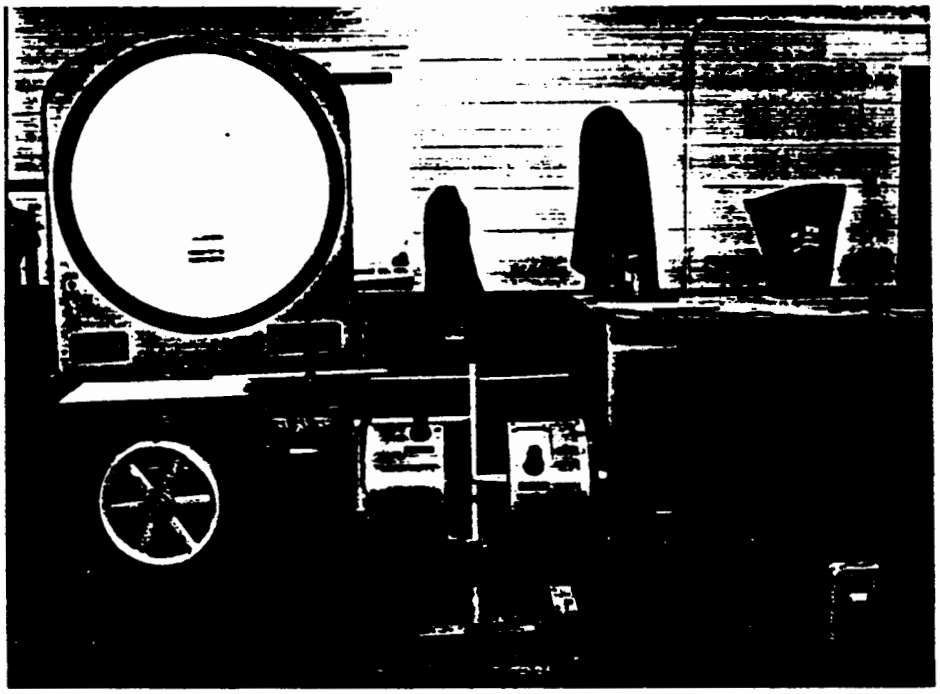

FIGURE 4.11 TORSION TEST SETUP

FIGURE 4.12 TORSION TEST SPECIMEN

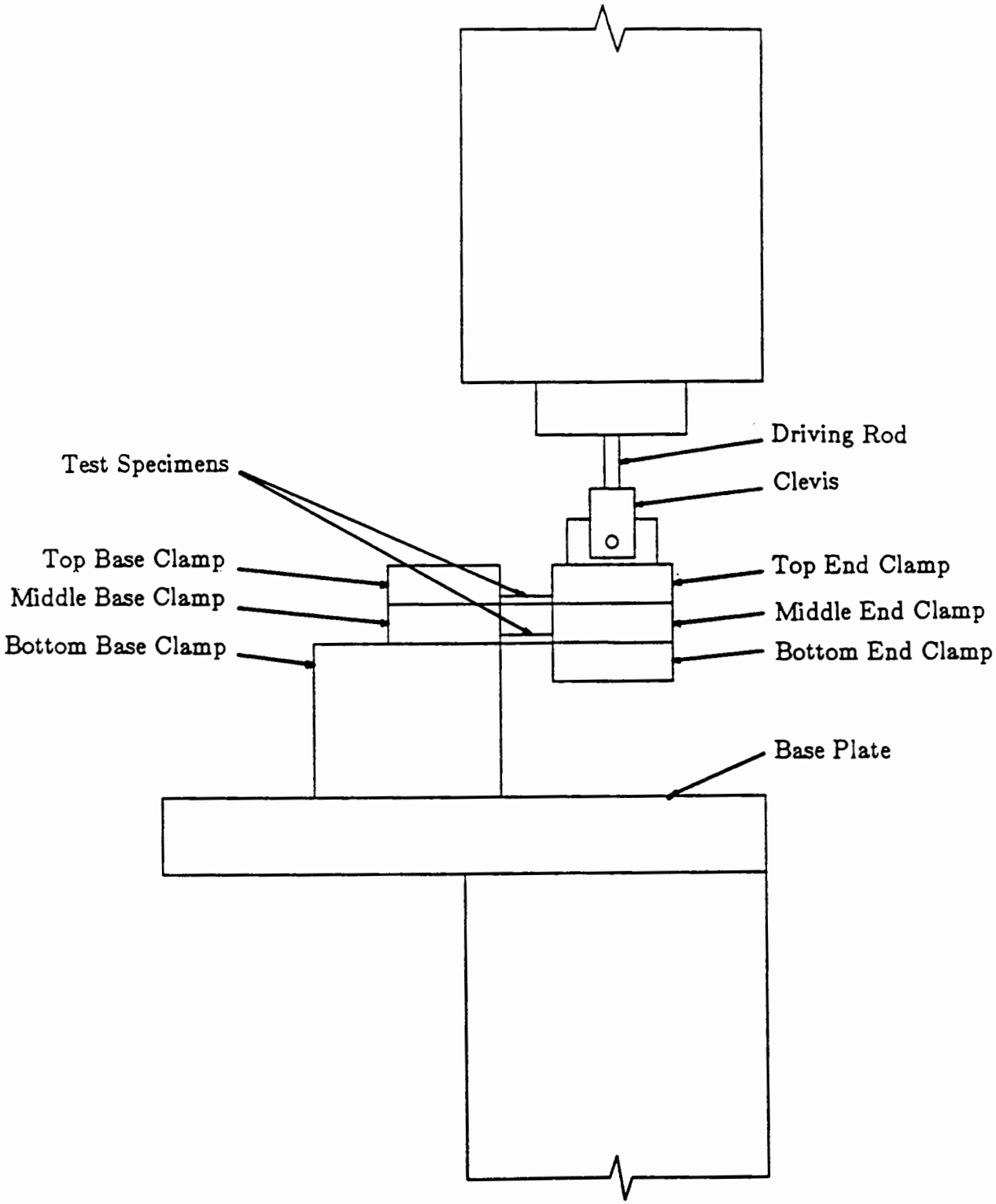

FIGURE 5.1 BENDING TEST FIXTURE (SYS1)

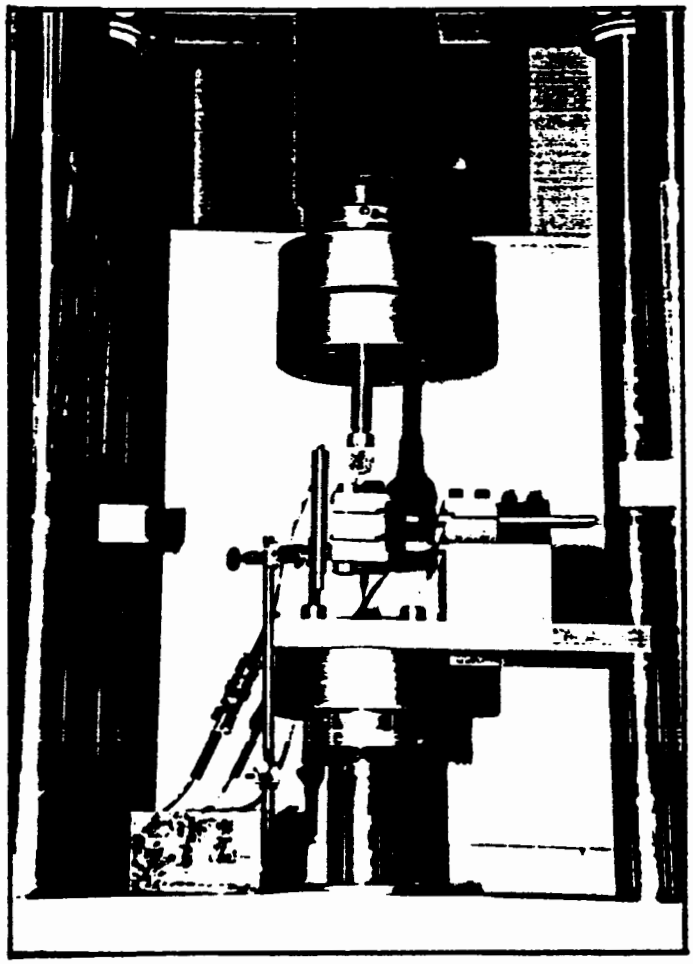

FIGURE 5.2 BENDING TEST FIXTURE (SYS4)

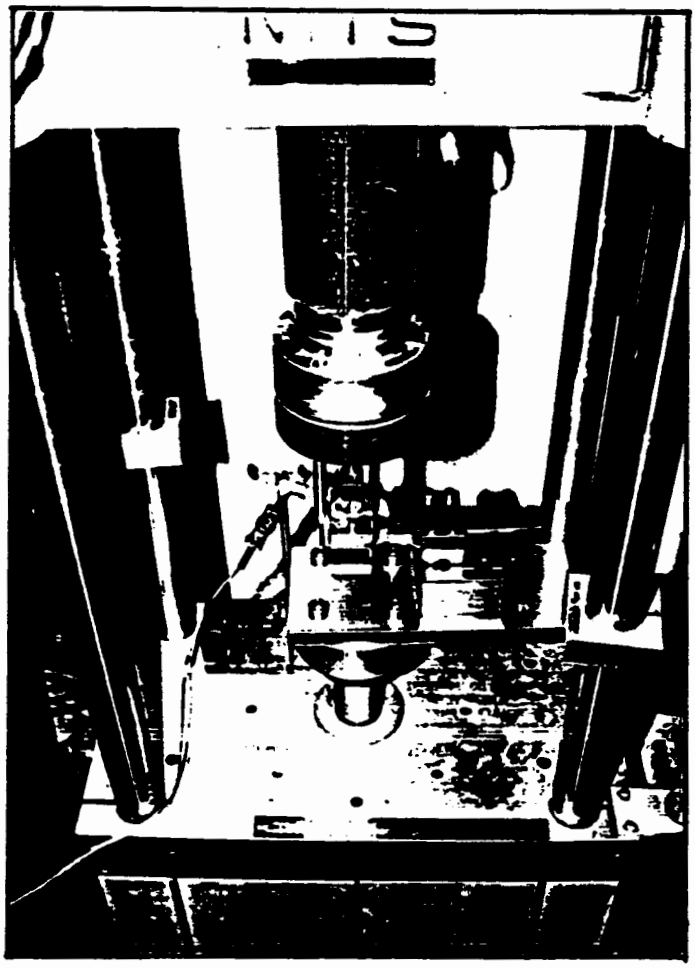

FIGURE 5.3 BENDING TEST FIXTURE (SYS4)

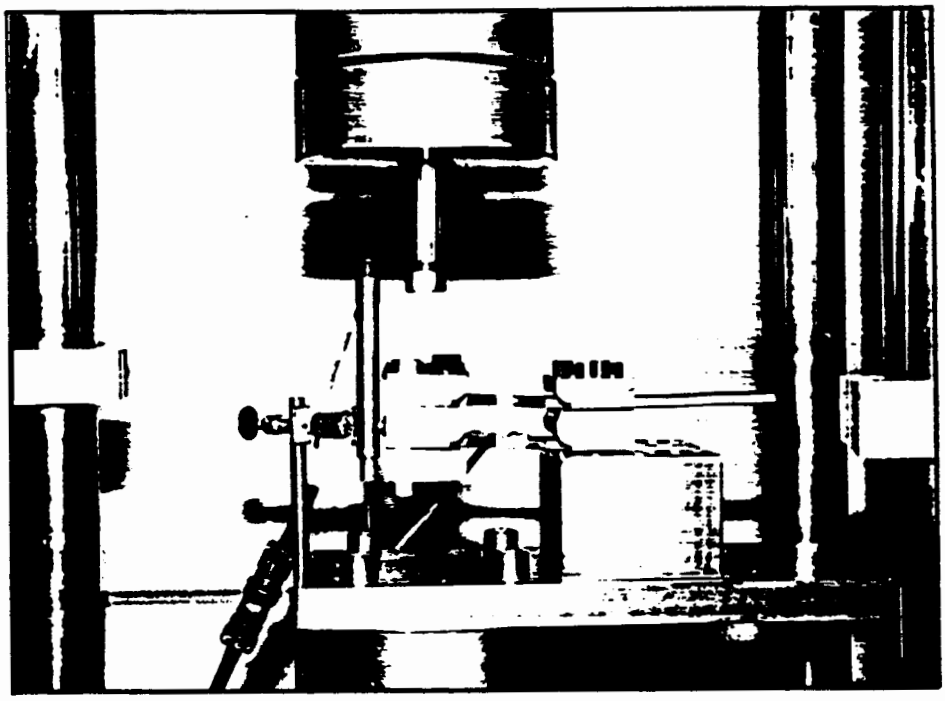

FIGURE 5.4 BENDING TEST FIXTURE (SYS4)

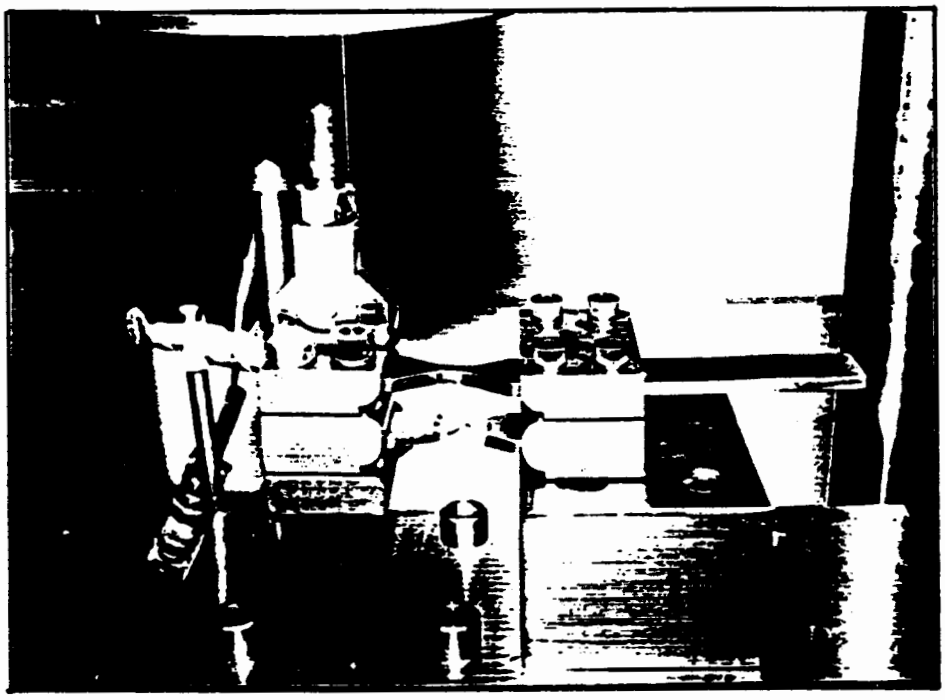

FIGURE 5.5 BENDING TEST FIXTURE (SYS4)

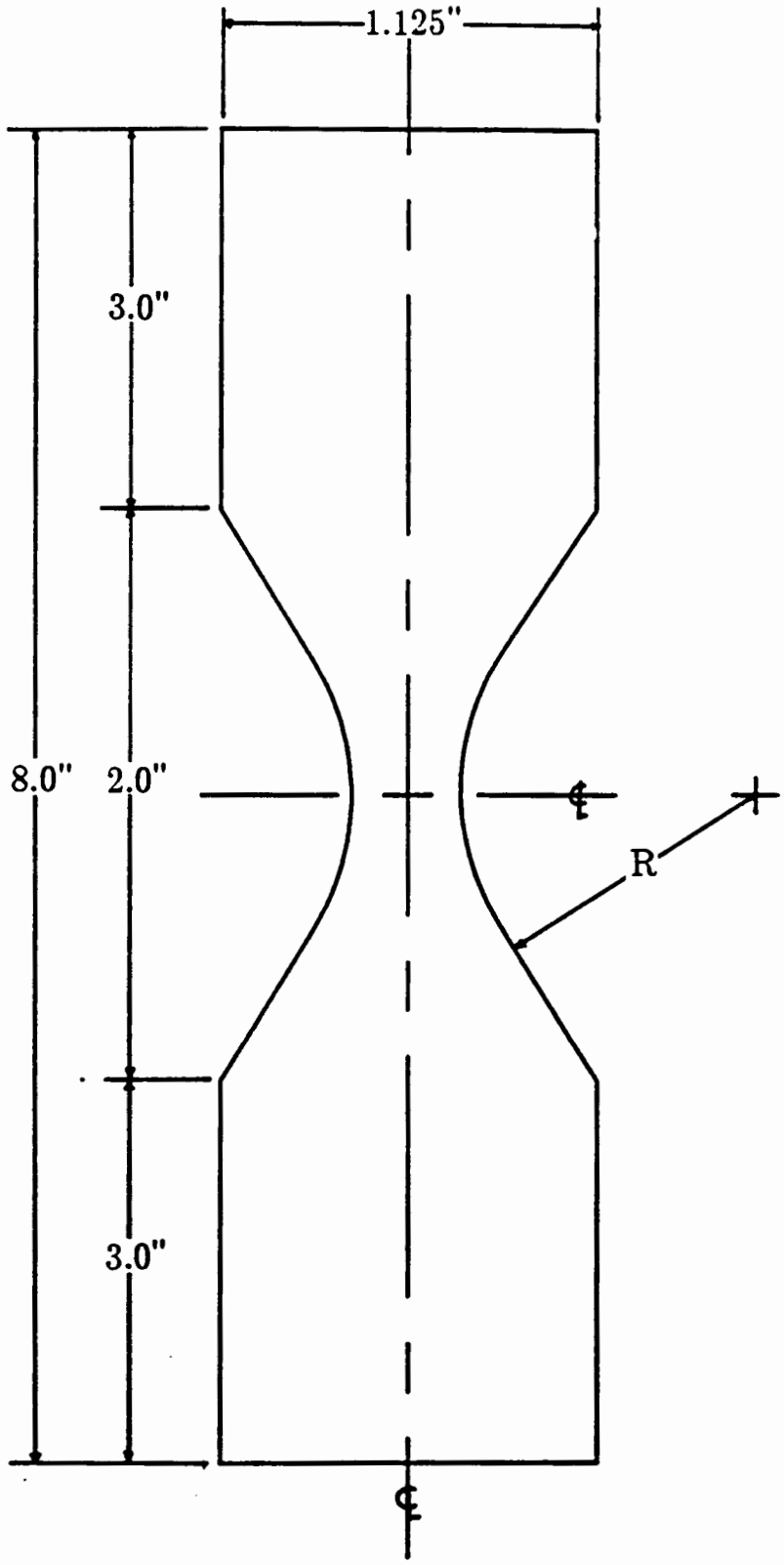

FIGURE 5.6 X - SHAPED TEST SPECIMEN

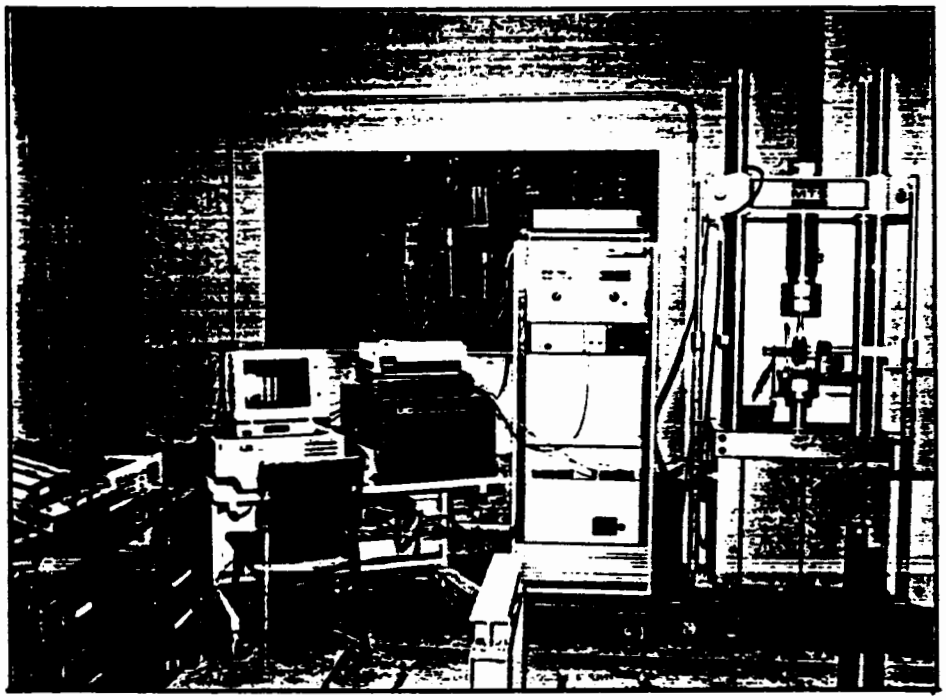

FIGURE 5.7 BENDING TEST SETUP

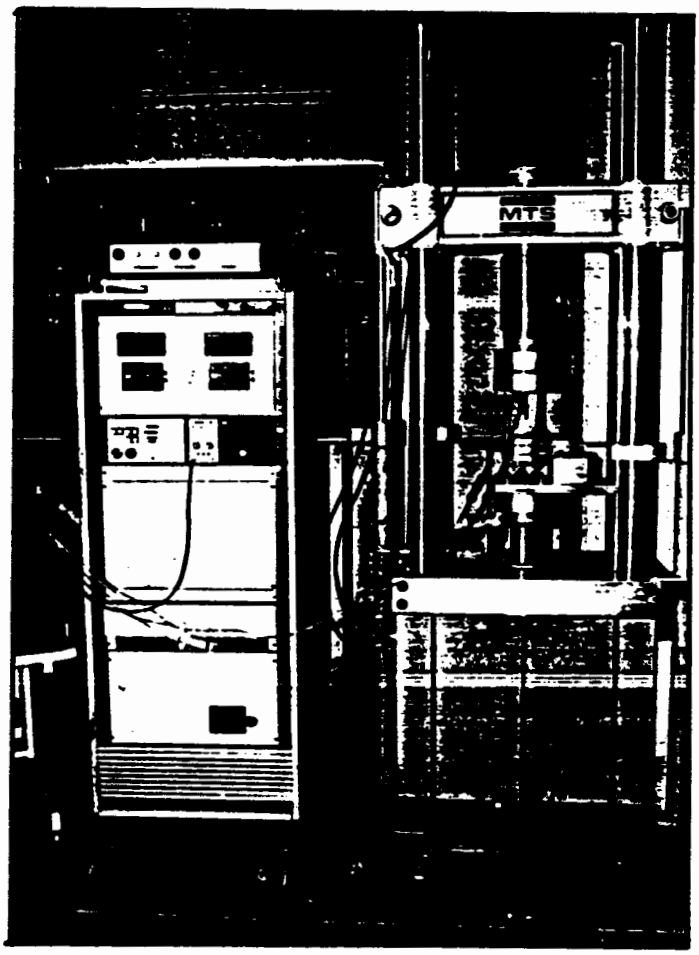

FIGURE 5.8 BENDING TEST SETUP

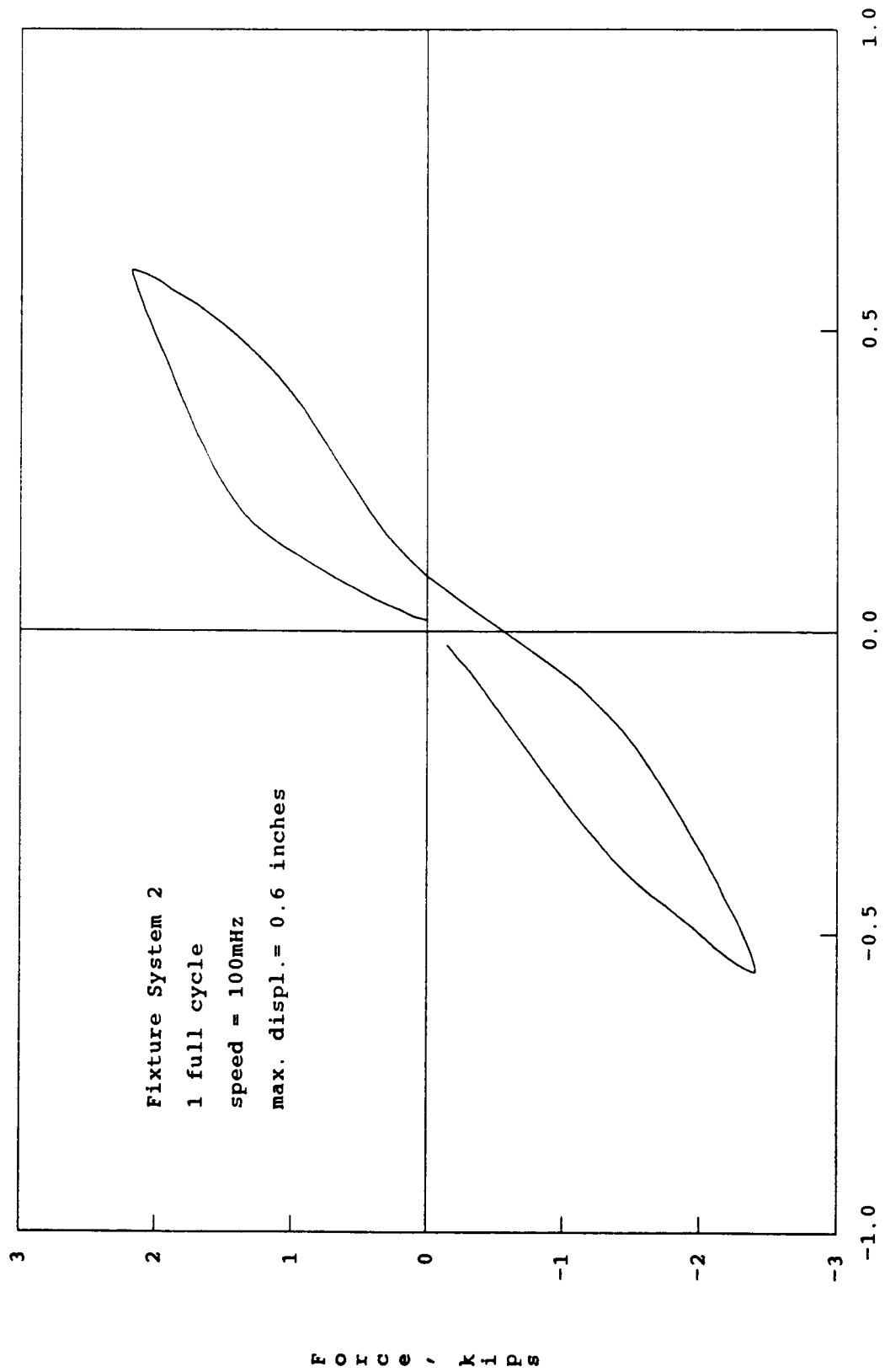

FIGURE 5.9 Force-Displacement Hysteresis Loops for BEND4

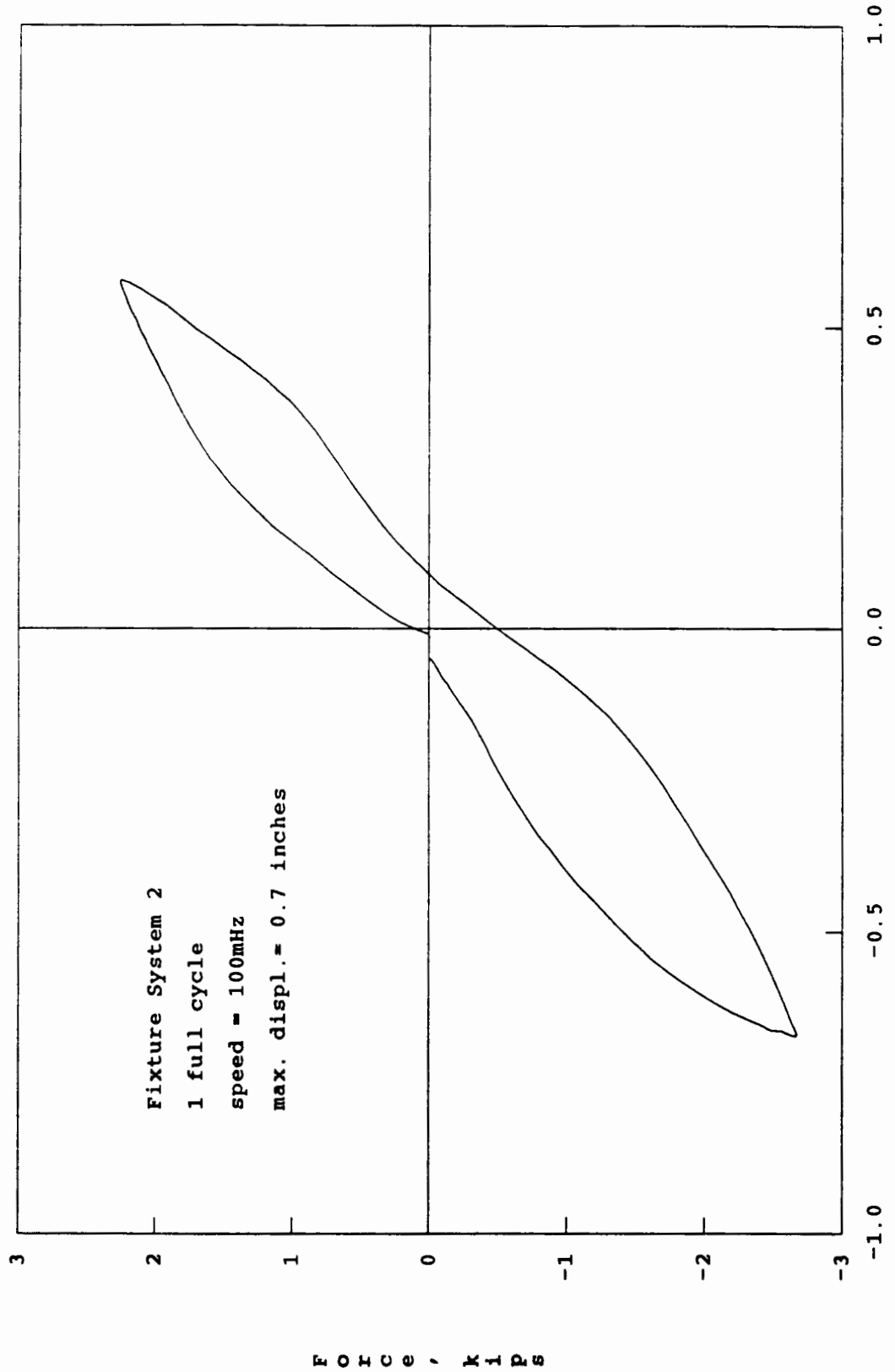

FIGURE 5.10 Force-Displacement Hysteresis Loops for BEND5

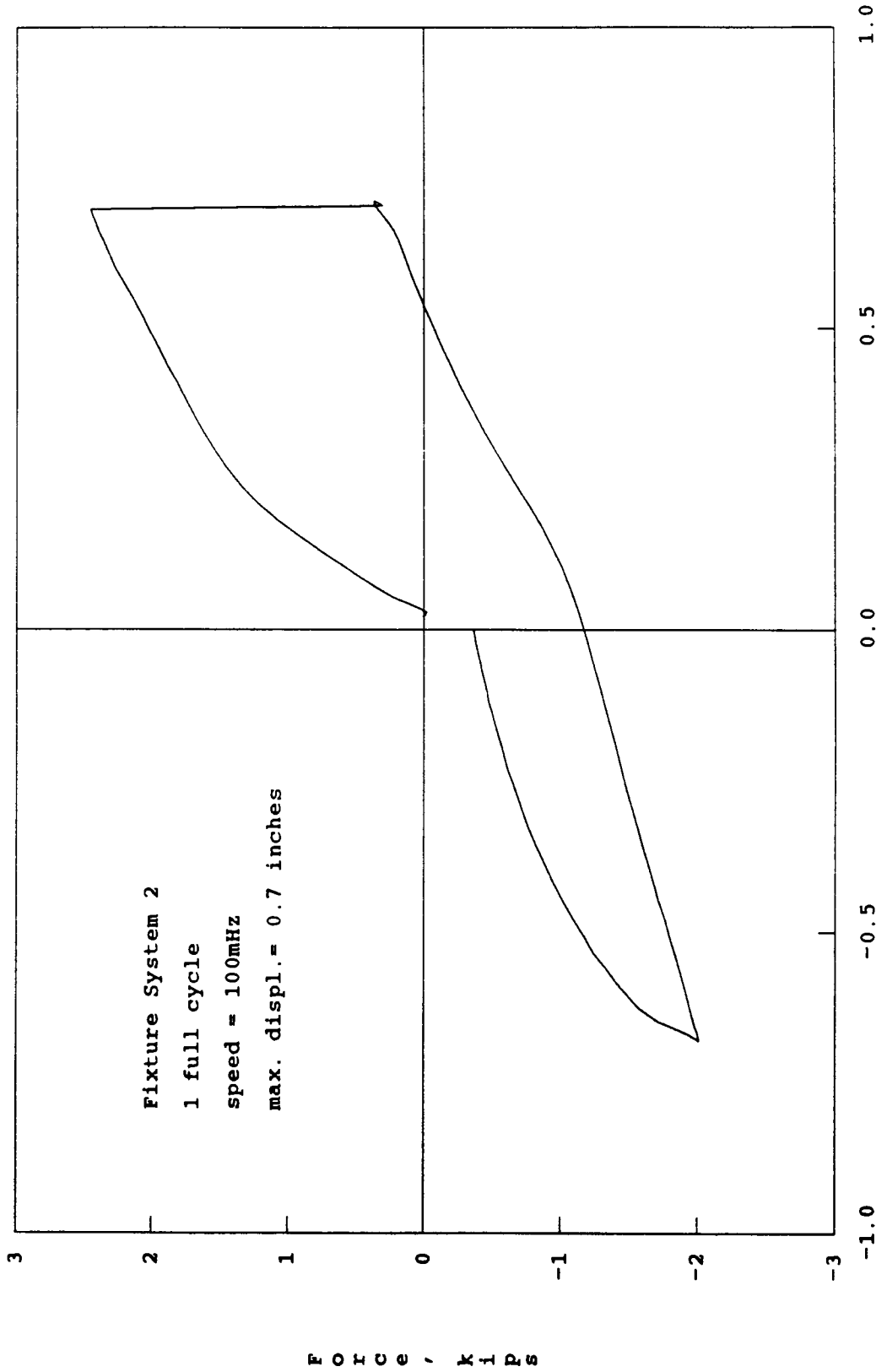

FIGURE 5.11 Force-Displacement Hysteresis Loops for BEND6

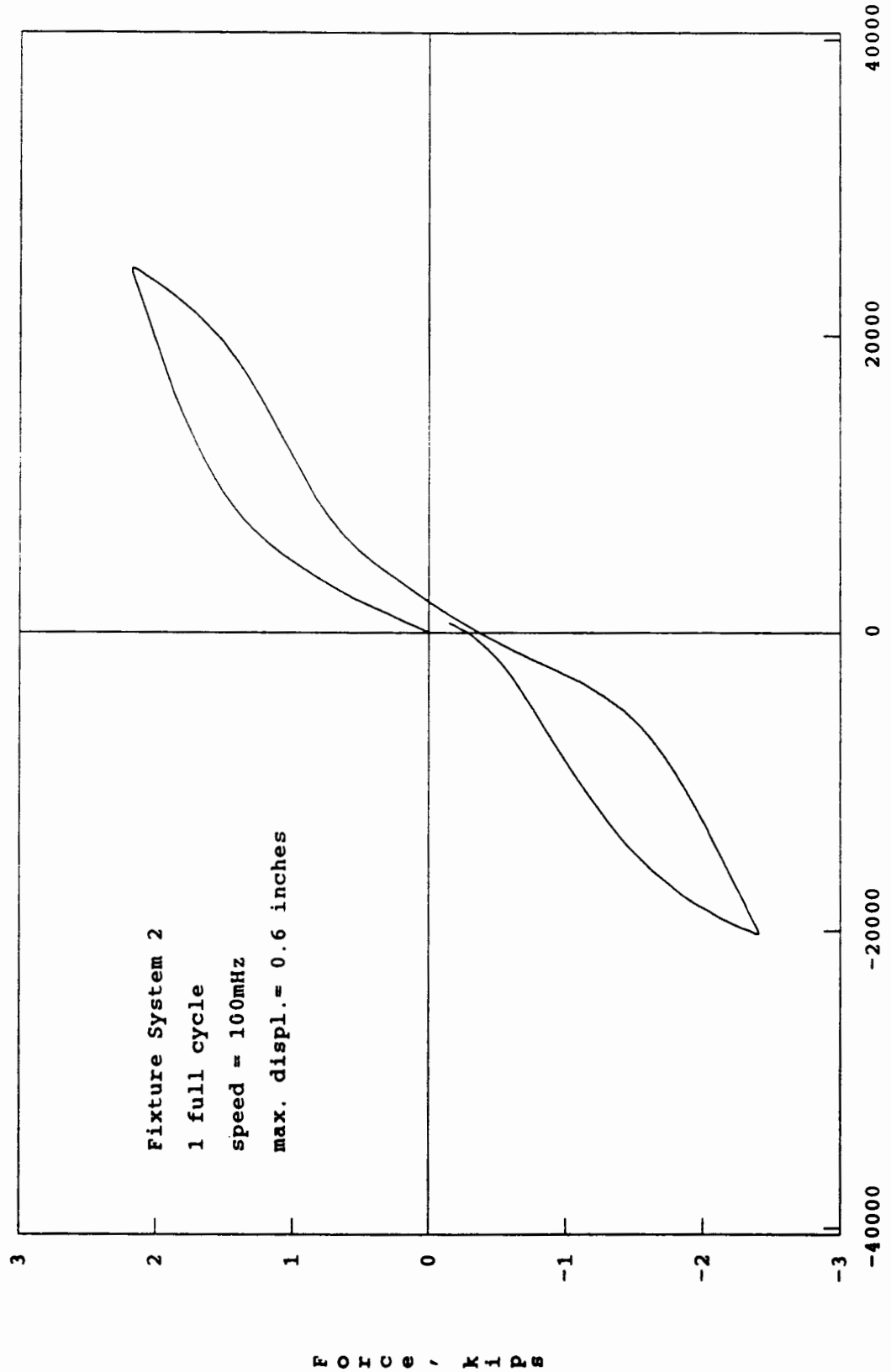

FIGURE 5.12 Force-Strain Hysteresis Loops for BEND4

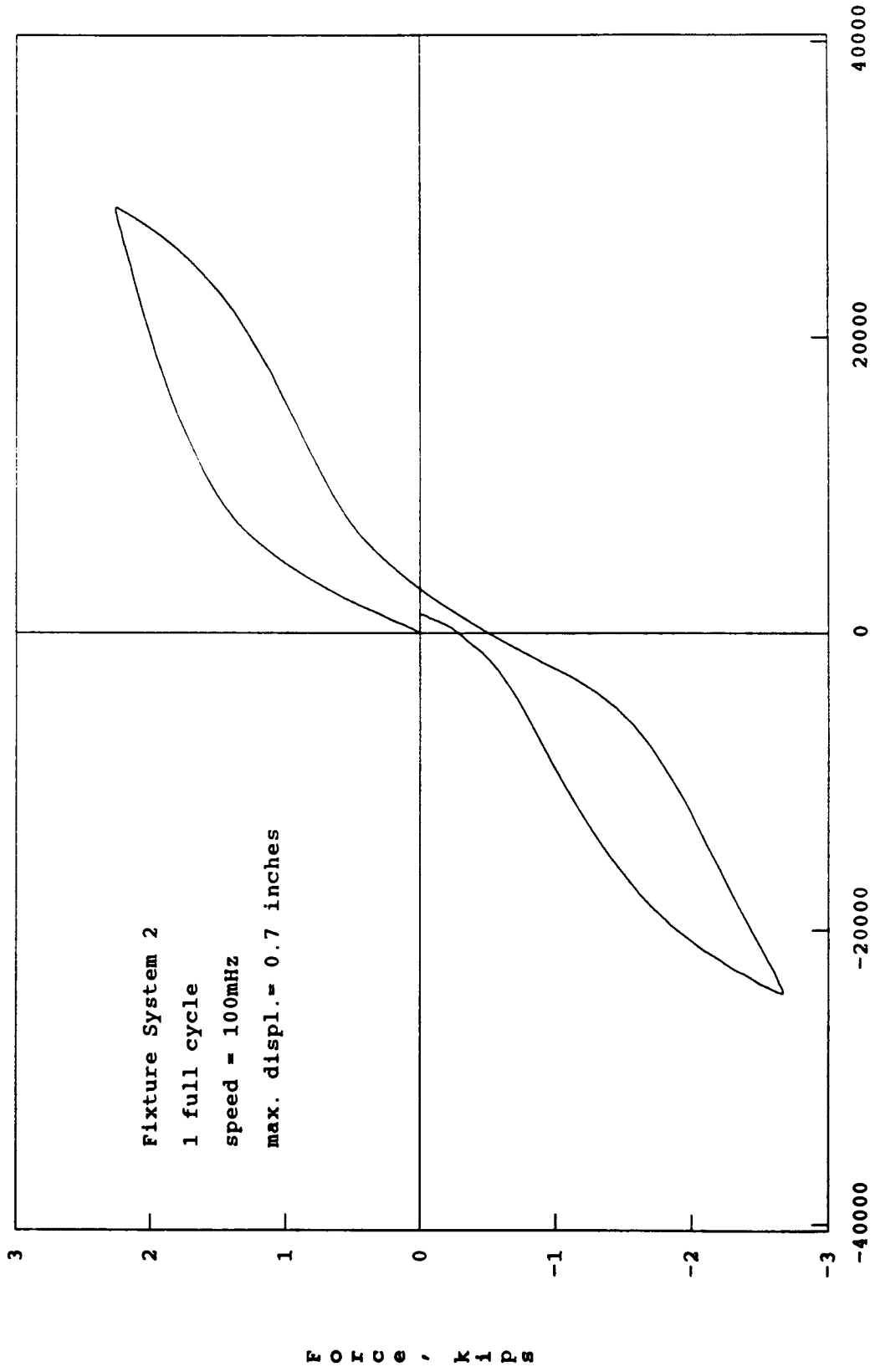

FIGURE 5.13 Force-Strain Hysteresis Loops for BEND5

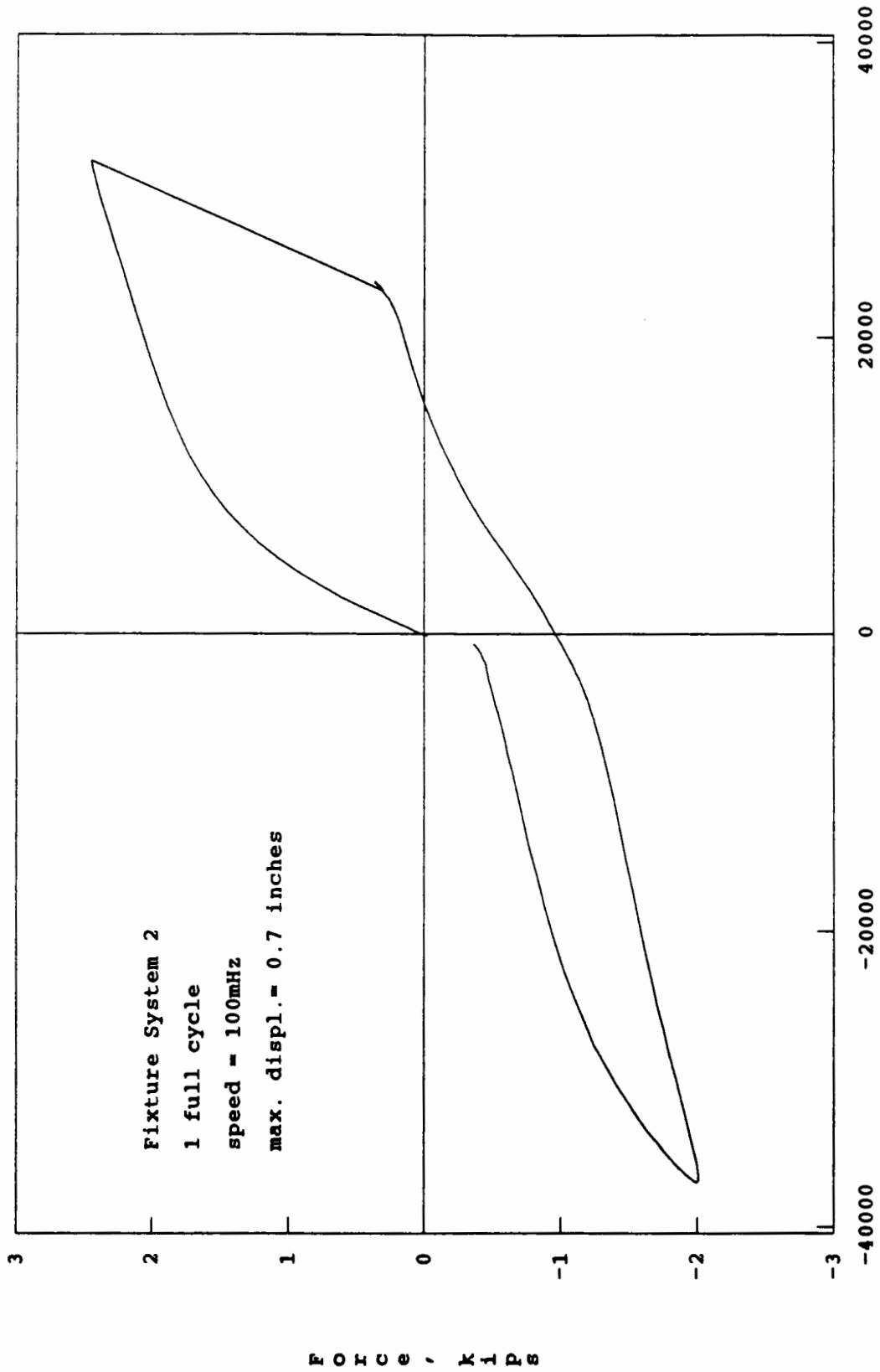

FIGURE 5.14 Force-Strain Hysteresis Loops for BEND6

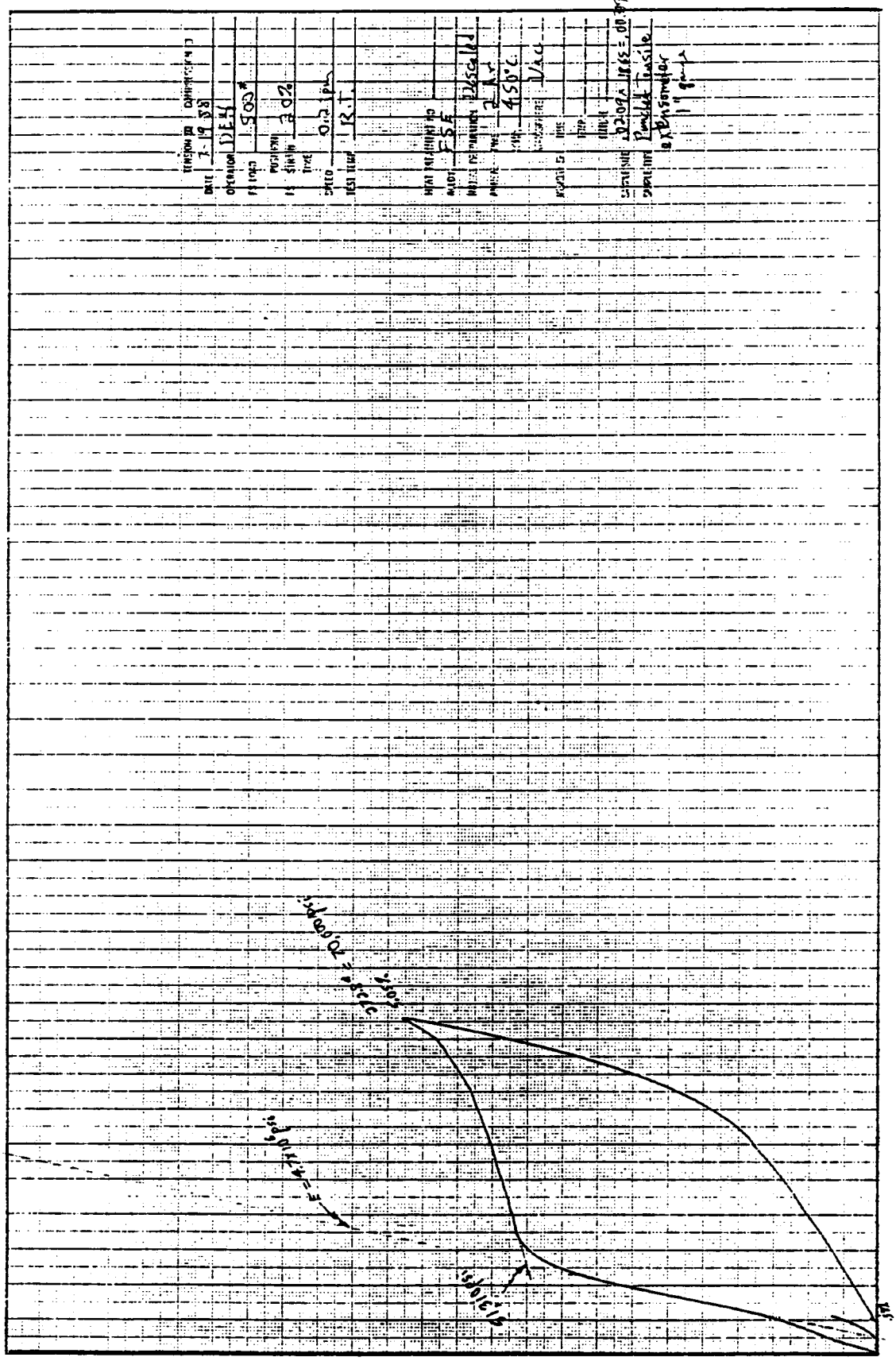

FIGURE 5.15 Stress-Strain Curve - Heat Treated Material, Fixture Sys 3

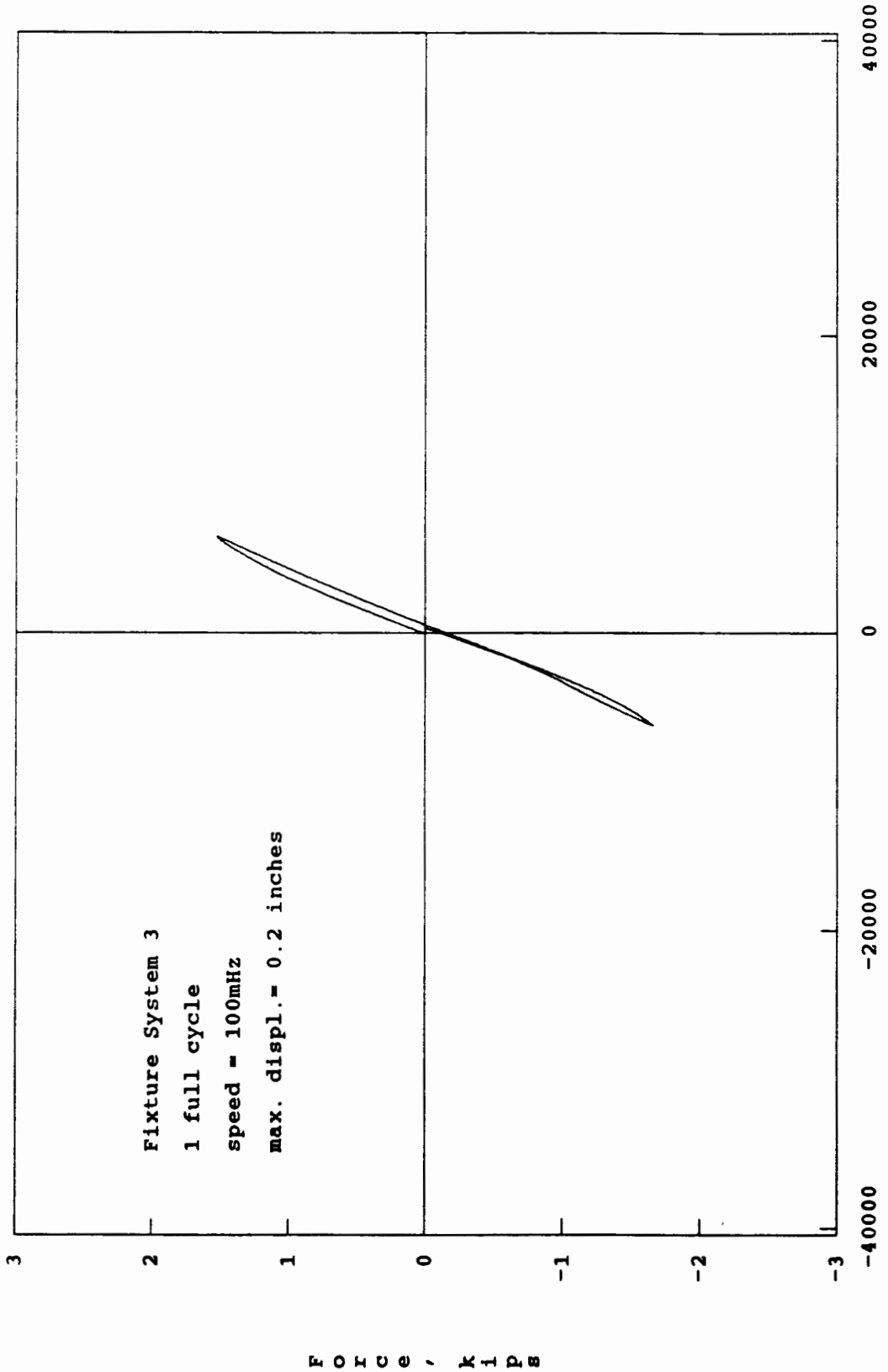

FIGURE 5.16 Force-Strain Hysteresis Loops for BN2F

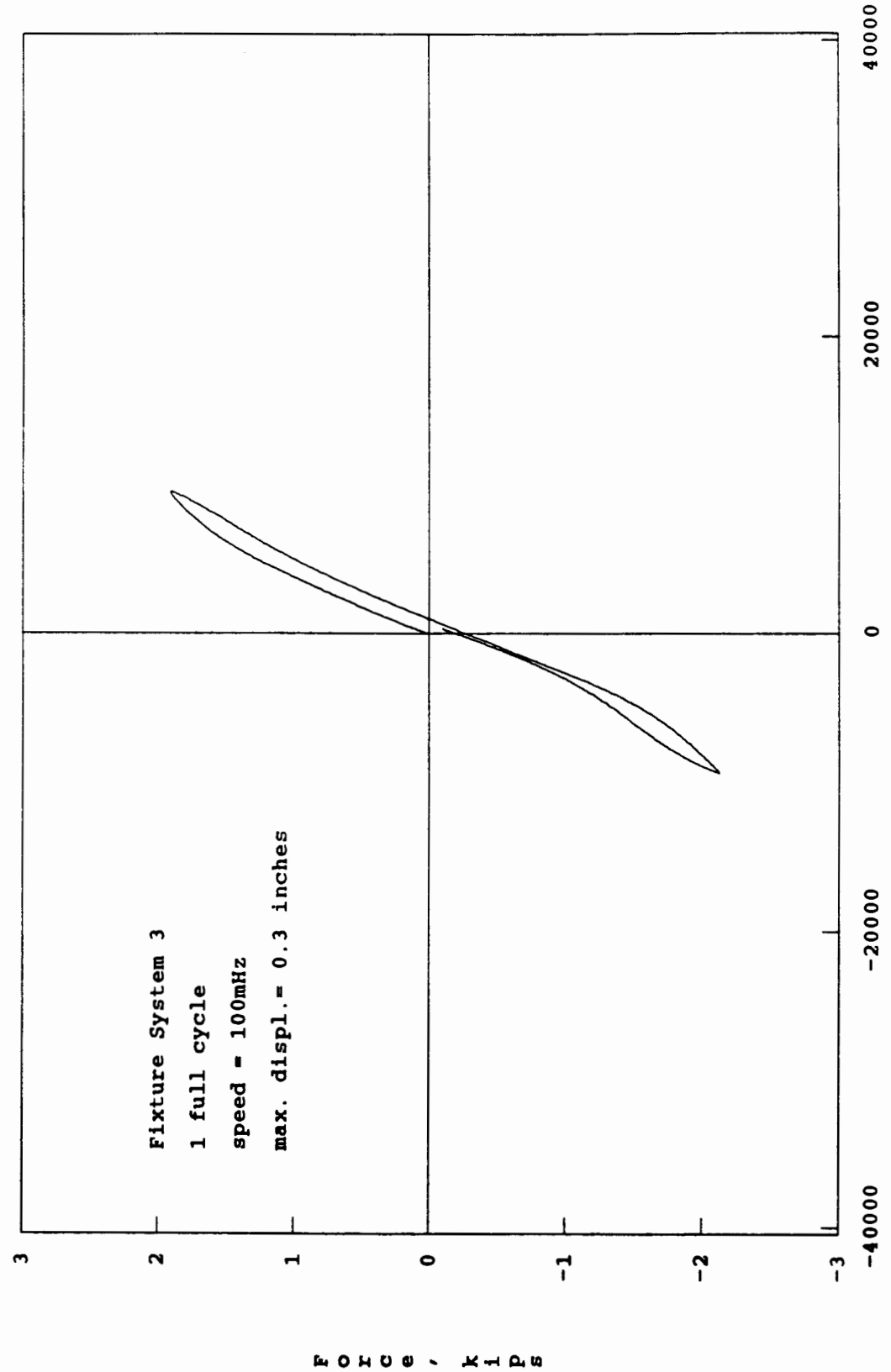

FIGURE 5.17 Force-Strain Hysteresis Loops for BN3F

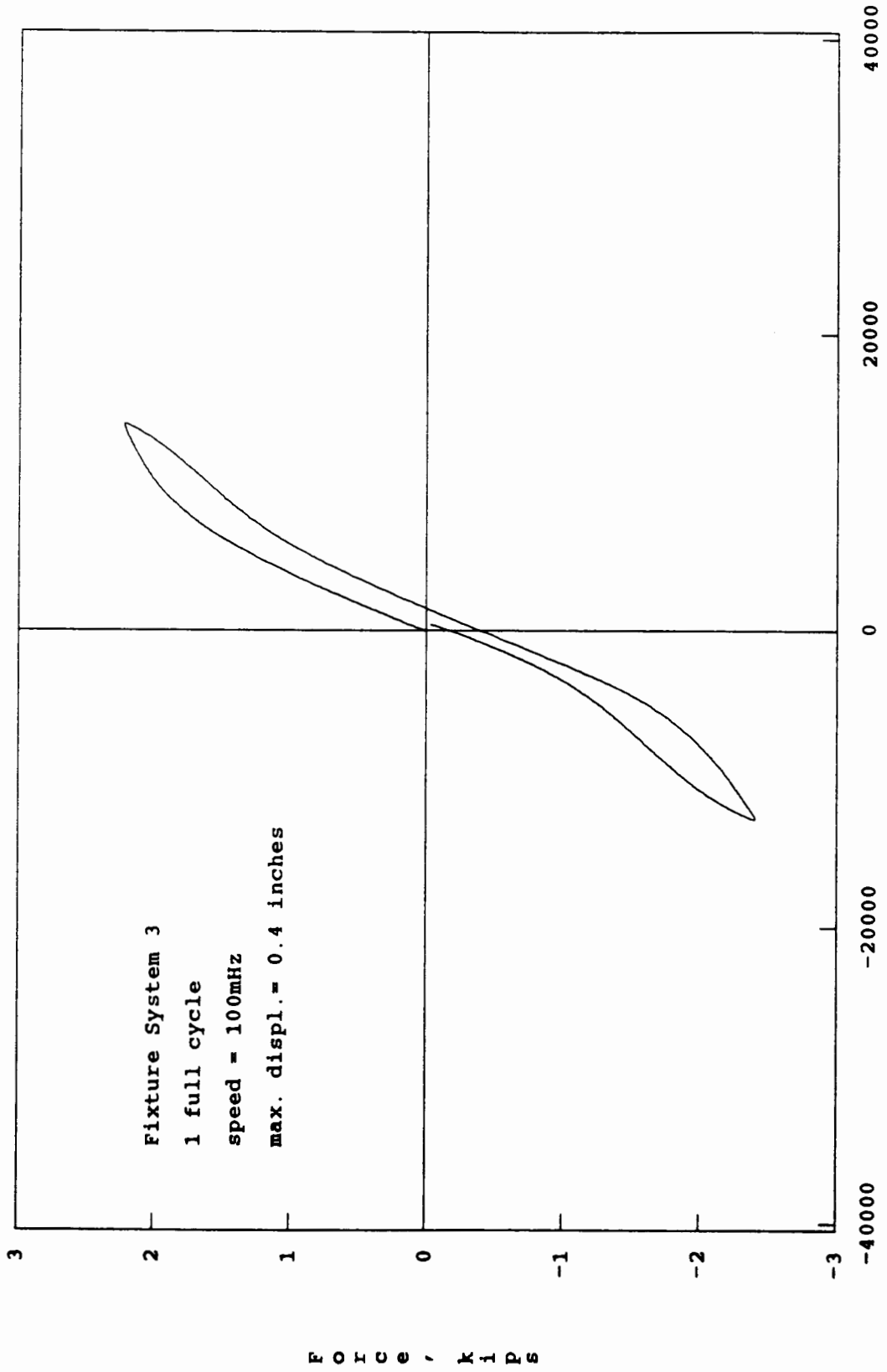

FIGURE 5.18 Force-Strain Hysteresis Loops for BN4F

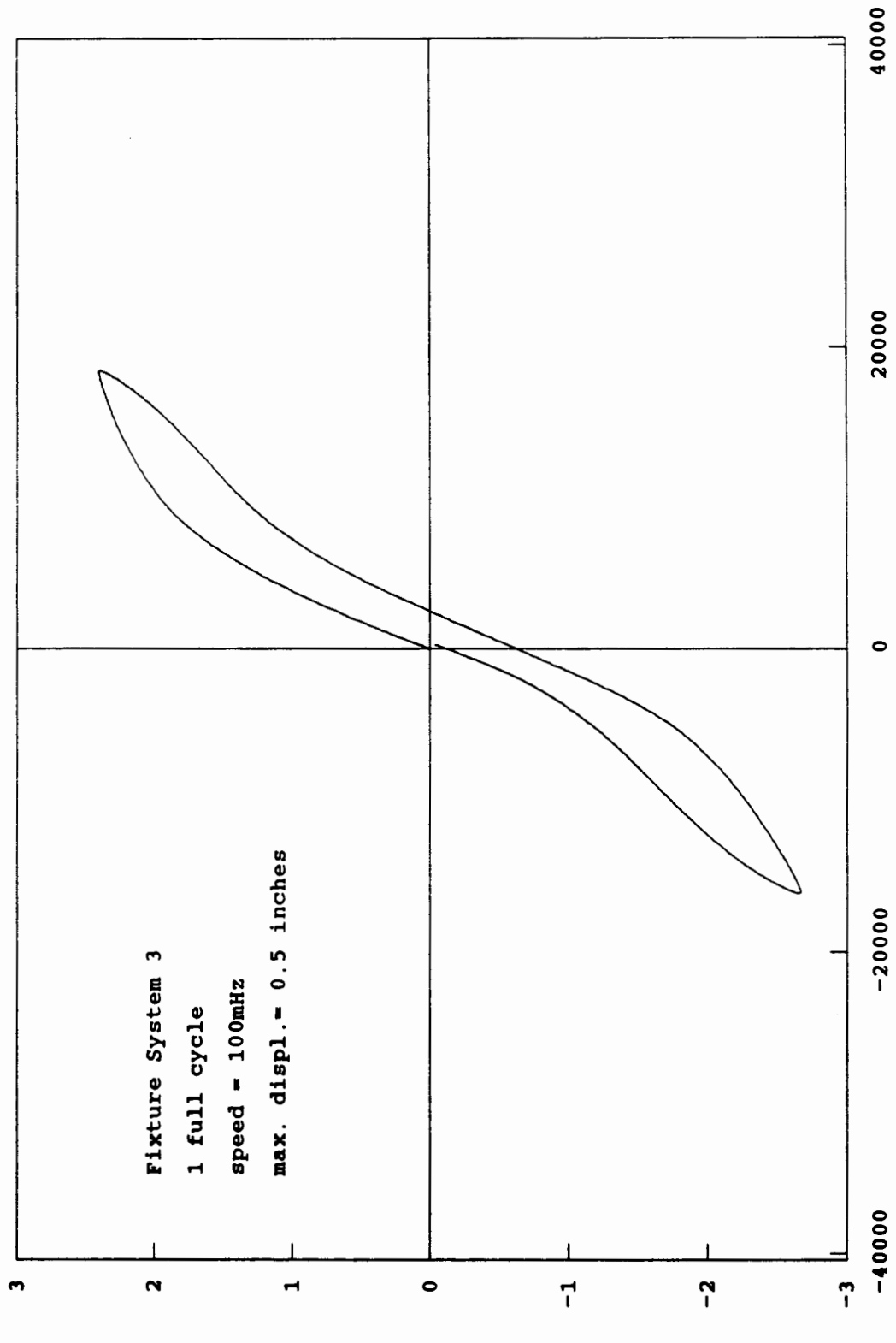

FIGURE 5.19 Force-Strain Hysteresis Loops for BN5F

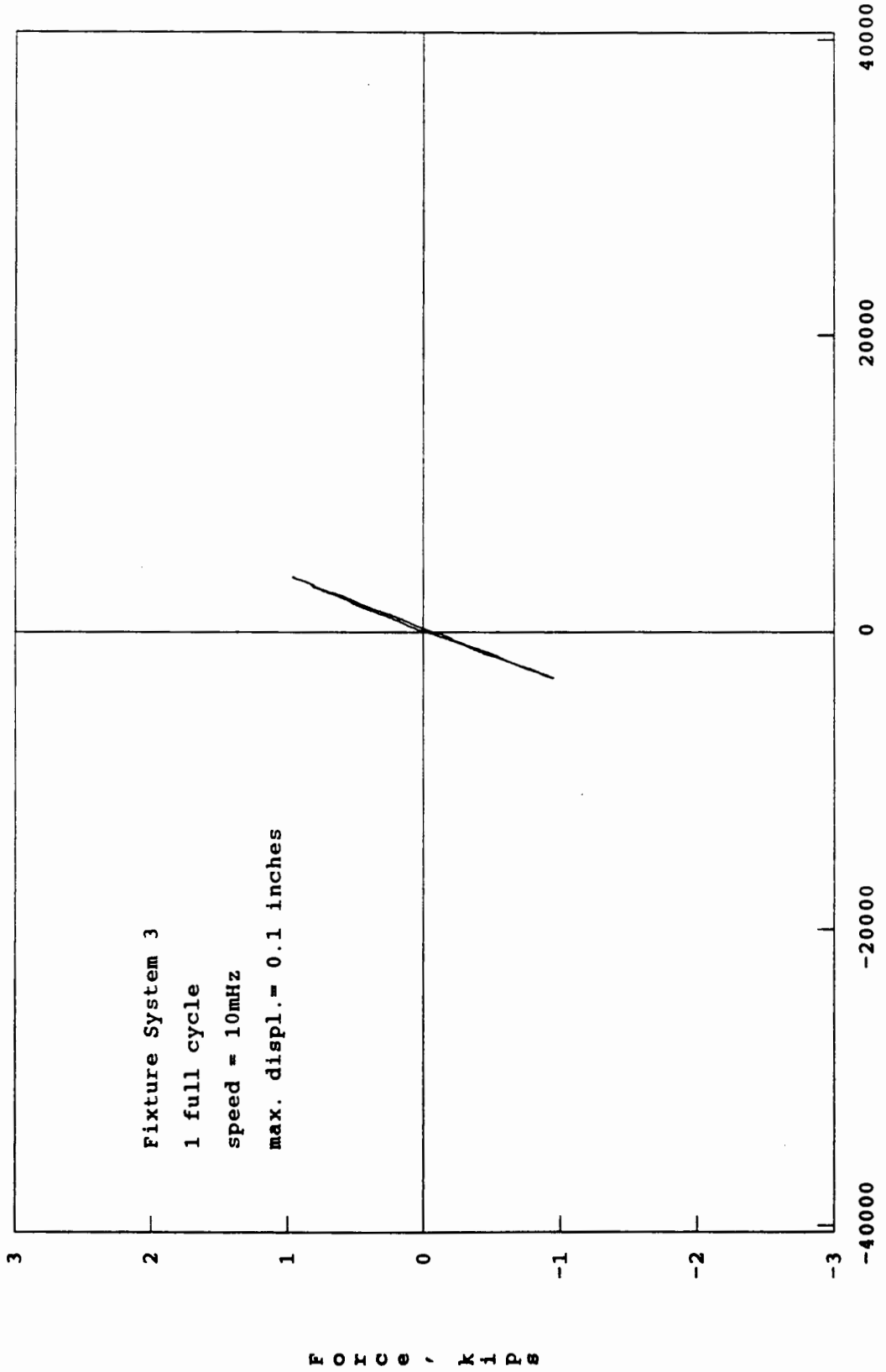

FIGURE 5.20 Force-Strain Hysteresis Loops for BN1S

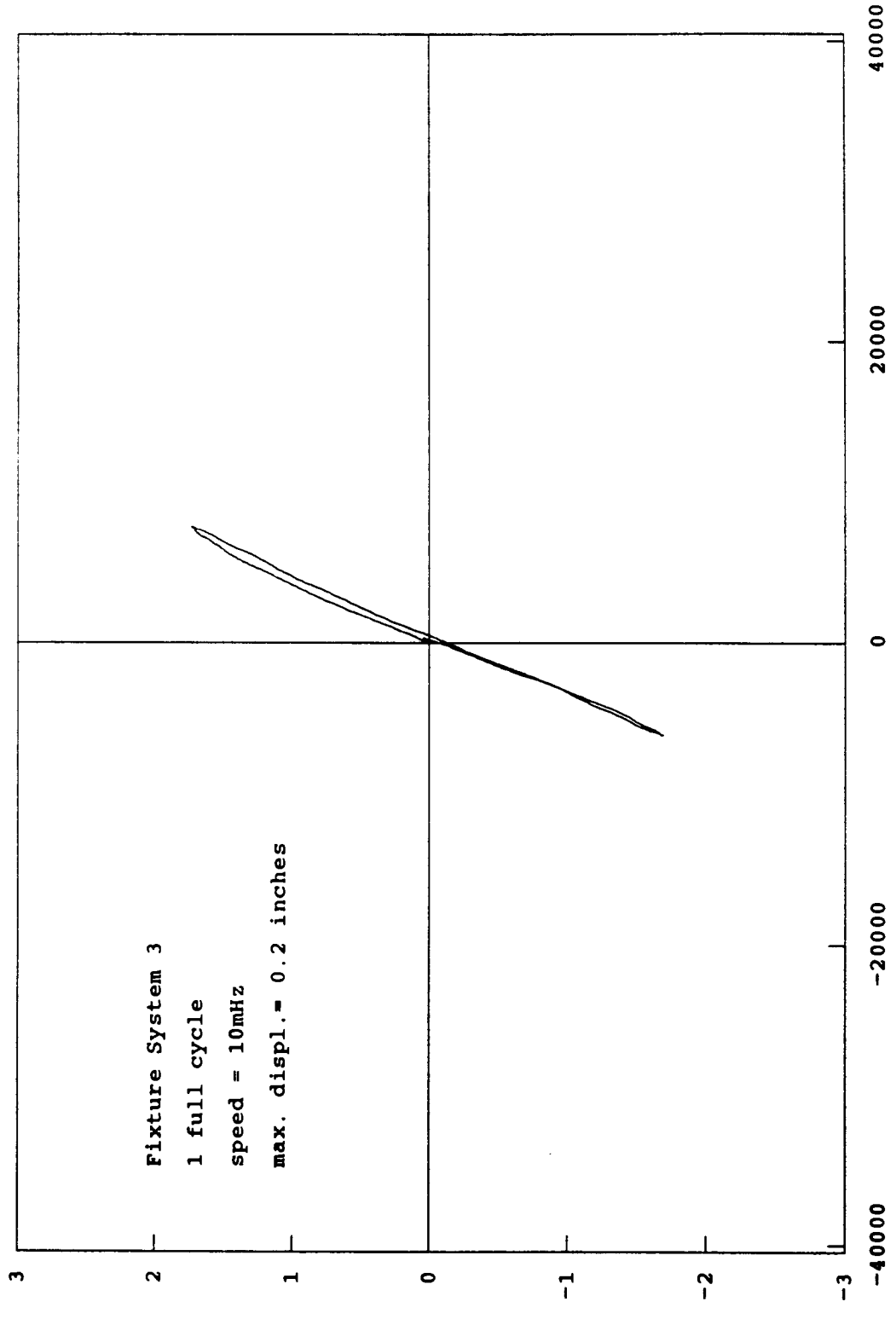

FIGURE 5.21 Force-Strain Hysteresis Loops for BN2S

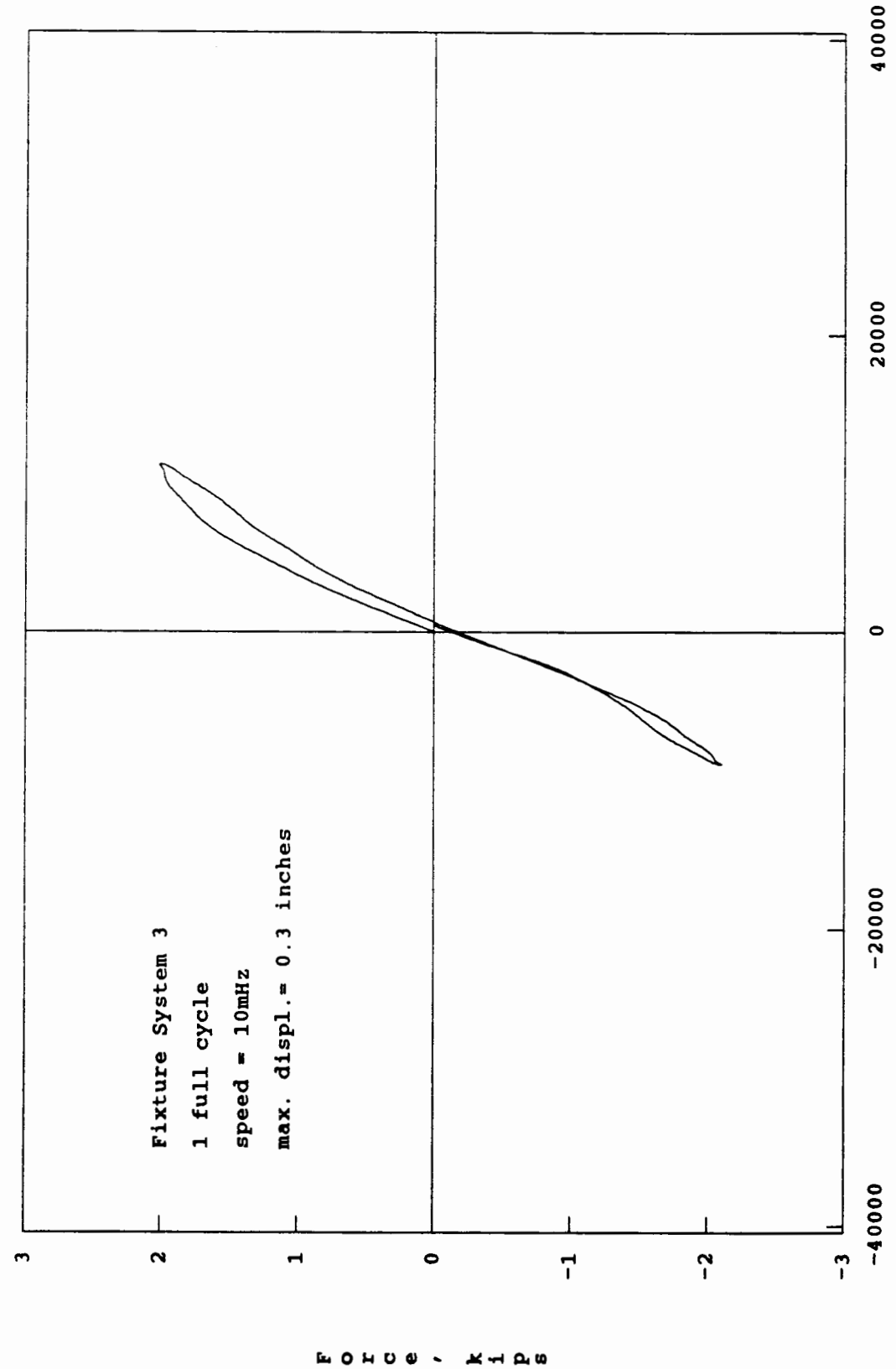

FIGURE 5.22 Force-Strain Hysteresis Loops for BN3S

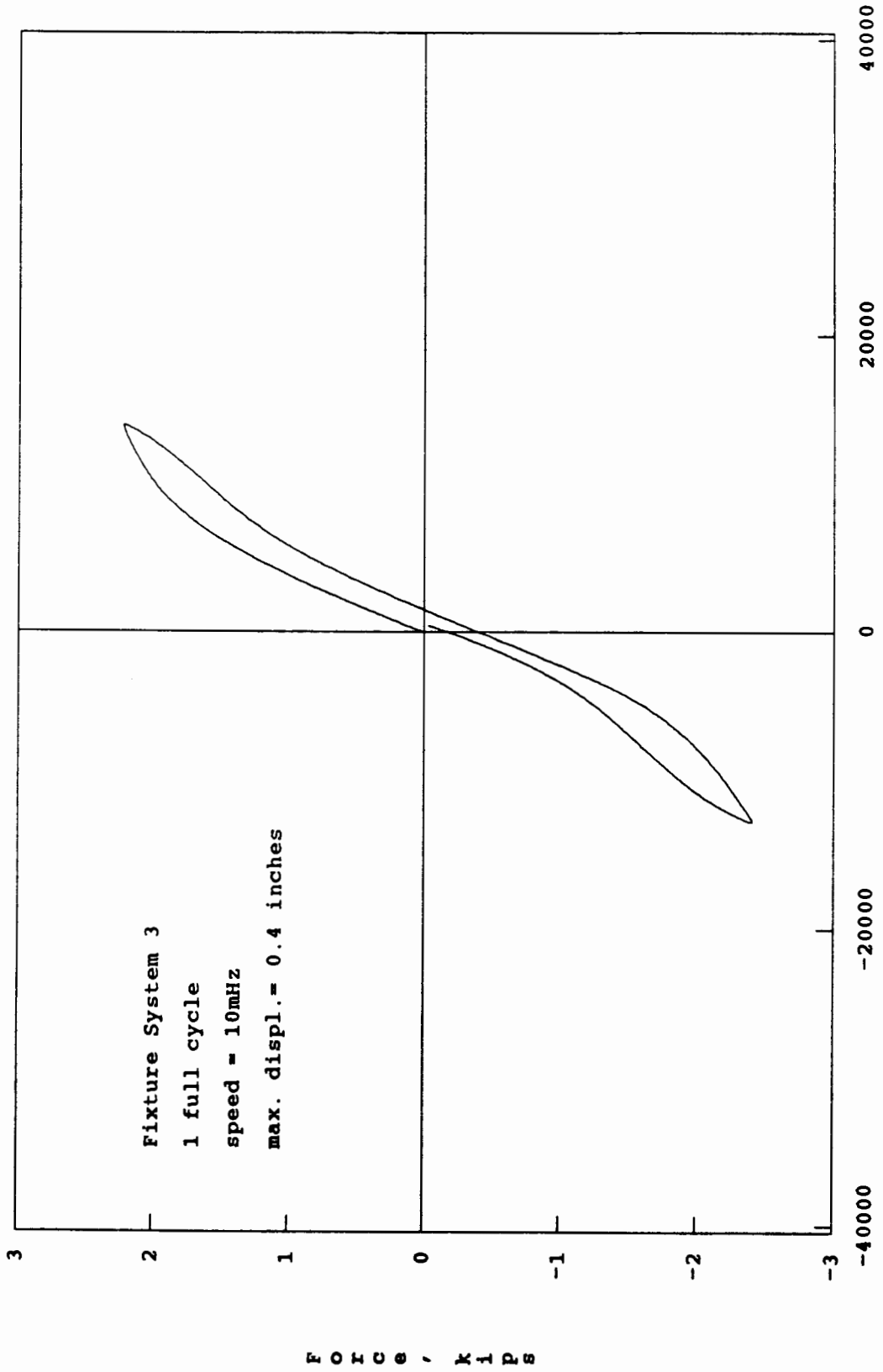

FIGURE 5.23 Force-Strain Hysteresis Loops for BN4S

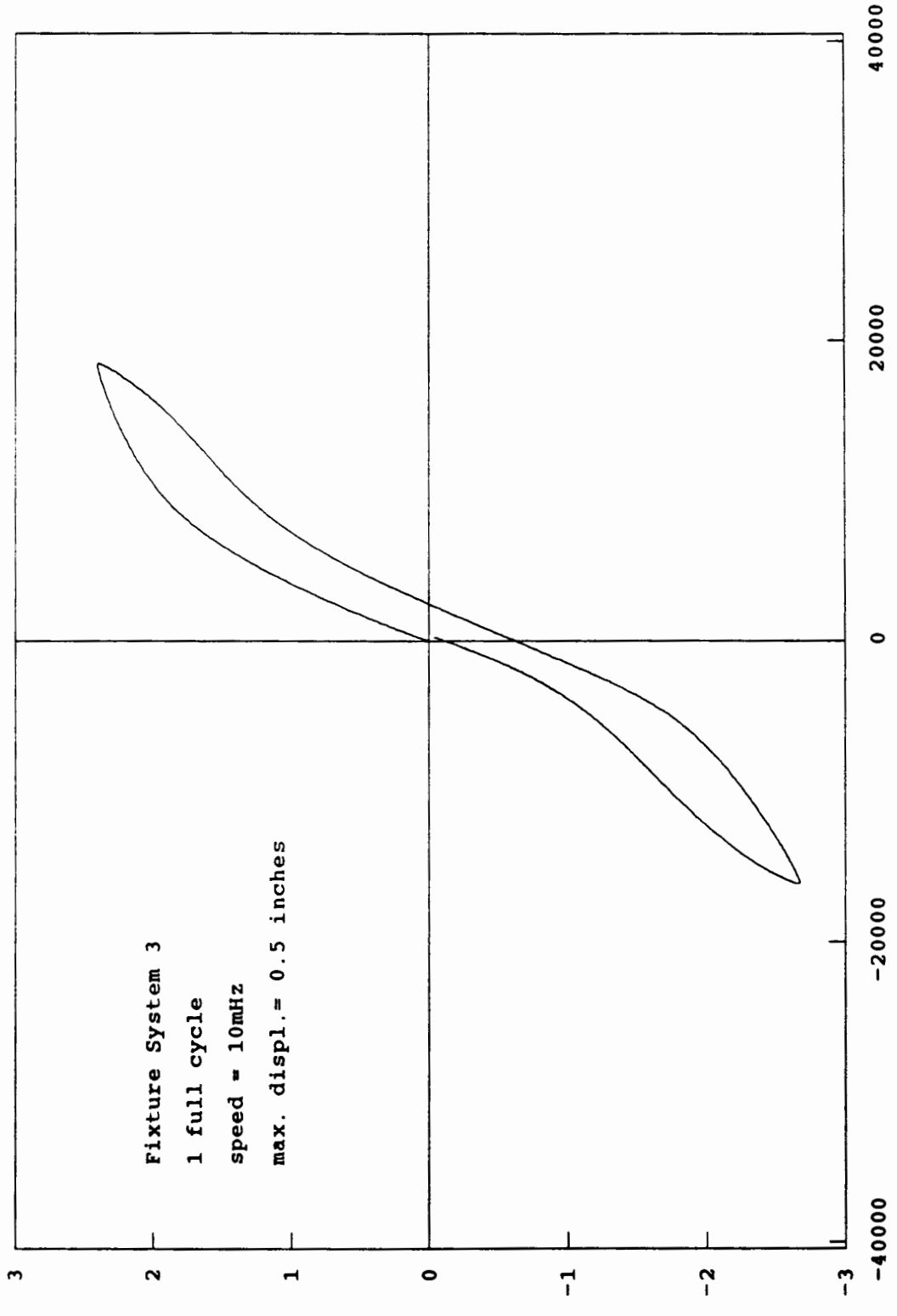

FIGURE 5.24 Force-Strain Hysteresis Loops for BN5S

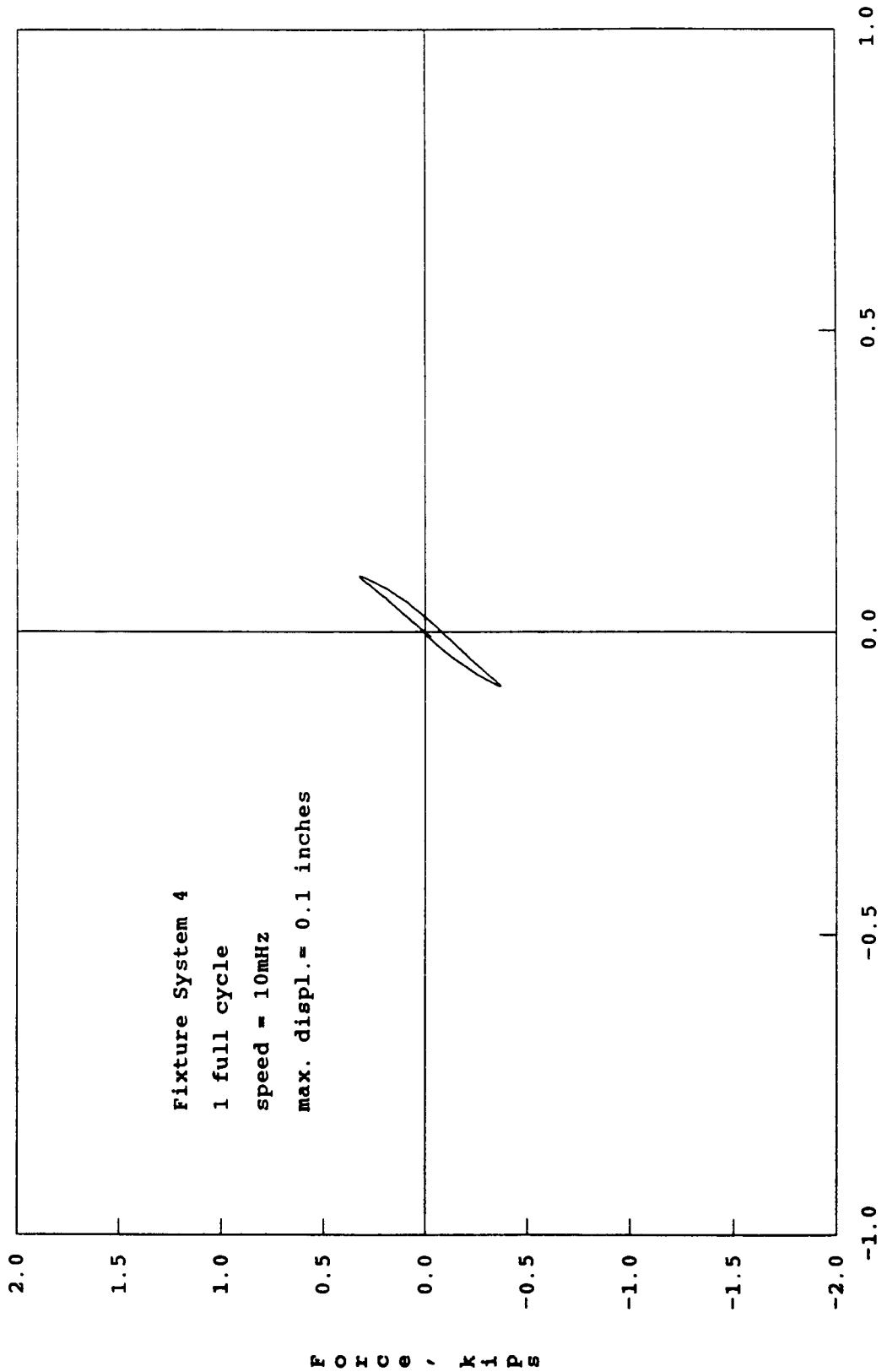

FIGURE 5.25 Force-Displacement Hysteresis Loops for BX1S

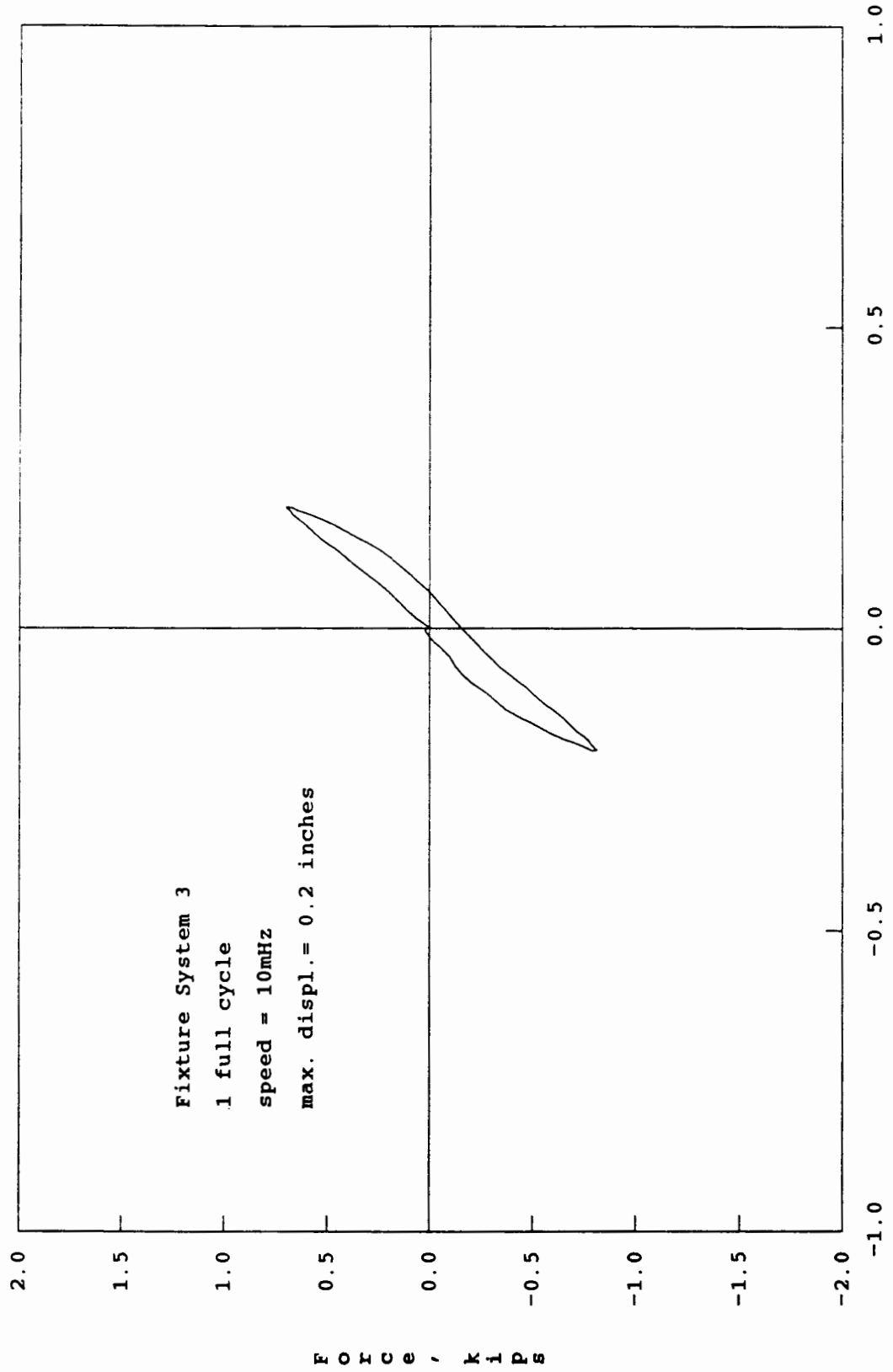

FIGURE 5.26 Force-Displacement Hysteresis Loops for BX2S

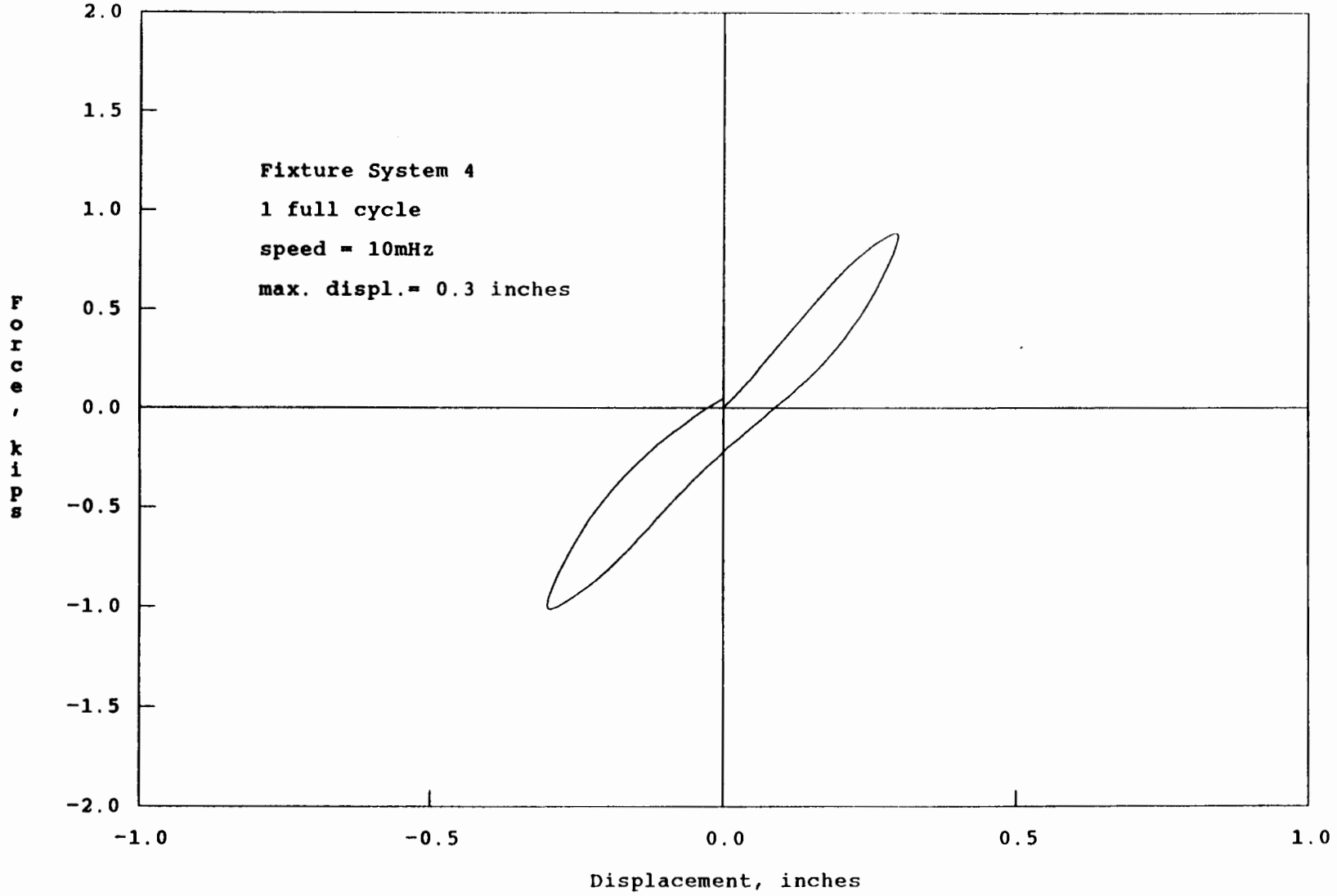

FIGURE 5.27 Force-Displacement Hysteresis Loops for BX3S

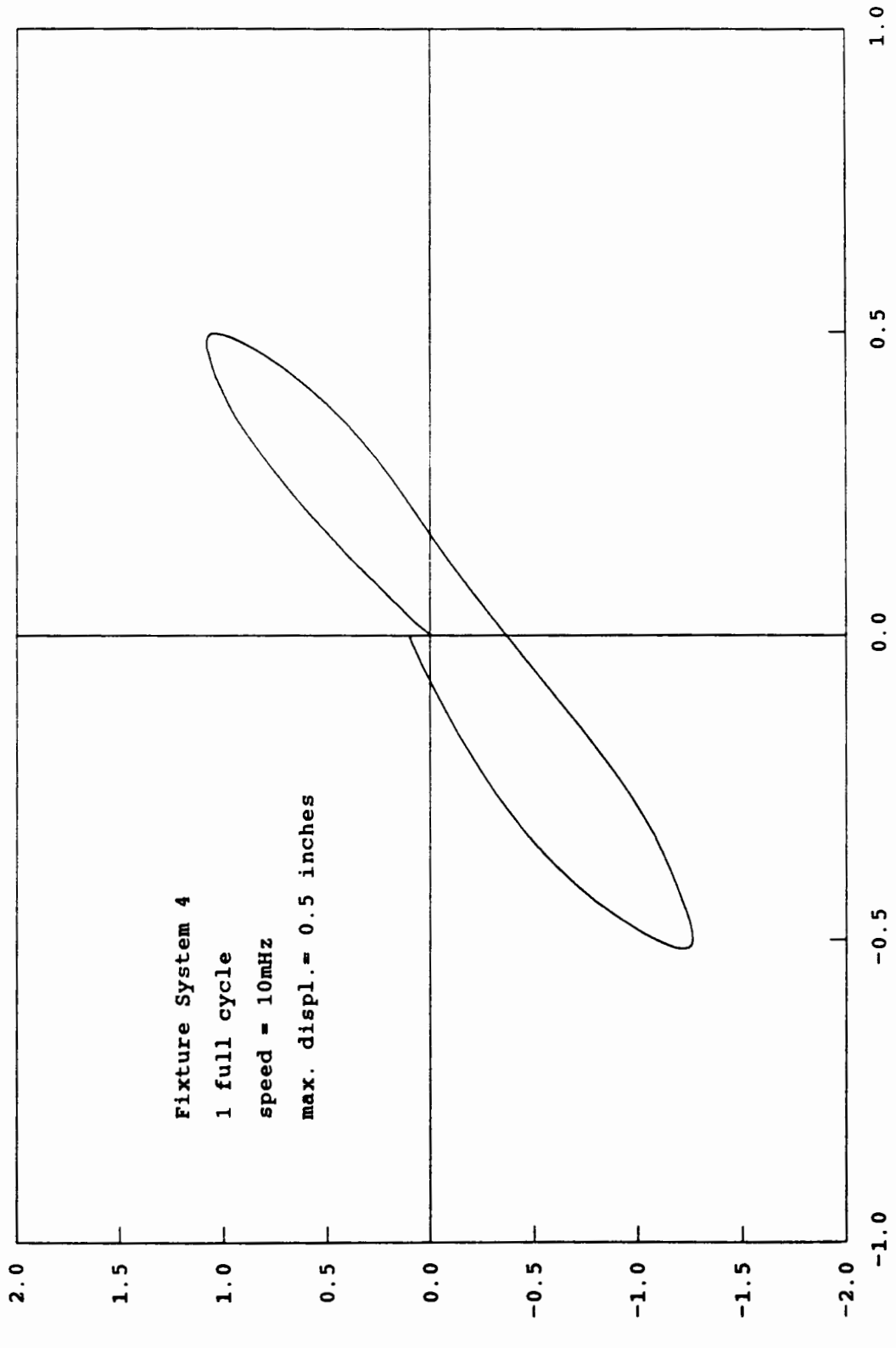

FIGURE 5.28 Force-Displacement Hysteresis Loops for BX5S

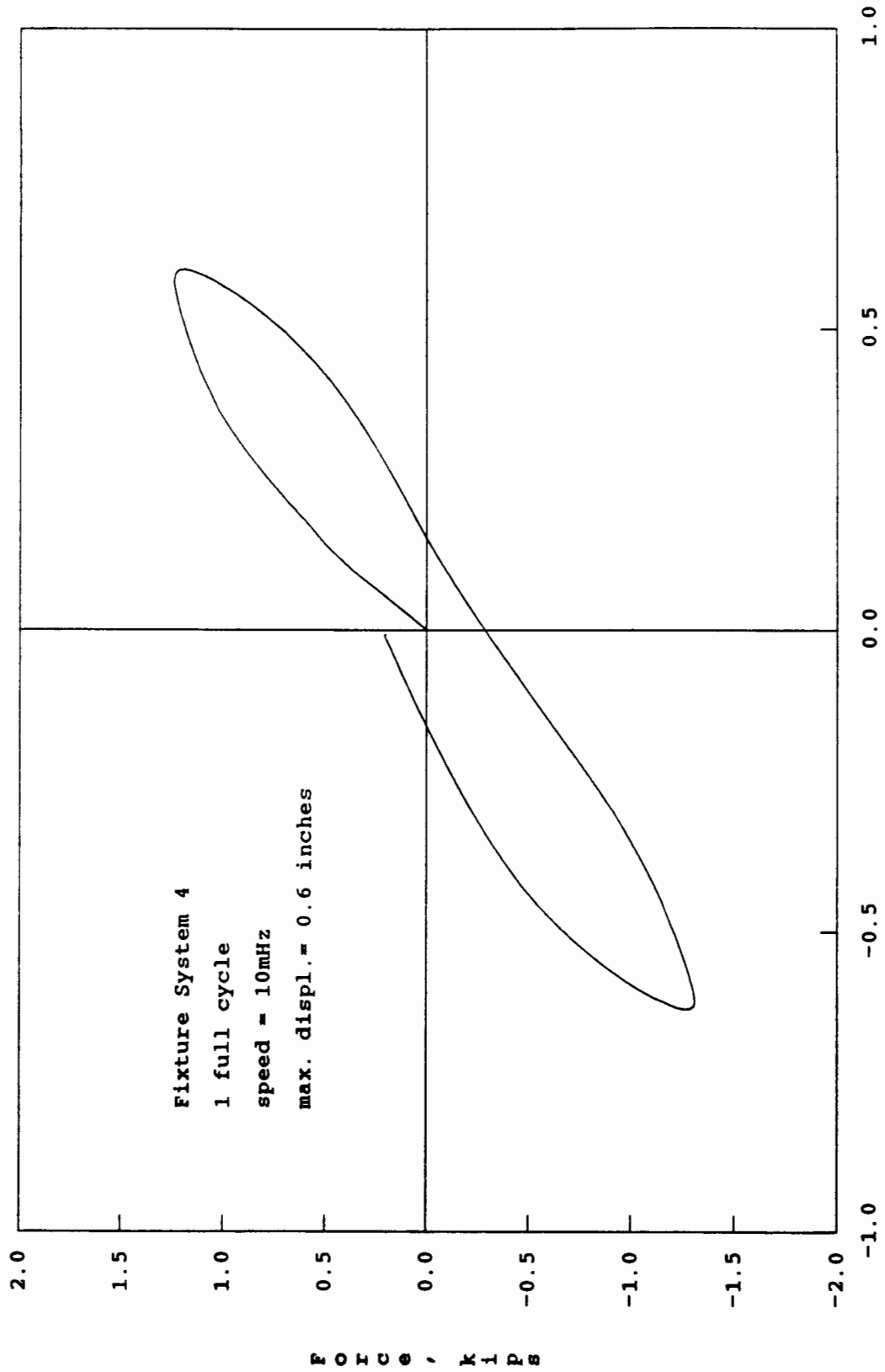

FIGURE 5.29 Force-Displacement Hysteresis Loops for BX6S

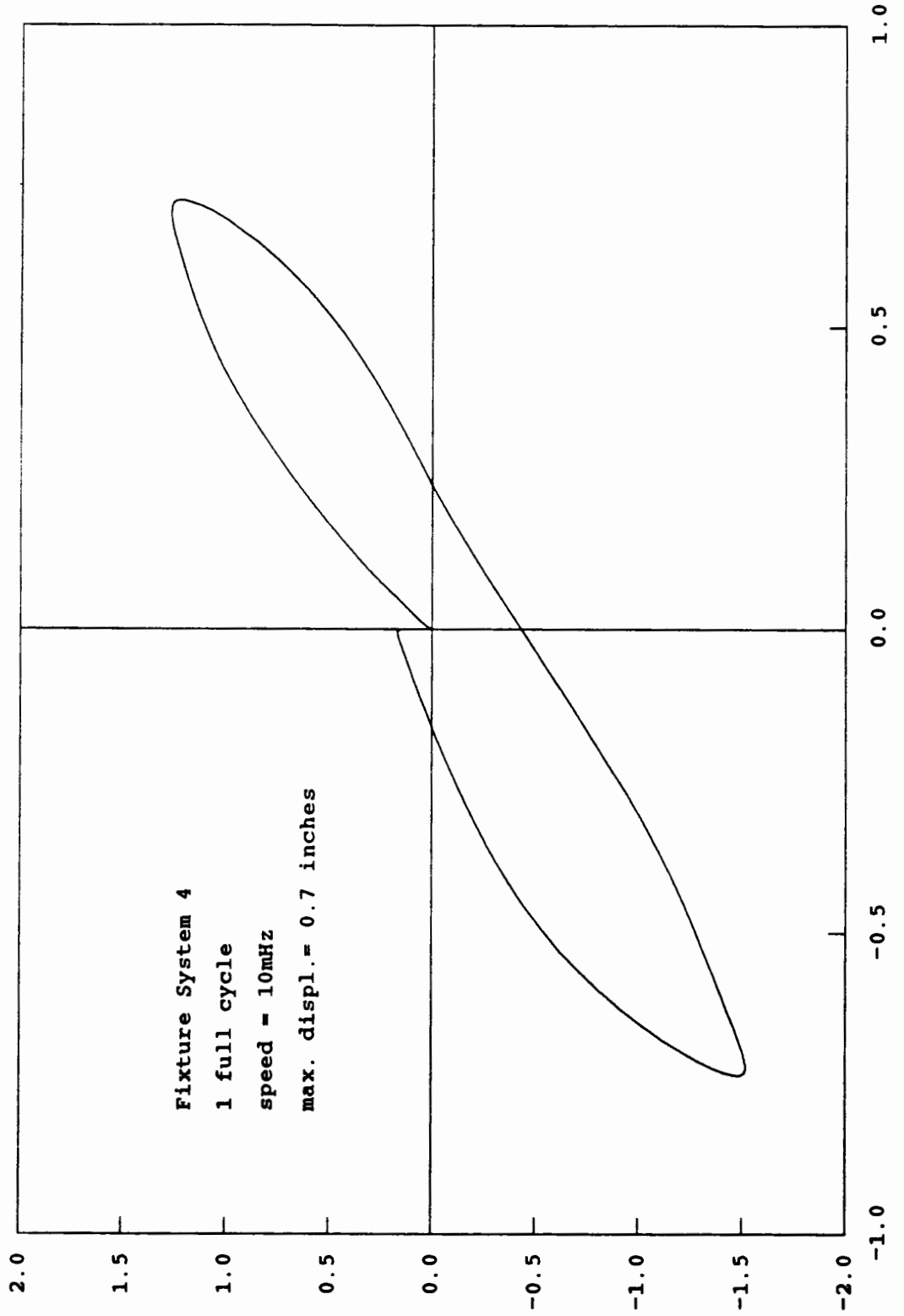

FIGURE 5.30 Force-Displacement Hysteresis Loops for BX7S

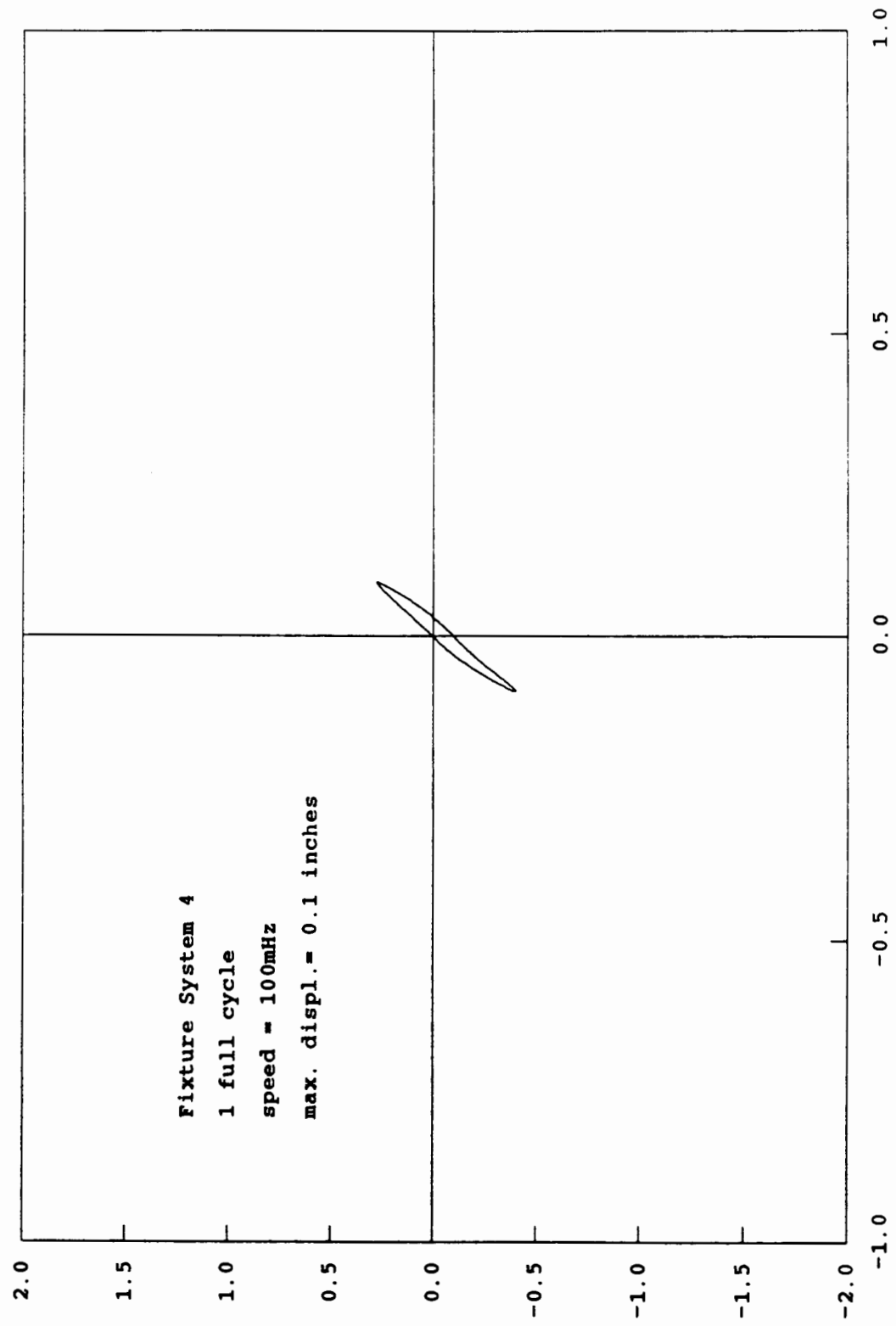

FIGURE 5.31 Force-Displacement Hysteresis Loops for BX1F

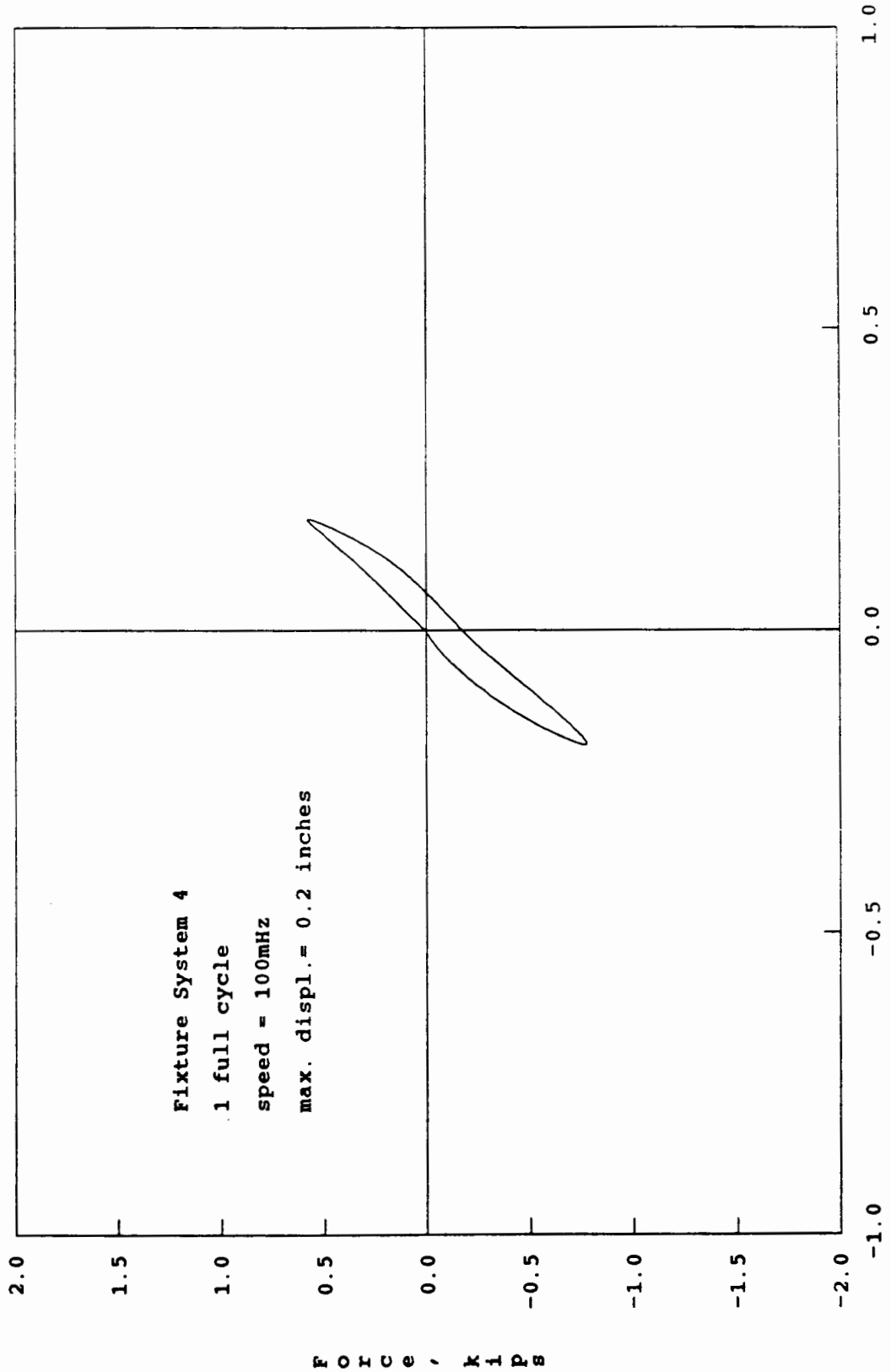

FIGURE 5.32 Force-Displacement Hysteresis Loops for BX2F

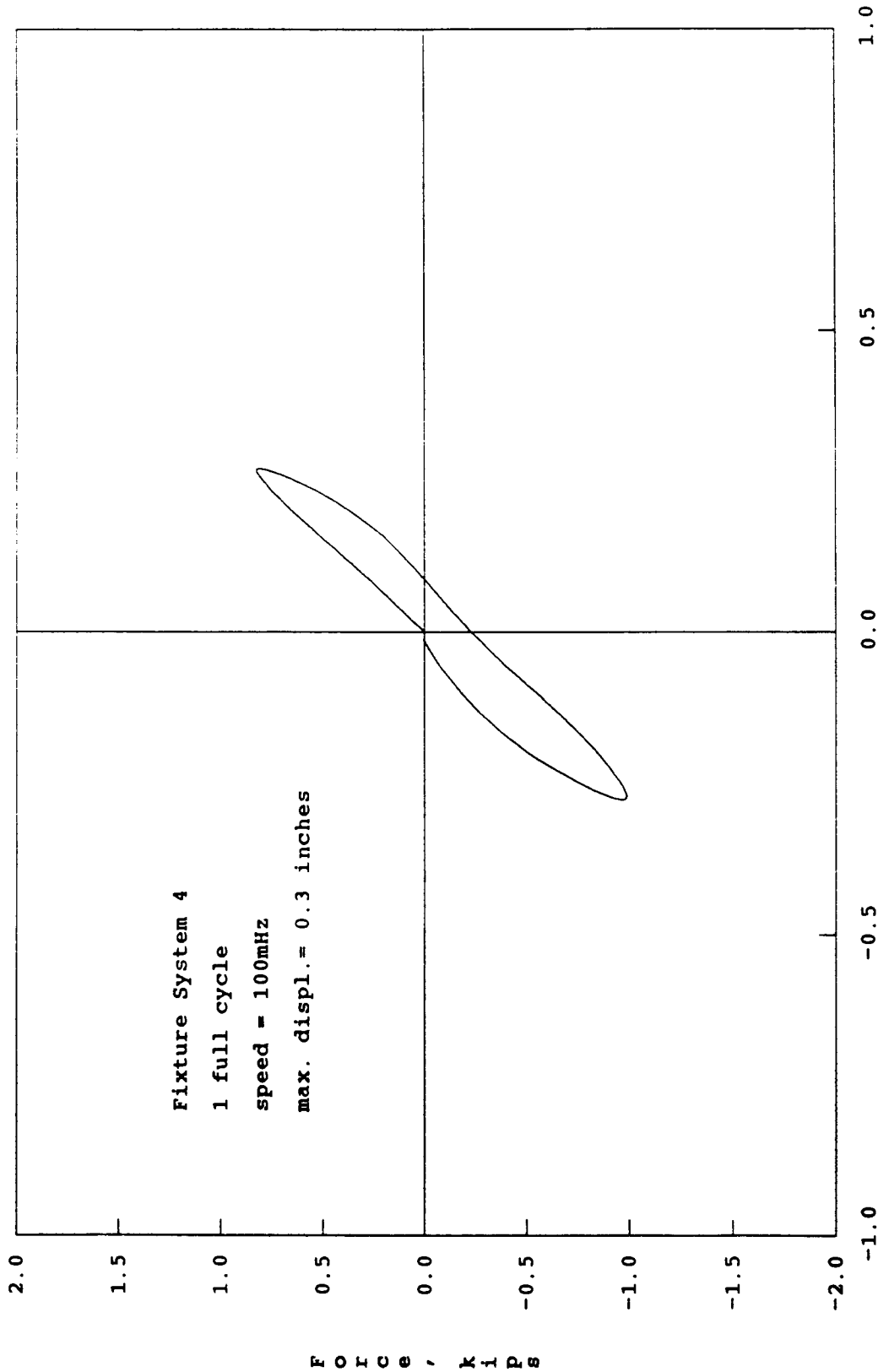

FIGURE 5.33 Force-Displacement Hysteresis Loops for BX3F

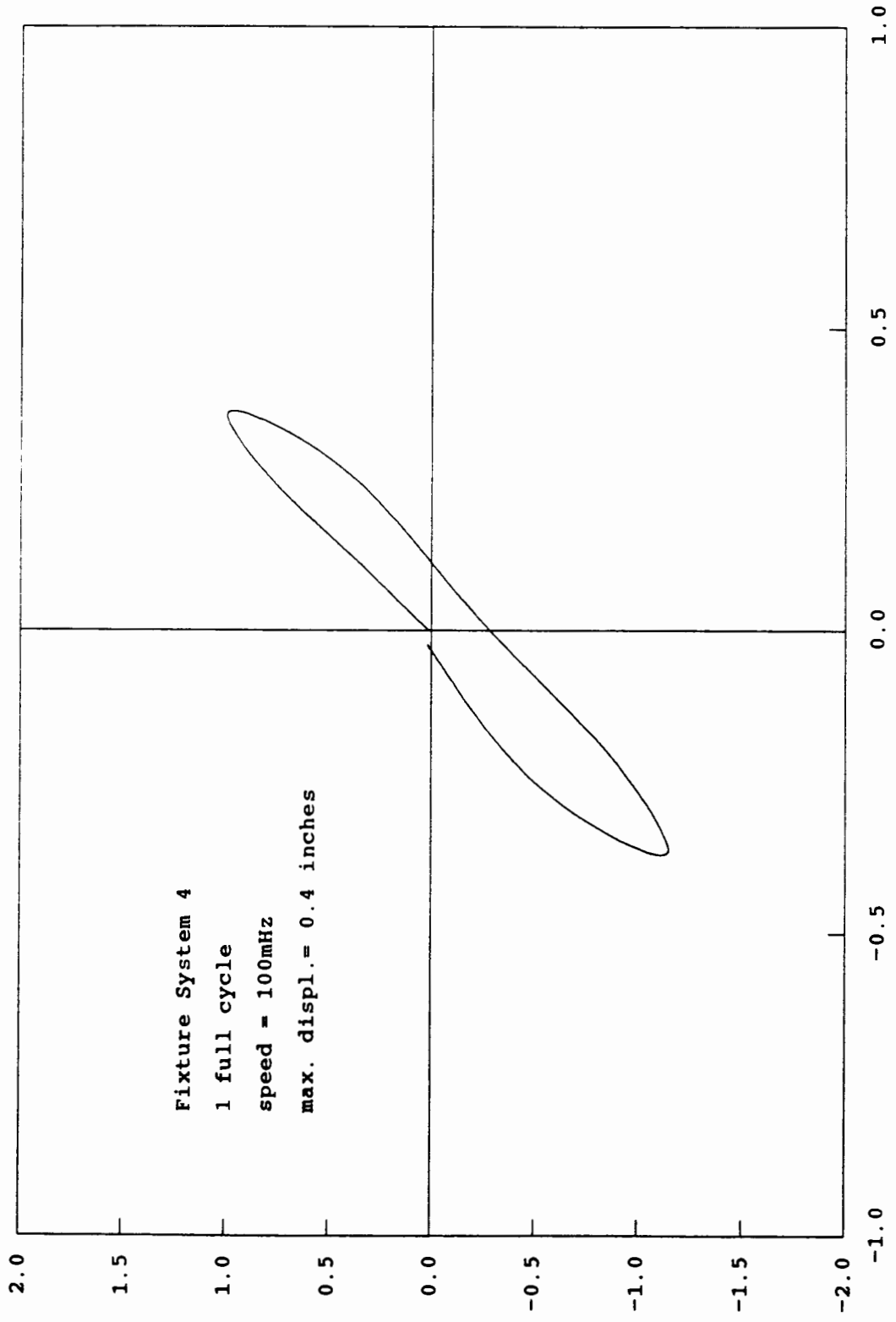

FIGURE 5.34 Force-Displacement Hysteresis Loops for BX4F

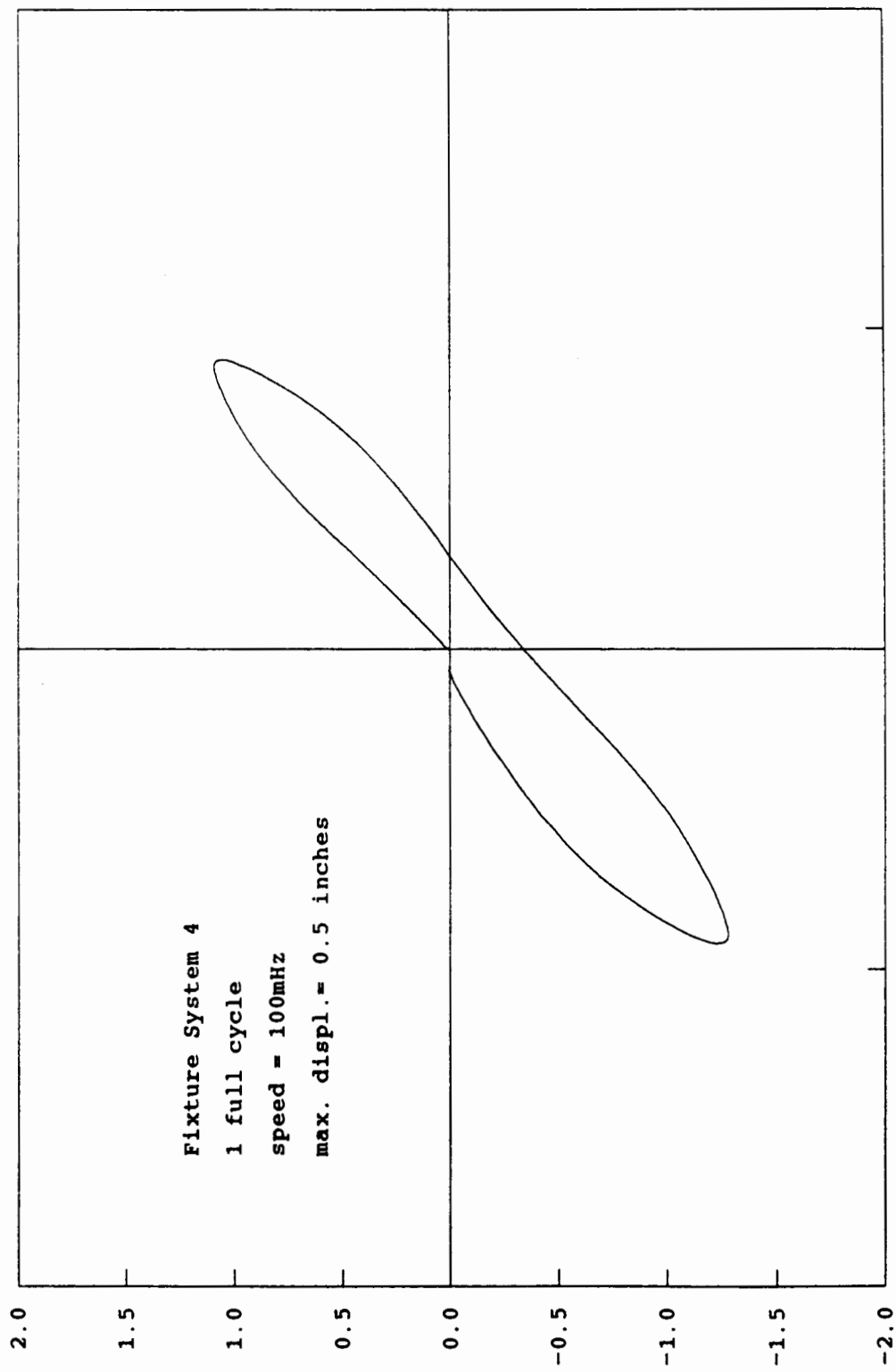

FIGURE 5.35 Force-Displacement Hysteresis Loops for BX5F

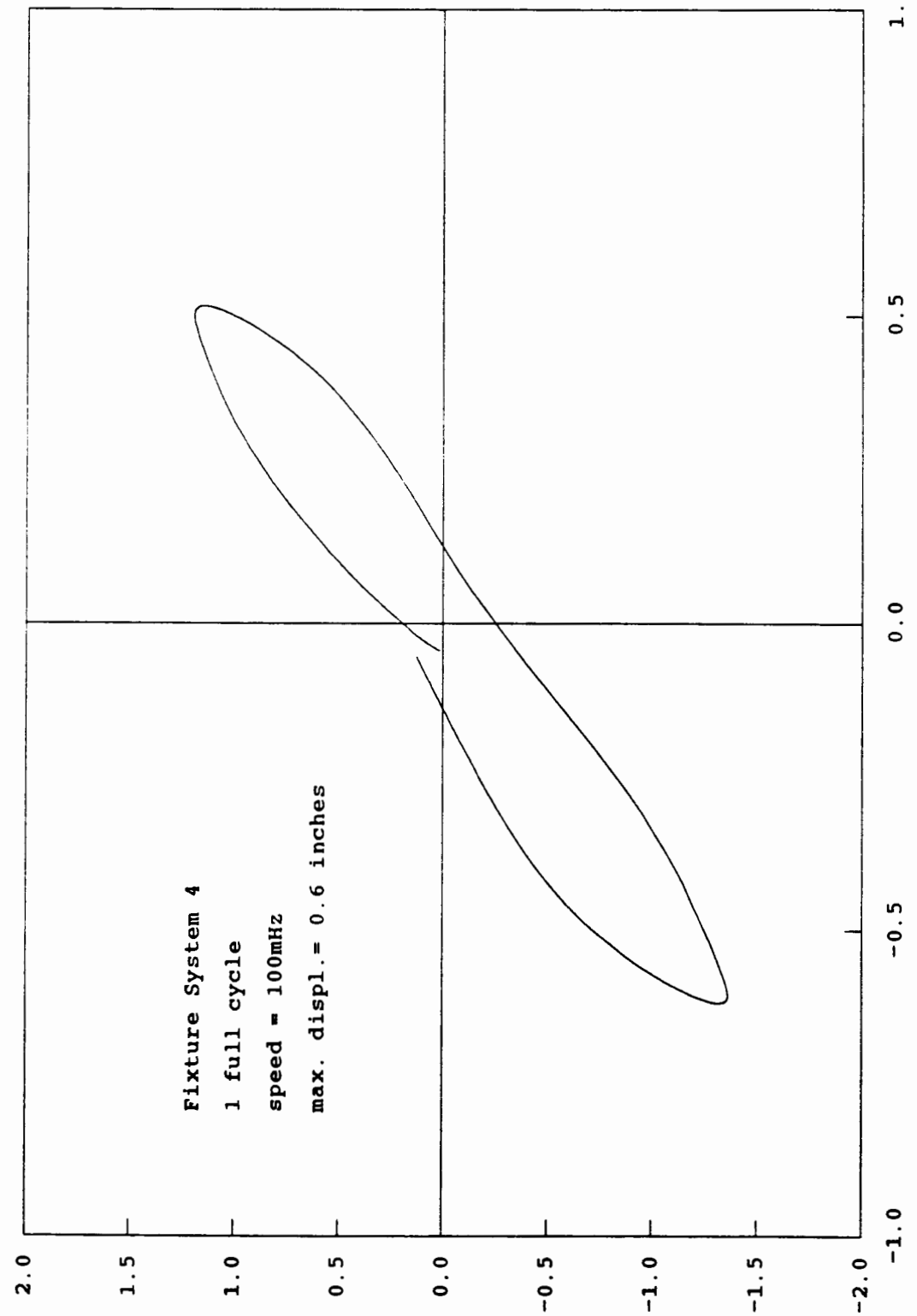

FIGURE 5.36 Force-Displacement Hysteresis Loops for BX6F

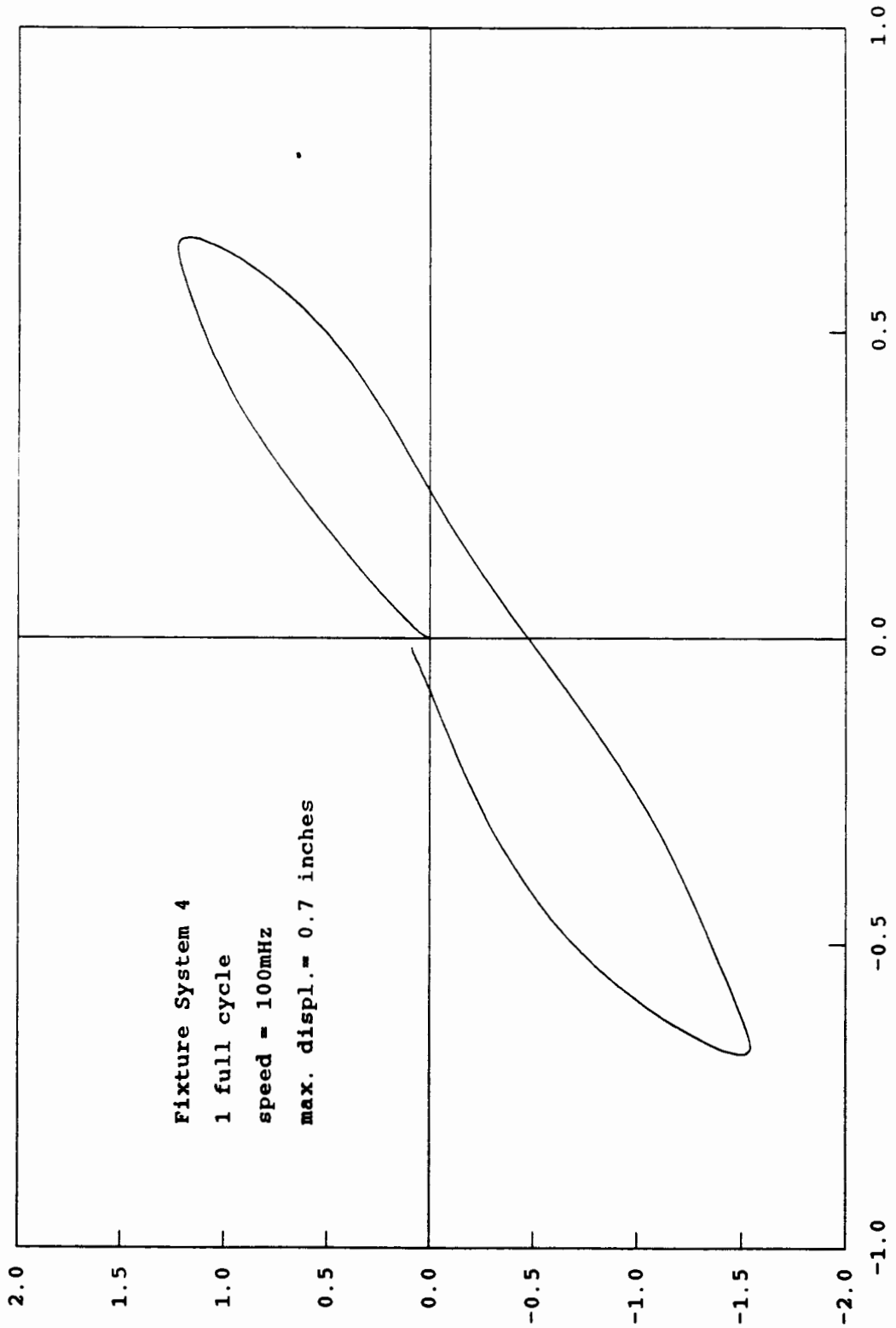

FIGURE 5.37 Force-Displacement Hysteresis Loops for BX7F

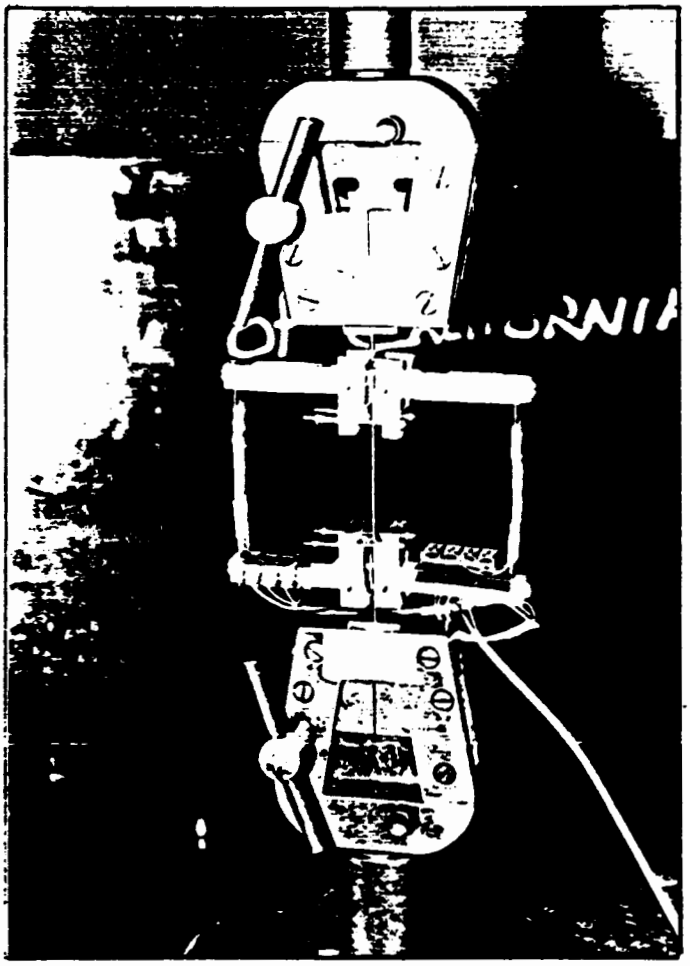

FIGURE 6.1 Tension Test Fixture

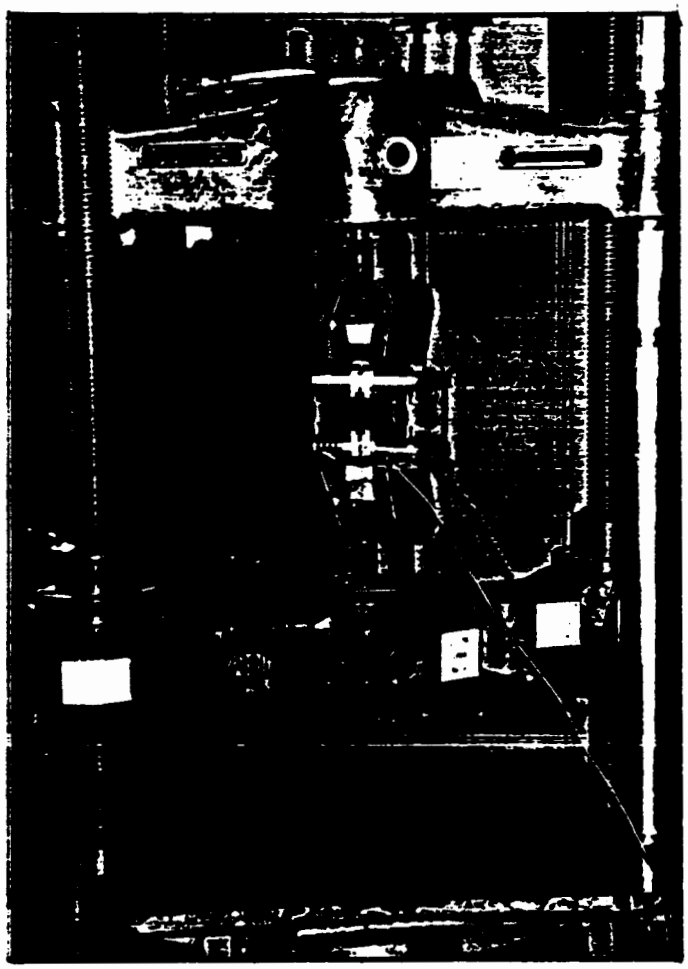

FIGURE 6.2 Tension Test Fixture

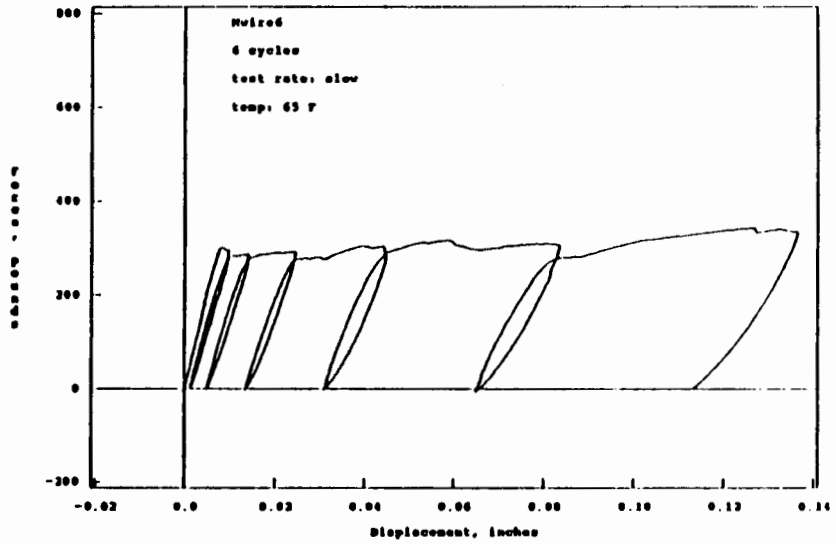

FIGURE 6.3a Force-Displacement Hysteresis Loops for Nitinol Wire

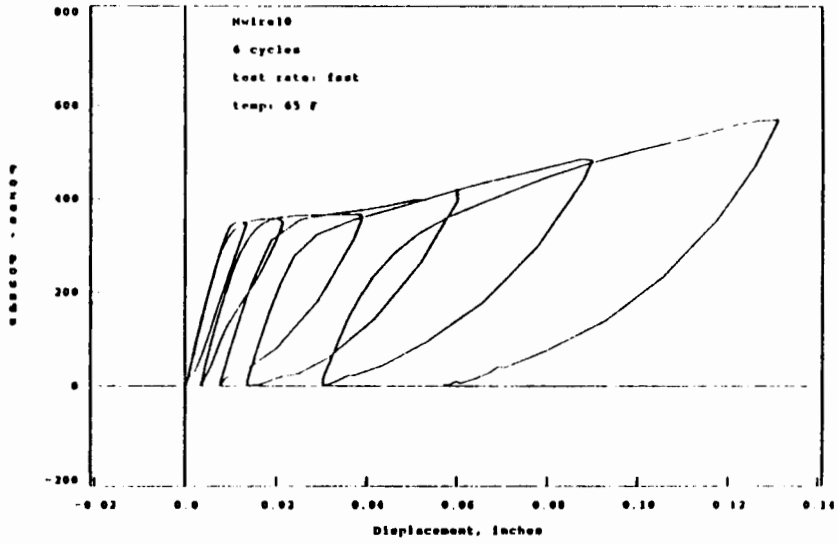

FIGURE 6.3b Force-Displacement Hysteresis Loops for Nitinol Wire

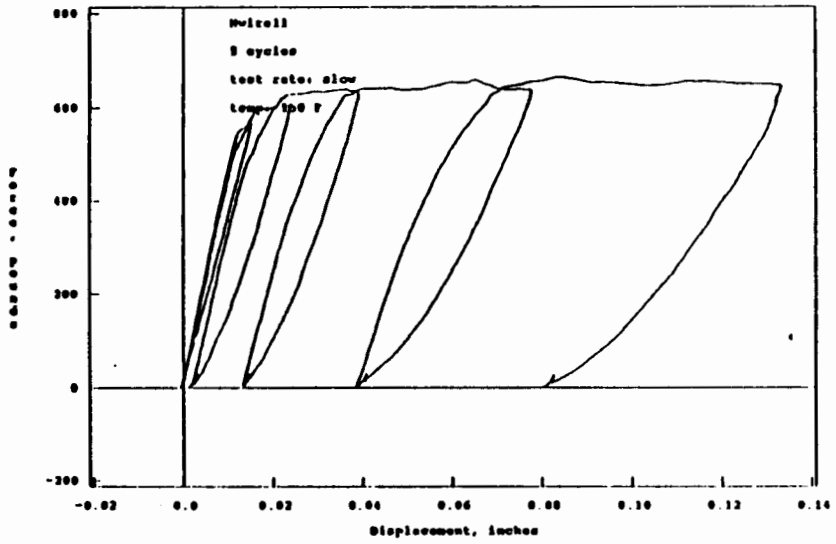

FIGURE 6.3c Force-Displacement Hysteresis Loops for Nitinol Wire

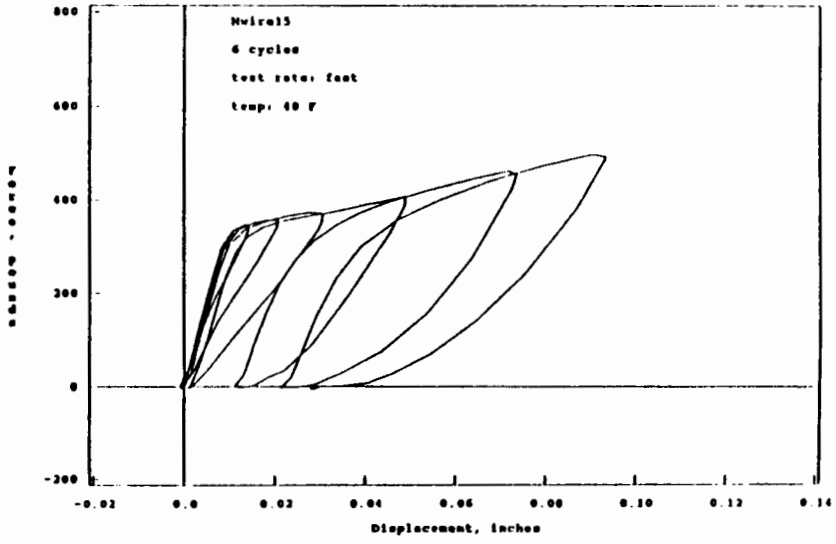

FIGURE 6.3d Force-Displacement Hysteresis Loops for Nitinol Wire

FIGURE 6.3 Force-Displacement Hysteresis Loops for Nitinol Wire

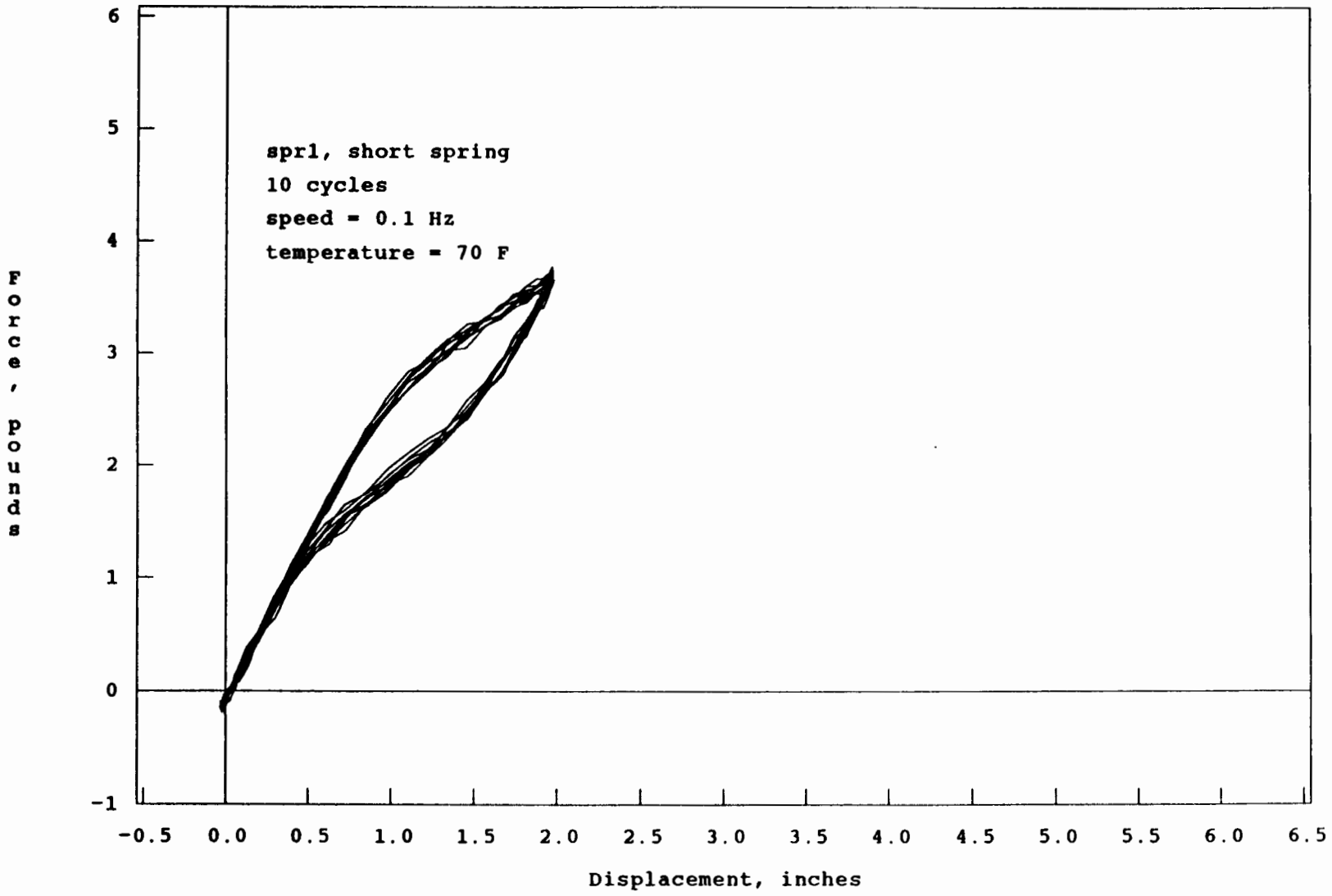

Figure 7.1 Force - Displacement Hysteresis Loops for Nitinol Springs

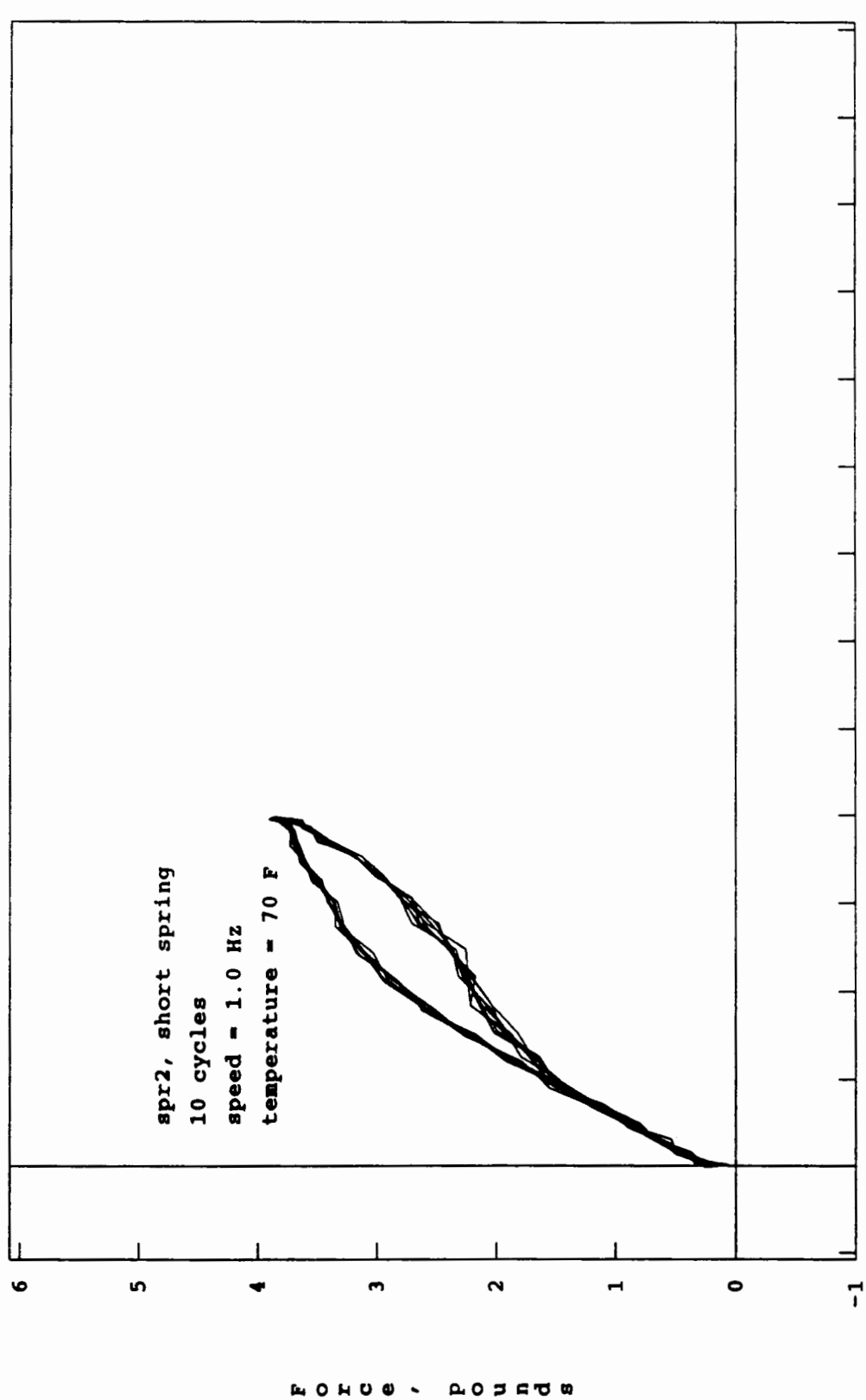

Figure 7.2 Force - Displacement Hysteresis Loops for Nitinol Springs

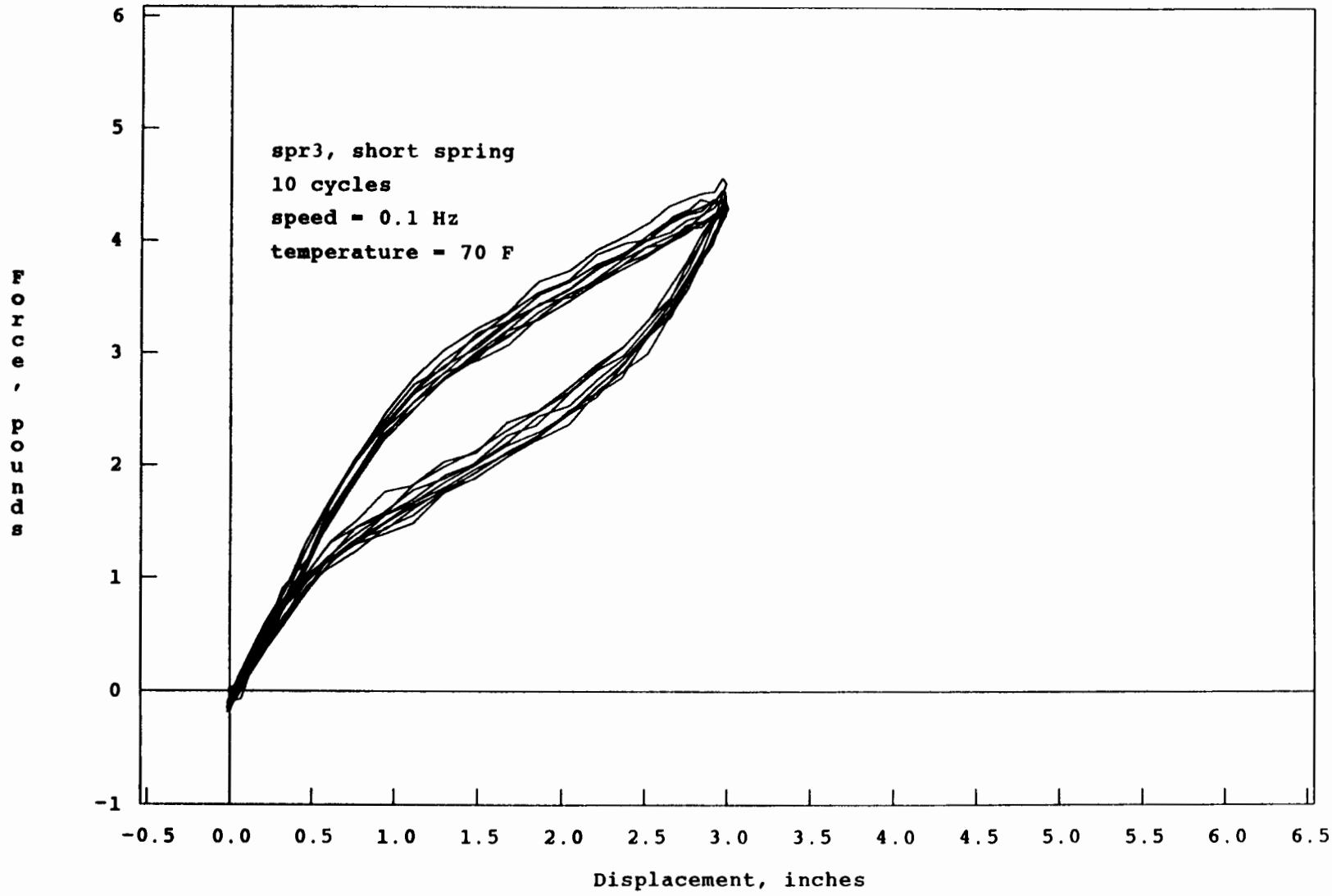

Figure 7.3 Force - Displacement Hysteresis Loops for Nitinol Springs

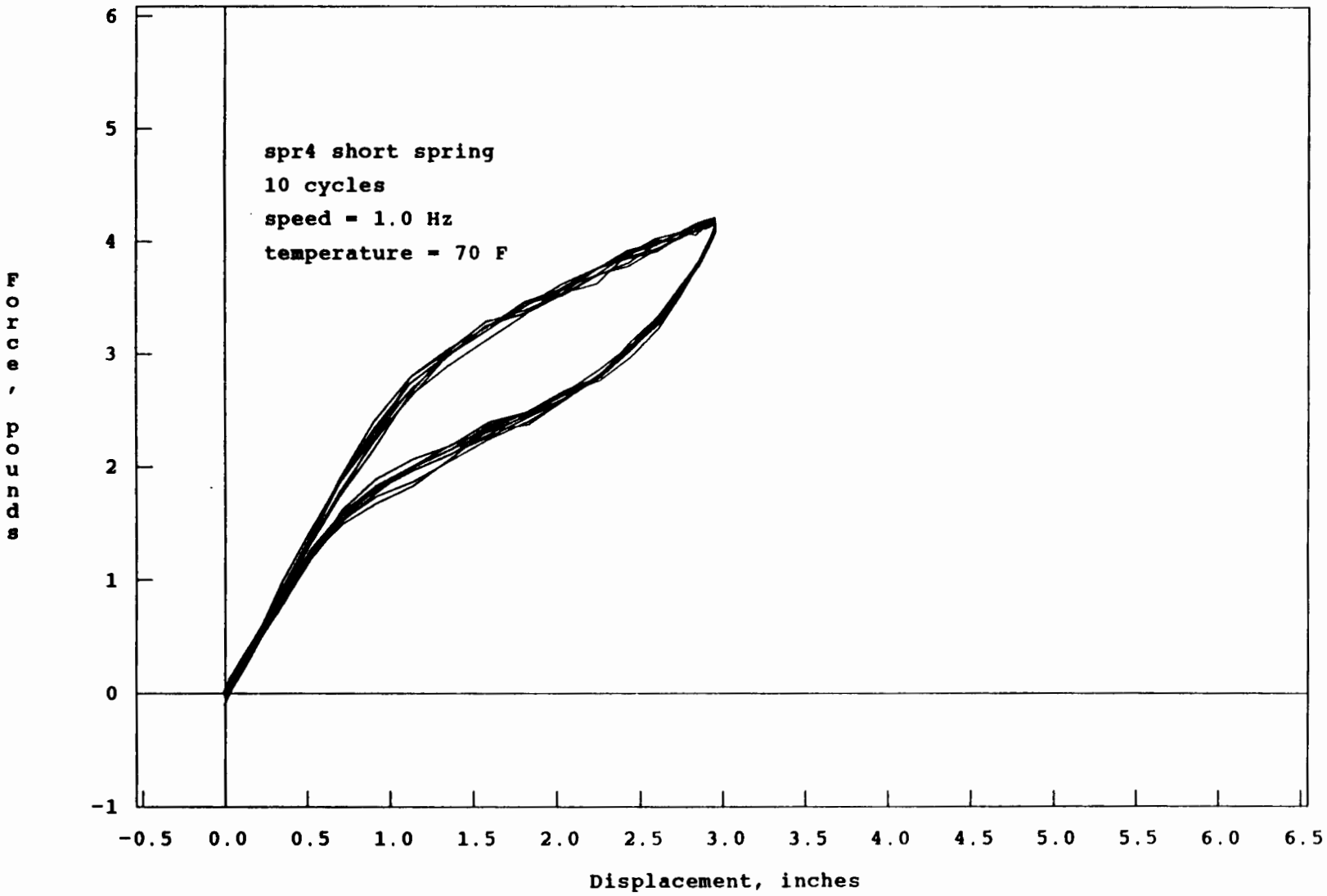

Figure 7.4 Force - Displacement Hysteresis Loops for Nitinol Springs

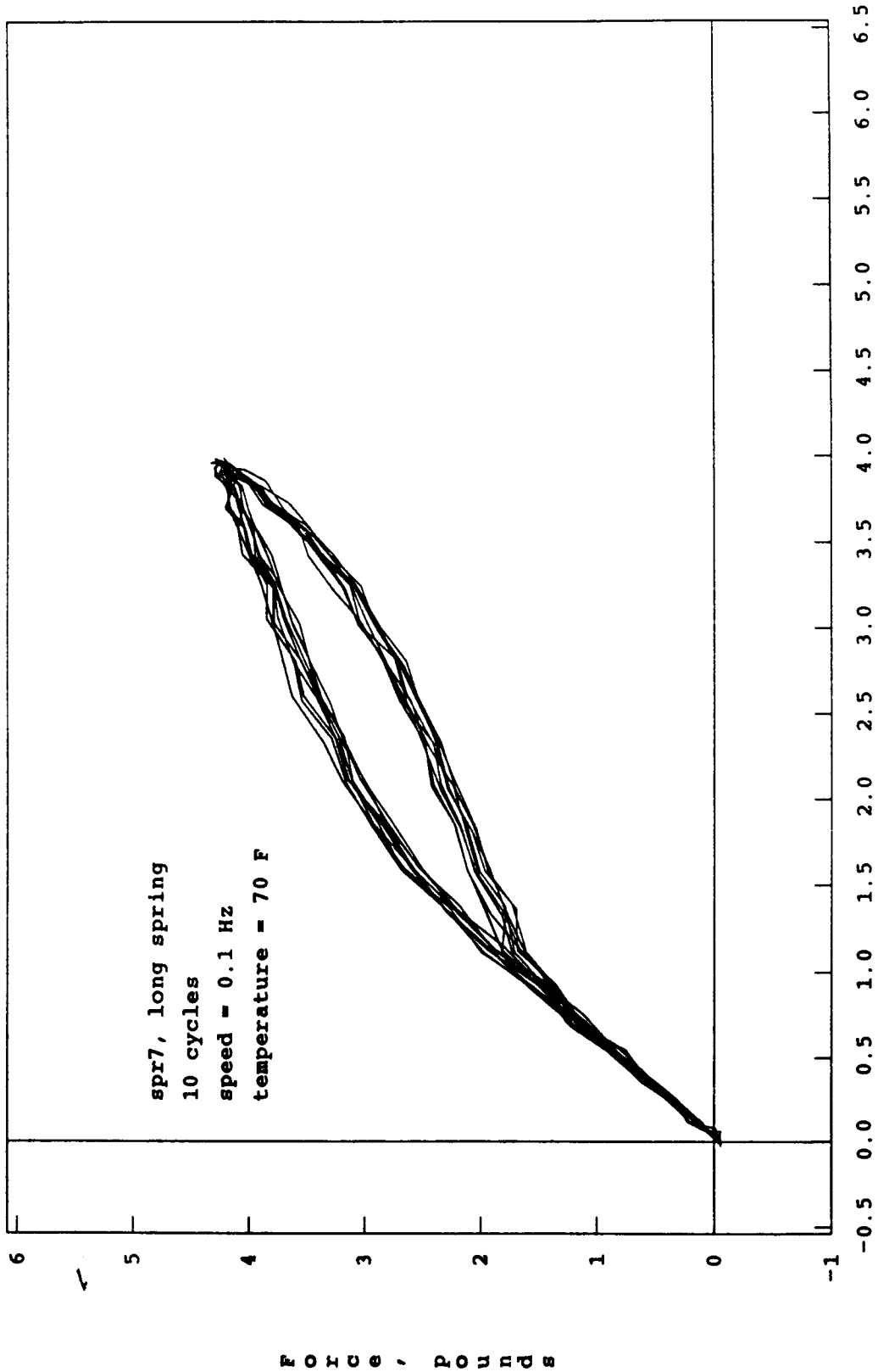

Figure 7.5 Force - Displacement Hysteresis Loops for Nitinol Springs

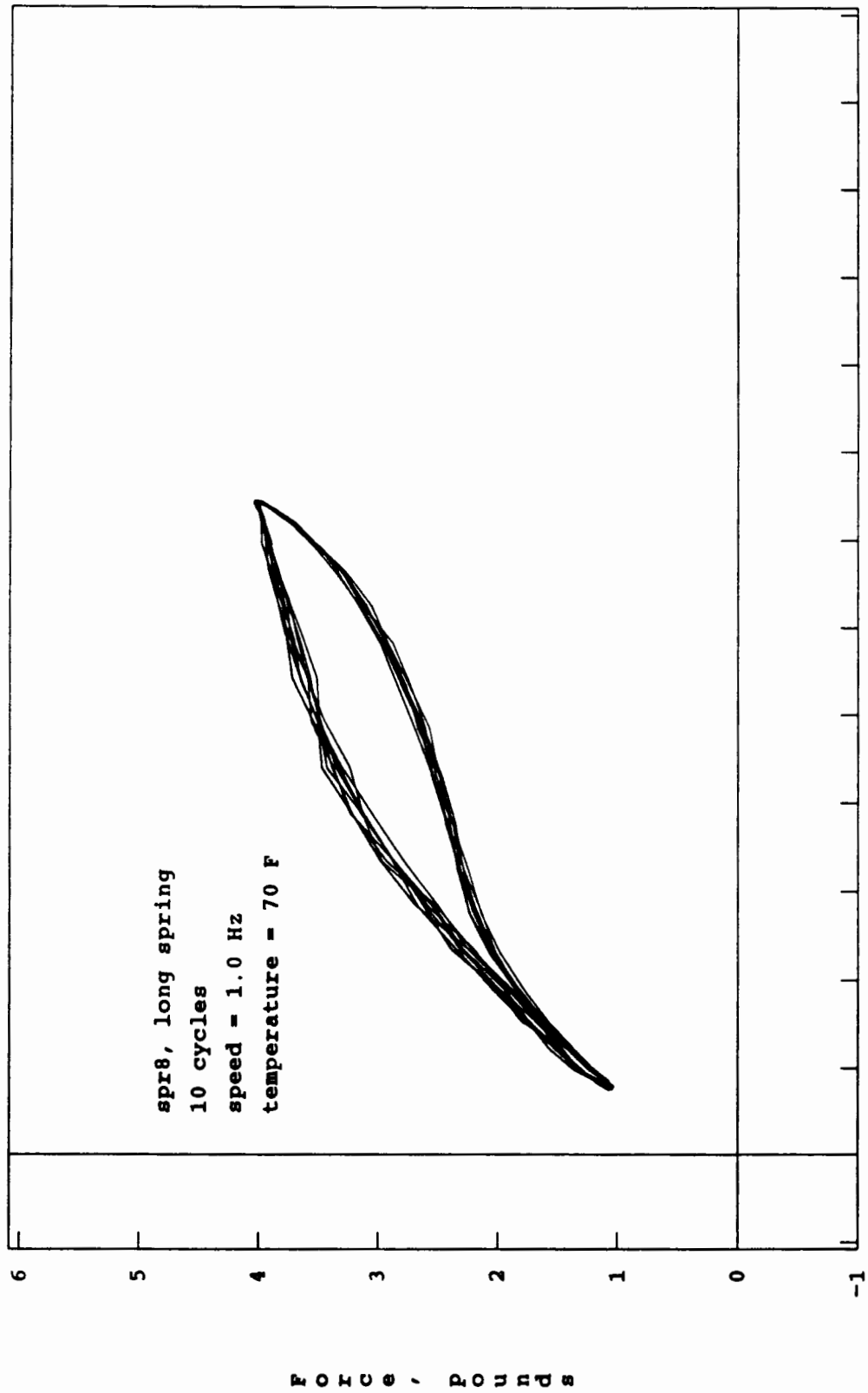

Figure 7.6 Force - Displacement Hysteresis Loops for Nitinol Springs

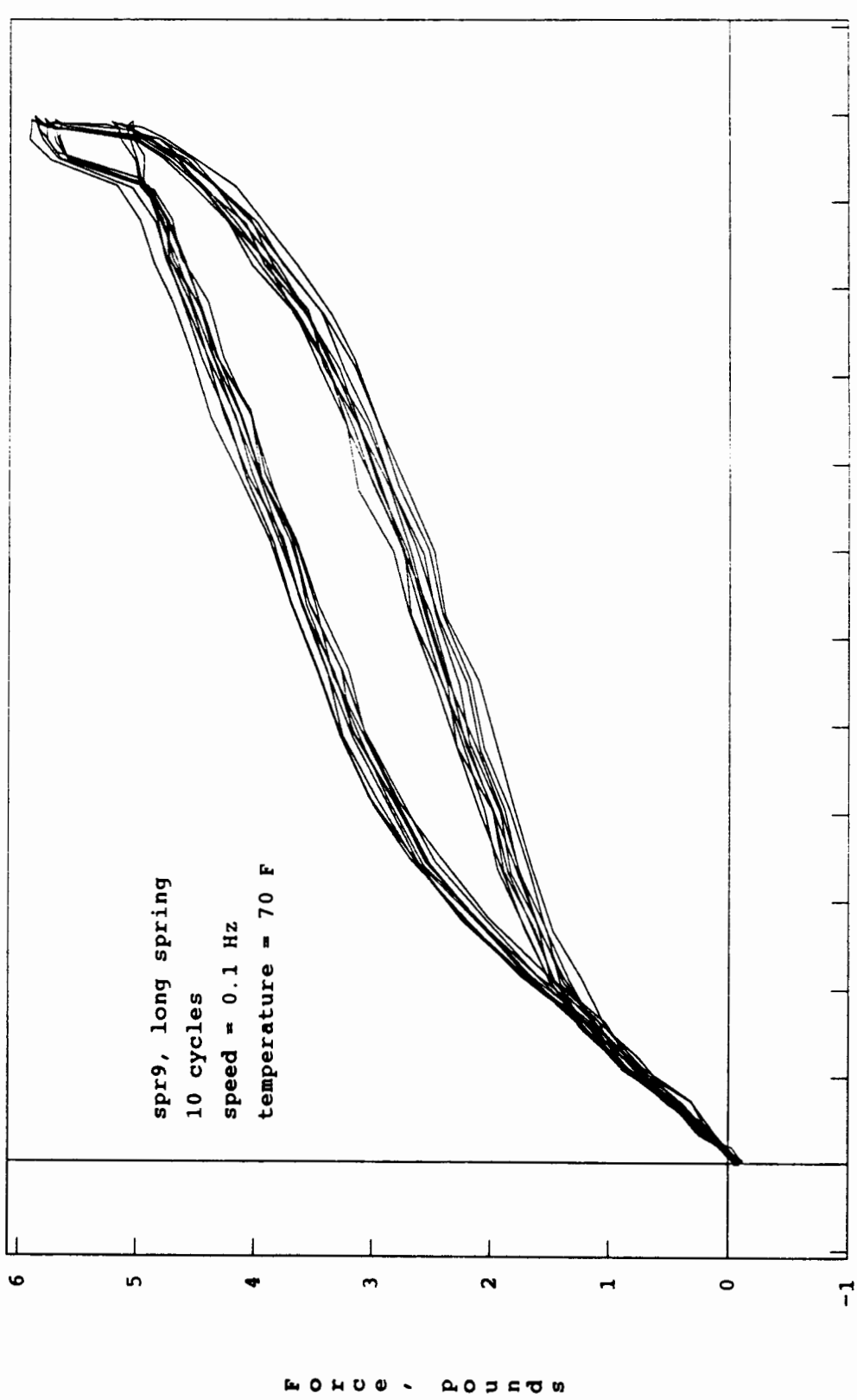

Figure 7.7 Force - Displacement Hysteresis Loops for Nitinol Springs

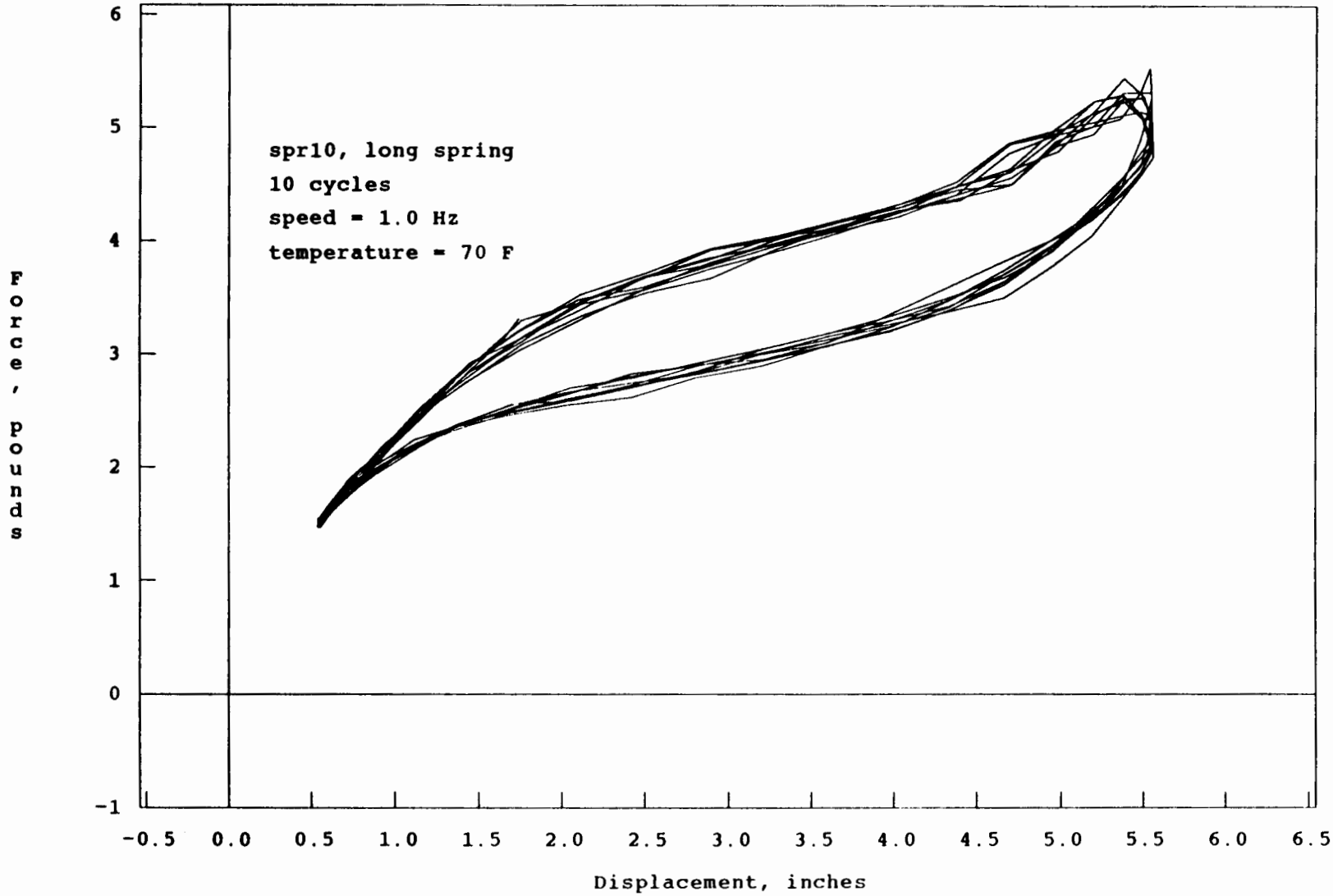

Figure 7.8 Force - Displacement Hysteresis Loops for Nitinol Springs

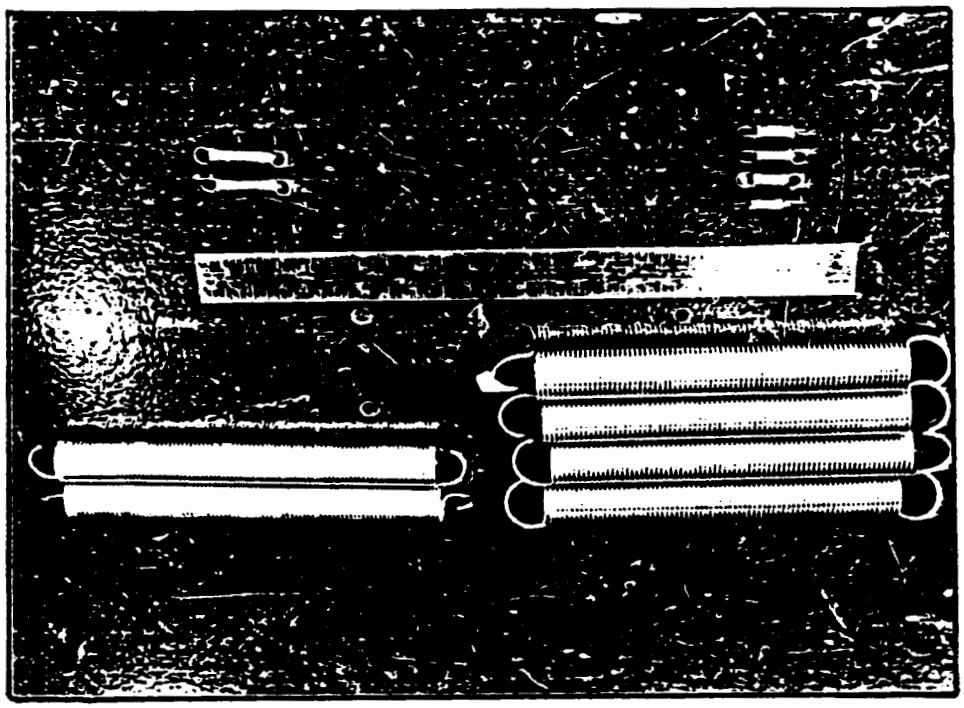

FIGURE 8.1 Base Isolation Springs

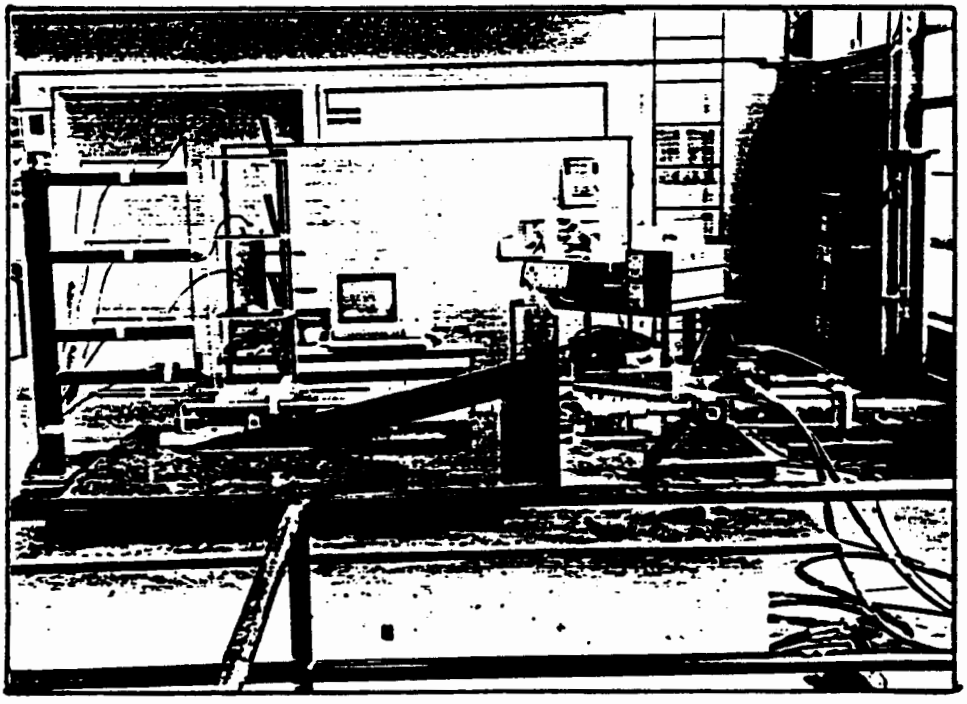

FIGURE 8.2 Test Setup

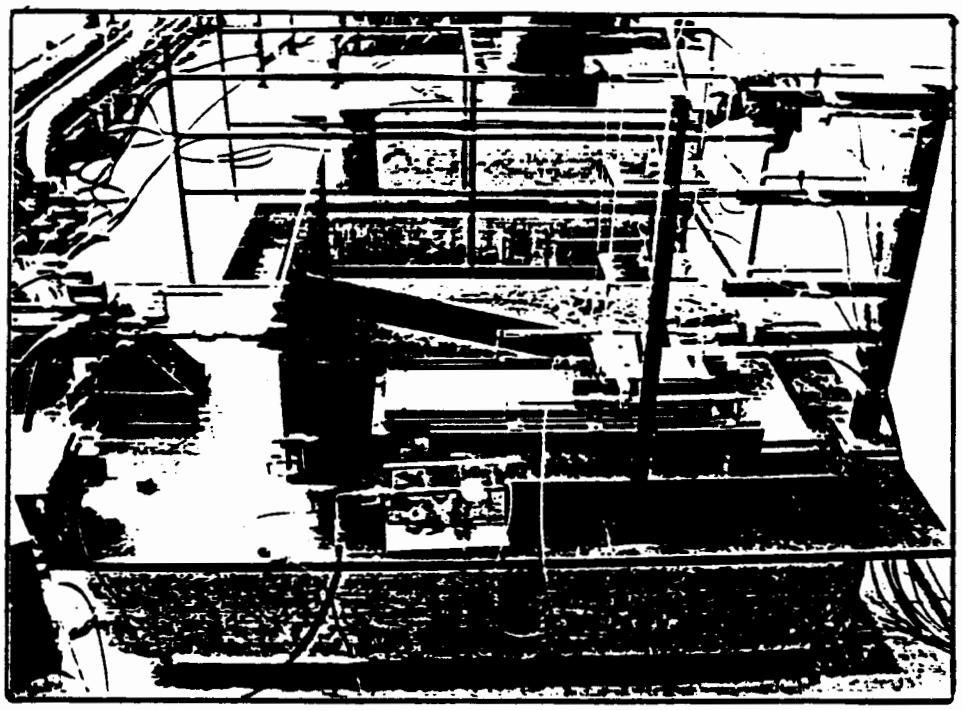

FIGURE 8.3 Test Setup

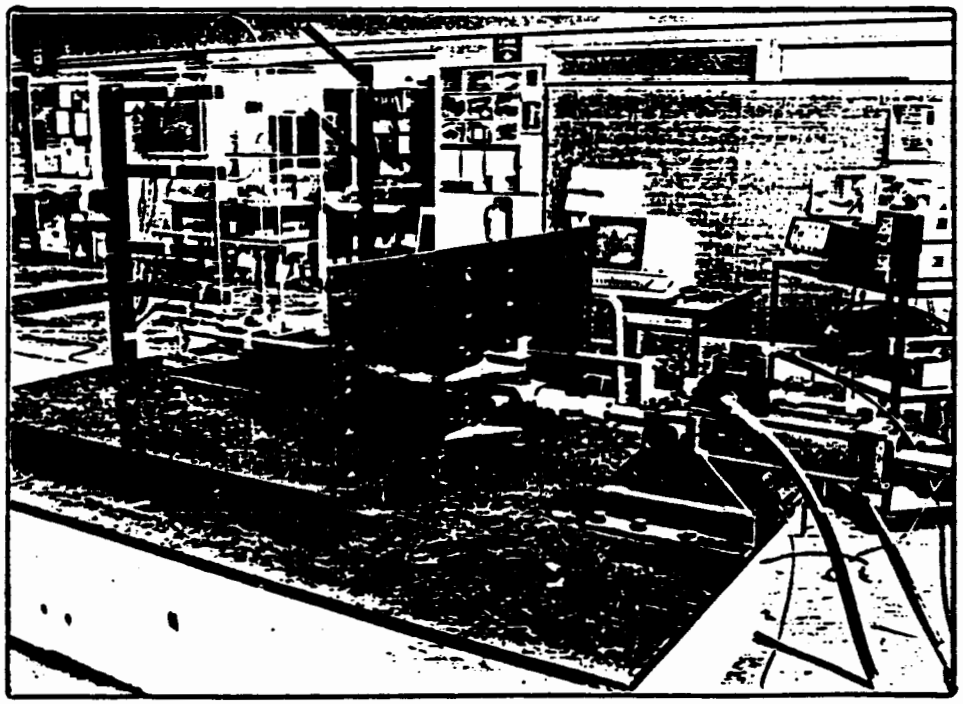

FIGURE 8.4 Test Setup

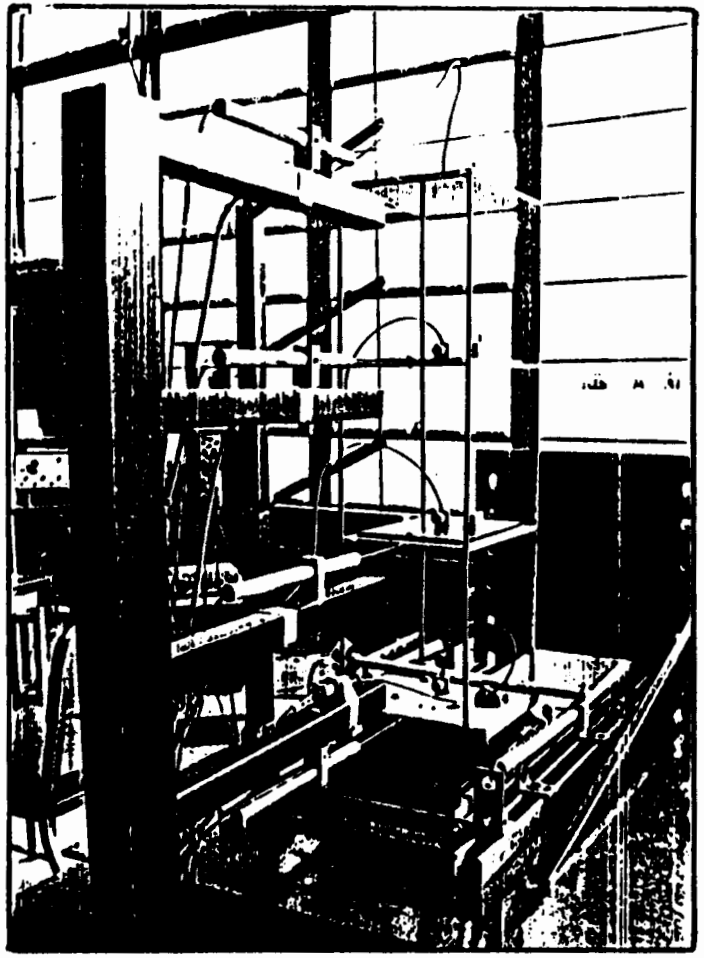

FIGURE 8.5 Base-Isolated Model - SE elevation

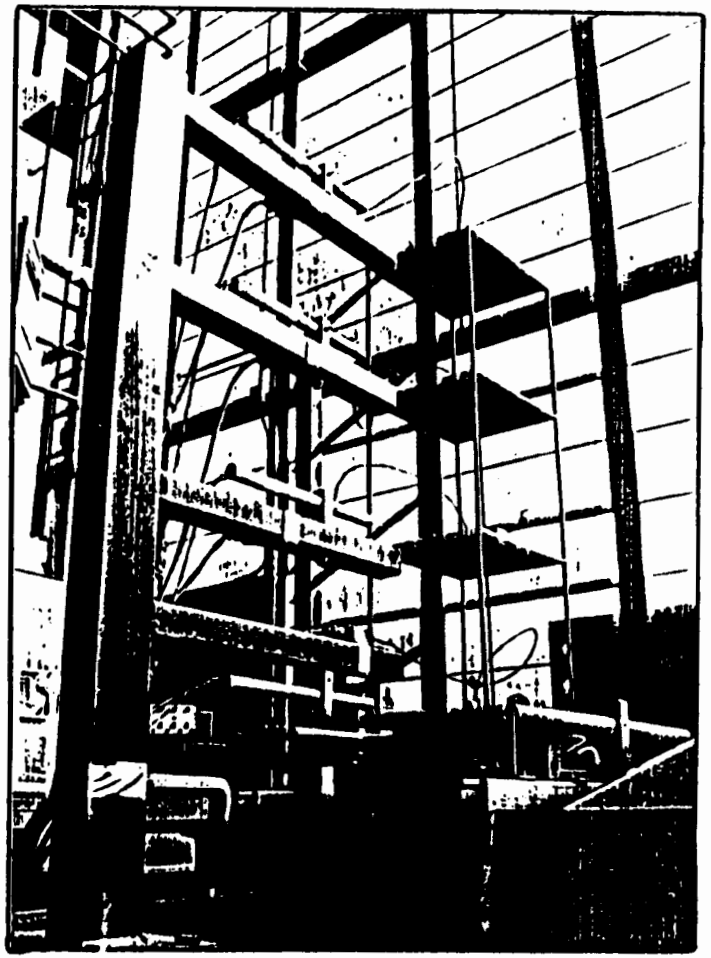

FIGURE 8.6 Base-Isolated Model - SE elevation

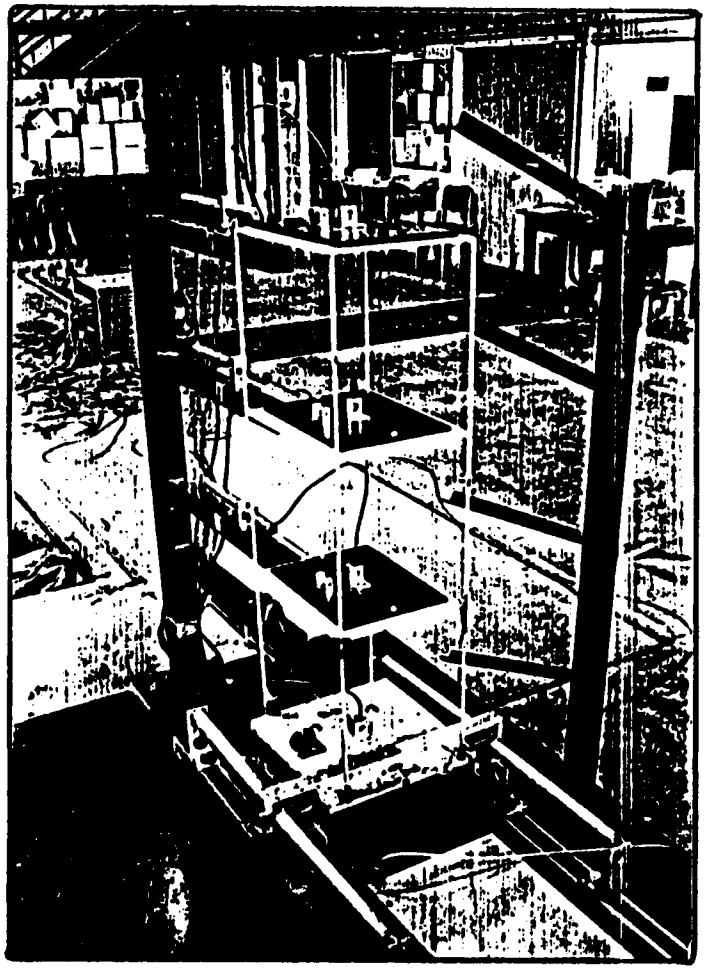

FIGURE 8.7 Base-Isolated Model - NE elevation

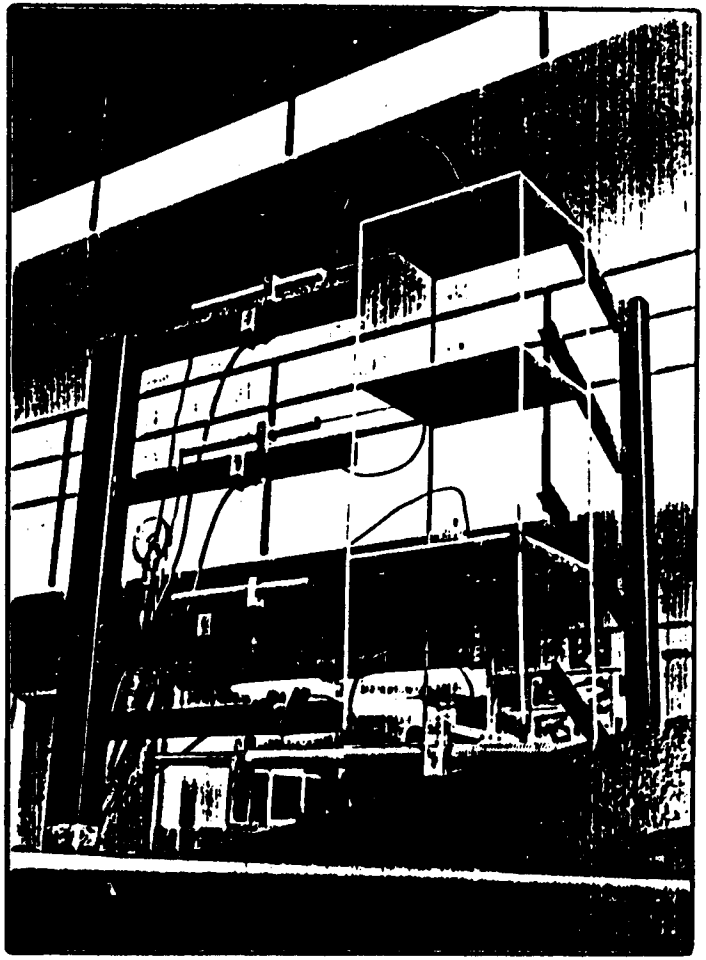

FIGURE 8.8 Base-Isolated Model - NE elevation

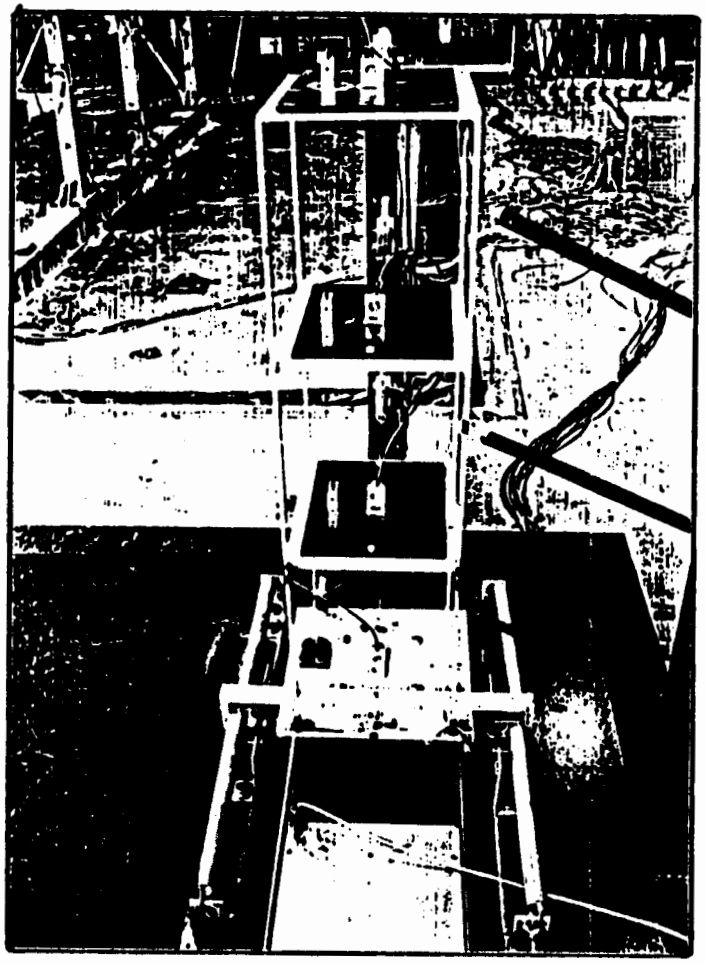

FIGURE 8.9 Base-Isolated Model - N elevation

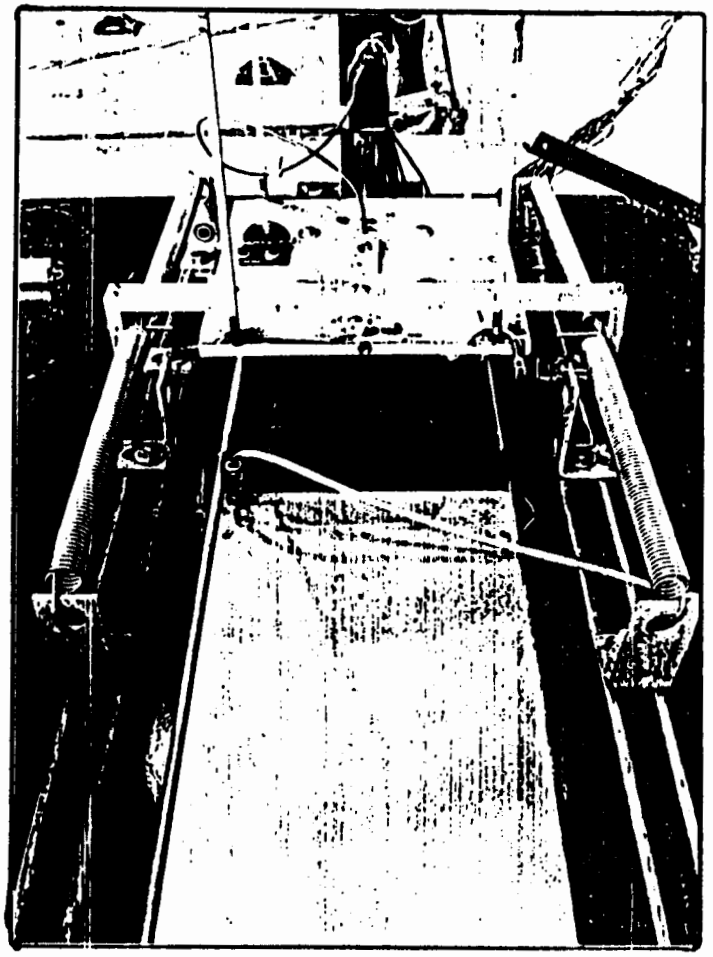

FIGURE 8.10 Spring Isolators - Linear Elastic (#142)

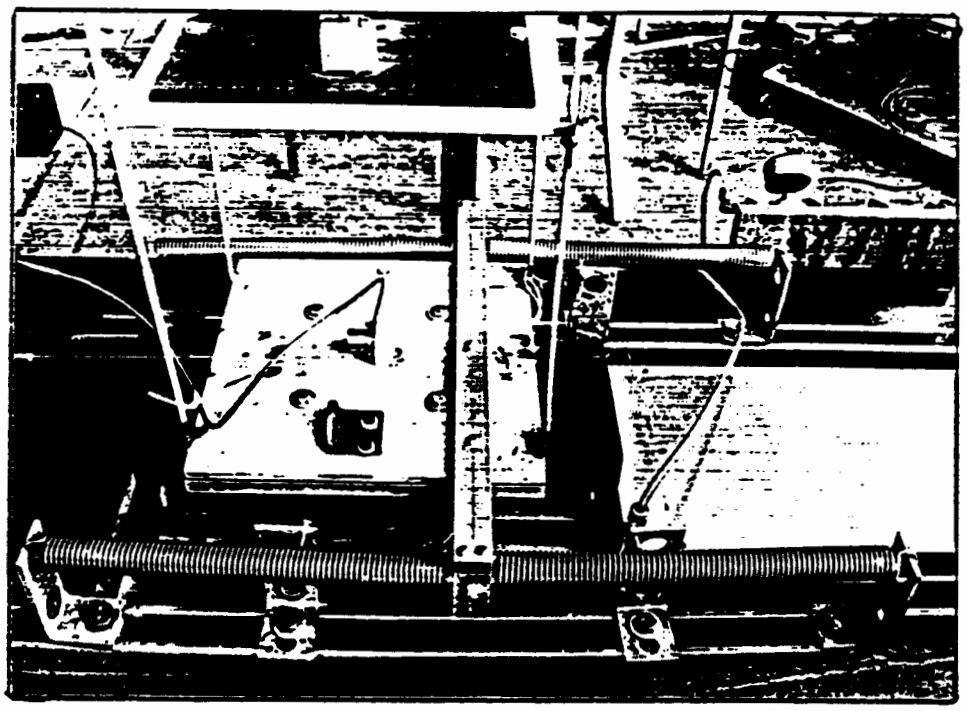

FIGURE 8.11 Spring Isolators - Linear Elastic (#142)

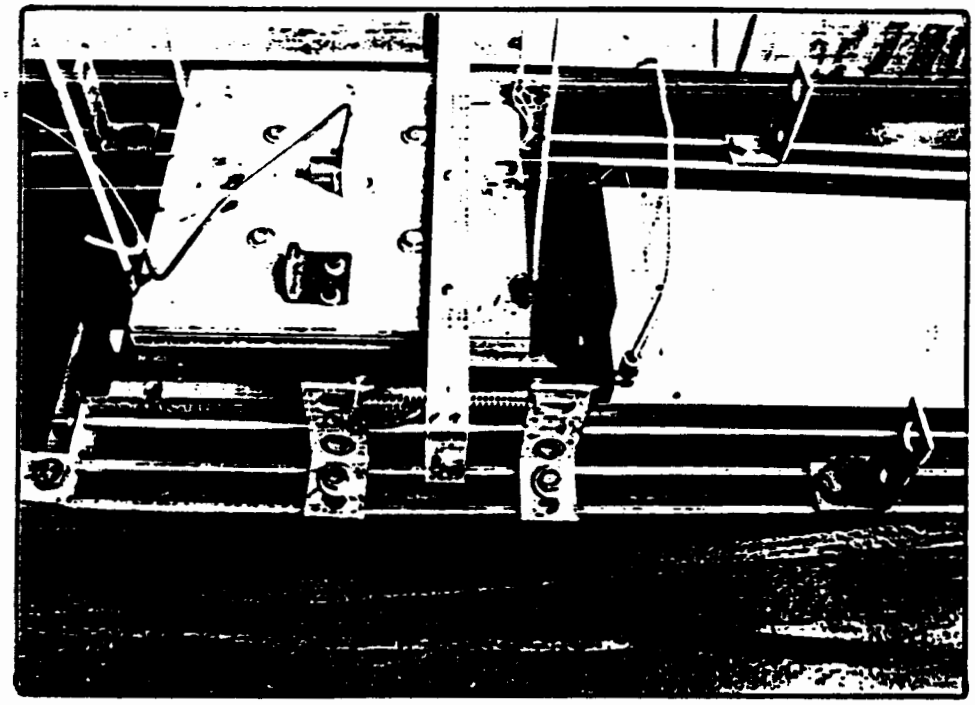

FIGURE 8.12 Spring Isolators - Nitinol (short)

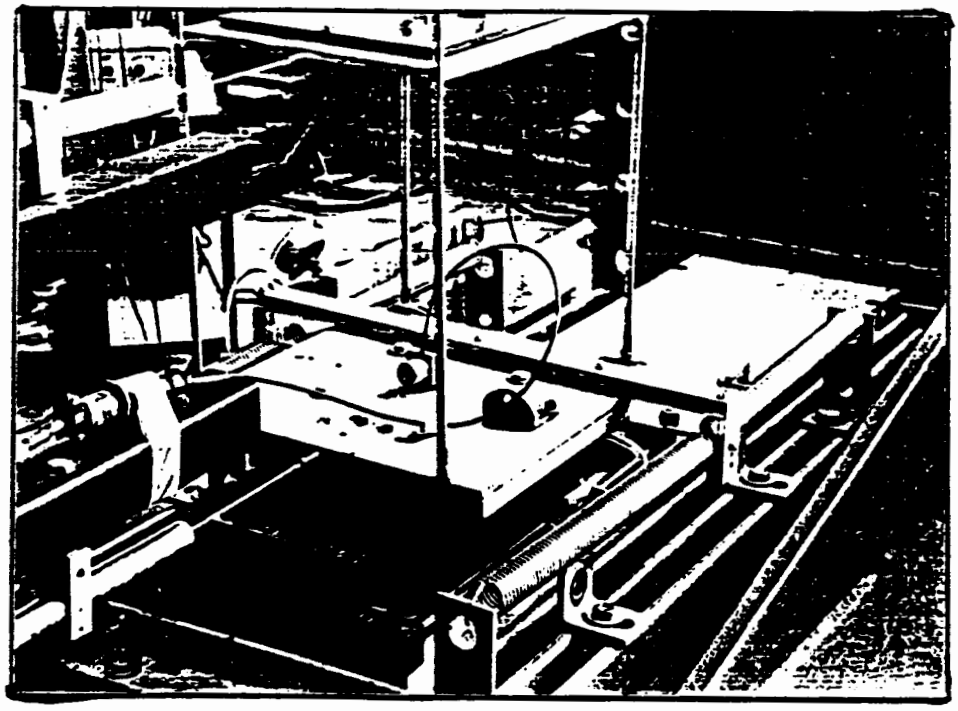

FIGURE 8.13 Spring Isolators - Linear Elastic (#142)

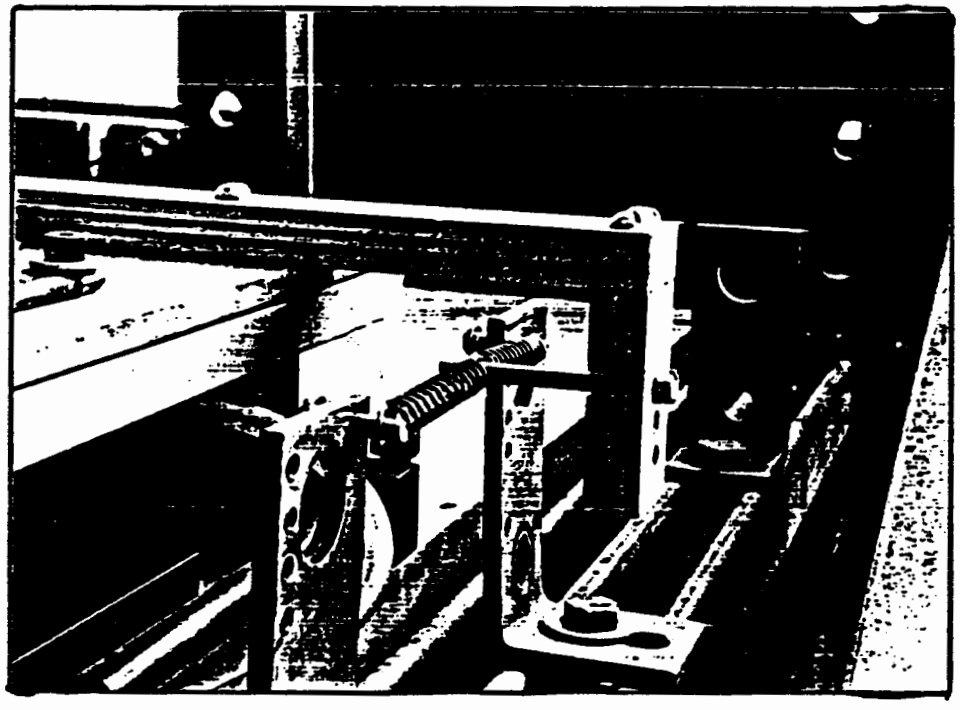

FIGURE 8.14 Spring Isolators - Nitinol (short)

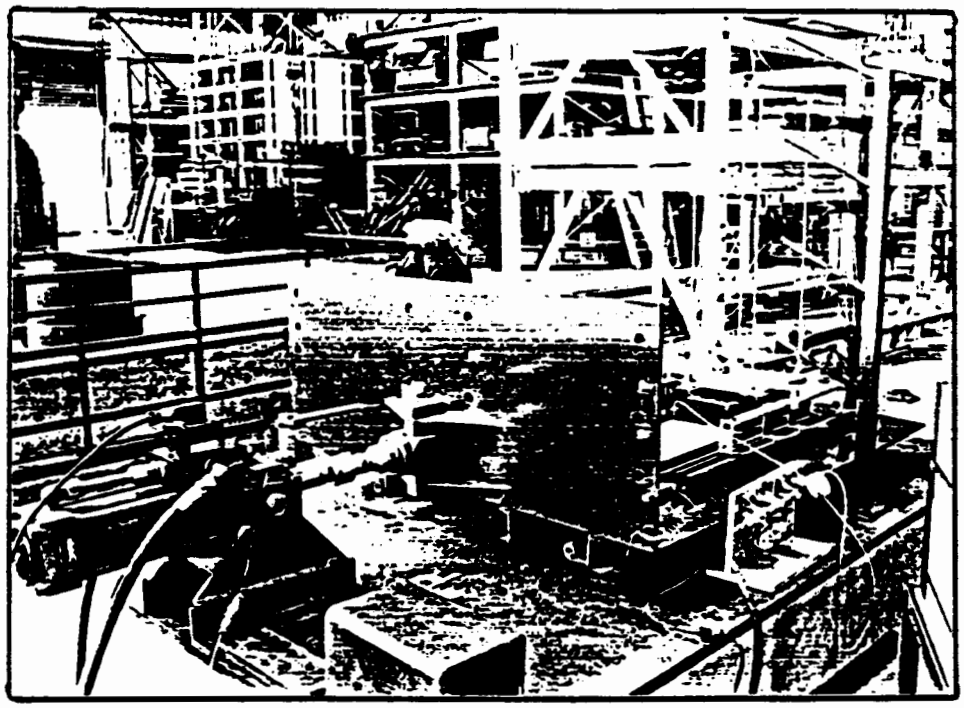

FIGURE 8.15 Hydraulic Actuator

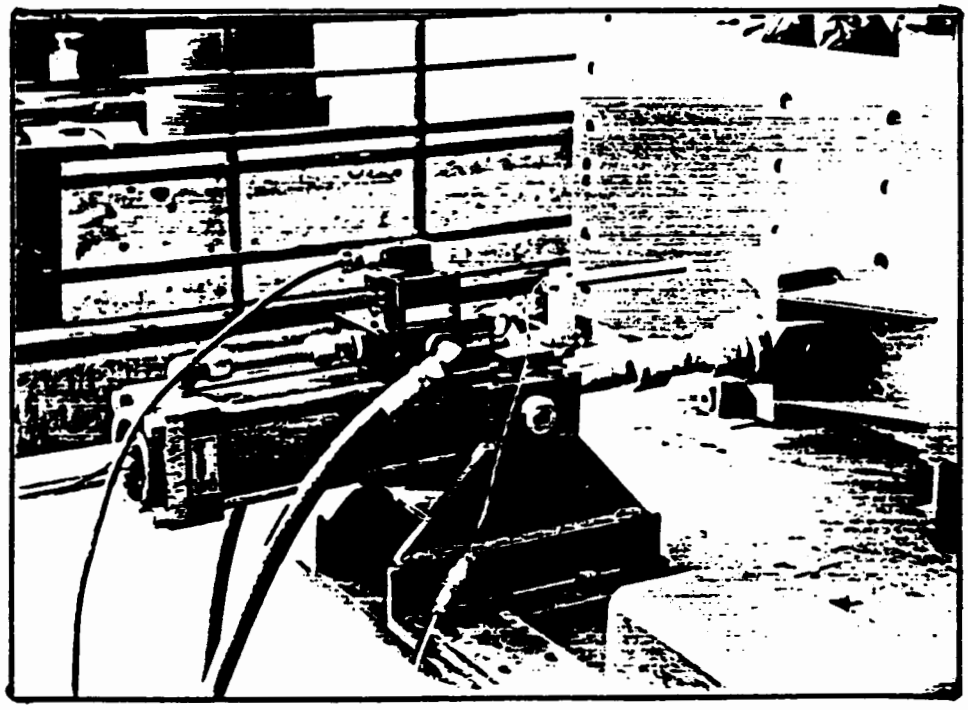

FIGURE 8.16 Hydraulic Actuator

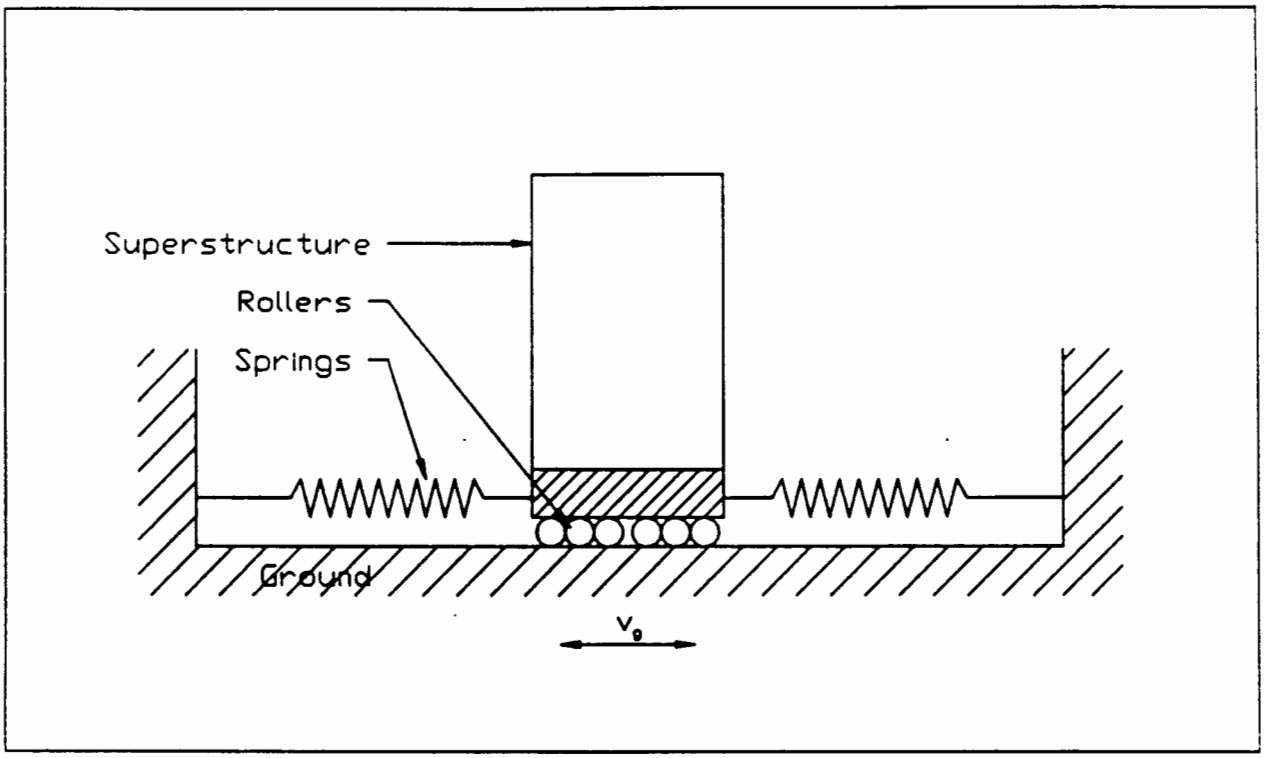

Figure 8.17 Theoretical Base Isolation Model

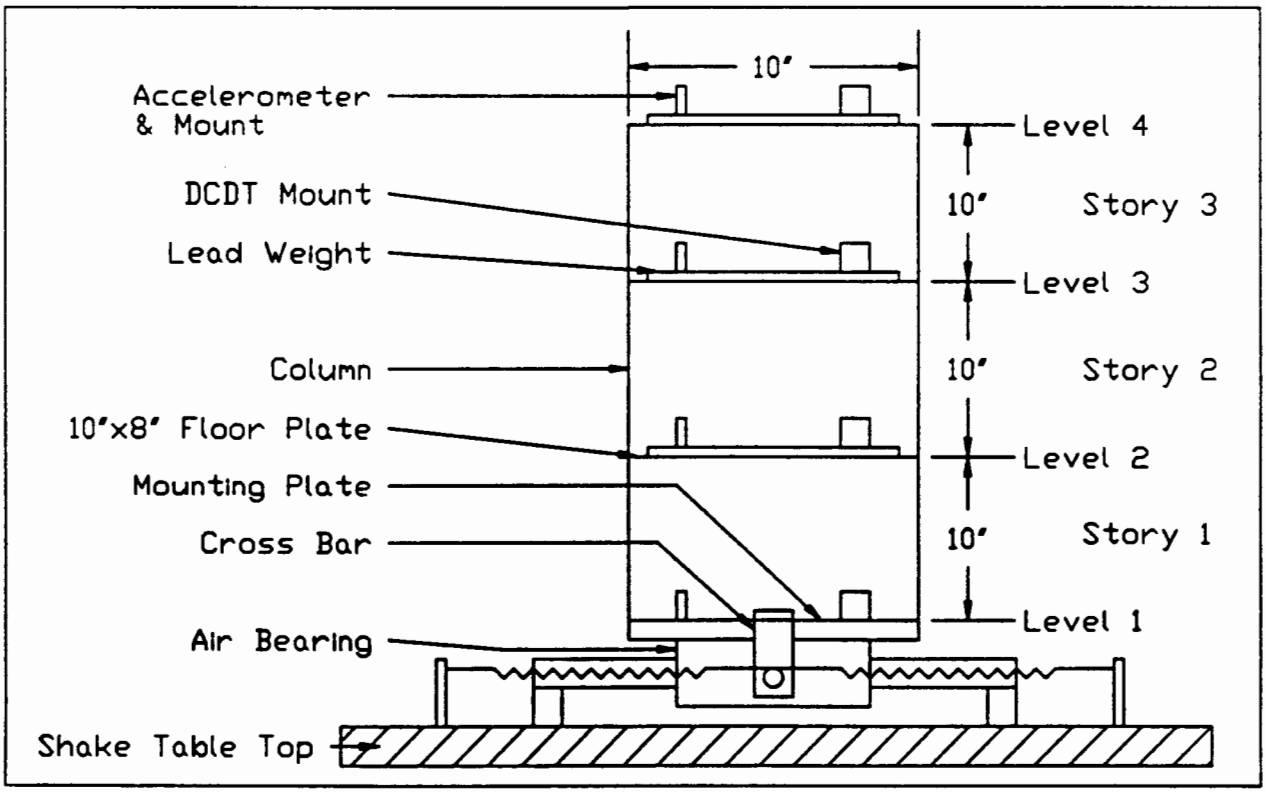

Figure 8.18 Experimental Base Isolation Model
West Elevation

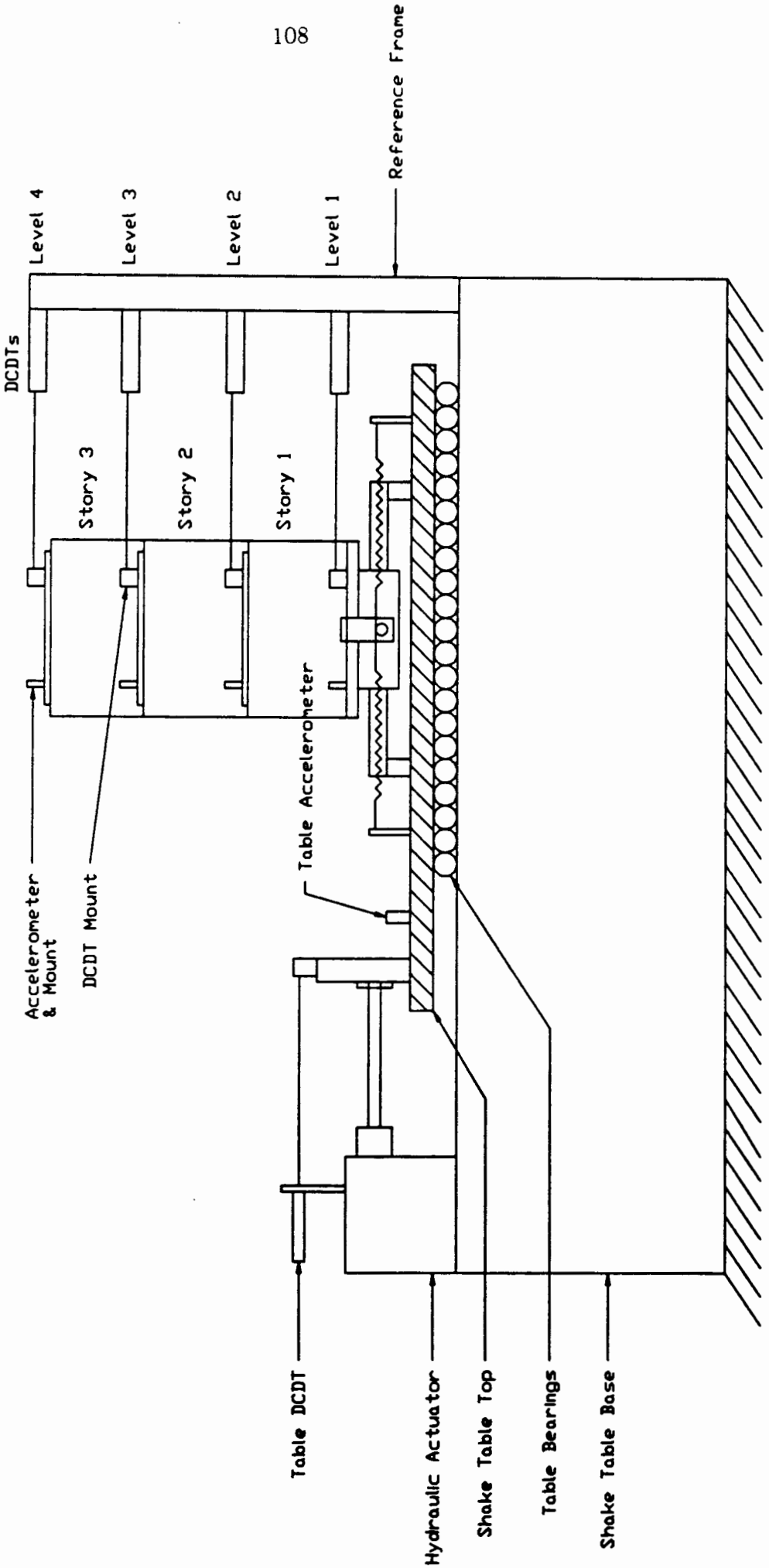

Figure 8.19 Shake Table and Instrumentation - W. Elevation

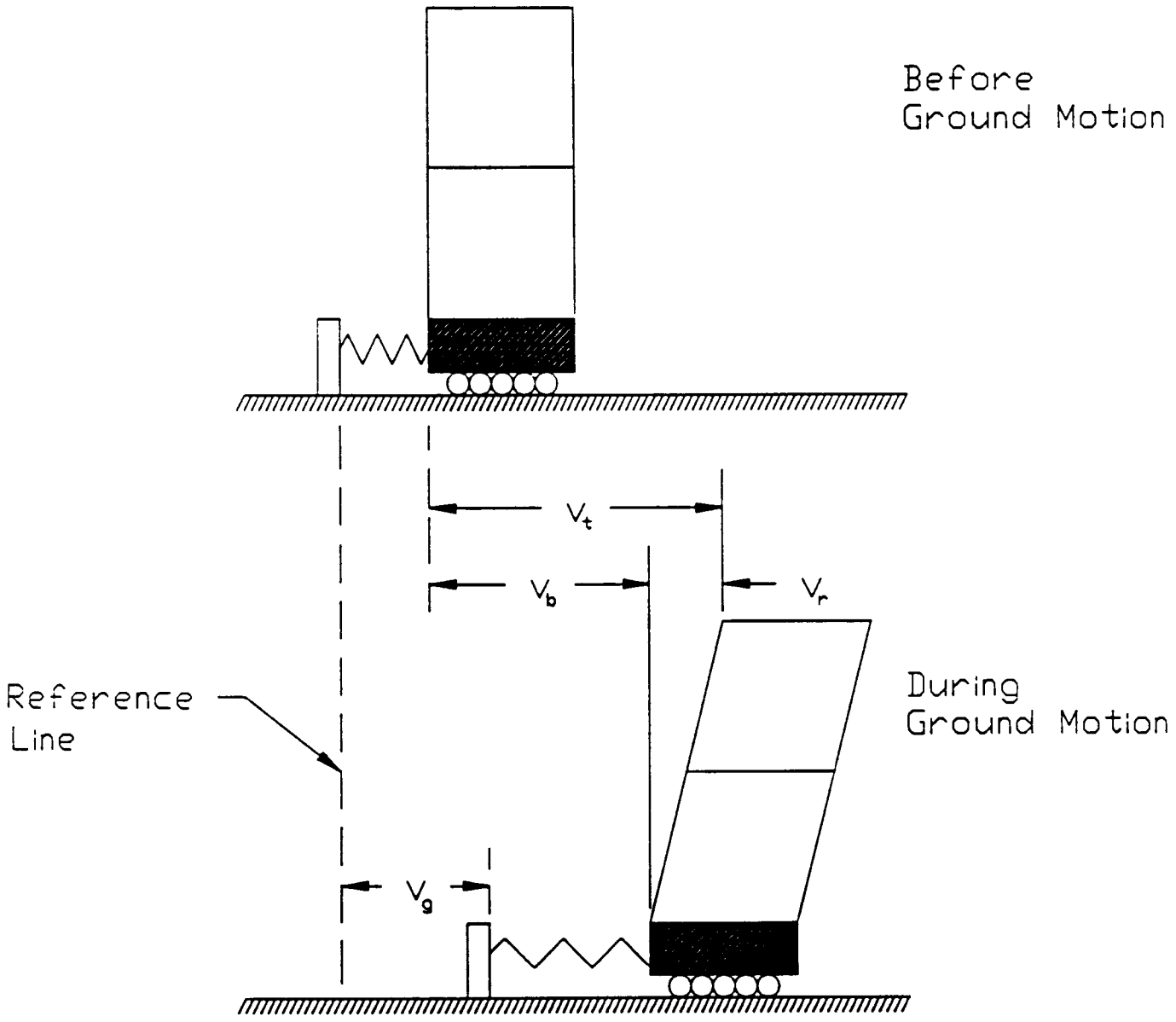

Figure 8.20 Displacement Quantities

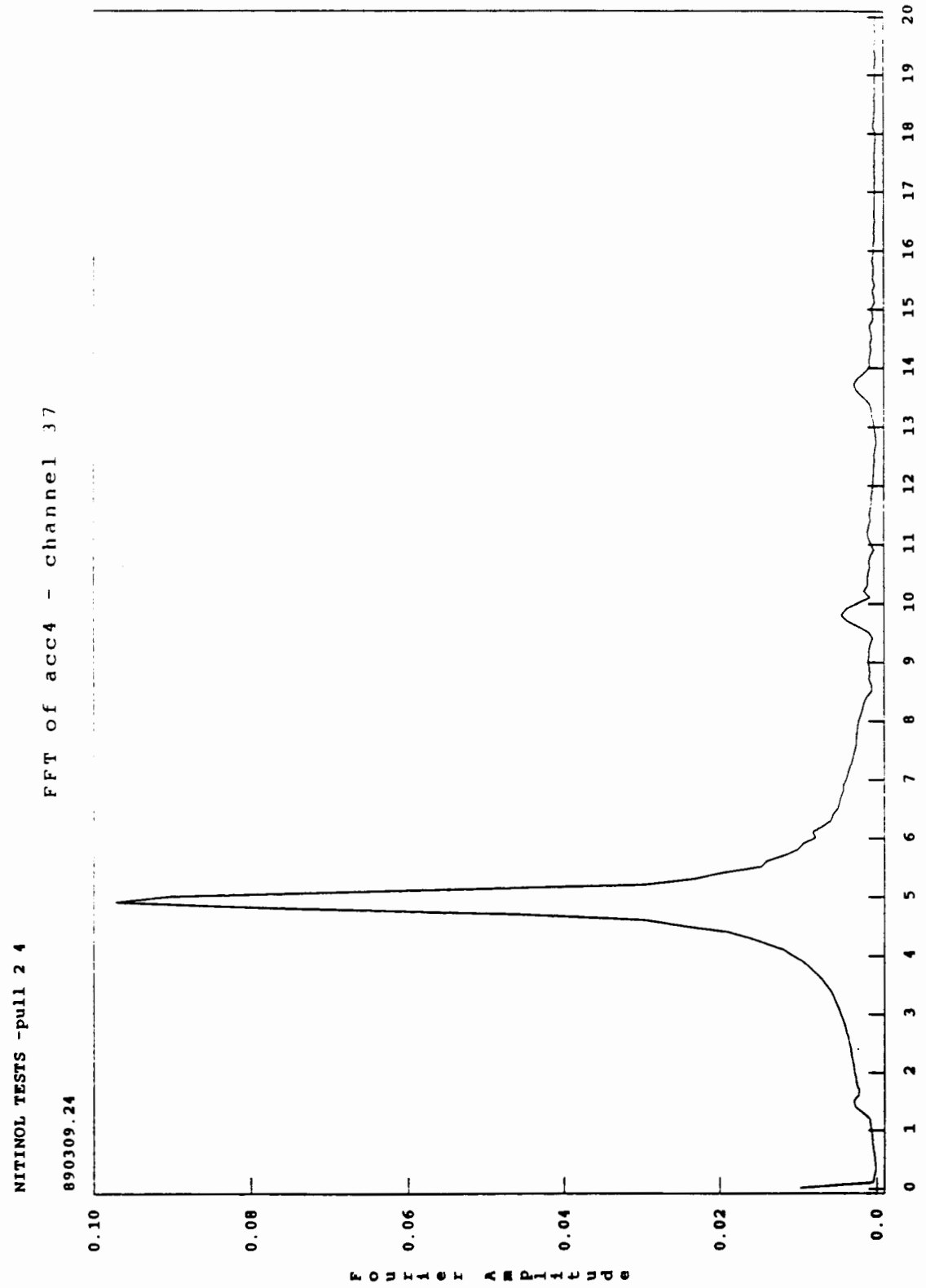

FIGURE 8.21 FFT of Level 4 Acceleration

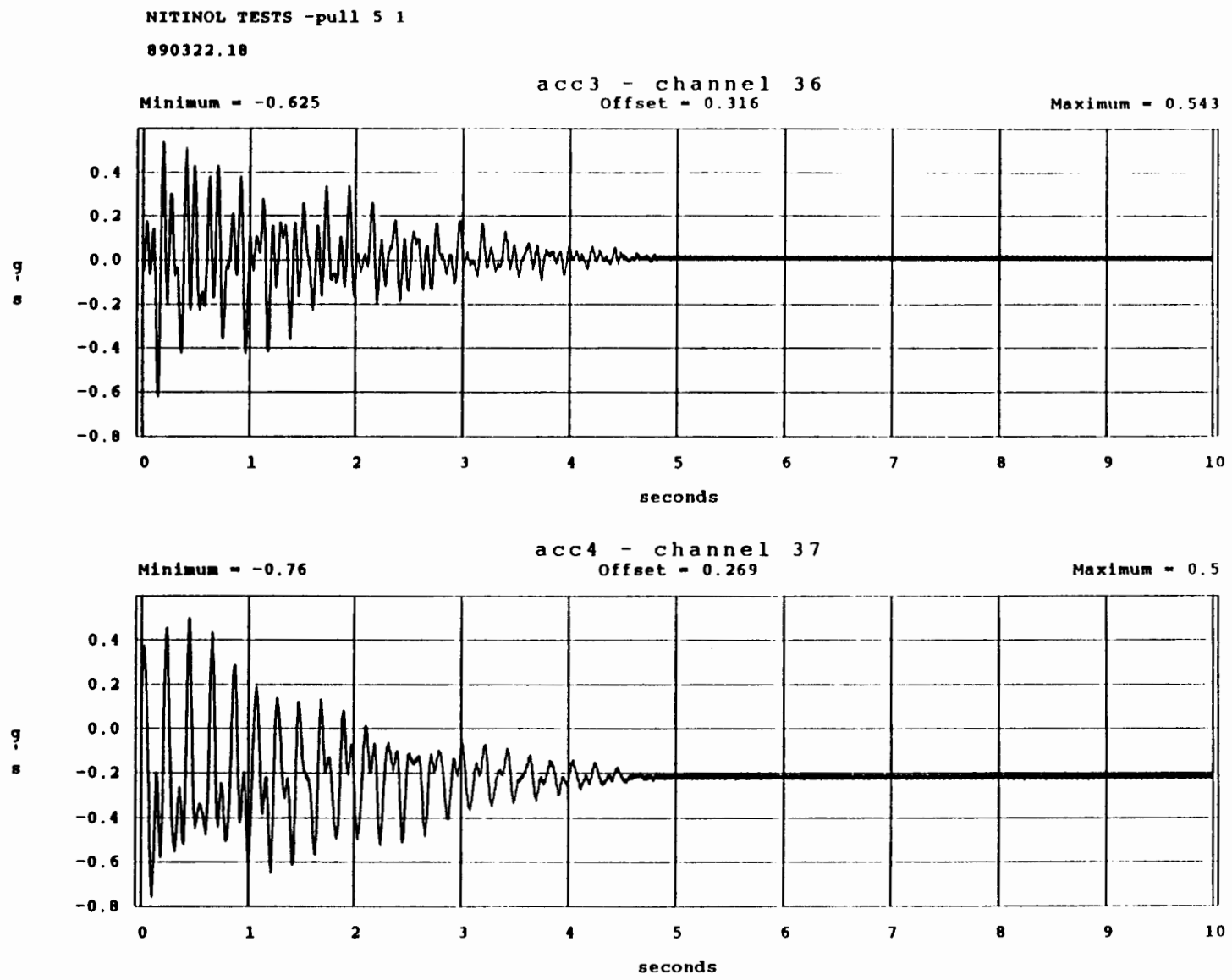

FIGURE 8.22 Acceleration Time Histories - Levels 3 & 4

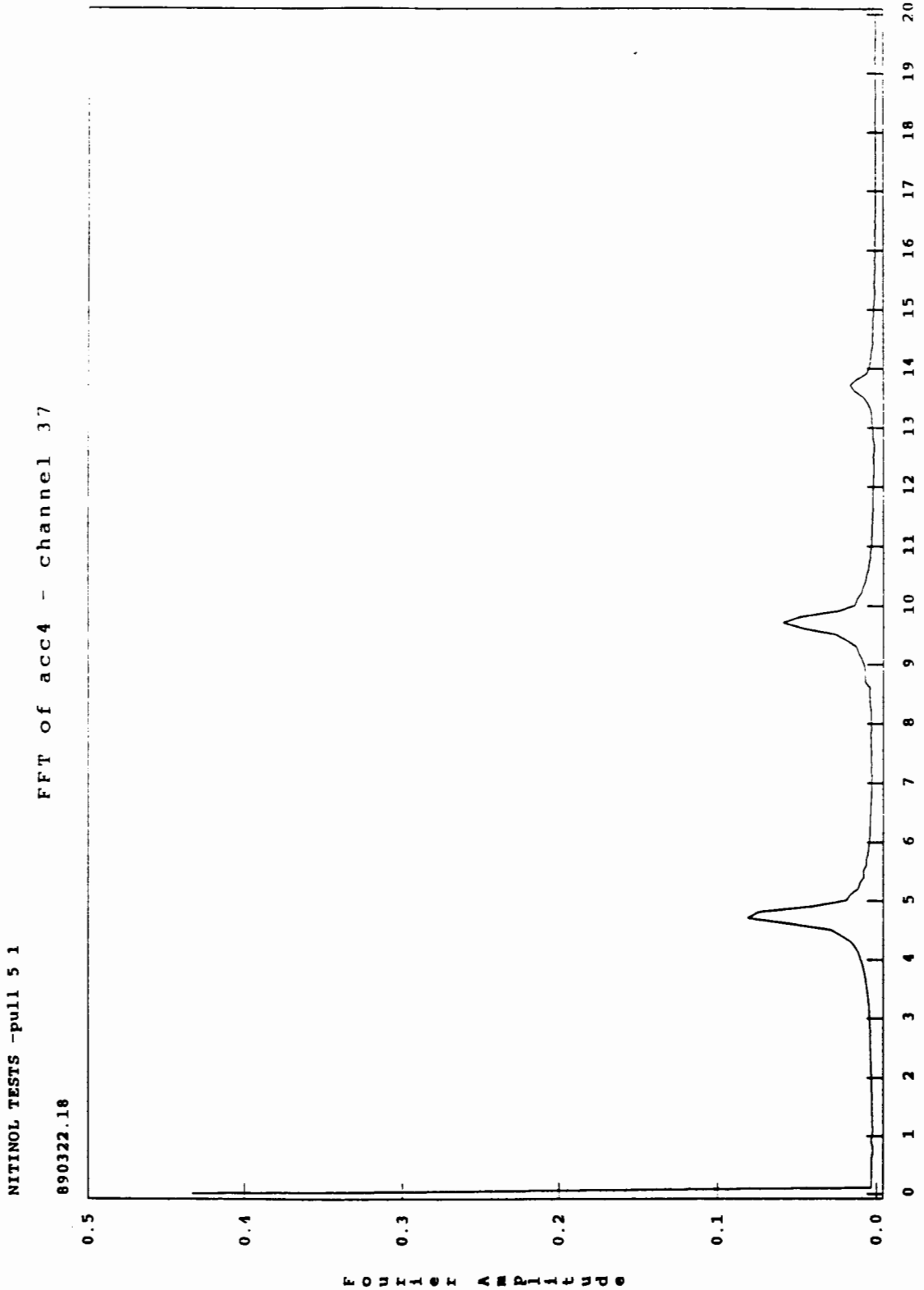

FIGURE 8.23 FFT of Level 4 Acceleration

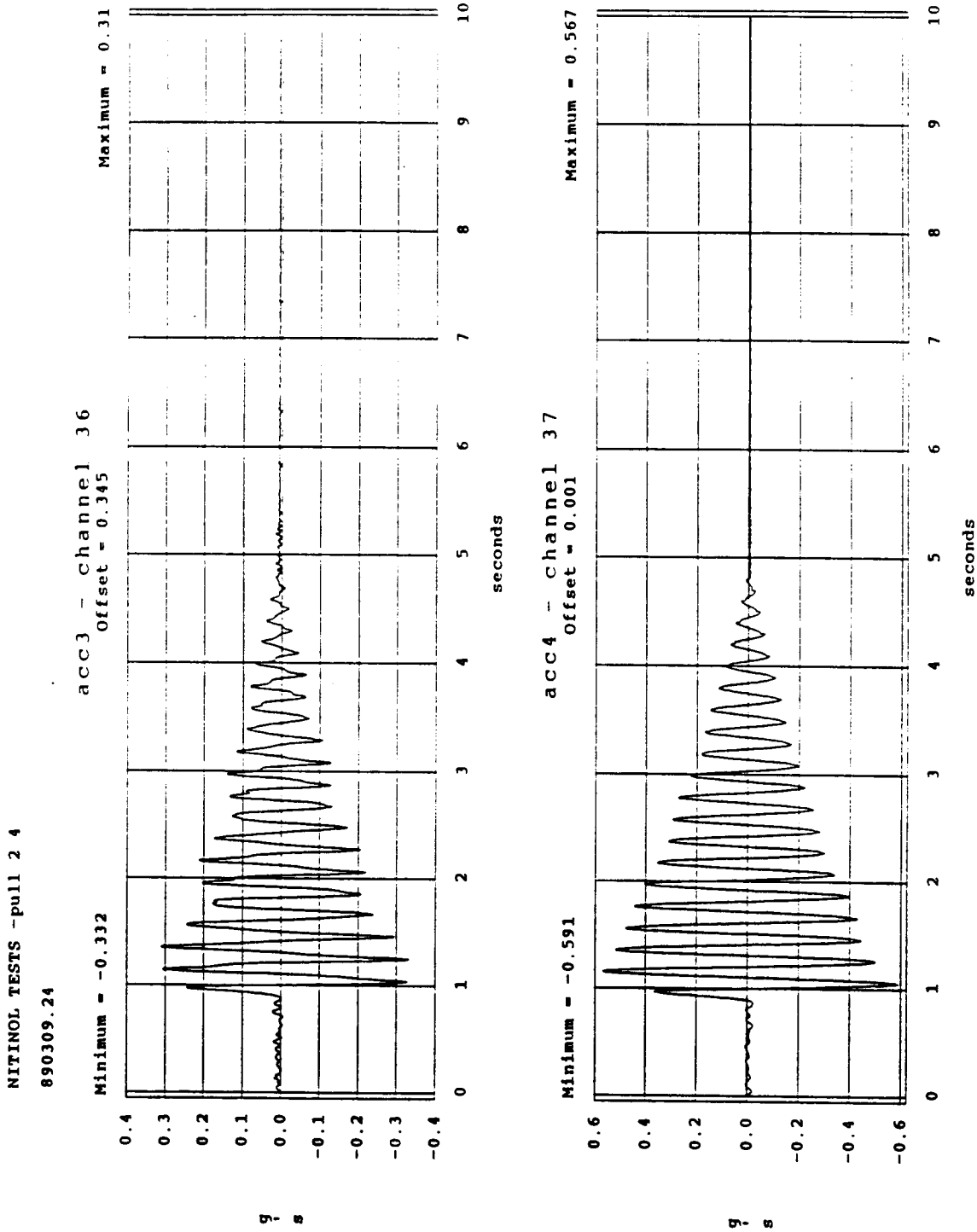

FIGURE 8.24 Acceleration Time Histories - Levels 3 & 4

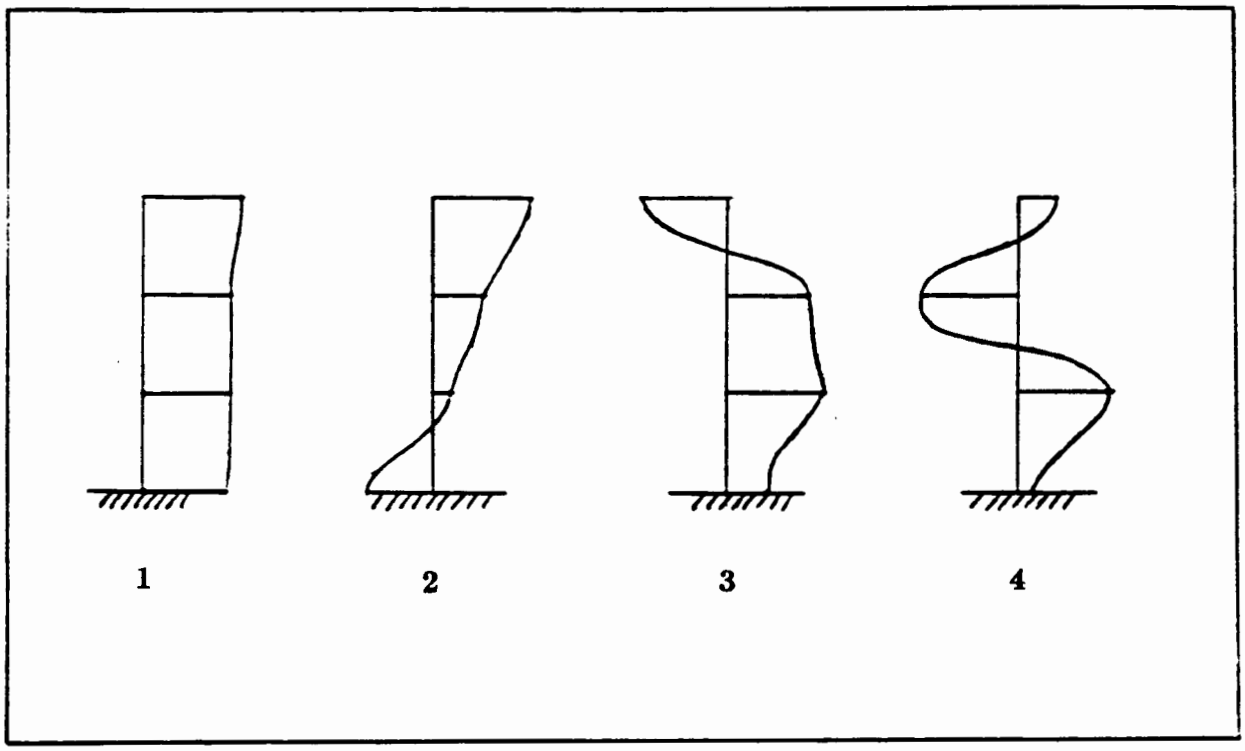

FIGURE 8.25 Experimental Mode Shapes - System 1

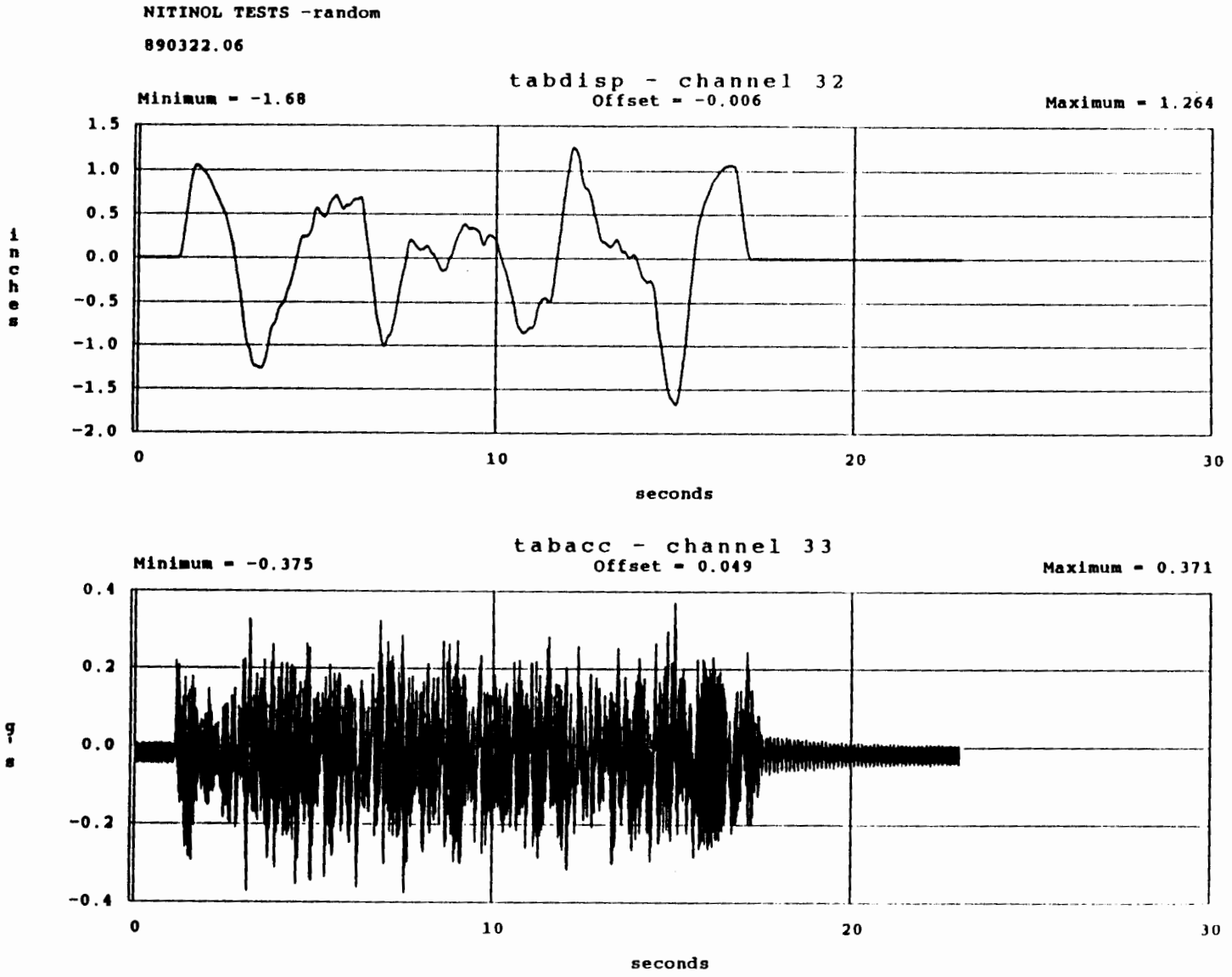

FIGURE 8.26 Time History of Table Displacement and Acceleration - Random Noise

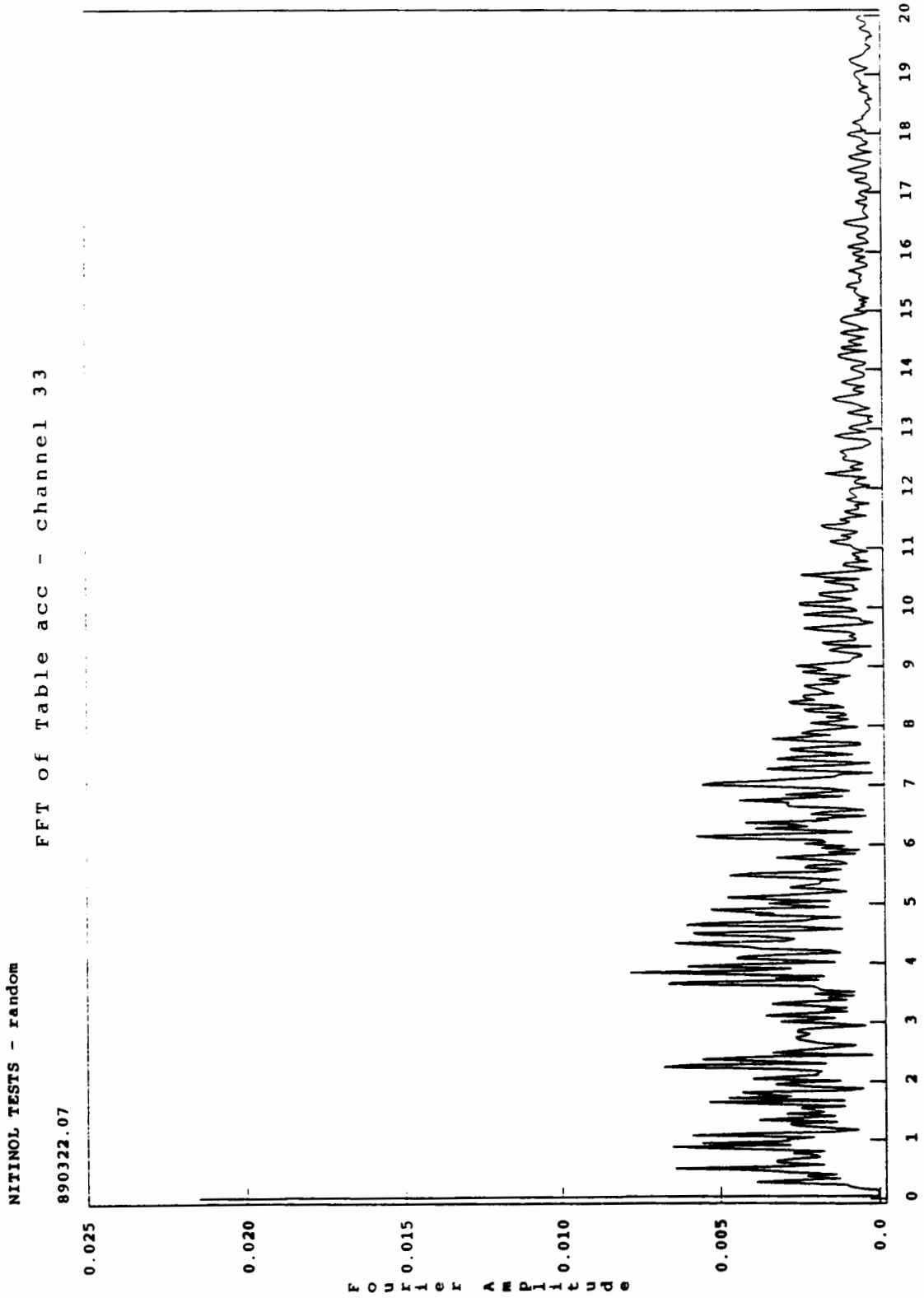

FIGURE 8.27 FFT of Table Acceleration - Random Noise

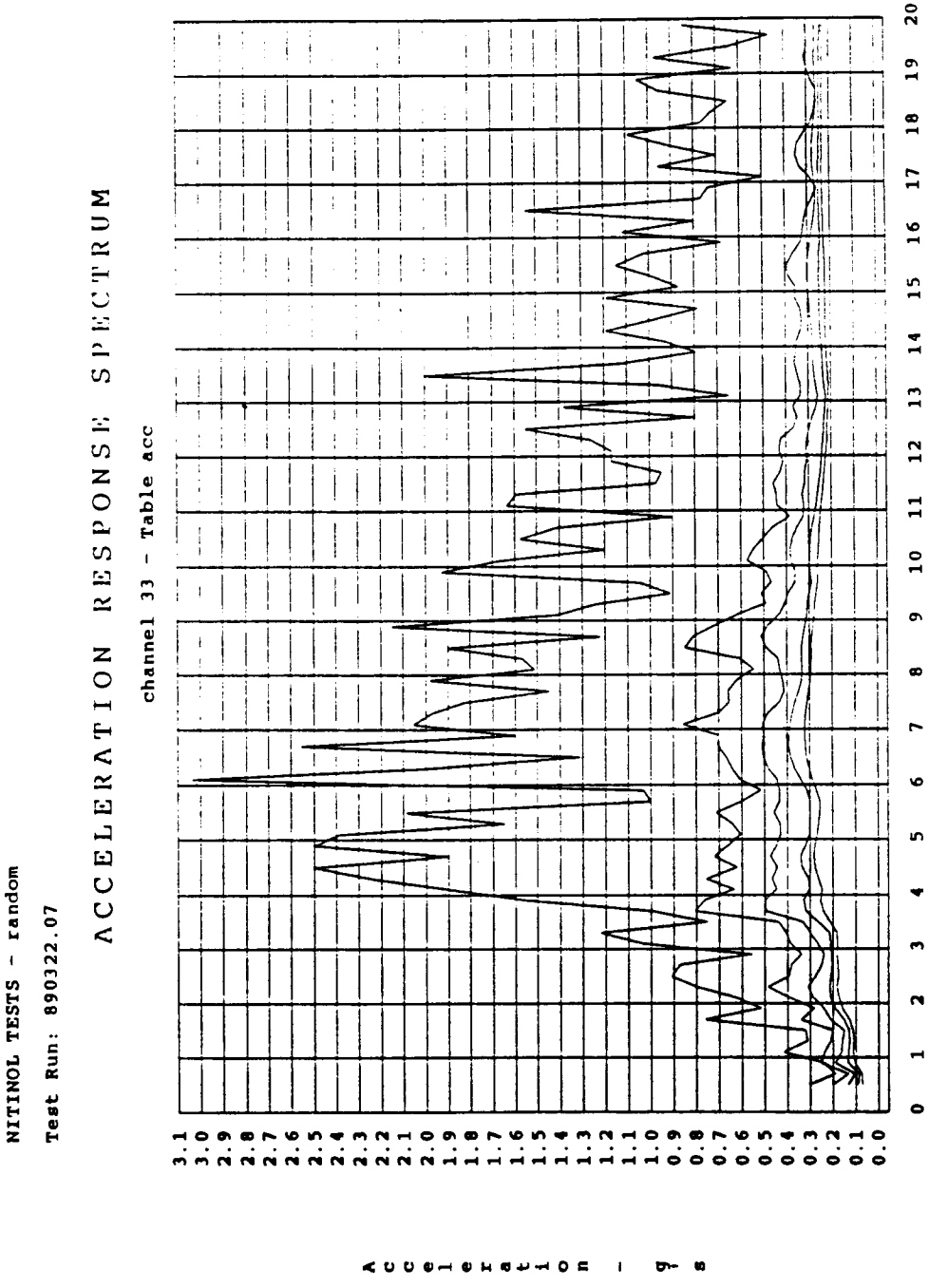

FIGURE 8.28 Elastic Acceleration Response Spectrum - Random Noise

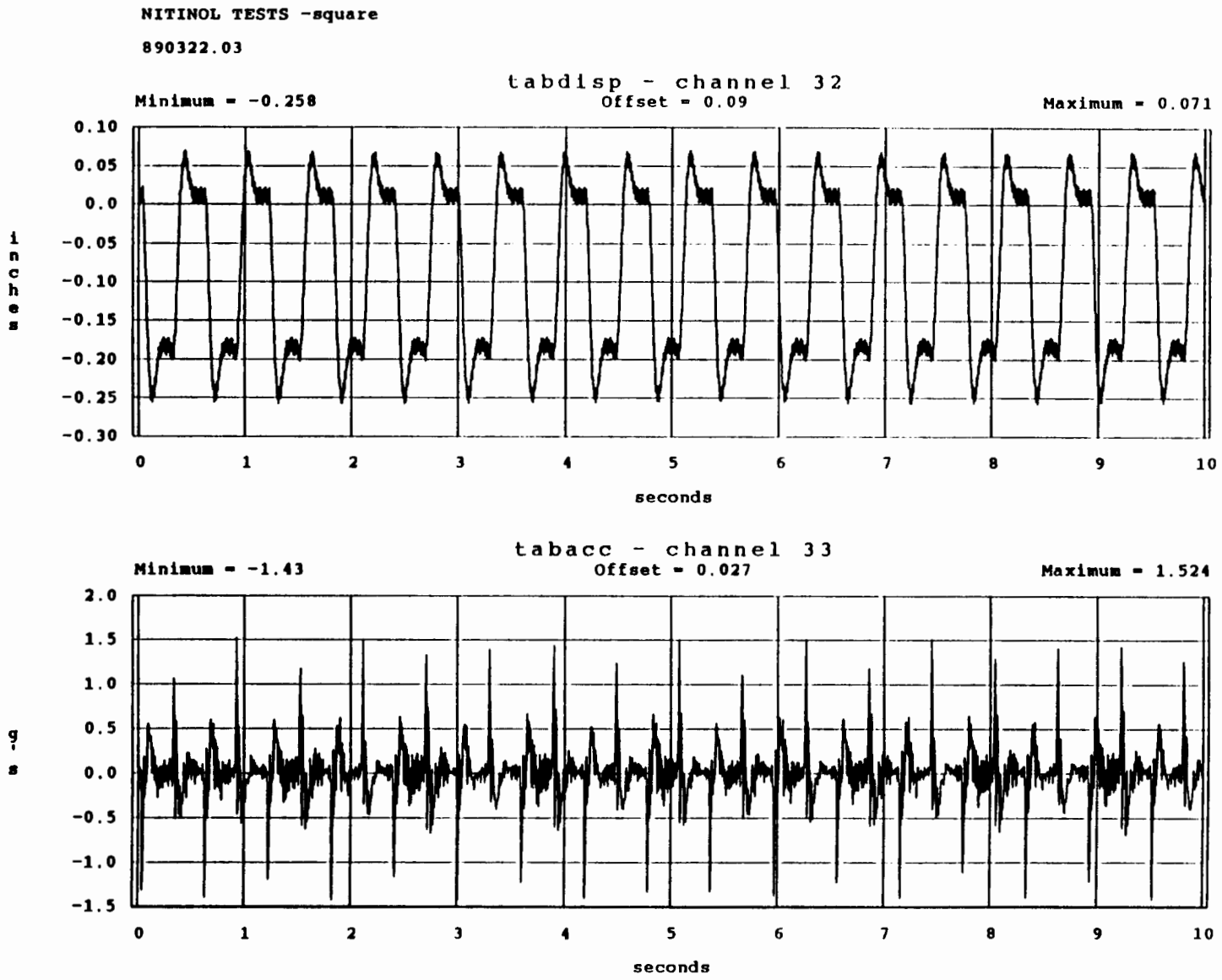

FIGURE 8.29 Time History of Table Displacement and Acceleration - Square Wave

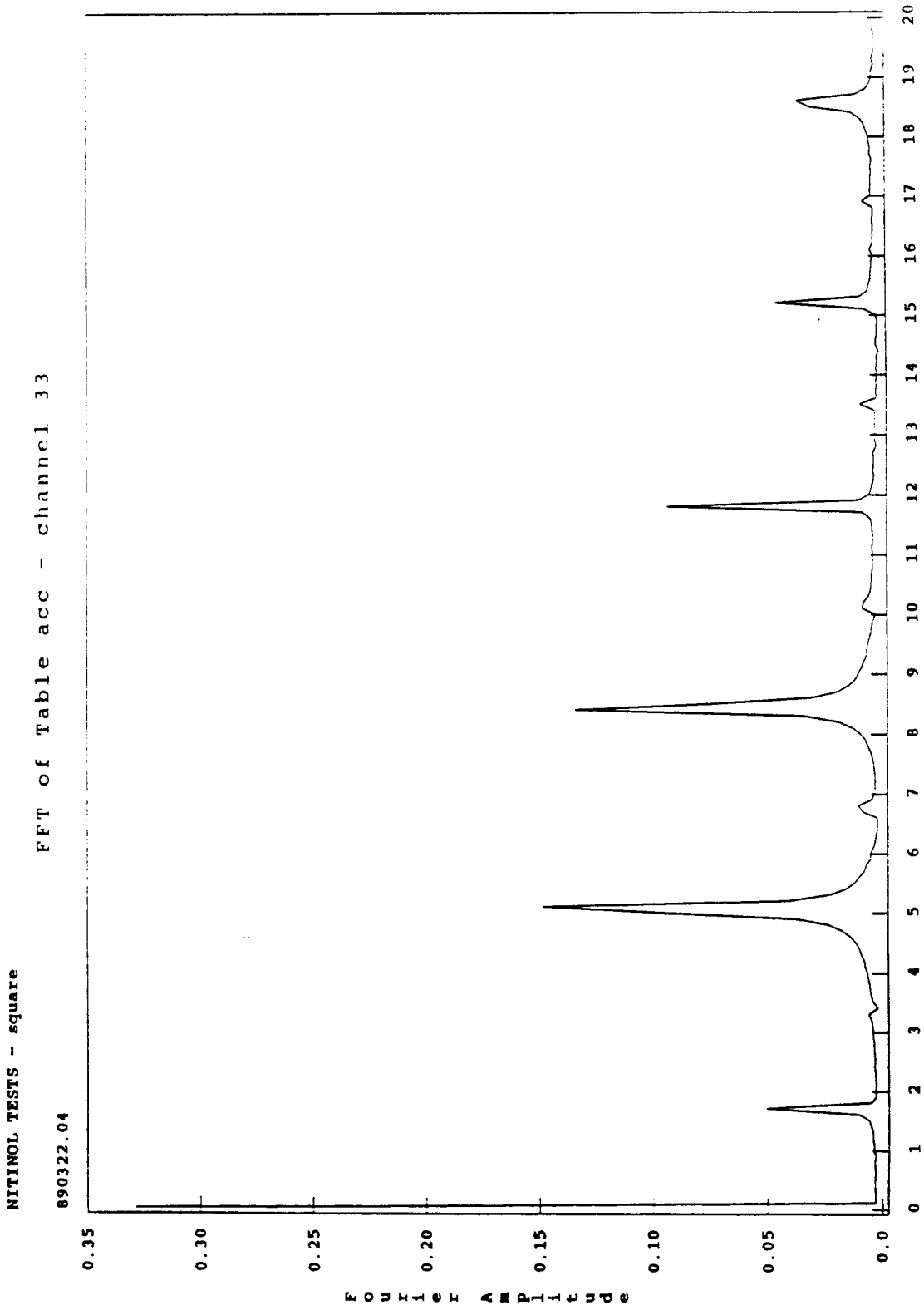

FIGURE 8.30 FFT of Table Acceleration - Square Wave

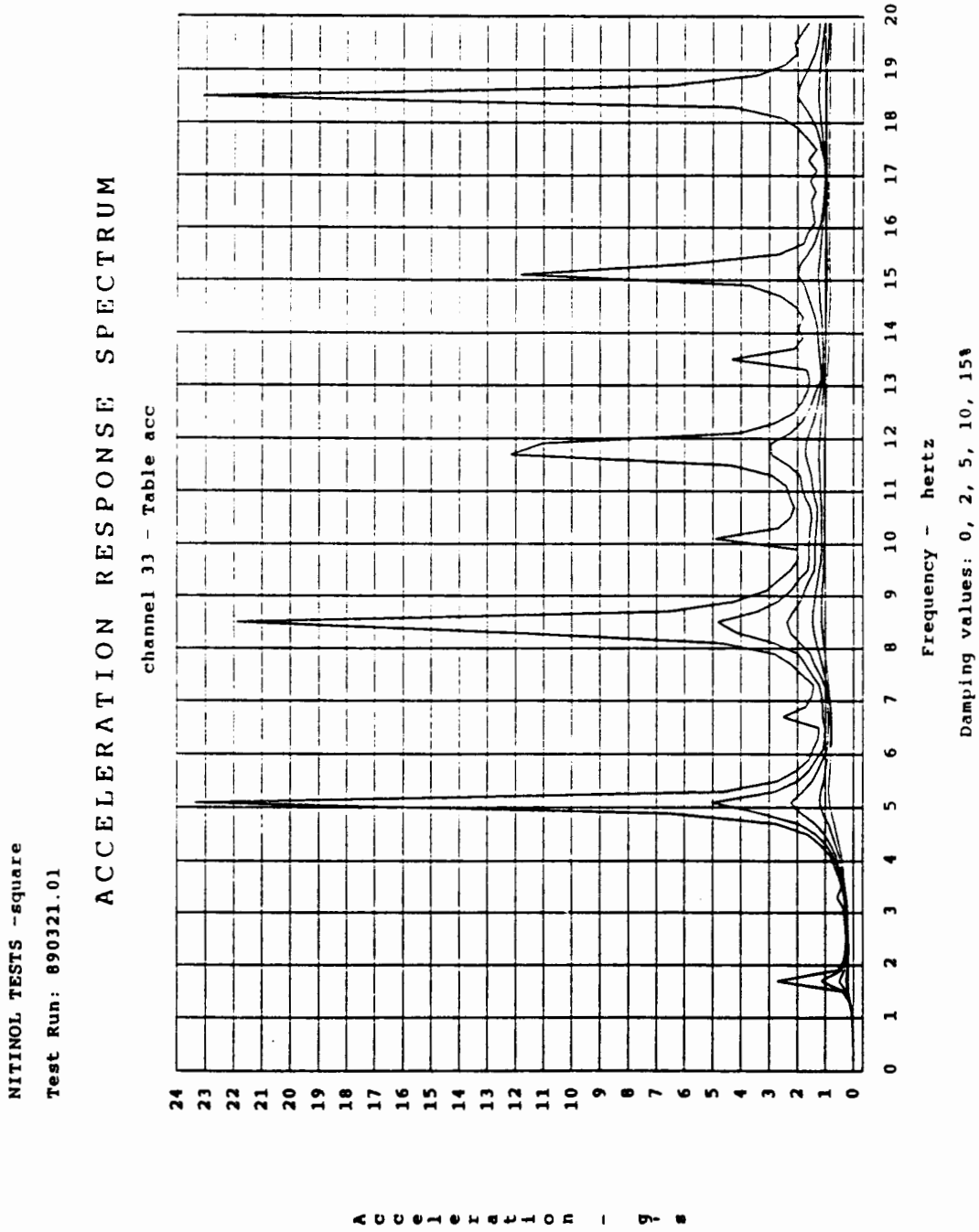

FIGURE 8.31 Elastic Acceleration Response Spectrum - Square Wave

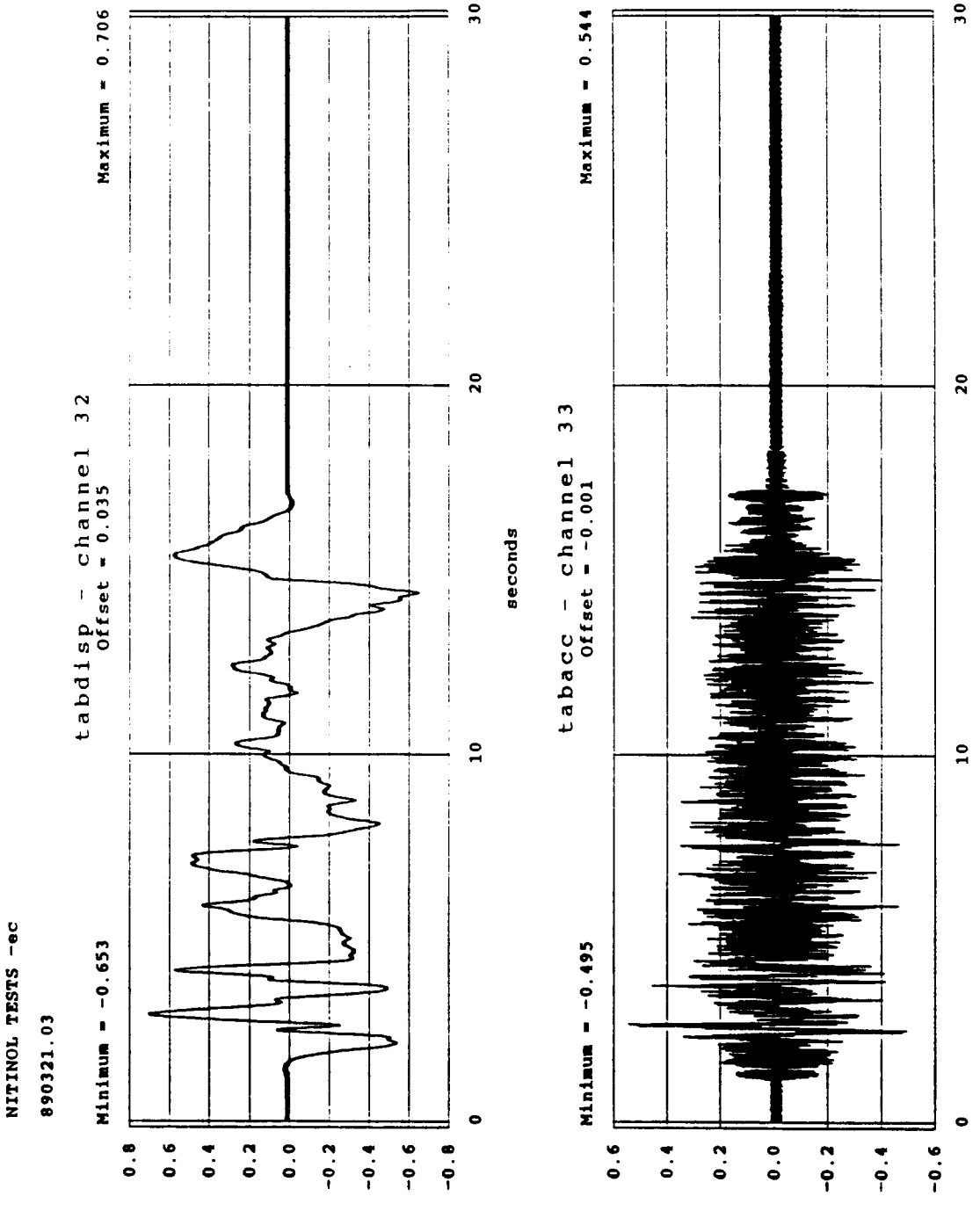

FIGURE 8.32 Time History of Table Displacement and Acceleration - El Centro

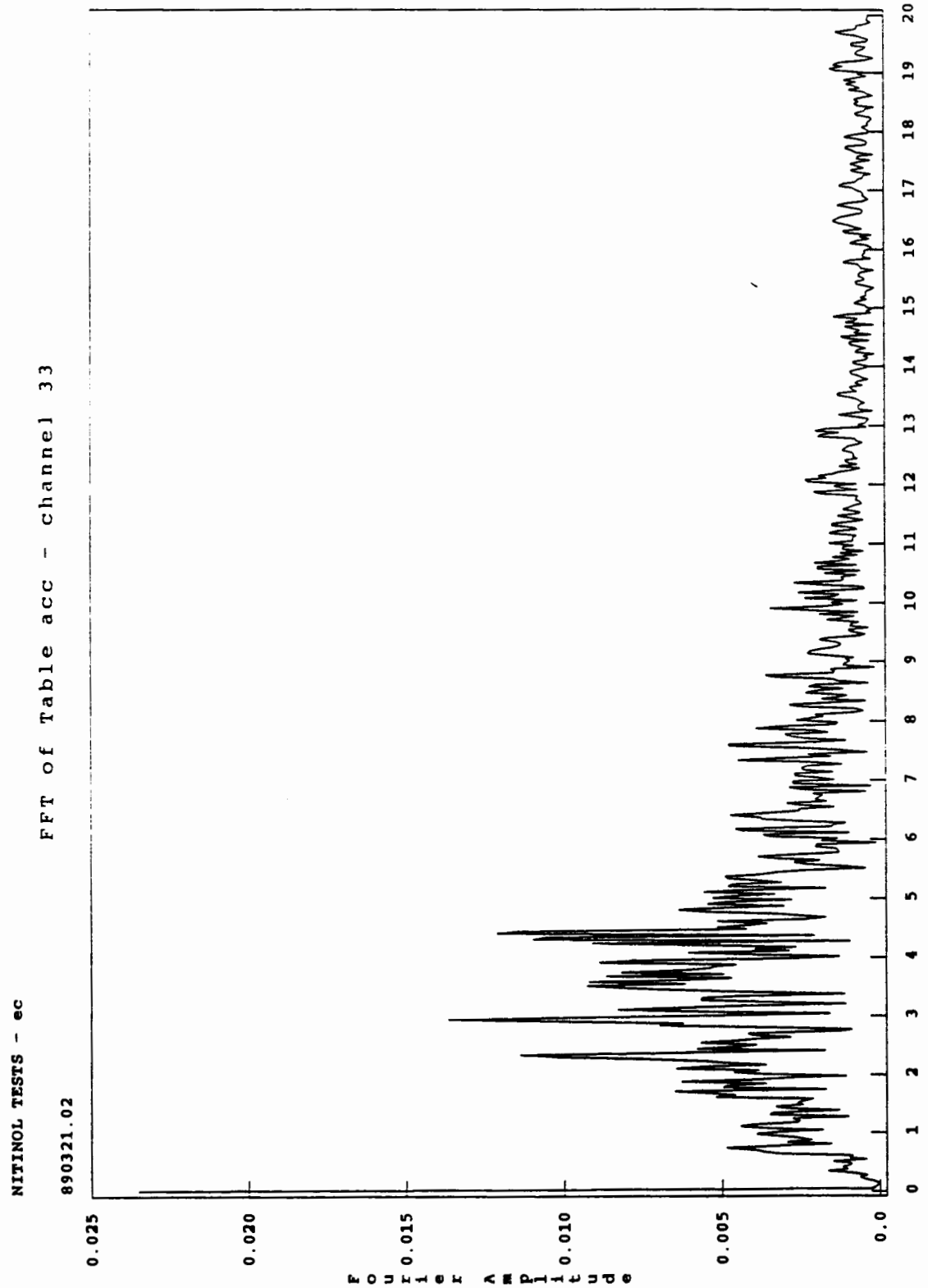

FIGURE 8.33 FFT of Table Acceleration - El Centro

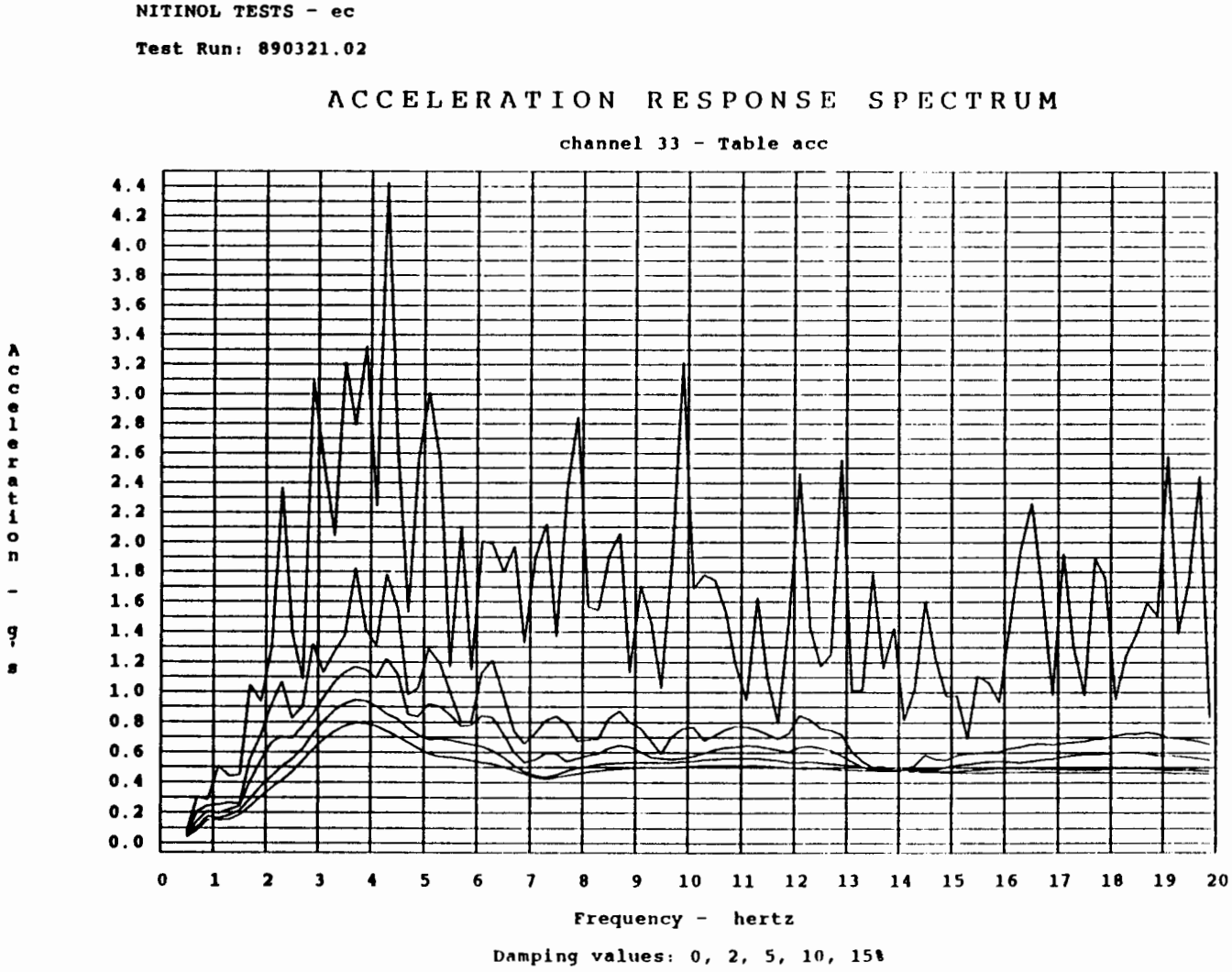

FIGURE 8.34 Elastic Acceleration Response Spectrum - El Centro

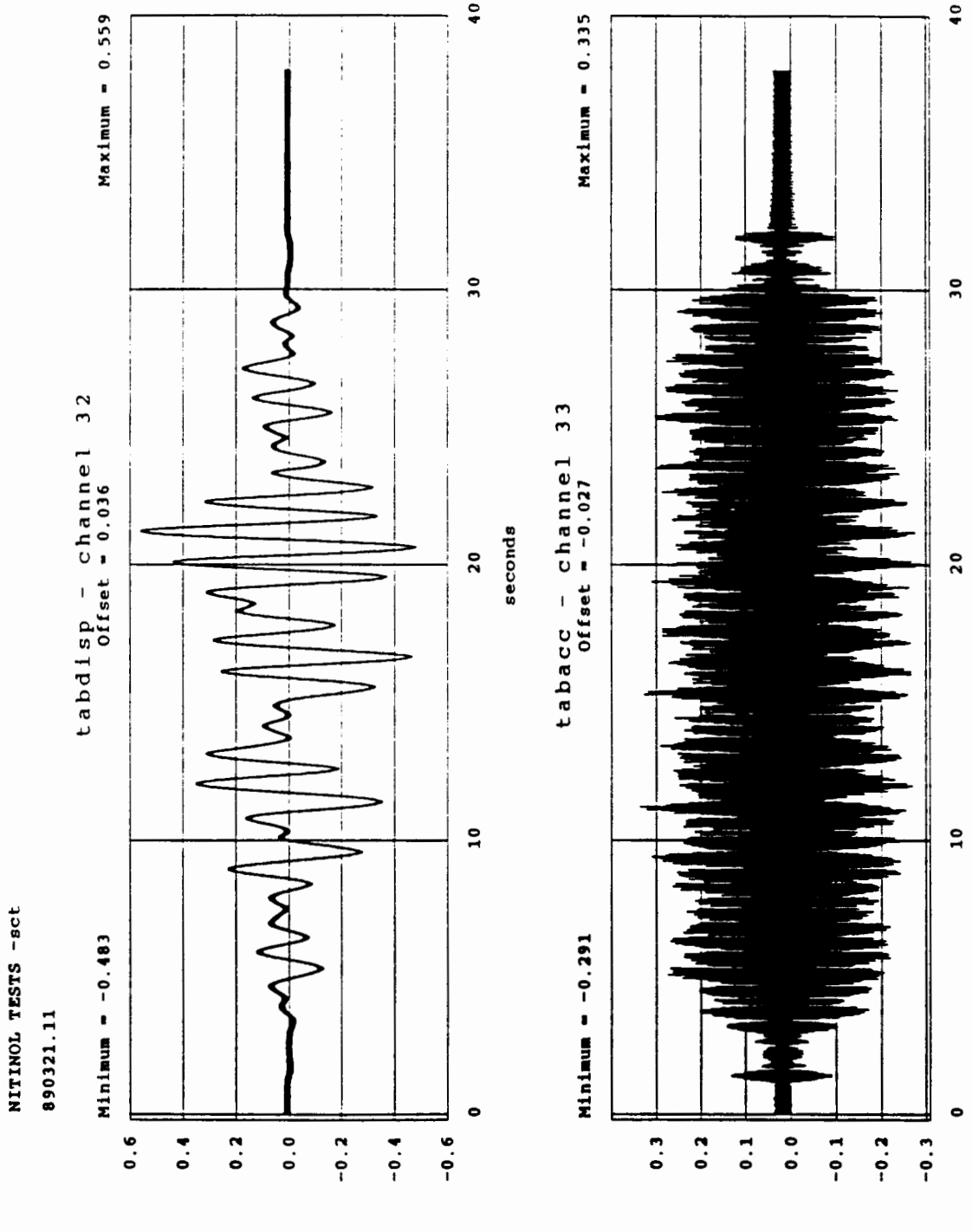

FIGURE 8.35 Time History of Table Displacement and Acceleration - SCT

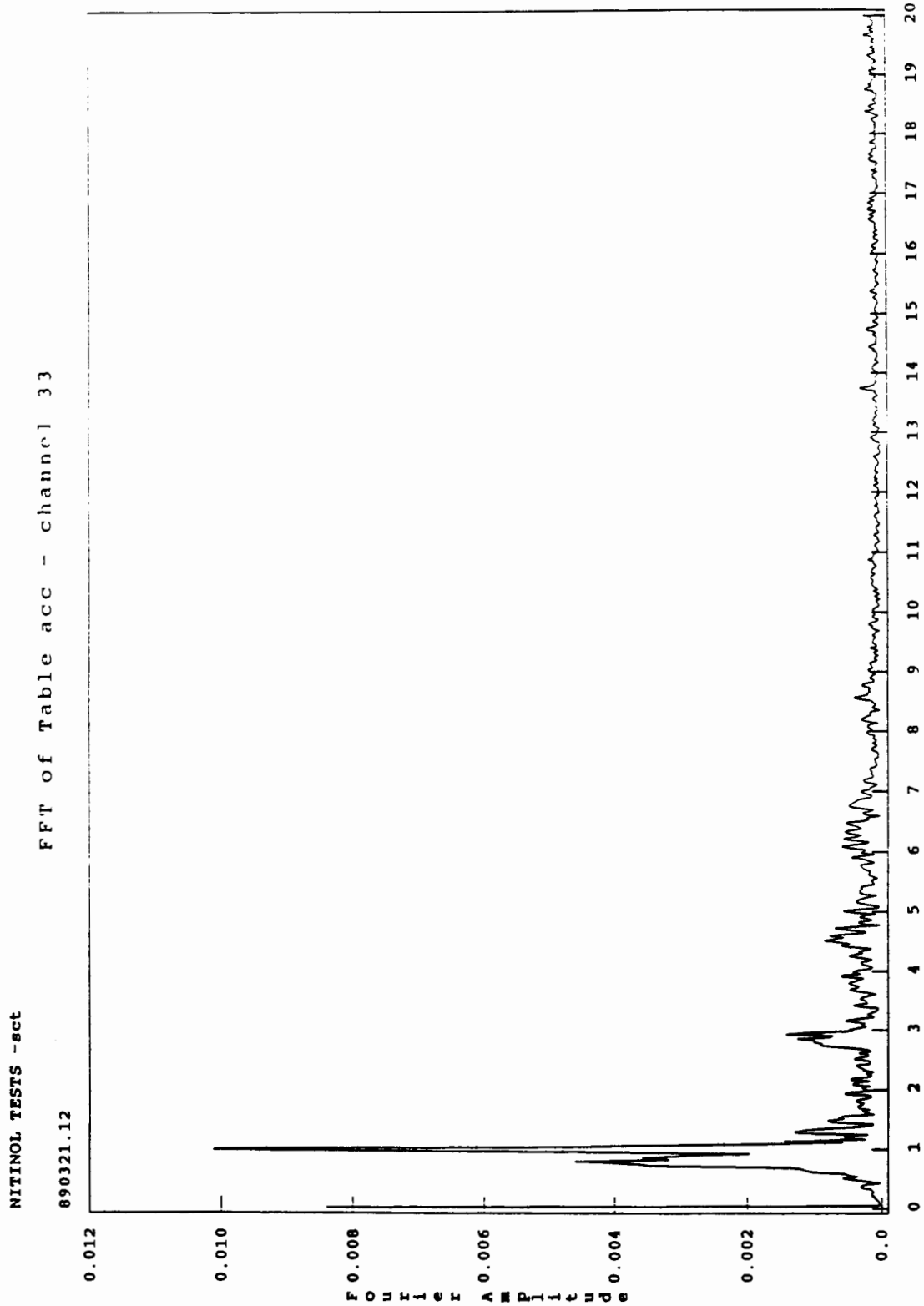

FIGURE 8.36 FFT of Table Acceleration - SCT

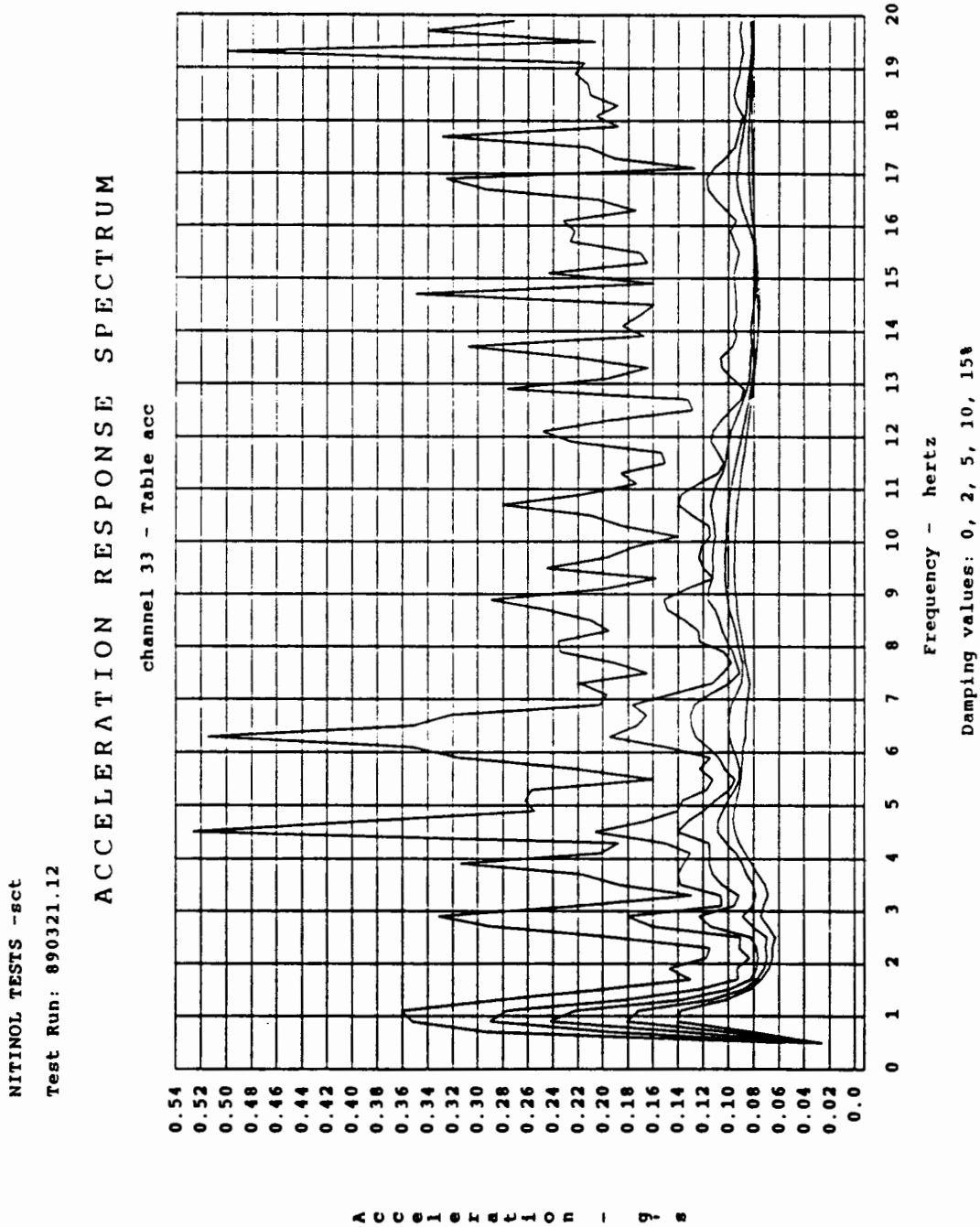

FIGURE 8.37 Elastic Acceleration Response Spectrum - SCT

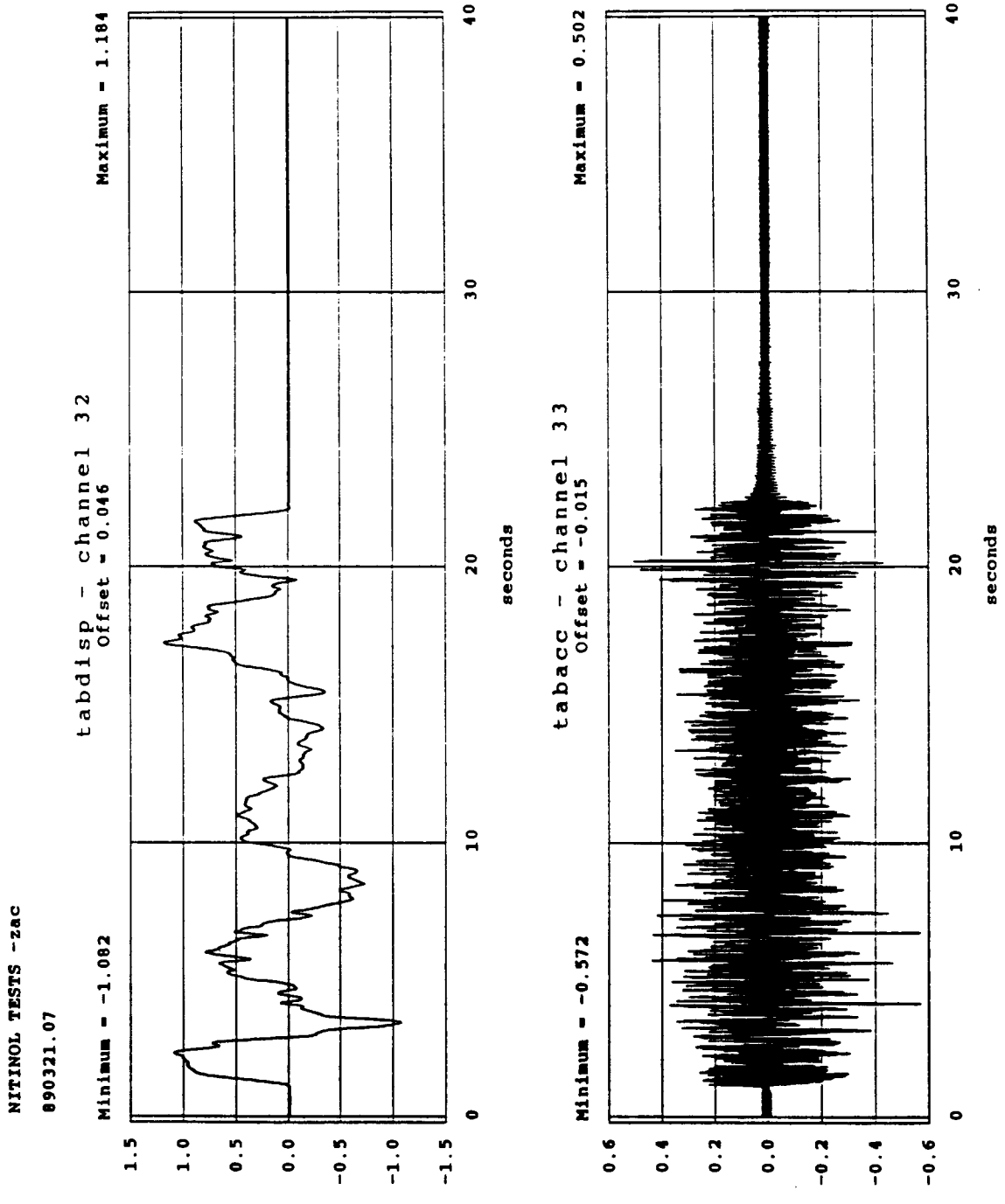

FIGURE 8.38 Time History of Table Displacement and Acceleration - Zacatula

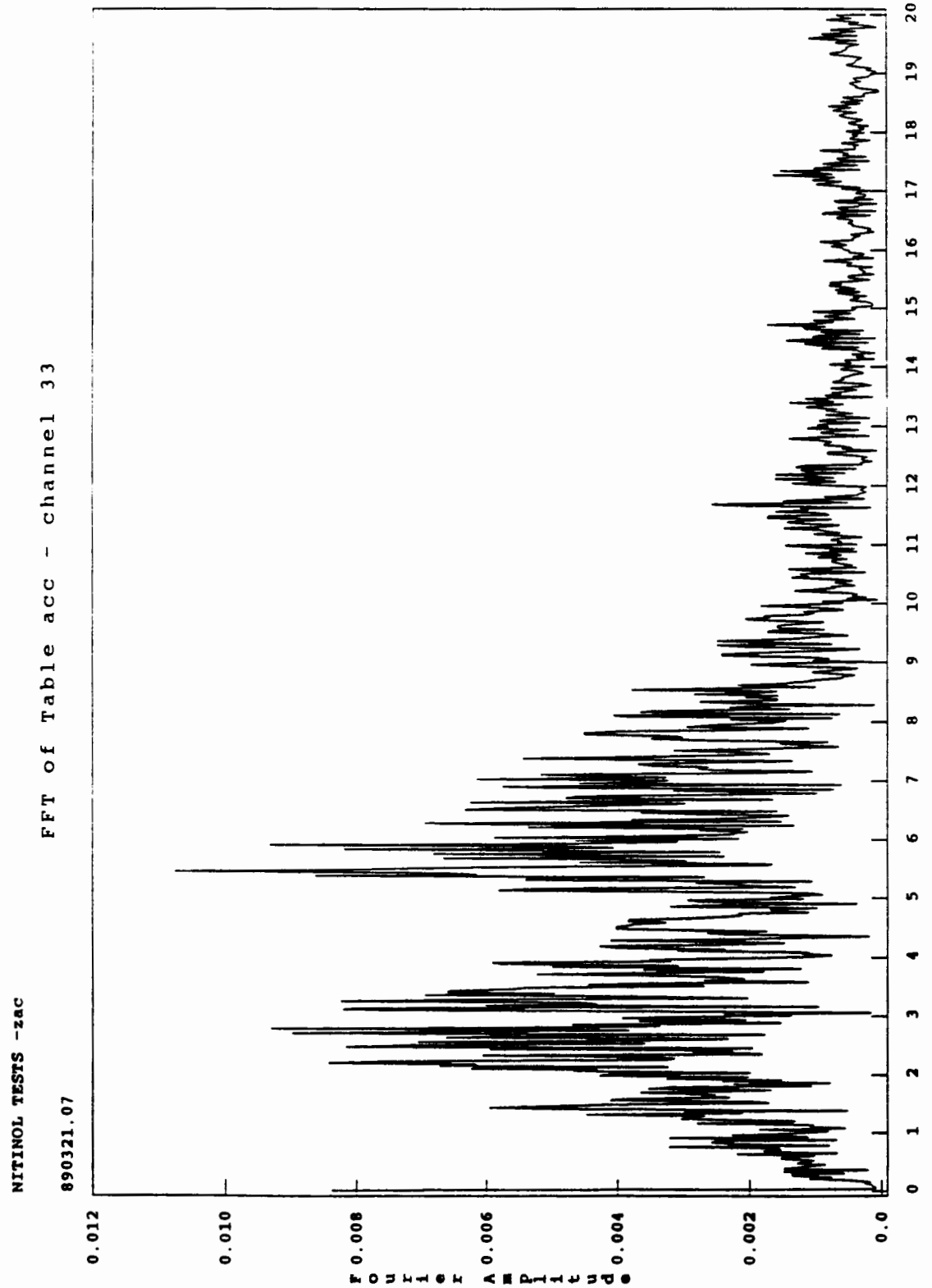

FIGURE 8.39 FFT of Table Acceleration - Zacatula

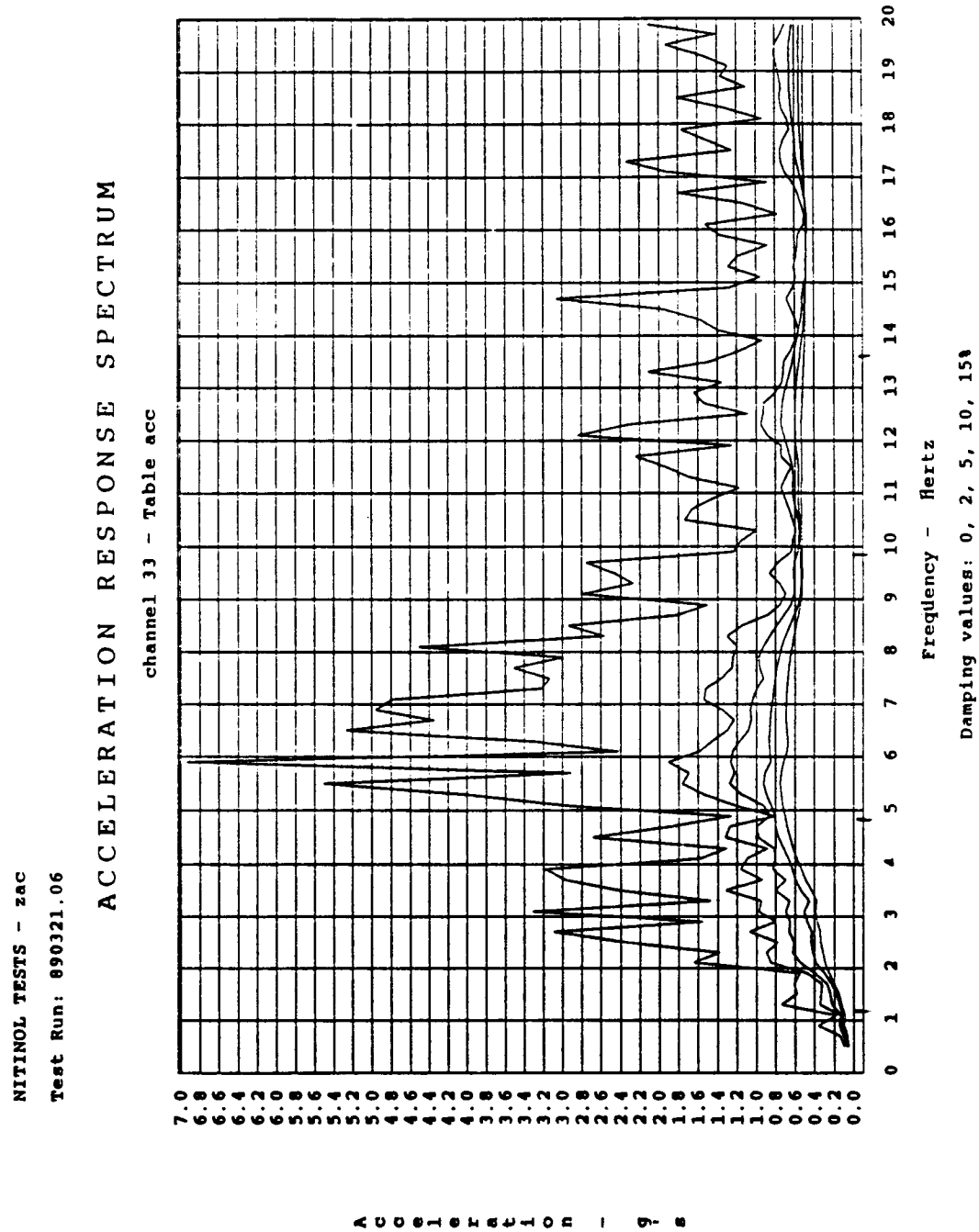

FIGURE 8.40 Elastic Acceleration Response Spectrum - Zacatula

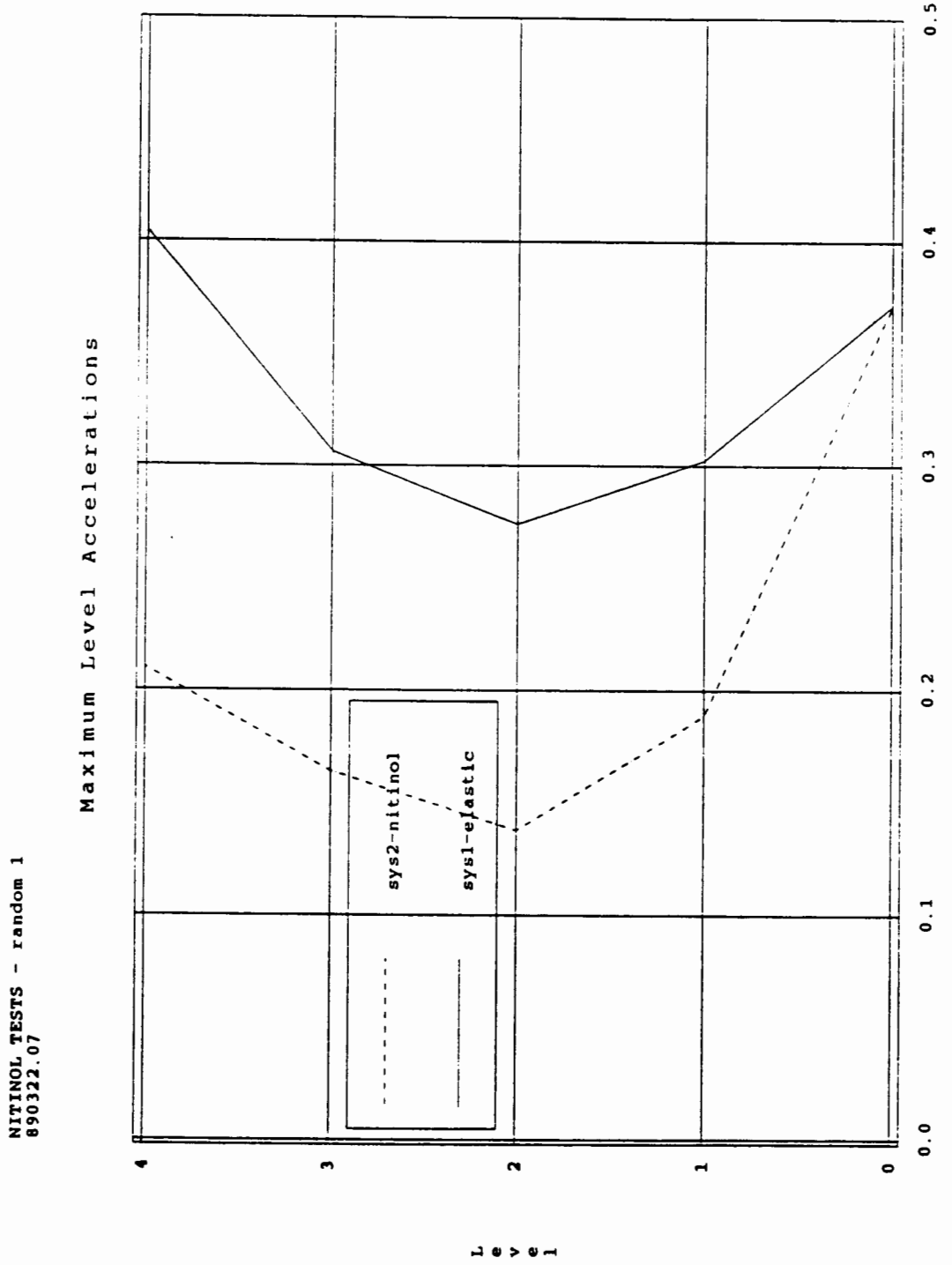

FIGURE 8.41 Maximum Level Accelerations, Sys 1 & 2 - Random Noise

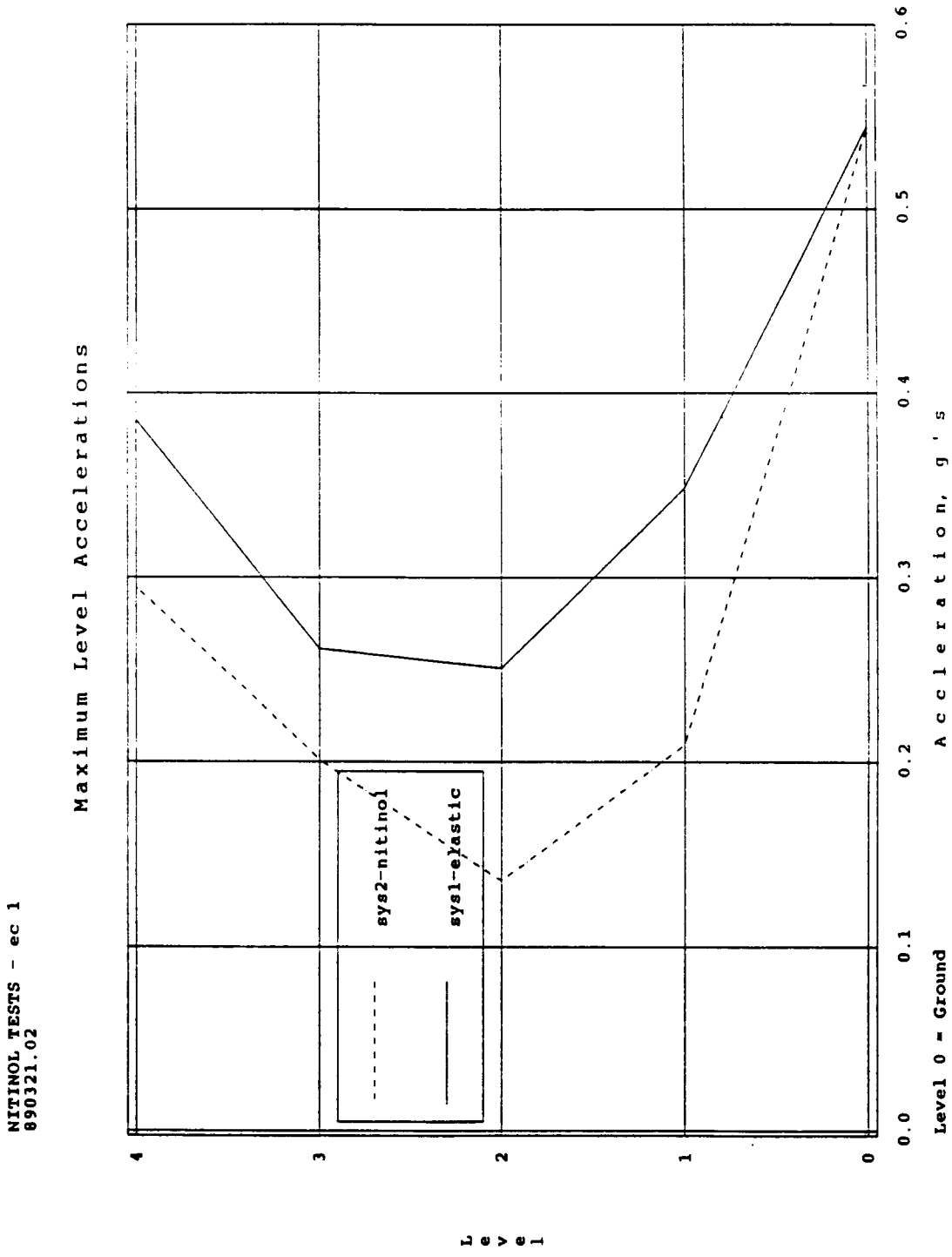

FIGURE 8.42 Maximum Level Accelerations, Sys 1 & 2 - El Centro

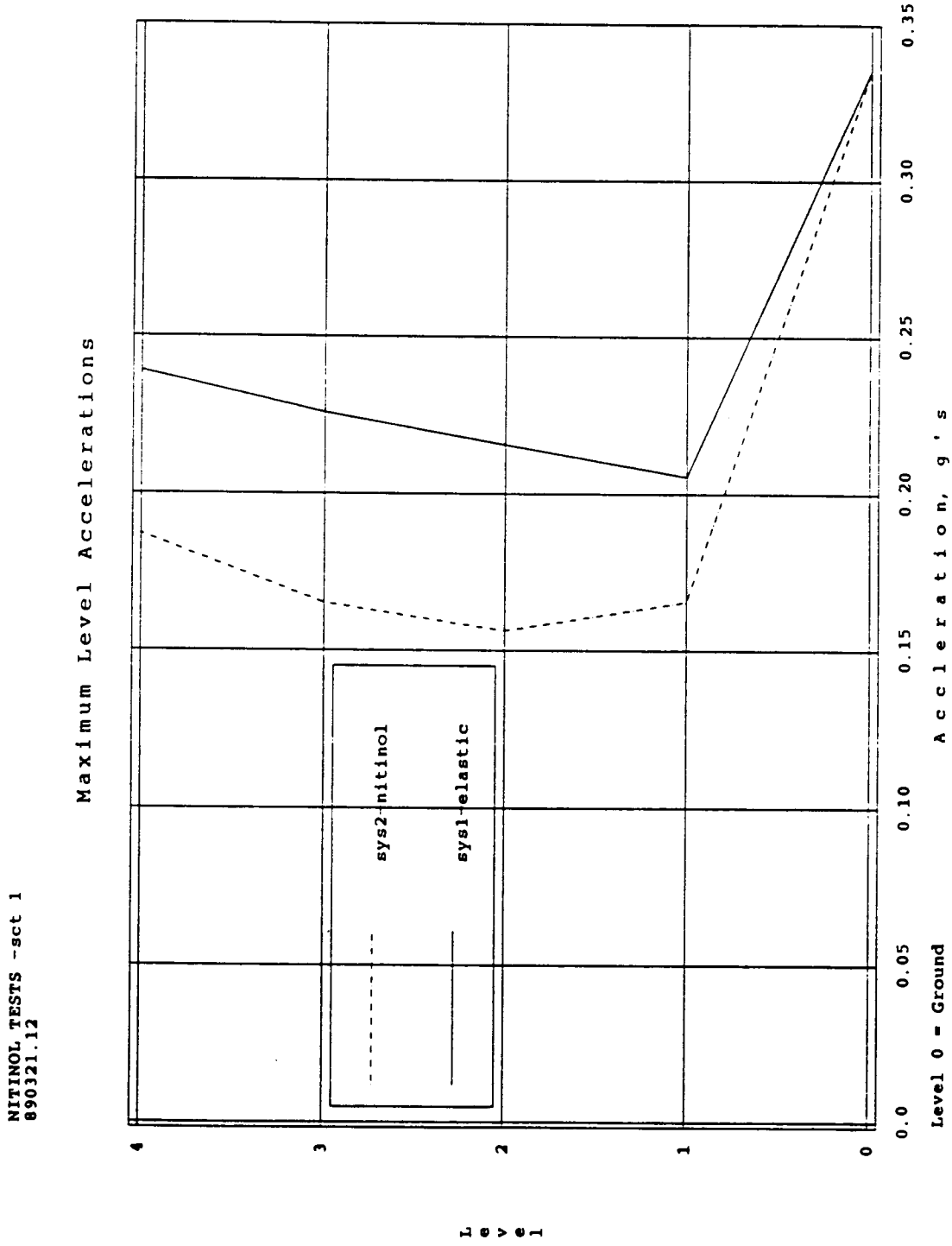

FIGURE 8.43 Maximum Level Accelerations, Sys 1 & 2 - SCT

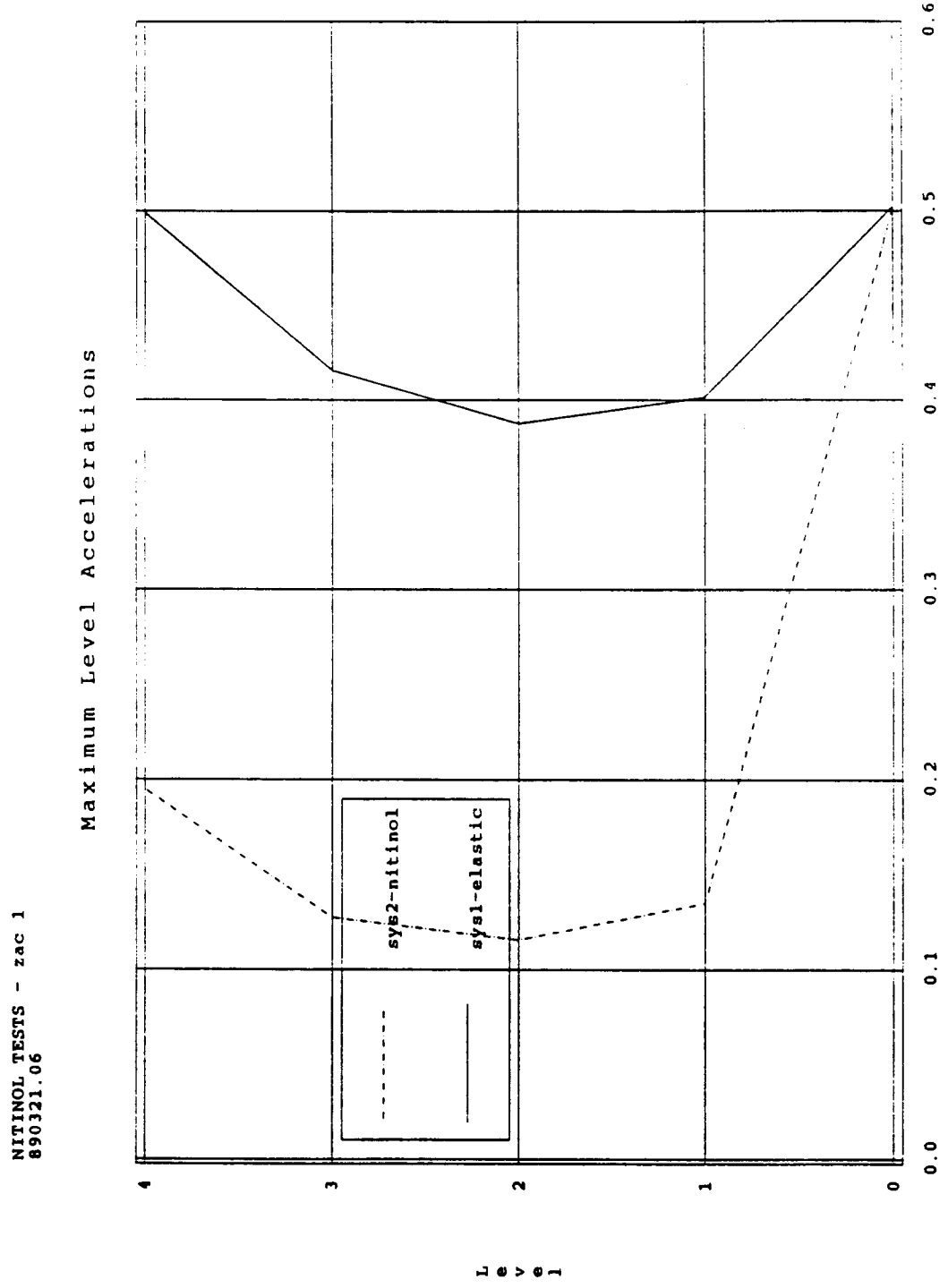

FIGURE 8.44 Maximum Level Accelerations, Sys 1 & 2 - Zacatula

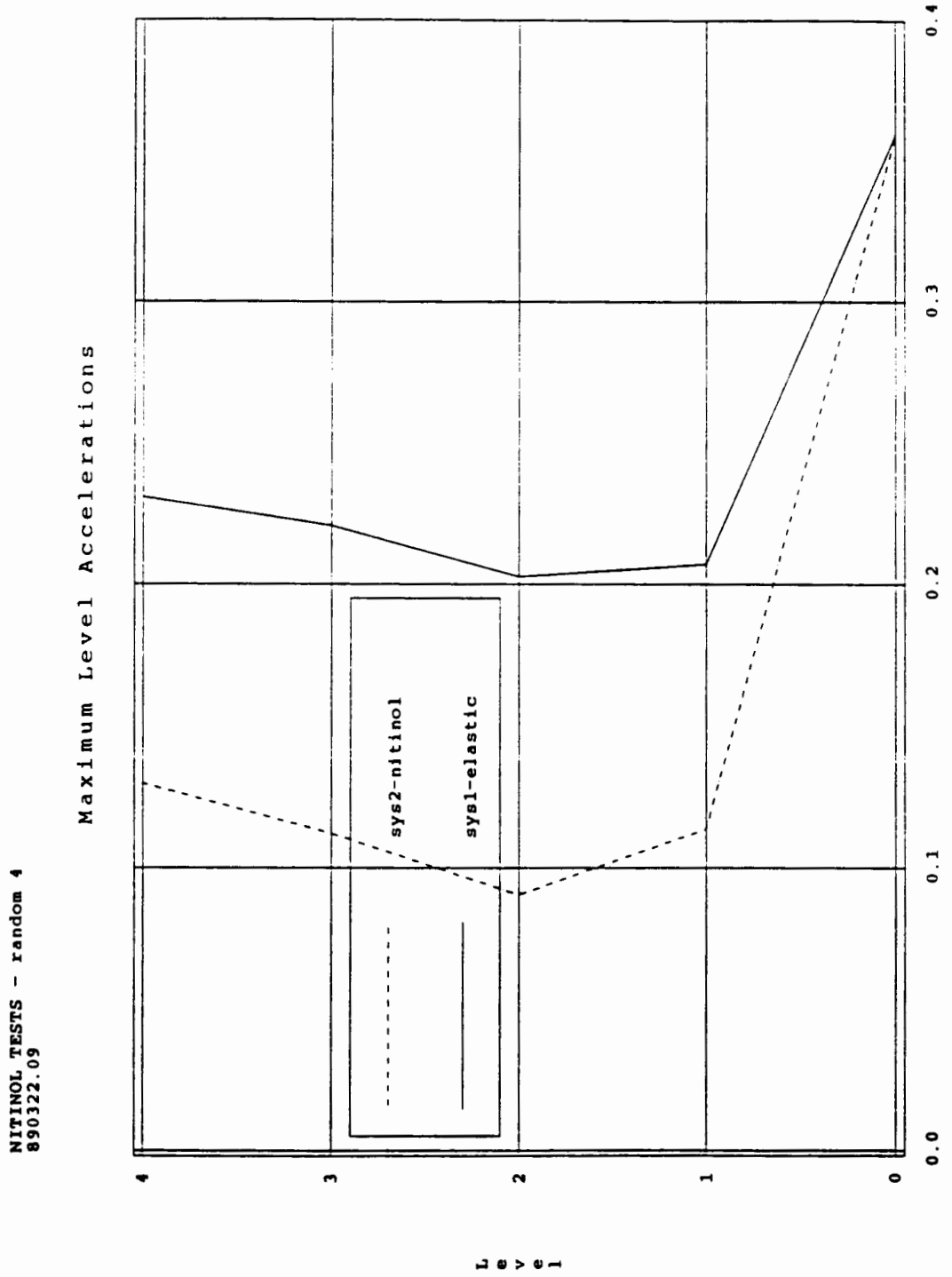

FIGURE 8.45 Maximum Level Accelerations, Sys 4 & 5 - Random Noise

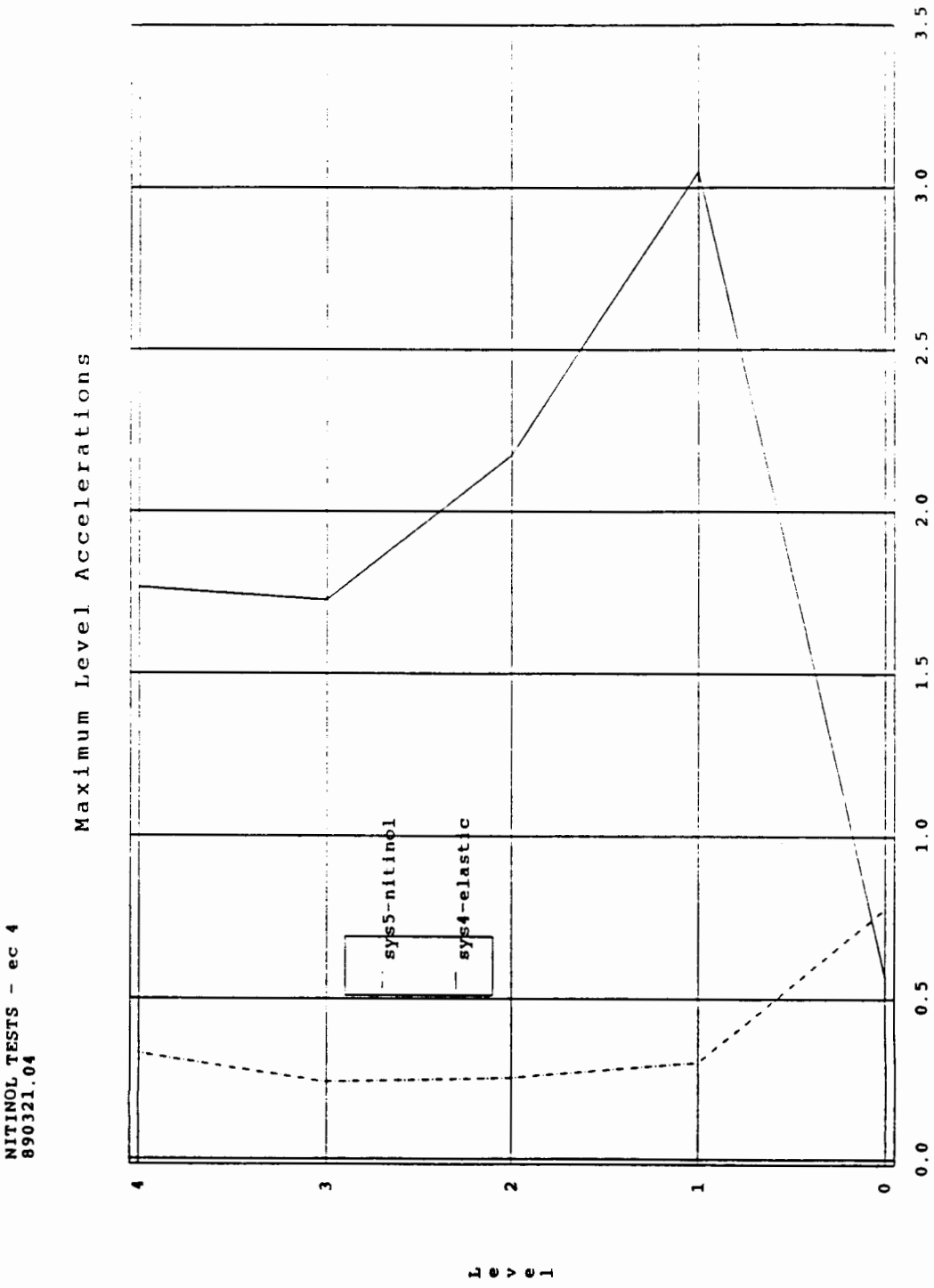

FIGURE 8.46 Maximum Level Accelerations, Sys 4 & 5 - El Centro

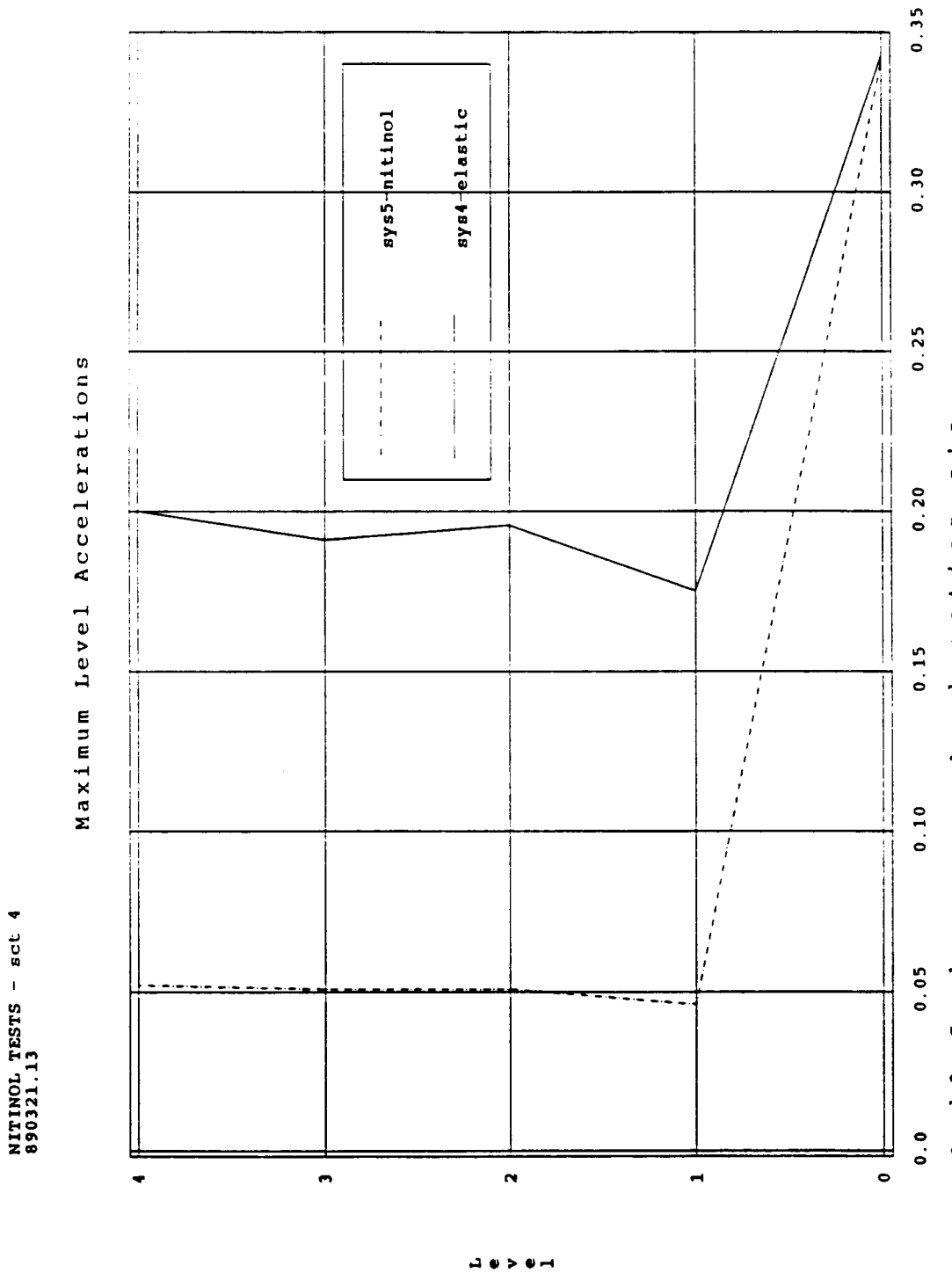

FIGURE 8.47 Maximum Level Accelerations, Sys 4 & 5 - SCT

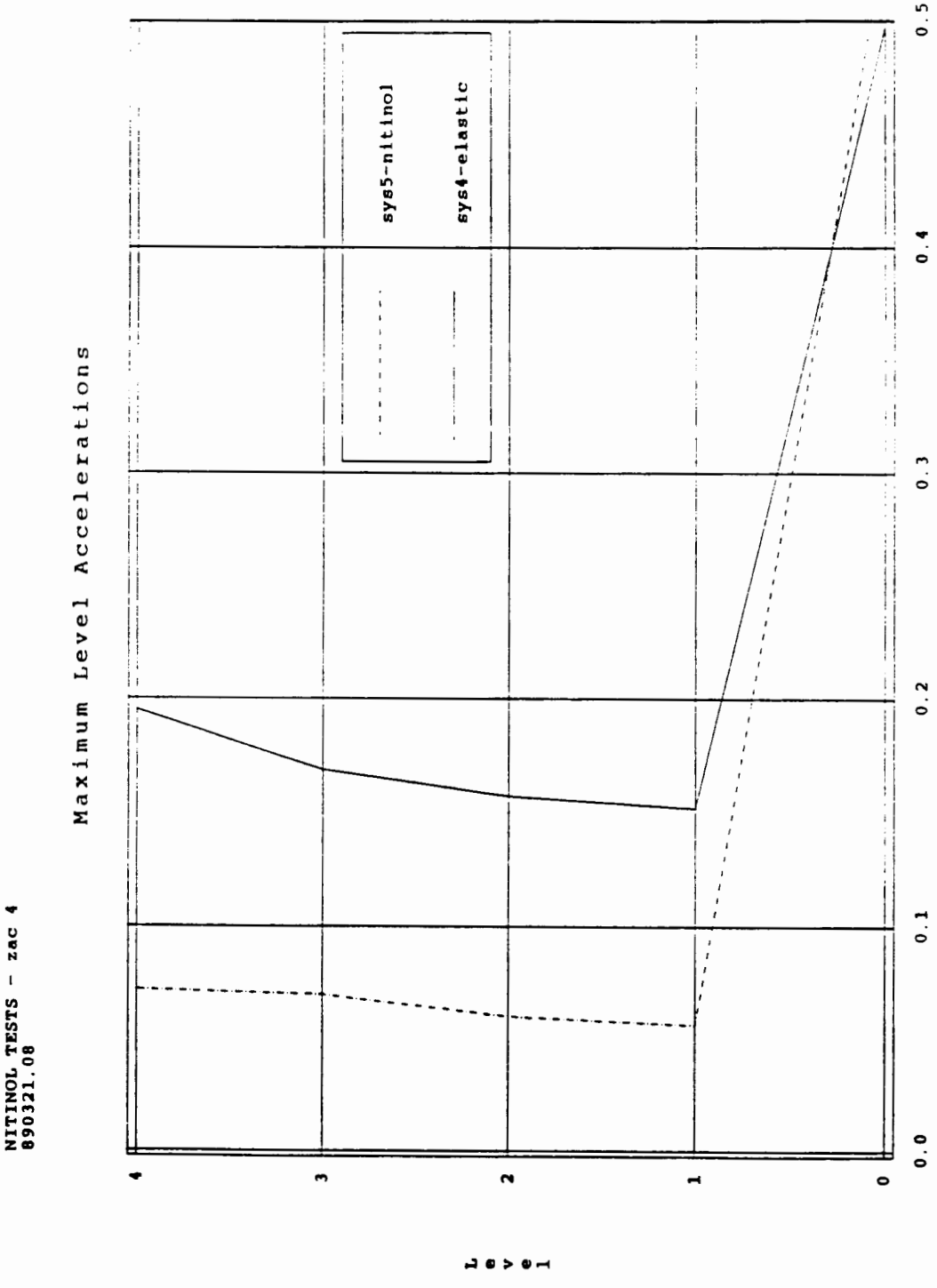

FIGURE 8.48 Maximum Level Accelerations, Sys 4 & 5 - Zacatula

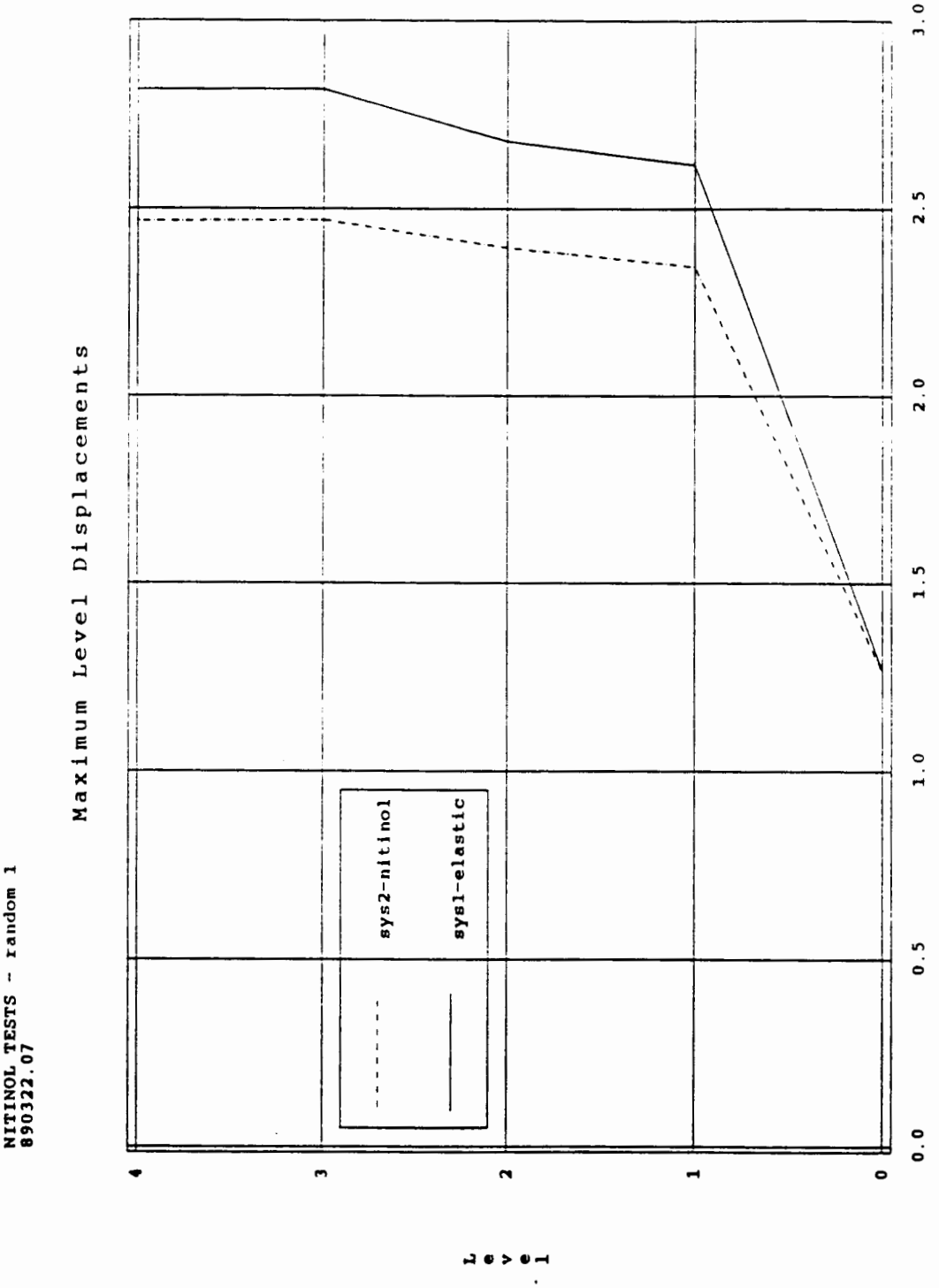

FIGURE 8.49 Maximum Level Displacements, Sys 1 & 2 - Random Noise

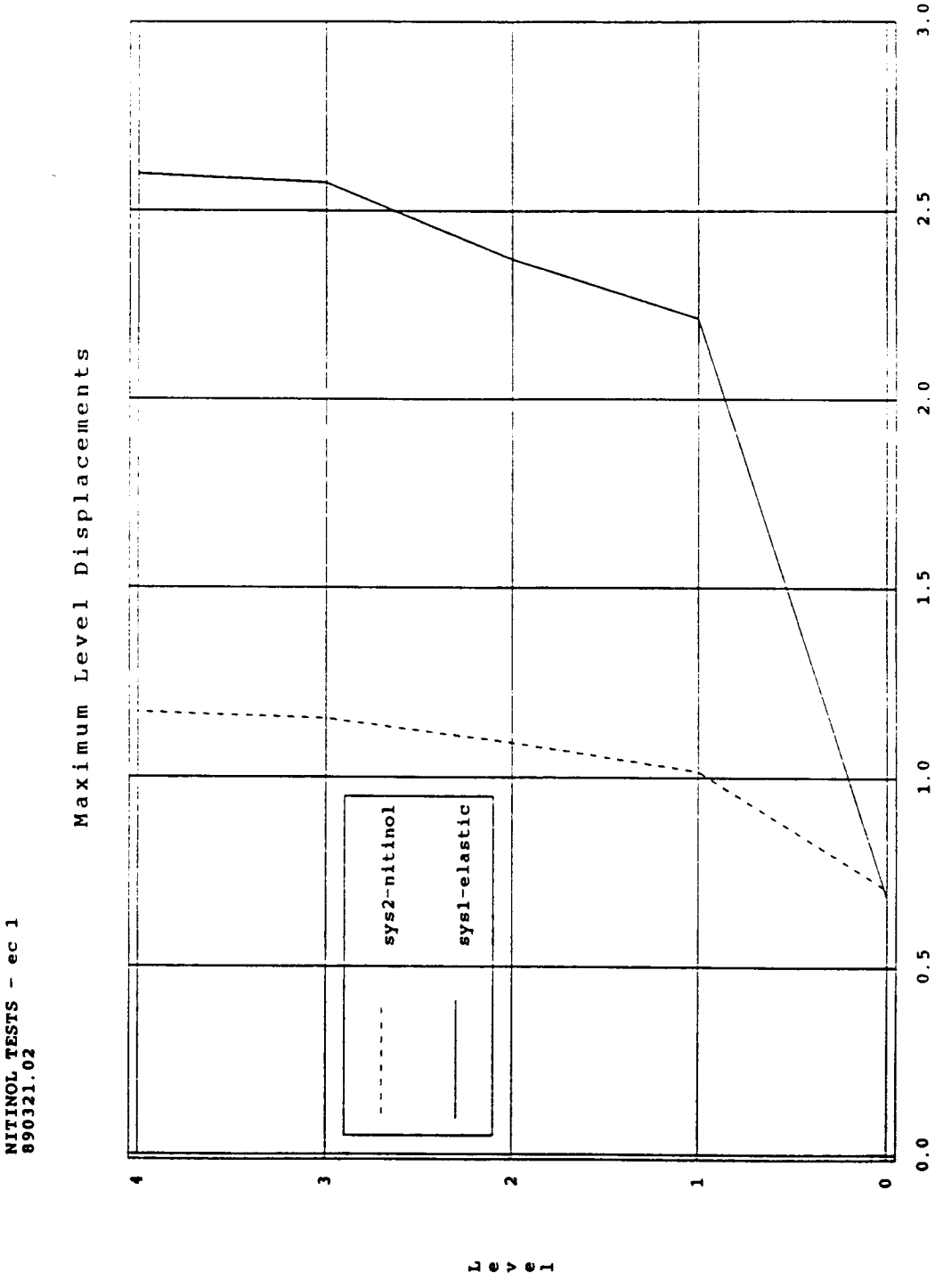

FIGURE 8.50 Maximum Level Displacements, Sys 1 & 2 - El Centro

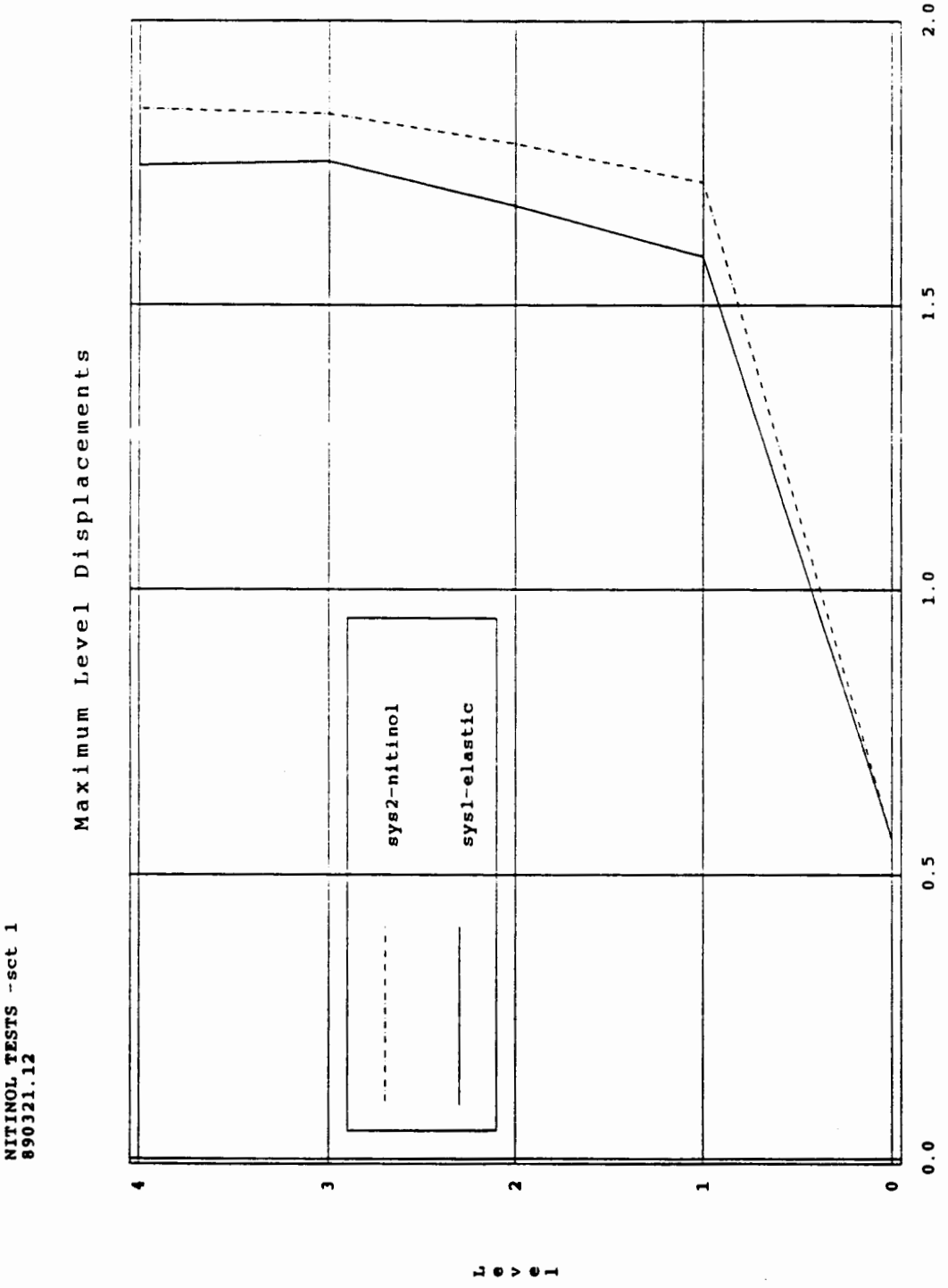

FIGURE 8.51 Maximum Level Displacements, Sys 1 & 2 - SCT

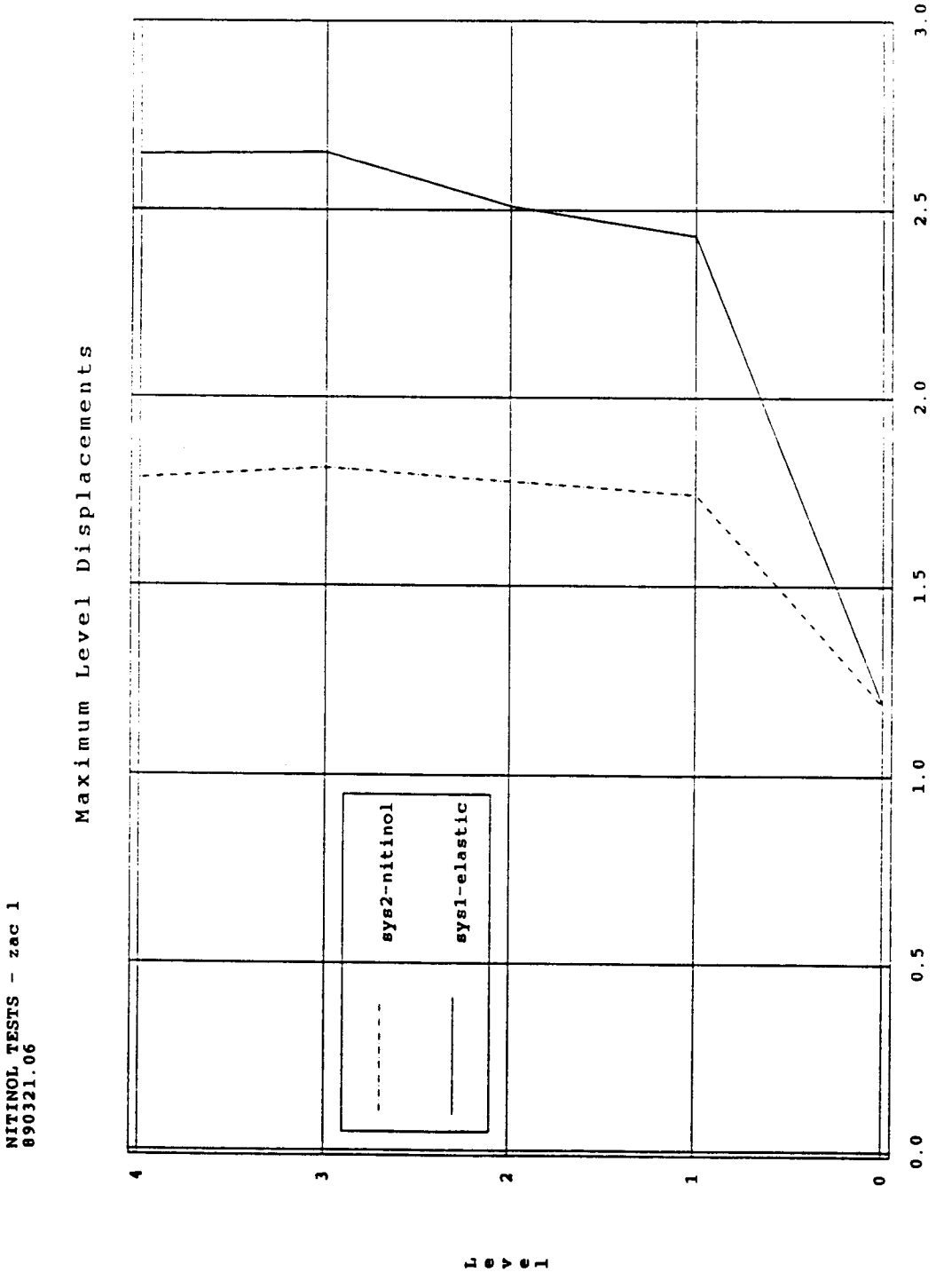

FIGURE 8.52 Maximum Level Displacements, Sys 1 & 2 - Zacatula

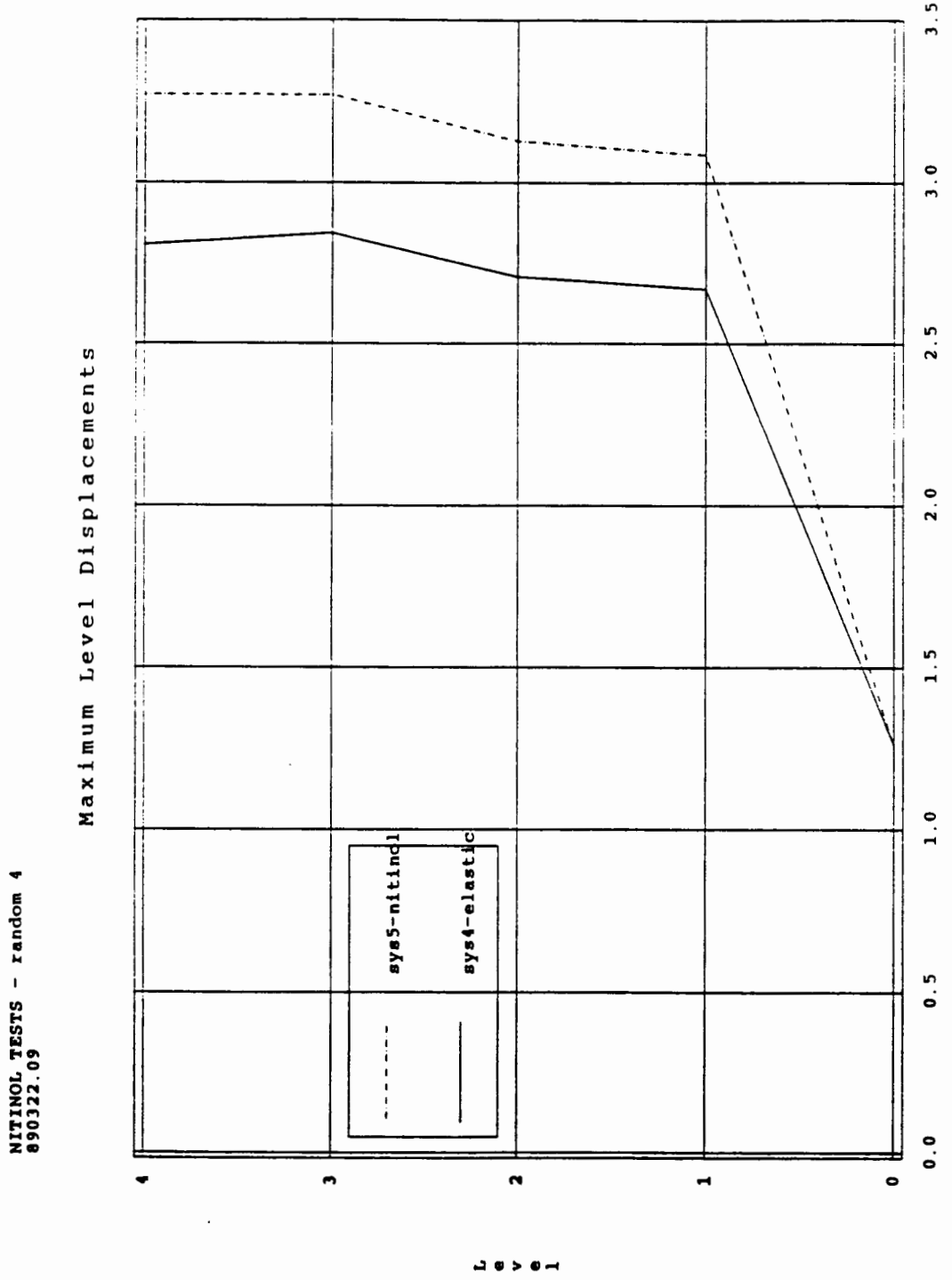

FIGURE 8.53 Maximum Level Displacements, Sys 4 & 5 - Random Noise

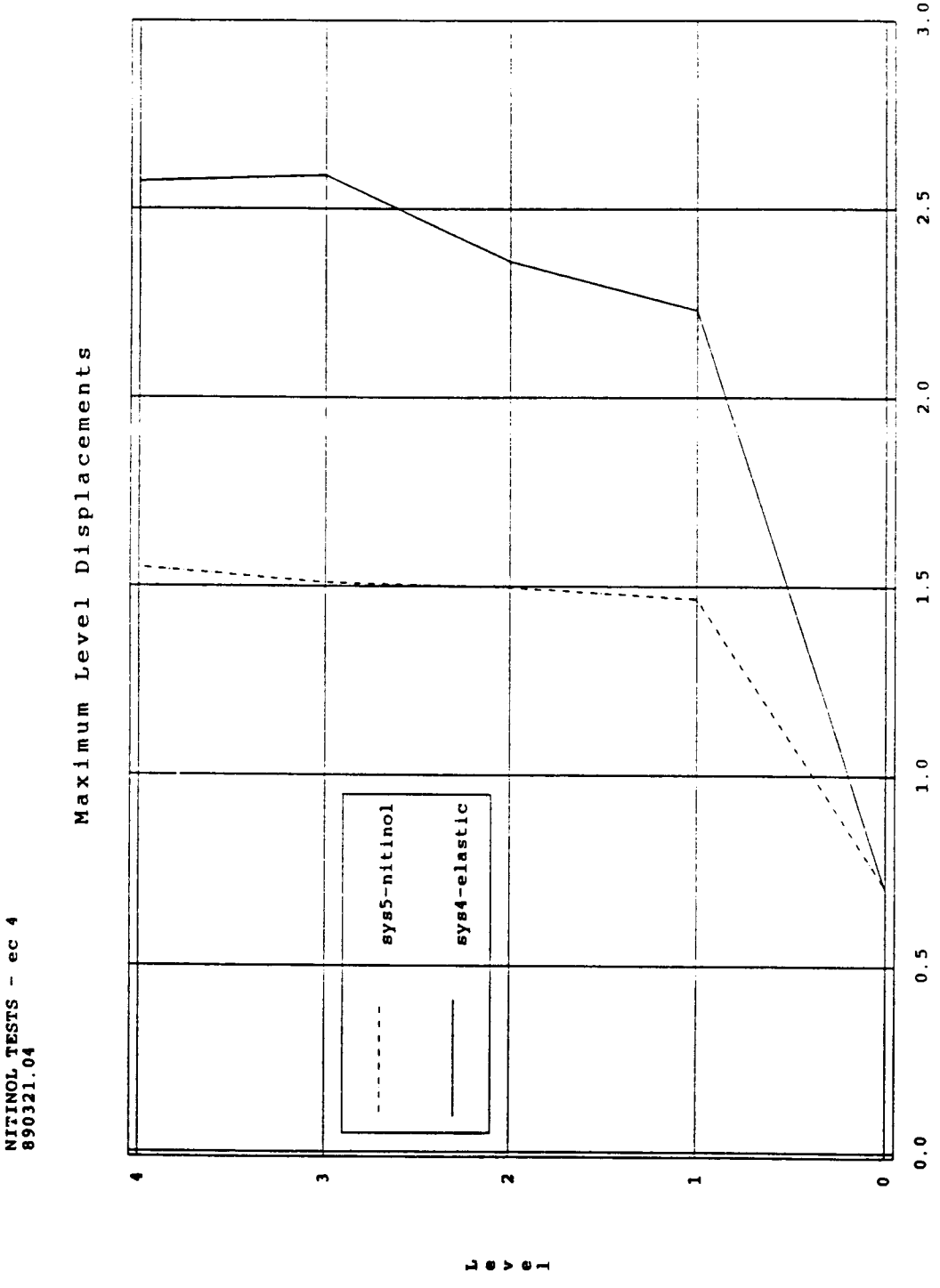

FIGURE 8.54 Maximum Level Displacements, Sys 4 & 5 - El Centro

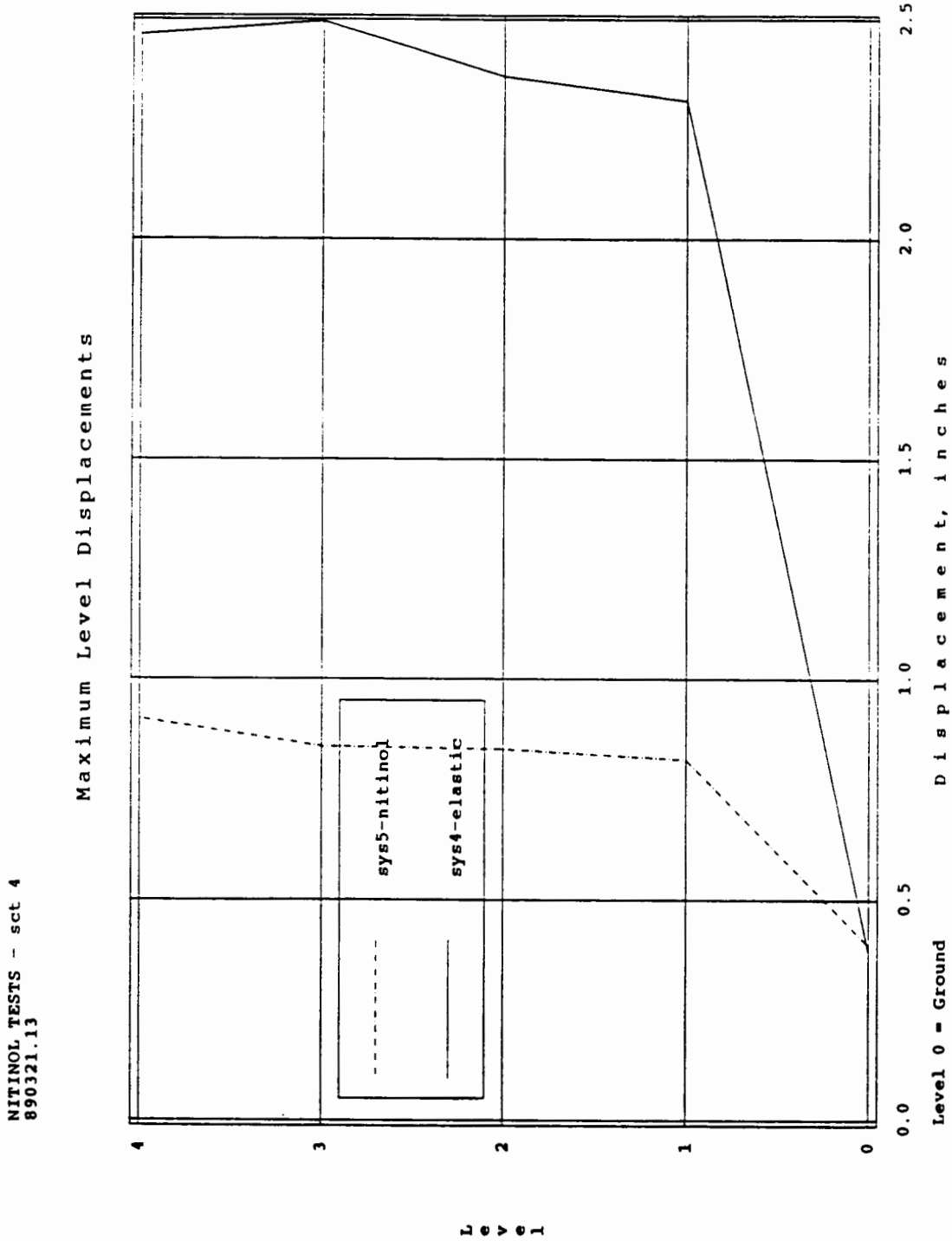

FIGURE 8.55 Maximum Level Displacements, Sys 4 & 5 - SCT

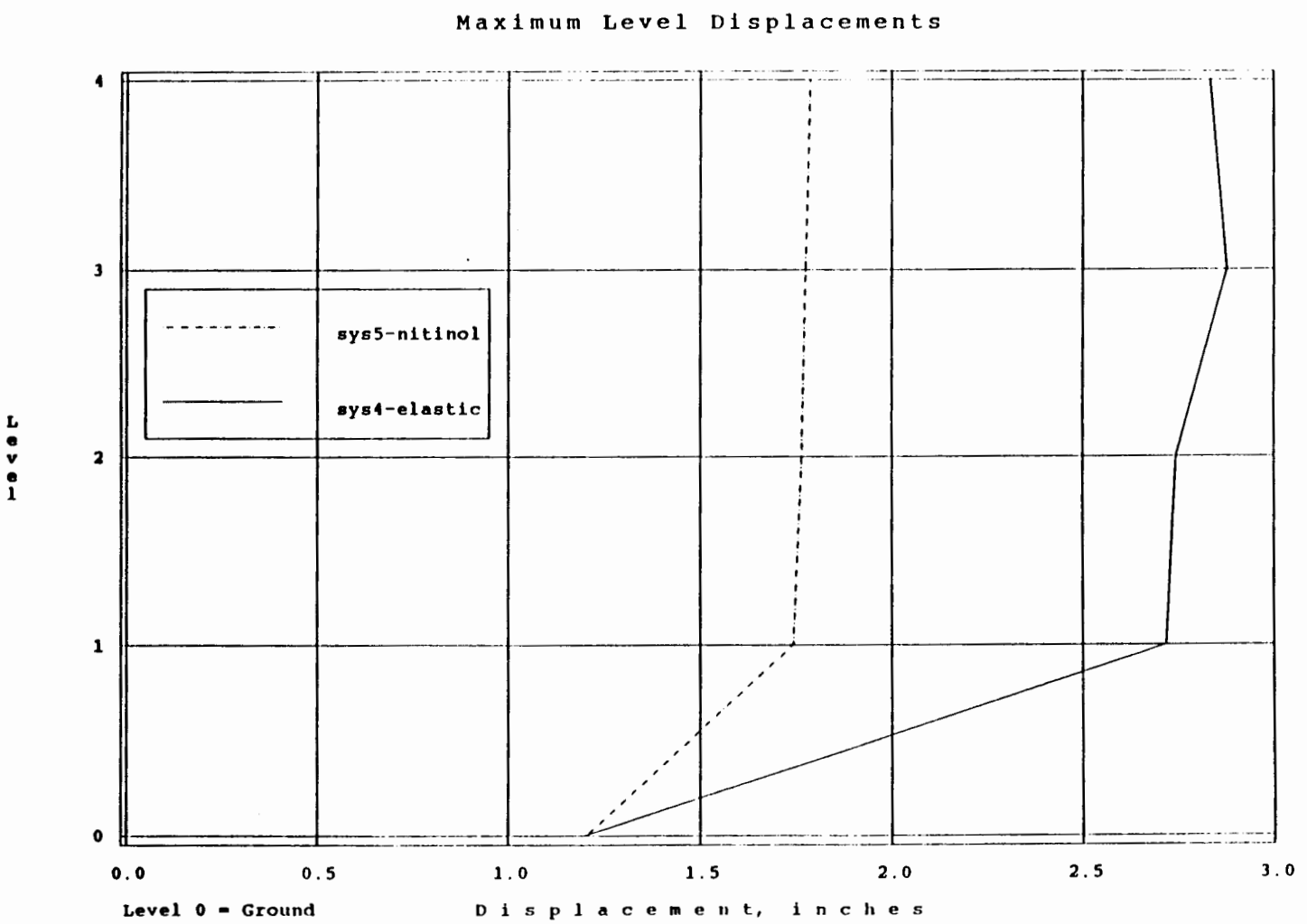

FIGURE 8.56 Maximum Level Displacements, Sys 4 & 5 - Zacatula

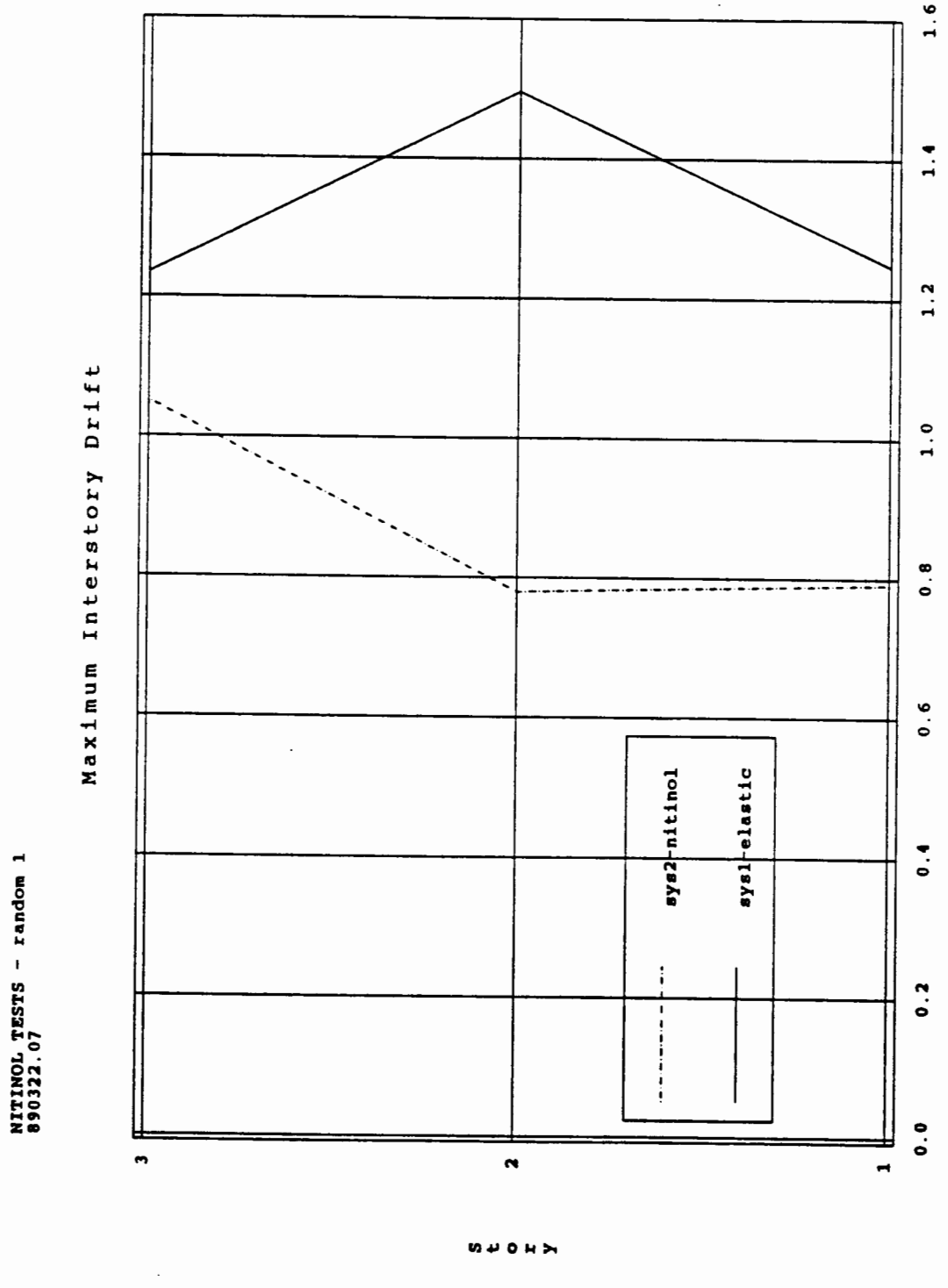

FIGURE 8.57 Maximum Interstory Drifts, Sys 1 & 2 - Random Noise

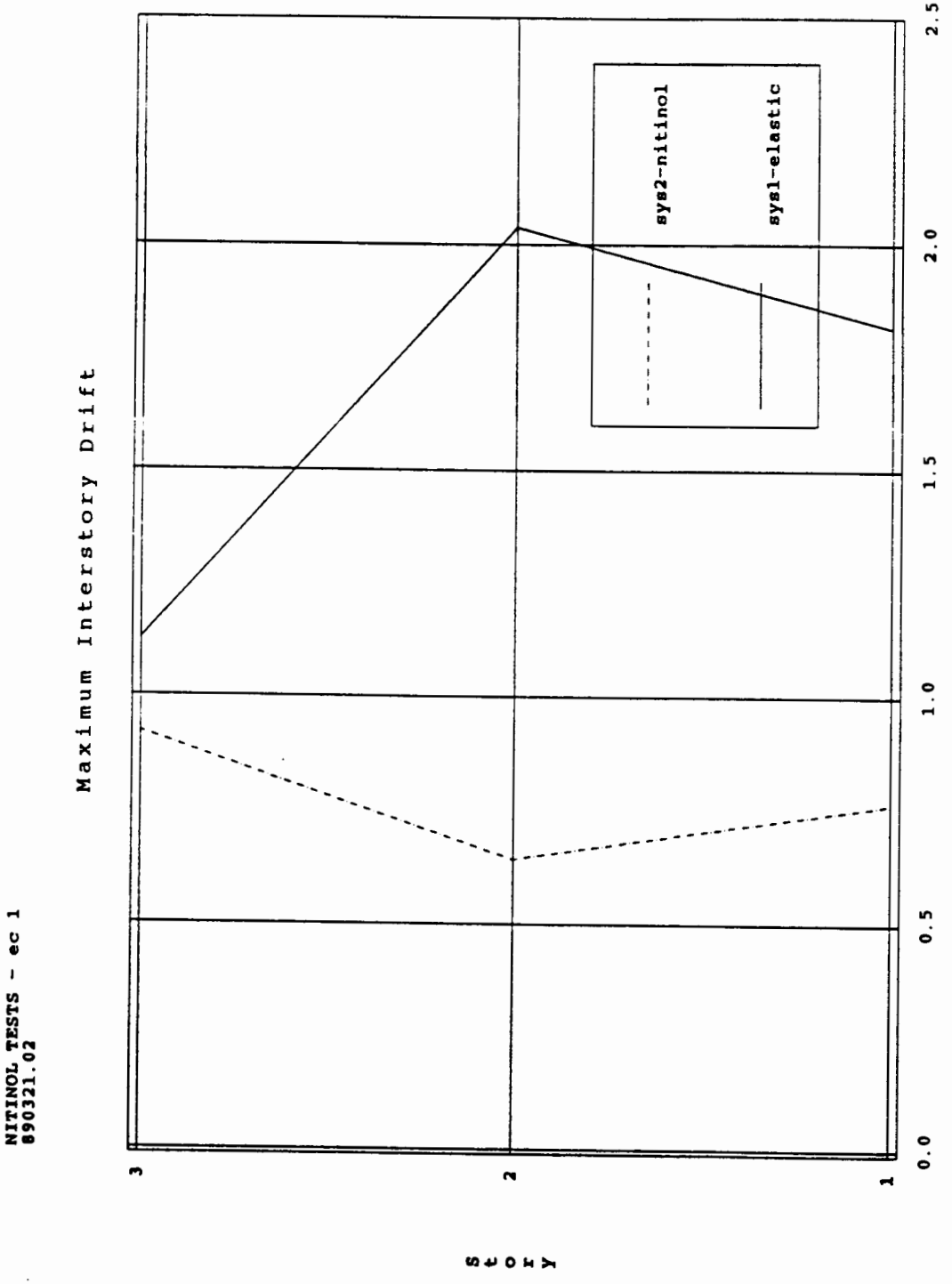

FIGURE 8.58 Maximum Interstory Drifts, Sys 1 & 2 - El Centro

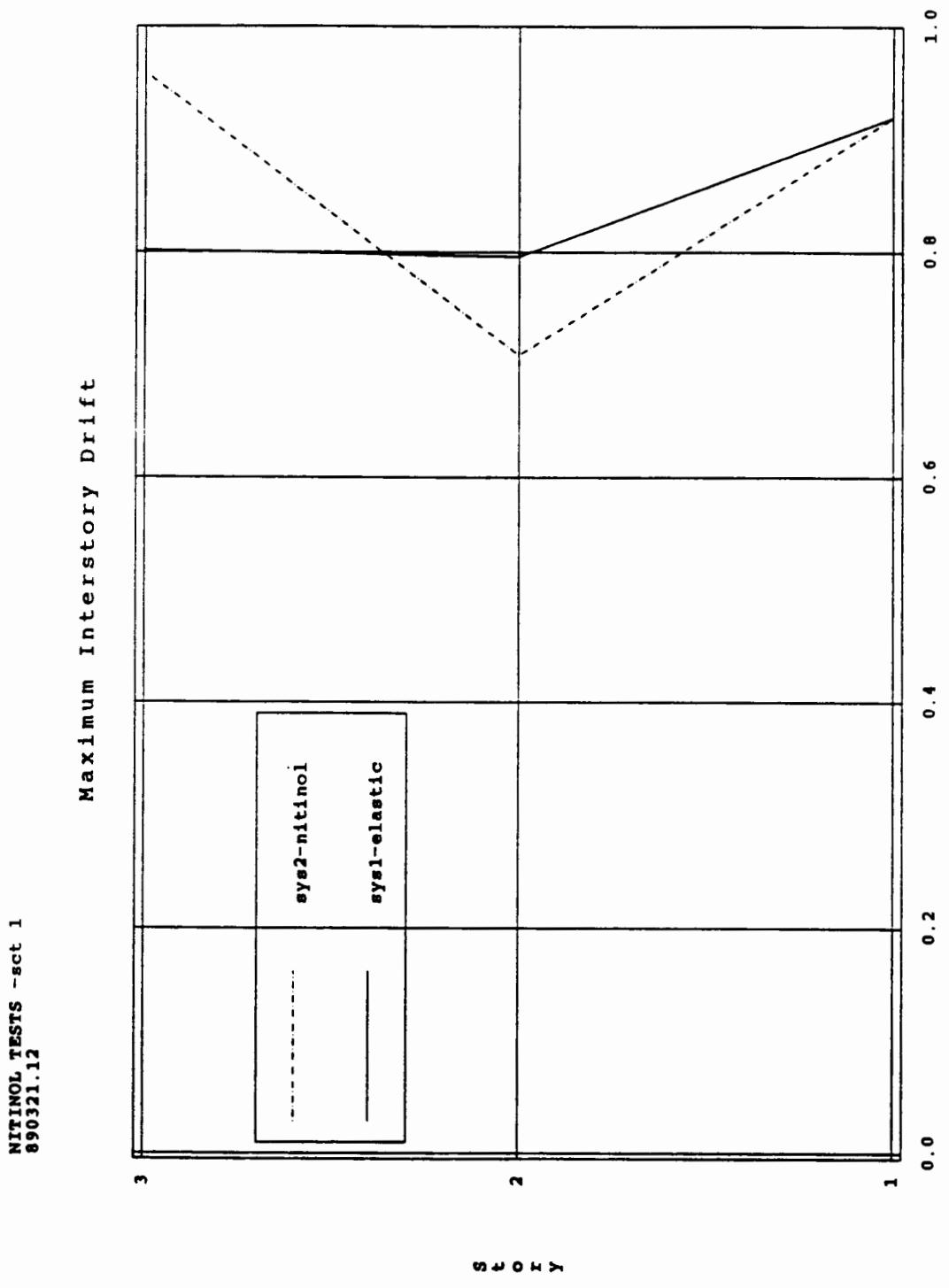

FIGURE 8.59 Maximum Interstory Drifts, Sys 1 & 2 - SCT

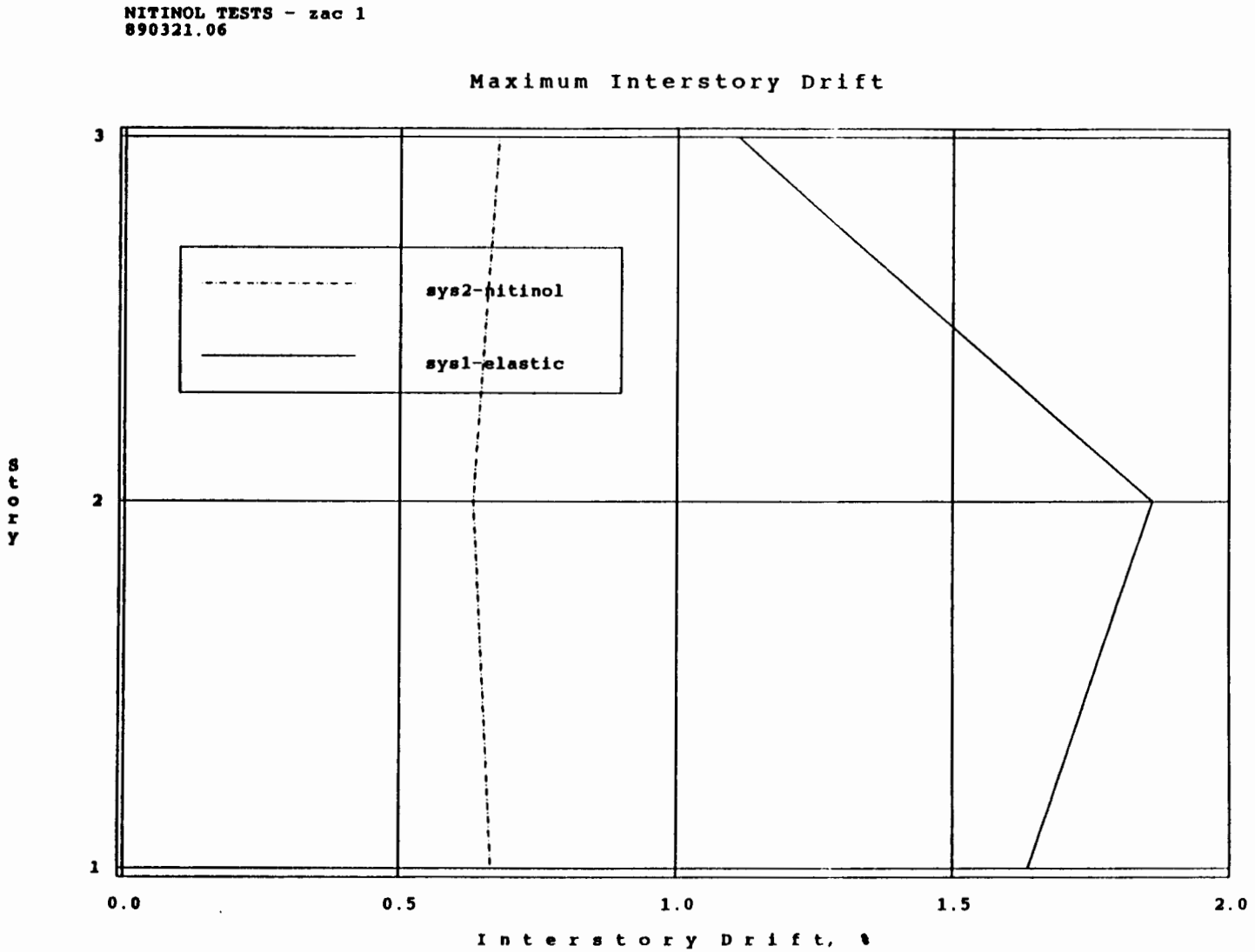

FIGURE 8.60 Maximum Interstory Drifts, Sys 1 & 2 - Zacatula

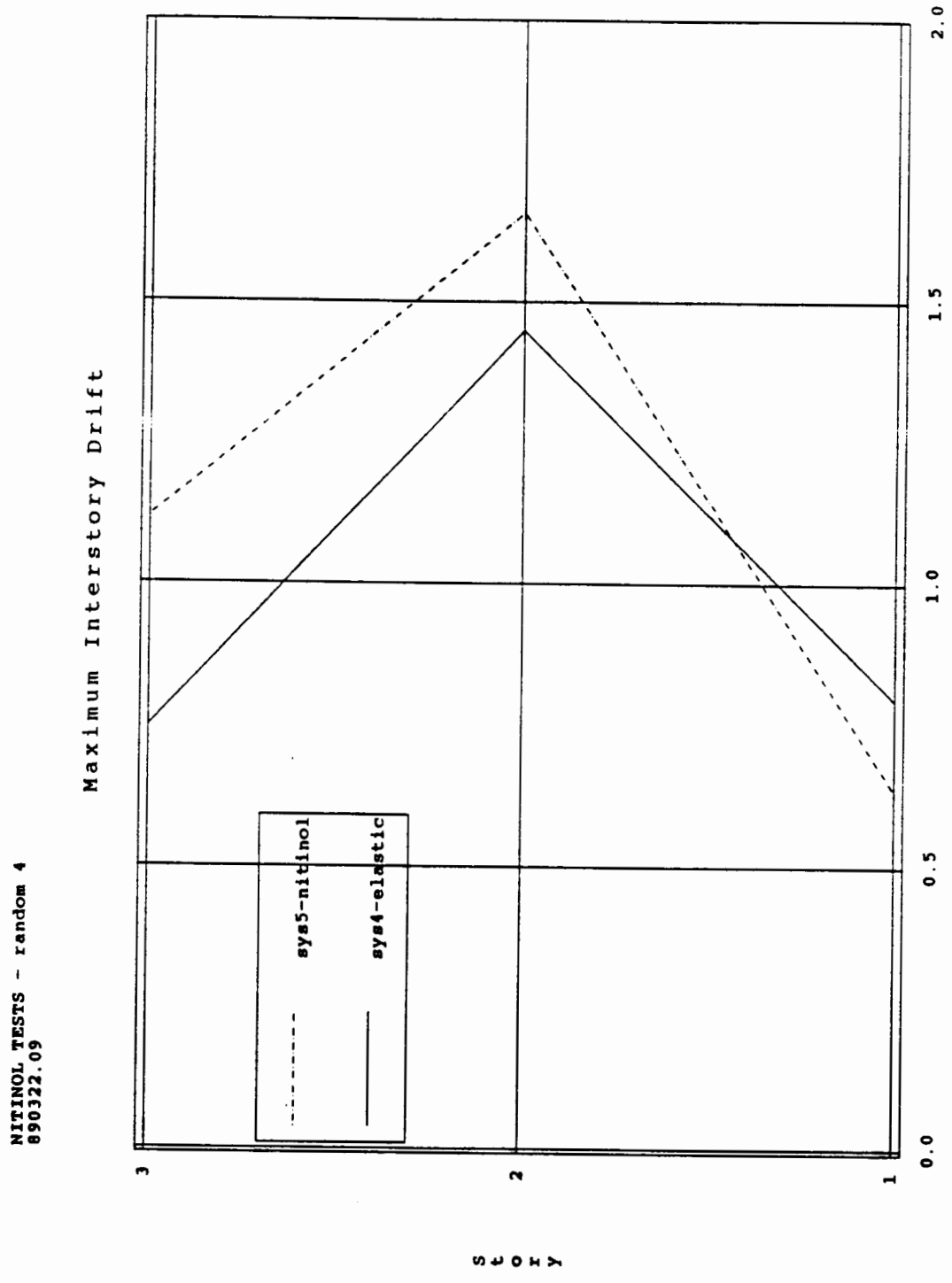

FIGURE 8.61 Maximum Interstory Drifts, Sys 4 & 5 - Random Noise

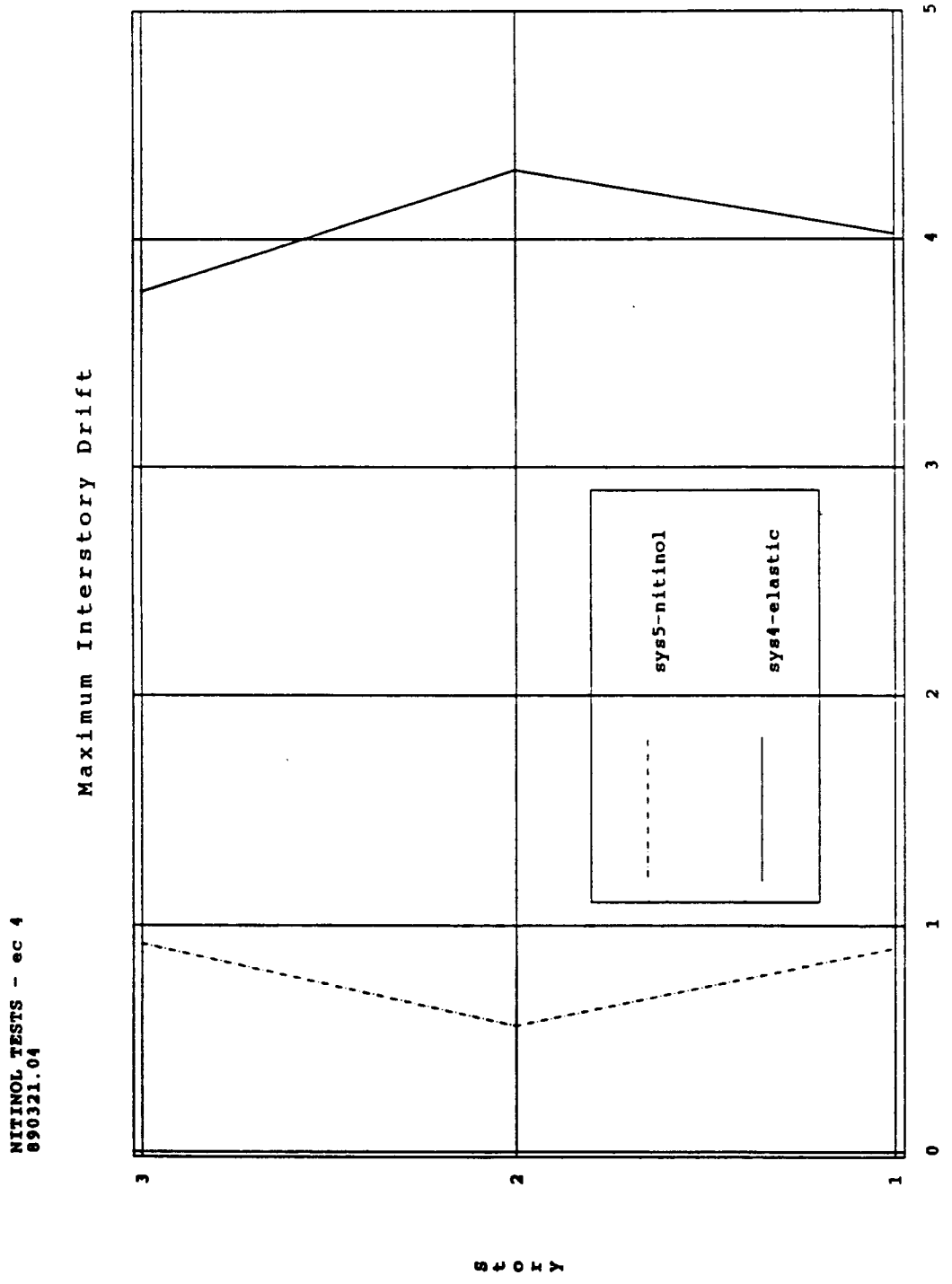

FIGURE 8.62 Maximum Interstory Drifts, Sys 4 & 5 - El Centro

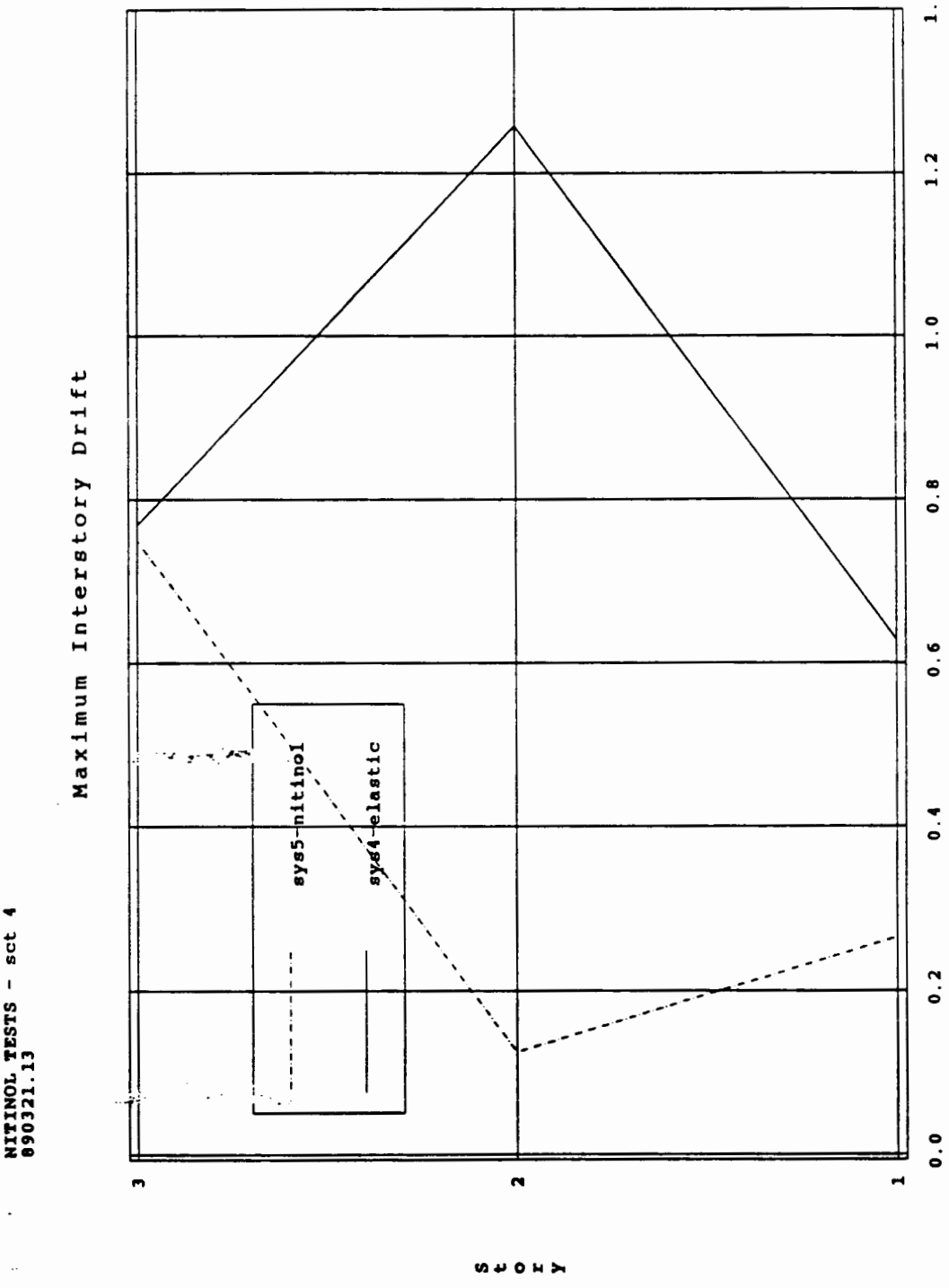

FIGURE 8.63 Maximum Interstory Drifts, Sys 4 & 5 - SCT

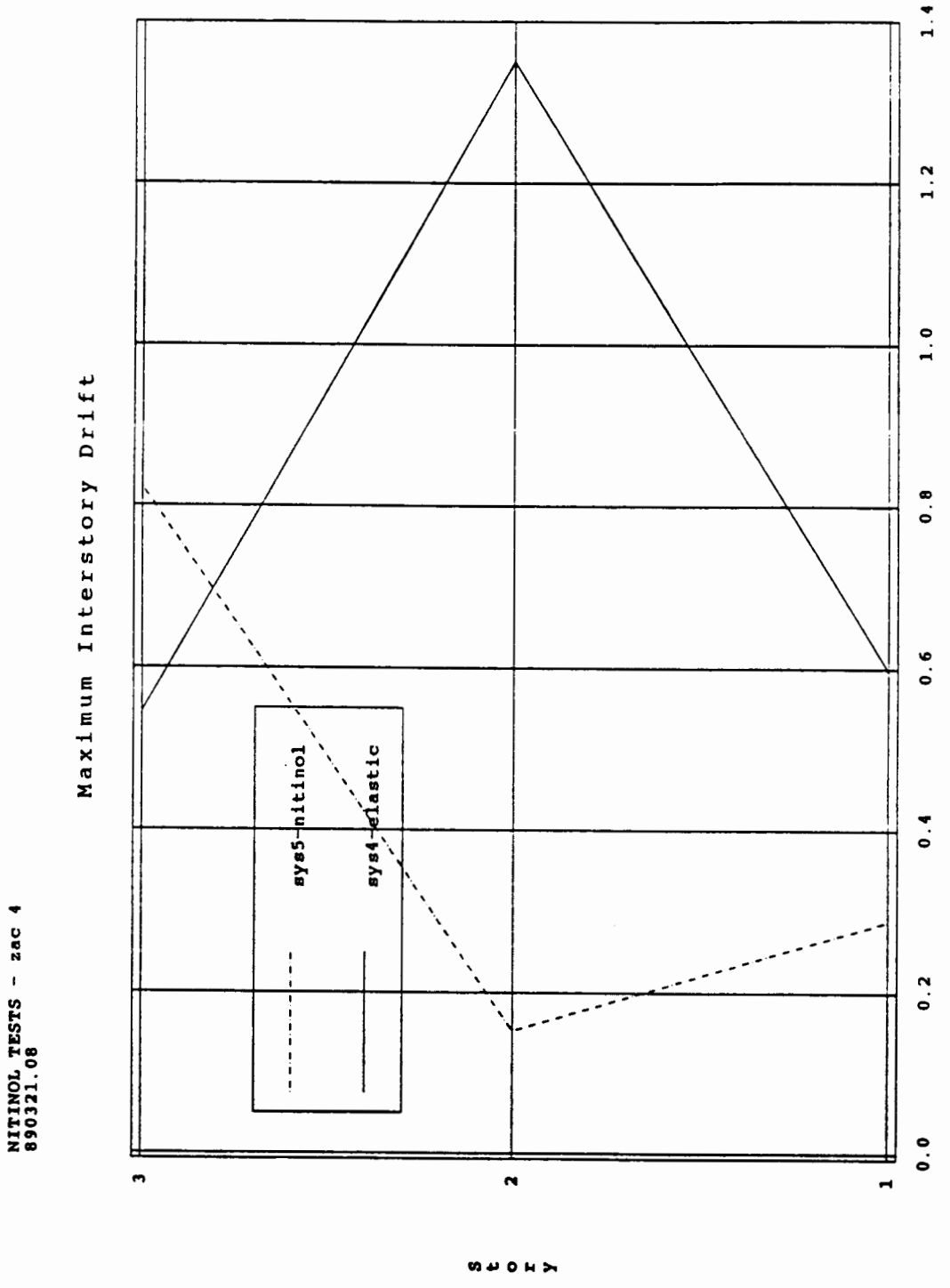

FIGURE 8.64 Maximum Interstory Drifts, Sys 4 & 5 - Zacatula